

A STATE SPACE AND CONTINUUM MECHANICS  
ANALYSIS OF STIRLING CYCLE MACHINES

---

LOUIS FRANKLIN GOLDBERG

VOLUME I

A thesis submitted to the Faculty of Engineering, University of the  
Witwatersrand, Johannesburg, in fulfilment of the requirements for the  
degree Doctor of Philosophy.

Minneapolis, Minnesota, July 1987

DECLARATION

I declare that this thesis is my own, unaided work. It is being submitted for the Degree of Doctor of Philosophy in the University of Minnesota, Minneapolis. It has not been submitted before for a degree or examination in any other University. I have performed most of the thesis research while being an employee of the Underground Railroad, University of Minnesota, Minneapolis.

*John*

10th day of July 1967



To my wife,  
Linda

#### ACKNOWLEDGEMENTS

I wish to express my gratitude and appreciation to the following people:

My supervisor, Prof. Anthony M. Starfield, for his encouragement, patience and meticulous scrutiny of the thesis draft.

My supervisor, Prof. Costa J. Rallis, who, despite the distance separating us, offered valuable advice and went out of his way to enable me to complete this thesis on a part-time basis in a location remote from the University of the Witwatersrand.

Dr Raymond L. Stelling, director of the Underground Space Center, University of Minnesota, whose wonderful generosity and support have been crucial to the completion of the thesis. Dr. Sterling not only enabled me to make unlimited use of Center computer facilities but also provided the funding for the thesis word-processing and original manuscript preparation. In addition, Dr. Sterling granted me considerably leeway in arranging my work schedule (including an extended leave of absence) in order that I could find the additional time necessary to undertake the thesis research.

Mr Peter Bigot who has transformed my often illegible scripts into a type-set quality text on a word processor. Peter also wrote and implemented the three-dimensional graphics programme used extensively to display the simulation results and spent many hours proof-reading the text and analysing it for logical integrity.

Dr Charles Fairhurst and the Department of Civil and Mineral Engineering for granting me usage of the departmental mainframe computer for thesis research purposes.

Mr Roy T. v and the NASA-Lewis Research Center for allowing the use of some of the results produced under the auspices of a NASA grant in the thesis.

Dr Colin West and the Oak Ridge National Laboratory for providing some of the pertinent experimental result publications used.

Mr Jeffrey Schreiber of NASA-Lewis for allowing me to make use of some of his unpublished experimental results.

Ms Andrea Spartz for her help in arranging for the thesis reproduction and for her administrative expertise in accommodating my often confusing work schedule.

My wife Linda and family Paul, Juliet and Erika for their unstinting support and patience in enabling me to spend so much time in conducting and completing the thesis research.

## CONTENTS

### VOLUME I.

	<u>Page</u>
DECLARATION .....	i
ABSTRACT .....	ii
ACKNOWLEDGEMENTS .....	iv
CONTENTS .....	v
LIST OF FIGURES .....	x
LIST OF TABLES AND COMPUTER PROGRAMMES .....	xvi
NOTATION .....	xxi
1 INTRODUCTION .....	1
1.1 MOTIVATIONAL BACKGROUND .....	1
1.2 AN HISTORICAL PERSPECTIVE .....	3
1.3 THE THESIS STATEMENTS AND OBJECTIVES .....	9
1.4 LIMITATIONS AND CRITERIA .....	11
1.5 PHILOSOPHICAL CONSIDERATIONS .....	14
1.6 THESIS ORGANISATION .....	17
1.7 CONVENTIONS USED .....	18
1.7.1 Operators .....	18
1.7.2 References .....	20
1.7.3 Flowcharts .....	21
2 A STATE SPACE ANALYSIS OF FREE-PISTON STIRLING CYCLE MACHINES .....	22
2.1 INTRODUCTION .....	22
2.2 STATE SPACE ANALYSIS FUNDAMENTALS .....	26
2.3 APPLICATION OF THE STATE SPACE ANALYSIS TO A BACK-TO-BACK FREE-PISTON STIRLING ENGINE .....	38
2.3.1 Introduction .....	38
2.3.2 Back-to-back FPSE State Space Analysis .....	41
2.3.3 Numerical Results .....	59
2.4 APPLICATION OF THE STATE SPACE ANALYSIS TO THE SUNPOWER RE-1000 FREE-PISTON STIRLING ENGINE .....	90
2.4.1 Introduction .....	90
2.4.2 RE-1000 FPSE State Space Analysis .....	92
2.4.3 Numerical Results .....	105
2.5 CLOSURE .....	131
3 A CONTINUUM MECHANICS DESCRIPTION OF COMPRESSIBLE FLUID FLOW .....	134
3.1 INTRODUCTION .....	134
3.2 THE GENERALISED TRANSPORT EQUATION .....	135
3.3 THE DIFFERENTIAL CONSERVATION EQUATIONS .....	139
3.3.1 Conservation of Mass .....	139
3.3.2 Conservation of Momentum .....	140
3.3.3 Conservation of Energy .....	142
3.4 THE INTEGRAL BALANCES .....	146
3.4.1 Conservation of Mass .....	147
3.4.2 Conservation of Momentum .....	148
3.4.3 Conservation of Energy .....	149

3.5	TURBULENT FLOW INTEGRAL BALANCES .....	151
3.6	CLOSURE .....	153
4	THE DISCRETE SIMULATION MODEL .....	155
4.1	INTRODUCTION .....	155
4.2	THE TURBULENCE MODEL .....	156
4.3	APPLICATION OF THE TURBULENCE MODEL .....	164
4.3.1	Thermodynamics of the Working Fluid .....	164
4.3.2	The Reduced Turbulent Integral Mass Balance .....	166
4.3.3	The Reduced Turbulent Integral Momentum Balance .....	166
4.3.4	The Reduced Turbulent Integral Energy Balance .....	168
4.4	THE SPATIAL DISCRETISATION SCHEME .....	170
4.4.1	The Staggered Control Volume Spatial Discretisation Scheme .....	173
4.5	APPLICATION OF THE REDUCED INTEGRAL BALANCES .....	178
4.5.1	Application of the Reduced Integral Mass Balance .....	178
4.5.2	Application of the Reduced Integral Momentum Balance .....	179
4.5.3	Application of the Reduced Integral Energy Balance .....	181
4.6	THE IMPLICIT CONTROL VOLUME BOUNDARY TERMS .....	185
4.6.1	Mass/Energy Control Volume Mass Flux and Velocity Gradient .....	186
4.6.2	The Boundary Advection of Momentum .....	189
4.6.3	The Boundary Advection of Energy .....	196
4.7	CLOSURE .....	200
5	NUMERICAL APPLICATION TO STIRLING CYCLE MACHINES .....	201
5.1	INTRODUCTION .....	201
5.2	NUMERICAL ALGORITHM SELECTION .....	207
5.3	THE ONE-DIMENSIONAL SIMULATION SYSTEM MODEL .....	217
5.4	THE REDUCED AND DISCRETISED ONE-DIMENSIONAL INTEGRAL BALANCES .....	220
5.4.1	One-Dimensional Integral Mass Balance .....	220
5.4.2	One-Dimensional Integral Momentum Balance .....	221
5.4.3	One-Dimensional Integral Energy Balance .....	227
5.5	THE IMPLICIT NUMERICAL ALGORITHM .....	233
5.5.1	The Implicit Pressure, Temperature, Velocity and Mass Flux Field Equations .....	234
5.5.2	The Implicit Numerical Algorithm Computing Sequence .....	244
5.5.3	Discussion of the Implicit Algorithm .....	250
5.5.4	Combined Eulerian/Lagrangian Control Volume Interfacing .....	254
5.6	CLOSURE .....	261

## VOLUME II

6	EMPIRICAL CONSIDERATIONS IN THE SIMULATION OF STIRLING CYCLE MACHINES .....	262
6.1	INTRODUCTION .....	262
6.2	TWO-DIMENSIONAL EFFECTS IN THE EXPANSION AND COMPRESSION SPACES .....	263
6.3	ADVECTION MODELLING IN THE REGENERATOR .....	265

6.4	EMPIRICAL CORRELATIONS.....	271
6.4.1	Friction and Dissipation Modelling.....	272
6.4.2	Heat Transfer Modelling.....	276
6.4.3	Empirical Correlation Selection.....	277
6.5	VALIDATION PROTOCOL.....	280
7	SIMULATION OF THE GENERAL MOTORS GROUND POWER UNIT 3.....	285
	STIRLING ENGINE	
7.1	INTRODUCTION.....	286
7.2	DESCRIPTION OF THE GM-GPU3 ENGINE.....	288
7.3	EXPERIMENTAL MEASUREMENTS.....	292
7.4	MODELLING ASSUMPTIONS.....	296
7.4.1	Fluid Dynamics.....	296
7.4.2	Boundary Conditions.....	297
7.4.3	Conduction Heat Transfers at the System Boundary.....	298
7.4.4	Regenerator Matrix Geometry.....	299
7.4.5	One-Dimensional Discretisation.....	300
7.5	EMPIRICAL CORRELATIONS.....	305
7.6	NUMERICAL TOPICS.....	313
7.6.1	Numerical Algorithm Constants.....	314
7.6.2	Cyclic Steady-State Convergence.....	316
7.6.3	Computer Hardware and Software.....	320
7.7	VALIDATION RESULTS.....	323
7.7.1	Baseline Calibration of the Simulation Model.....	327
7.7.2	Baseline Calibration Phase Evaluation of the Simulation Model.....	339
7.7.3	Baseline Simulation of the Experimental Test Map.....	391
7.7.4	Corrected Simulation of the Experimental Test Map.....	411
7.8	CLOSURE.....	431
8	SPACE POWER DEMONSTRATOR ENGINE SIMULATION SUMMARY.....	434
8.1	INTRODUCTION.....	434
8.2	SIMULATION OF THE SPDE.....	434
8.3	CLOSURE.....	443
9	CONCLUSION.....	444
9.1	SUMMARY AND RESEARCH ACHIEVEMENTS.....	444
9.1.1	Coupled Dynamic/Thermodynamic Analysis.....	444
9.1.2	Fluid Dynamic Simulation.....	446
9.2	CONCLUSIONS.....	455
9.2.1	Coupled Dynamic/Thermodynamic Analysis.....	455
9.2.2	Fluid Dynamic Simulation.....	456
9.3	RECOMMENDATIONS FOR FUTURE WORK.....	458
	APPENDIX A STATE SPACE ANALYSIS APPLICATION.....	460
A.1	BACK-TO-BACK FREE-PISTON STIRLING ENGINE.....	460
A.1.1	Assumptions.....	460
A.1.2	Geometry.....	461
A.1.3	Thermodynamics.....	462

A.1.4	Dynamics.....	463
A.1.5	State Space Analysis.....	464
A.2	SUNPOWER RE-1000 FREE-PISTON STIRLING ENGINE.....	469
A.2.1	Assumptions.....	469
A.2.2	Geometry.....	471
A.2.3	Thermodynamics.....	472
A.2.4	Dynamics.....	473
A.2.5	State Space Analysis.....	474
A.3	SOLUTION OF THE STATE SPACE EQUATIONS.....	478

### VOLUME III

APPENDIX B	STATE SPACE ANALYSIS COMPUTER PROGRAMMES.....	487
------------	---	-----

APPENDIX C	CONTINUUM MECHANICS ANALYSIS.....	513
------------	-----------------------------------	-----

C.1	ASSUMPTIONS.....	513
C.2	GENERALISED TRANSPORT EQUATION.....	513
C.3	VECTOR DIFFERENTIAL EQUATIONS.....	518
C.3.1	Continuity.....	518
C.3.2	Momentum.....	519
C.3.3	Energy.....	523
C.4	INTEGRAL BALANCES.....	527
C.4.1	Conservation of Mass.....	527
C.4.2	Conservation of Momentum.....	529
C.5	TURBULENT INTEGRAL BALANCES.....	532

APPENDIX D	SIMULATION MODEL DEVELOPMENT.....	535
------------	-----------------------------------	-----

D.1	TURBULENCE MODEL.....	535
D.2	THERMODYNAMICS OF THE WORKING FLUID.....	537
D.3	REDUCED TURBULENT INTEGRAL BALANCES.....	539
D.3.1	Reduced Turbulent Integral Mass Balance.....	539
D.3.2	Reduced Turbulent Integral Momentum Balance.....	540
D.3.3	Reduced Turbulent Integral Energy Balance.....	541
D.4	APPLICATION OF THE INTEGRAL BALANCES TO THE STAGGERED CONTROL VOLUME GRID.....	543
D.4.1	Staggered Grid Application of the Turbulent Integral Mass Balance.....	544
D.4.2	Staggered Grid Application of the Turbulent Integral Momentum Balance.....	545
D.4.3	Staggered Grid Application of the Turbulent Integral Energy Balance.....	547
D.5	MASS/ENERGY CONTROL VOLUME MASS FLUX AND VELOCITY GRADIENT.....	552
D.6	BOUNDARY ADVECTION OF MOMENTUM.....	557
D.7	BOUNDARY ADVECTION OF ENERGY.....	563

APPENDIX E	GENERAL MOTORS GROUND POWER UNIT 3 DESCRIPTION.....	569
------------	---	-----

E.1	WORKING SPACE KINEMATICS.....	569
E.2	EXPANSION SPACE PARAMETERS.....	572
E.3	COMPRESSION SPACE PARAMETERS.....	580

E.4	HEATER PARAMETERS.....	582
E.5	REGENERATOR PARAMETERS.....	586
E.6	COOLER PARAMETERS.....	595
E.7	EMPIRICAL CORRELATIONS.....	598
APPENDIX F FLUID DYNAMIC SIMULATION PROGRAMMES.....		607
F.1	INTRODUCTION.....	607
F.2	INITIAL CONDITIONS.....	608
F.3	WORKING FLUID VISCOSITY AND THERMAL CONDUCTIVITY.....	610
F.4	DETAILS OF THE SIMULATION PROGRAMMES.....	611
APPENDIX G SUPPORTING TABULAR AND GRAPHICAL DATA.....		678
REFERENCES.....		703

LIST OF FIGURES

<u>Figure</u>	<u>Title</u>	<u>Page</u>
1.1	The ideal Stirling cycle.....	3
1.2	Stirling machine fluid dynamic simulation development.....	5
2.1	Stable equilibrium condition.....	28
2.2	Asymptotically stable equilibrium condition.....	29
2.3	Operating stability condition.....	30
2.4	Schematic of the back-to-back free-piston Stirling engine....	40
2.5	Back-to-back free piston Stirling engine parameters.....	42
2.6	Piston and displacer motions.....	51
2.7	Operating hypersurface in the parameter space.....	58
2.8	Back-to-back FPSE performance: displacer stroke.....	65
	variation	
2.9	Back-to-back FPSE power output: displacer stroke.....	66
	variation	
2.10	Back-to-back FPSE performance: piston stroke variation.....	67
2.11	Back-to-back FPSE power output: piston stroke variation.....	68
2.12	Back-to-back FPSE performance: displacer rod diameter.....	70
	variation	
2.13	Back-to-back FPSE power output: displacer rod diameter.....	72
	variation	
2.14	Back-to-back FPSE performance: displacer damping.....	74
	coefficient variation	
2.15	Back-to-back FPSE power output: displacer damping.....	75
	coefficient variation	
2.16	Back-to-back FPSE performance: displacer mass variation.....	76
2.17	Back-to-back FPSE power output: displacer mass variation....	77
2.18	Back-to-back FPSE performance: piston mass variation.....	79
2.19	Back-to-back FPSE power output: piston mass variation.....	80
2.20	Back-to-back FPSE performance: piston diameter variation....	81
2.21	Back-to-back FPSE power output: piston diameter variation...	82
2.22	Back-to-back FPSE optimised performance: displacer stroke...	85
	variation	
2.23	Back-to-back FPSE optimised power yield: displacer stroke...	86
	variation	
2.24	Back-to-back FPSE optimised performance: piston stroke.....	87
	variation	

2.25	Back-to-back FPSE optimised power yield: piston stroke.....	88
	variation	
2.26	Schematic of the RE-1000 Free-piston Stirling engine.....	91
2.27	RE-1000 free-piston Stirling engine parameters.....	94
2.28	RE-1000 FPSE performance: displacer rod diameter.....	115
	variation	
2.29	RE-1000 FPSE power output: displacer rod diameter.....	116
	variation	
2.30	RE-1000 FPSE performance: displacer damping coefficient....	118
	variation	
2.31	RE-1000 FPSE power output: displacer damping coefficient....	119
	variation	
2.32	RE-1000 FPSE performance: displacer mass variation.....	121
2.33	RE-1000 FPSE power output: displacer mass variation.....	122
2.34	RE-1000 FPSE performance: exp space / heater.....	124
	temperature variation	
2.35	RE-1000 FPSE power output: exp space / heater.....	125
	temperature variation	
2.36	RE-1000 FPSE performance: comp space / cooler.....	126
	temperature variation	
2.37	RE-1000 FPSE power output: comp space / cooler.....	127
	temperature variation	
2.38	RE-1000 FPSE performance: charge pressure variation.....	129
2.39	RE-1000 FPSE power output: charge pressure variation.....	130
3.1	Turbulent flow profile.....	151
4.1	Double velocity correlation.....	158
4.2	Spatially staggered two-dimensional grid.....	171
4.3	Temporally staggered, spatially coincident.....	171
	one-dimensional grid	
4.4	Temporally and spatially staggered one-dimensional grid....	172
4.5	Spatial discretisation scheme characteristics.....	174
4.6	One-dimensional mass/energy control volume.....	187
4.7	One-dimensional, Eulerian mass/energy control volume.....	191
4.8	Net momentum flux dependence on the Peclet number.....	194
4.9	Normalised Eulerian momentum control volume.....	197
5.1	Incremental property profile of the explicit integration....	206
	algorithm	
5.2	Incremental property profile of an implicit integration....	210
	algorithm	

5.3	Structure of the pressure domain splitting algorithm.....	212
5.4	Alpha-configuration Stirling engine Mach line net for.....	213
	4000 rpm	
5.5	One-dimensional Stirling machine working space system.....	218
	model	
5.6	Flow area discontinuity.....	222
5.7	Pressure gradient discretisation.....	230
5.8	Elimination of a Lagrangian mass/energy control volume.....	255
5.9	Creation of a Lagrangian mass/energy control volume.....	258
6.1	Examples of strongly two-dimensional flows in Stirling.....	264
	machine cylinders	
6.2	Discretisation of a single regenerator mass/energy.....	267
	control volume	
6.3	Extrapolation of the linear regenerator temperature field...	269
7.1	Schematic of the GM-GPU3 Stirling engine. ....	289
7.2	Actual two-dimensional expansion space topology.....	301
7.3	Simulated one-dimensional expansion space topology.....	301
7.4	Actual two-dimensional compression space topology.....	302
7.5	Simulated one-dimensional compression space topology.....	302
7.6	Pseudo-two-dimensional compression space discretisation....	304
7.7	Gas flow inside circular tubes with abrupt contraction.....	306
	entrances	
7.8	Friction characteristics of flow through an infinite.....	310
	randomly stacked woven-screen matrix	
7.9	Heat transfer characteristics of gas flow through an.....	311
	infinite randomly stacked woven-screen matrix	
7.10	HE3-63B/1 baseline, equilibrium run temperature field.....	360
7.11	HE3-63B/2 baseline, equilibrium run temperature field.....	361
7.12	HE3-63B/3 baseline, equilibrium run temperature field.....	362
7.13	HE3-63B/4 baseline, equilibrium run temperature field.....	363
7.14	HE3-63B/6 baseline, equilibrium run temperature field.....	364
7.15	HE3-63B/1 baseline, equilibrium run velocity field.....	365
7.16	HE3-63B/3 baseline, equilibrium run velocity field.....	366
7.17	HE3-63B/6 baseline, equilibrium run velocity field.....	367
7.18	HE3-63B/1 baseline equilibrium run: pressure-volume.....	368
	diagrams	
7.19	HE3-63B/2 baseline equilibrium run: pressure-volume.....	369
	diagrams	

7.20	HE3-63B/3 baseline equilibrium run: pressure-volume.....	370
	diagrams	
7.21	HE3-63B/4 baseline equilibrium run: pressure-volume.....	371
	diagrams	
7.22	HE3-63B/6 baseline equilibrium run: pressure-volume.....	372
	diagrams	
7.23	Experimental helium pressure-volume diagrams.....	373
7.24	HE3-63B/1 baseline equilibrium run: piston face.....	374
	pressure profiles	
7.25	HE3-63B/2 baseline equilibrium run: piston face.....	375
	pressure profiles	
7.26	HE3-63B/3 baseline equilibrium run: piston face.....	376
	pressure profiles	
7.27	HE3-63B/4 baseline equilibrium run: piston face.....	377
	pressure profiles	
7.28	HE3-63B/6 baseline equilibrium run: piston face.....	378
	pressure profiles	
7.29	GM-GPU3 pressure and volume variation phasor diagram.....	345
7.30	HE3-63B baseline, UPD run temperature field.....	379
7.31	HE3-63B baseline, UPD run velocity field.....	380
7.32	HE3-63B baseline, UPD run pressure field.....	381
7.33	HE3-63B/1 baseline, equilibrium run pressure field.....	382
7.34	HE3-63B baseline, UPD run: pressure-volume diagrams.....	383
7.35	HE3-63B baseline, UPD run: piston face pressure profiles...	384
7.36	HE3-63B/3 baseline, equilibrium run pressure field.....	385
7.37	HE3-63B/6 baseline, equilibrium run pressure field.....	386
7.38	HE3-63B baseline UPD run: cumulative heat transfers.....	387
7.39	HE3-63B/3 baseline equilibrium run: cumulative heat.....	388
	transfers	
7.40	HE3-63B baseline UPD run: regenerator matrix.....	389
	temperature profile	
7.41	HE3-63B/3 baseline equilibrium run: regenerator matrix.....	390
	temperature profile	
7.42	H25-105A baseline, equilibrium run temperature field.....	401
7.43	H25-105A baseline, equilibrium run velocity field.....	402
7.44	H25-105A baseline, equilibrium run pressure field.....	403
7.45	Experimental hydrogen pressure-volume diagrams.....	423
7.46	H2-42A corrected UPD run: pressure-volume diagrams.....	424

7.47	H2-42A corrected equilibrium run: pressure-volume.....	425
	diagrams	
8.1	Schematic of the Space Power Demonstrator Engine.....	436
8.2.1	Expansion space / heater plenum pseudo-two-dimensional.....	438
	discretisation	
8.2.2	Upper compression space pseudo-two-dimensional.....	438
	discretisation	
8.2.3	Lower compression space pseudo-two-dimensional.....	438
	discretisation	
B.1	'PROGRAM FPSYM' and 'PROGRAM RE1000' main programme.....	490
	flowchart	
B.2	'PROGRAM FPSYM' subsidiary programme flowchart: state.....	492
	space analysis computation block	
B.3	'PROGRAM RE1000' subsidiary programme flowchart: state.....	494
	space analysis computation block	
C.1	Cohesive material body configuration.....	514
C.2	Tetrahedral material body segment.....	520
C.3	Turbulent flow time series profile.....	532
D.1	Staggered control volume grid.....	543
D.2	One-dimensional mass/energy control volume.....	553
D.3	One-dimensional incremental control volume.....	558
D.4	One-dimensional mass/energy control volume boundary.....	560
	conditions	
D.5	One-dimensional normalised momentum Eulerian control.....	564
	volume	
D.6	One-dimensional control volume boundary conditions.....	566
E.1	GM-GPU3 working space topology.....	570
E.2	Rhombic drive mechanism.....	570
E.3.1	Actual expansion space geometry and thermocouple.....	573
	locations	
E.3.2	One-dimensional representation of the expansion space.....	573
E.4	Expansion space wall heat transfer geometry.....	574
E.5	Displacer wall heat transfer geometry.....	577
E.6.1	Actual compression space geometry.....	581
E.6.2	One-dimensional representation of the compression space.....	581
E.7.1	Schematic of actual heater geometry.....	583
E.7.2	One-dimensional representation of the heater including.....	584
	thermocouple locations	

E.8	Actual regenerator/cooler assembly geometry.....	586
E.9	One-dimensional representation of the regenerator.....	587
	including thermocouple locations	
E.10	Linear gauze construction.....	589
E.11	Orthogonally projected free flow area.....	590
E.12	Sinusoidal gauze construction and free flow area shape.....	591
E.13	Regenerator matrix energy balance.....	594
E.14	One-dimensional representation of the cooler.....	595
F.1.1	UPD algorithm main programme flowchart.....	616
F.1.2	UPD algorithm subsidiary programme flowchart:.....	619
	simulation initialisation block	
F.2.1	Equilibrium algorithm main programme flowchart.....	621
F.2.2	Equilibrium algorithm subsidiary programme flowchart:.....	625
	simulation initialisation block	
F.2.3	Equilibrium algorithm subsidiary programme flowchart:.....	627
	expansion space initialisation block	
F.2.4	Equilibrium algorithm subsidiary programme flowchart.....	628
	compression space initialisation block	
F.2.5	Equilibrium algorithm subsidiary programme flowchart.....	629
	integration time increment control block	
F.3	UPD and equilibrium algorithm subsidiary programme.....	630
	flowchart: implicit integration subroutine block	
F.4	UPD and equilibrium algorithm subsidiary programme.....	632
	flowchart: empirical correlation block	
G.1	H2-42A corrected, equilibrium run temperature field.....	681
G.2	H2-42A corrected, equilibrium run velocity field.....	682
G.3	H2-42A corrected, equilibrium run pressure field.....	683
G.4	H3-61A corrected, equilibrium run temperature field.....	684
G.5	H3-61A corrected, equilibrium run velocity field.....	685
G.6	H3-61A corrected, equilibrium run pressure field.....	686
G.7	HE2-101B corrected, equilibrium run temperature field.....	687
G.8	HE2-101B corrected, equilibrium run velocity field.....	688
G.9	HE2-101B corrected, equilibrium run pressure field.....	689
G.10	H2-42A corrected UPD run: piston face pressure profiles.....	690
G.11	H2-42A corrected equilibrium run: piston face pressure.....	691
	profiles	

LIST OF TABLES AND COMPUTER PROGRAMMES

A TABLES

<u>Table</u>	<u>Title</u>	<u>Page</u>
1.1	Hierarchy of operators.....	19
1.2	Computer programme flowchart conventions.....	21
2.1	Back-to-back FPSE parameter vector components.....	44
2.2	Back-to-back FPSE baseline parameter vector .....	60
2.3	Back-to-back FPSE baseline parameter set performance.....	61
2.4	Back-to-back FPSE optimised parameter vector.....	83
2.5	Back-to-back FPSE optimised parameter set performance.....	84
2.6	RE-1000 FPSE parameter vector components.....	95
2.7	RE-1000 FPSE baseline parameter set.....	106
2.8	RE-1000 FPSE baseline parameter set performance.....	107
2.9	RE-1000 FPSE state space analysis / experimental data.....	110
	comparison	
2.10	Comparison of the indicated power discrepancies.....	113
5.1	Stirling machine numerical algorithm hierarchy.....	209
6.1	Parametric validation protocol.....	283
7.1	Salient specifications of the simulated GM-GPU3 Stirling....	291
	engine	
7.2	Simulation programme development hardware and software.....	321
	chronology	
7.3	Input parameter set.....	325
7.4	Working fluid properties.....	326
7.5	Heater spatial discretisation calibration with 6.....	329
	regenerator and cooler control volumes	
7.6	Cooler spatial discretisation calibration with 14 heater....	329
	and 6 regenerator control volumes	
7.7	Regenerator spatial discretisation calibration with 14.....	330
	heater and 7 cooler control volumes	
7.8	Test HE3-63B baseline calibration simulation runs:.....	332
	cyclic energy balance comparison	
7.9	Test HE3-63B baseline calibration simulation runs:.....	340
	cyclic parameter comparison	
7.10	Test HE3-63B baseline calibration simulation runs:.....	348
	ideal indicated work results generated using pressure profile parameters	

7.11	Test HE3-63B baseline simulation runs: simulation model.....	352
	characteristics	
7.12	Baseline calibration phase energy baseline discrepancies.....	358
7.13	Baseline simulation runs: non-dimensional parameters.....	392
7.14	Baseline simulation runs: cyclic energy balance.....	394
	comparison	
7.15	Baseline simulation runs: simulation/experimental.....	395
	cyclic energy balance data discrepancies	
7.16.1	Hydrogen working fluid baseline simulation runs:.....	399
	cyclic parameter comparison	
7.16.2	Helium working fluid baseline simulation runs: cyclic.....	406
	parameter comparison	
7.17	Corrected simulation runs: non-dimensional parameters.....	412
	and correction factors	
7.18	Corrected simulation runs: cyclic energy balance.....	416
	comparison	
7.19	Corrected simulation runs: simulation/experimental.....	417
	cyclic energy balance data discrepancies	
7.20.1	Hydrogen working fluid corrected simulation runs:.....	419
	cyclic parameter comparison	
7.20.2	Helium working fluid corrected simulation runs: cyclic.....	420
	parameter comparison	
7.21.1	Hydrogen working fluid corrected simulation runs: ideal.....	427
	indicated work results generated using pressure profile parameters	
7.21.2	Helium working fluid corrected simulation runs: ideal.....	428
	indicated work results generated using pressure profile parameters	
8.1	UPD simulation run input parameters.....	439
8.2	Corrected UPD simulation runs: n n-dimensional. ....	440
	parameters and correction factors	
8.3	Corrected UPD simulation runs: cyclic energy balance.....	441
	comparison	
8.4	Corrected UPD simulation runs: cyclic parameter.....	442
	comparison	
B.1.1	SYMENG programme: 'COMMON' block variable definitions.....	502
B.1.2	SYMENG programme: 'PROGRAM SYMENG' local variable.....	502
	definitions	

B.1.3	SYNENG programme: 'SUBROUTINE CALCUL' local variable.....	502
	definitions	
B.1.4	SYNENG programme: 'SUBROUTINE COMEQL' local variable.....	503
	definitions	
B.1.5	SYNENG programme: 'SUBROUTINE COMMUL' local variable.....	503
	definitions	
B.2.1	RE1000 programme: 'COMMON' block variable definitions.....	510
B.2.2	RE1000 programme: 'PROGRAM RE1000' local variable.....	510
	definitions	
B.2.3	RE1000 programme: 'SUBROUTINE CALCUL' local variable.....	510
	definitions	
B.2.4	RE1000 programme: 'SUBROUTINE COMMUL' local variable.....	512
	definitions	
E.1	Working space kinematic parameters.....	572
E.2	Expansion space parameters.....	579
E.3	Compression space parameters.....	582
E.4	Heater wall temperatures.....	585
E.5	Aggregate one-dimensional regenerator matrix parameters.....	593
E.6	Aggregate one-dimensional cooler parameters.....	596
E.7	Correlation digitisation for a circular tube with an.....	600
	abrupt contraction entrance	
E.8	Extrapolation curve linear regression correlation.....	601
	coefficients	
E.9	Friction factor correlation digitisation and.....	603
	interpolation for an infinite, randomly stacked woven-	
	screen matrix	
E.10	Heat transfer coefficient correlation digitisation and.....	604
	interpolation for an infinite, randomly stacked woven-	
	screen matrix	
F.1.1	GM-GPU3 simulation programme: UPD and equilibrium.....	633
	algorithm 'COMMON' block common variable definitions	
F.1.2	GM-GPU3 simulation programme: UPD algorithm 'COMMON'.....	634
	block variable definitions	
F.1.3	GM-GPU3 simulation programme: equilibrium algorithm.....	634
	'COMMON' block variable definitions	
F.2.1	GM-GPU3 simulation programme: UPD and equilibrium.....	635
	algorithm 'PROGRAM GPU3' common local variable definitions	
F.2.2	GM-GPU3 simulation programme: UPD algorithm 'PROGRAM.....	637
	GPU3' local variable definitions	

F.2.3	GM-GPU3 simulation programme: equilibrium algorithm.....	637
	'PROGRAM GPU3' local variable definitions	
F.3	GM-GPU3 simulation programme: UPD and equilibrium.....	637
	algorithm 'SUBROUTINE OUT' common local variable definitions	
F.4	GM-GPU3 simulation programme: UPD and equilibrium.....	637
	algorithm 'SUBROUTINE EWCONS' common local variable definitions	
F.5	GM-GPU3 simulation programme: UPD and equilibrium.....	638
	algorithm 'FUNCTION EWTEMP' common local variable definitions	
F.6	GM-GPU3 simulation programme: UPD and equilibrium.....	638
	algorithm 'SUBROUTINE RWCONS' common local variable definitions	
F.7	GM-GPU3 simulation programme: UPD and equilibrium.....	638
	algorithm 'SUBROUTINE TINGR' common local variable definitions	
F.8	GM-GPU3 simulation programme: UPD and equilibrium.....	638
	algorithm 'SUBROUTINE LOTWRT' common local variable definitions	
F.9.1	GM-GPU3 simulation programme: UPD and equilibrium.....	638
	algorithm 'SUBROUTINE CMPUT' common local variable definitions	
F.9.2	GM-GPU3 simulation programme: UPD algorithm 'SUBROUTINE.....	639
	CMPUT' local variable definitions	
F.9.3	GM-GPU3 simulation programme: equilibrium algorithm.....	639
	'SUBROUTINE CMPUT' local variable definitions	
F.10	GM-GPU3 simulation programme: UPD and equilibrium.....	639
	algorithm 'FUNCTION SS304' common local variable definitions	
F.11	GM-GPU3 simulation programme: UPD and equilibrium.....	639
	algorithm 'FUNCTION SS310' common local variable definitions	
F.12	GM-GPU3 simulation programme: UPD and equilibrium.....	640
	algorithm 'FUNCTION VISC' common local variable definitions	
F.13	GM-GPU3 simulation programme: UPD and equilibrium.....	640
	algorithm 'SUBROUTINE CYLIN' and 'SUBROUTINE PIPE' common local variable definitions	

F.14	GM-GPU3 simulation programme: UPD and equilibrium.....	640
	algorithm 'SUBROUTINE MECH' common local variable definitions	
F.15	GM-GPU3 simulation programme: UPD and equilibrium.....	640
	algorithm 'SUBROUTINE LACTRP' common local variable definitions	
F.16	GM-GPU3 simulation programme: UPD and equilibrium.....	641
	algorithm 'SUBROUTINE TDMA' common local variable definitions	
G.1	Test HE3-63B baseline simulation calibration run: UPD.....	692
	algorithm tabular output	
G.2	Test HE3-63B baseline simulation calibration run:.....	697
	equilibrium algorithm tabular output	

B COMPUTER PROGRAMMES

<u>Table</u>	<u>Title</u>	<u>Page</u>
B.1	Back-to-back free-piston Stirling engine state space.....	498
	analysis	
B.2	RE-1000 free-piston Stirling engine state space analysis....	504
F.1	GM-GPU3 UPD algorithm simulation programme.....	641
F.2	GM-GPU3 equilibrium algorithm simulation programme.....	655
F.3	Common UPD and equilibrium algorithm programme.....	674
	subroutines	

## NOTATION

### ROMAN

#### 1. Italicised Lower Case

- a real part of eigenvalue
- b imaginary part of eigenvalue
- c damping coefficient
- d diameter
- f force
- g scalar mass flux
- h convective heat transfer coefficient
- i index
- j index
- k index
- l length
- m index limit
- n unit outward normal vector component
- p index limit
- q contact heat flux scalar
- r radius
- t time
- v velocity scalar
- x displacement scalar
- y state space vector component
- z transformed state space vector component

#### 2. Italicised Upper Case

- A area
- B element in Jacobian matrix
- C heat capacity
- E external and mutual energy
- F compatibility matrix coefficients
- G total flux
- H enthalpy
- J Jacobian
- K constant
- M mass

*N* non-dimensional parameter  
*P* pressure  
*Q* heat  
*R* gas constant  
*S* stress tensor component  
*T* temperature  
*U* internal energy  
*V* volume  
*W* work  
*X* coordinate direction  
*Y* dummy integral variable or coordinate direction  
*Z* state space coefficient matrix component

3. Bold Lower Case

*b* parameter space vector  
*c* parameter space boundary excess vector  
*e* unit tensor  
*f* external and mutual force  
*g* mass flux density  
*n* unit outward normal  
*q* contact heat flux  
*s* contact force  
*v* velocity  
*x* displacement  
*y* state space vector  
*z* transformed state space vector

4. Bold Upper Case

*B* Jacobian matrix  
*D* deformation tensor  
*E* constant matrix  
*F* compatibility matrix  
*I* identity matrix  
*Q* 2nd order correlation tensor  
*S* stress tensor  
*T* extra stress tensor  
*X* real part of *Z*  
*Y* imaginary part of *Z*

Z state space coefficient matrix

5 Uniticised

g gravitational acceleration ( $9.81 \text{ m/s}^2$ )

j  $(-1)^{j-1}$

p particle

t auxiliary time parameter

6. Computer Programme Variables

NC no. of compression space Lagrangian mass/energy control volumes

NE no. of expansion space Lagrangian mass/energy control volumes

NH no. of heater mass/energy control volumes

NHL index of last heater mass/energy control volume

NC no. of cooler mass/energy control volumes

NKF index of first cooler mass/energy control volume

NR no. of regenerator mass/energy control volumes

NRF index of first regenerator mass/energy control volume

NRL index of last regenerator mass/energy control volume

NT total no. of mass/energy control volumes in the transfer space

GREEK

1. Upper Case

$\Gamma$  mole number

A bulk compressibility

E entropy

T gravitational potential energy

$\Phi$  dissipation

$\chi$  friction factor

$\omega$  empirical stress tensor correlation

2. Lower Case

$\alpha$  constant

$\beta$  constant

$\gamma$  ratio of specific heats

c stability constant

$\zeta$  error  
 $\eta$  efficiency  
 $\theta$  angular displacement  
 $\kappa$  conductivity  
 $\lambda$  eigenvalue  
 $\mu$  dynamic viscosity  
 $\xi$  volumetric porosity  
 $\pi$  ratio of circumference to diameter of circle  
 $\rho$  density  
 $\sigma$  free flow area ratio  
 $\tau$  extra shear stress tensor component  
 $\phi$  phase angle  
 $\psi$  generalised scalar, vector or tensor quantity  
 $\omega$  angular velocity

3. Bold Lower Case

$\phi$  state space coefficient matrix phase angle

OPERATORS

$d$  total derivative  
 $ddt$  total derivative with respect to time  
 $D$  substantive derivative  
 $DDt$  substantive derivative with respect to time  
 $f( )$  function of  
 $f( )$  vector function of  
 $F( )$  function of  
 $G( )$  vector function of  
 $h( )$  function of  
 $\partial$  partial derivative  
 $\mathcal{L}$  Laplace transform  
 $\delta$  differential incremental change  
 $\Delta$  incremental change  
 $\nabla$  divergence  
 $\int$  integral

$\Sigma$	summation
$\Pi$	product
$\bar{\psi} - (t) \bar{\psi}$	time average of $\psi$
$(L) \bar{\psi}$	length average of $\psi$
$(V) \bar{\psi}$	volume average of $\psi$
$(tV) \bar{\psi}$	time average of volume average of $\psi$
$\bar{\psi} - (t,t) \bar{\psi}$	time average of time average of $\psi$
$  \psi  $	norm of $\psi$
$ \psi $	absolute value or magnitude of $\psi$
$\cdot$	scalar product of vectors, vector product of vector and tensor
$:$	scalar product of tensors
$\det( )$	determinant

#### SUBSCRIPTS

Unlisted subscripts are spelt out in full, explained in the text or are a combination of listed subscripts separated by brackets

<i>a</i>	acoustic
<i>A</i>	location indicator
<i>amp</i>	amplitude
<i>b</i>	bounce space
<i>B</i>	location indicator
<i>BDC</i>	bottom dead center
<i>c</i>	compression space
<i>ccla</i>	compression space axial clearance
<i>cclr</i>	compression space radial clearance
<i>cd</i>	compression space / displacer interface
<i>cdd</i>	compression space, dead
<i>ch</i>	characteristic
<i>comp</i>	compensated
<i>con</i>	connecting rod

<i>conv</i>	convergence
<i>cr</i>	crank
<i>crg</i>	charge
<i>cw</i>	compression space wall
<i>cyc</i>	cycle
<i>cyl</i>	cylinder
<i>d</i>	displacer
<i>dead</i>	dead space
<i>DIS</i>	dissipation
<i>dmax</i>	displacer, maximum
<i>dmin</i>	displacer, minimum
<i>dp</i>	displacer/piston
<i>dr</i>	displacer rod
<i>ds</i>	displacer stop
<i>dw</i>	displacer wall
<i>e</i>	expansion space
<i>ecc</i>	eccentricity
<i>ecla</i>	expansion space axial clearance
<i>eclr</i>	expansion space radial clearance
<i>ed</i>	expansion space / displacer interface
<i>edd</i>	expansion space, dead
<i>ent</i>	entrance
<i>eq</i>	equilibrium
<i>ew</i>	expansion space wall
<i>ex</i>	exchanger
<i>ext</i>	exit
<i>ga</i>	gauze
<i>h</i>	heater
<i>H</i>	hydraulic
<i>ht</i>	heat transfer
<i>hw</i>	heater wall
<i>i</i>	index
<i>in</i>	boundary input
<i>IN</i>	input
<i>inc</i>	increment
<i>j</i>	index
<i>J</i>	index
<i>k</i>	cooler

<i>kw</i>	cooler wall
<i>L</i>	left hand
<i>m</i>	mesh or matrix
<i>(m)</i>	material body
<i>ma</i>	mesh or matrix, axial
<i>Ma</i>	Mach
<i>max</i>	maximum
<i>min</i>	minimum
<i>mr</i>	mesh or matrix, radial
<i>n</i>	momentum control volume
<i>nc</i>	momentum control volume, compression space
<i>ne</i>	momentum control volume, expansion space
<i>nk<sub>w</sub></i>	momentum control volume, cooler wall
<i>nL</i>	momentum control volume, left hand
<i>nm</i>	momentum control volume, mesh or matrix
<i>nma</i>	momentum control volume, mesh or matrix, axial
<i>nR</i>	momentum control volume, right hand
<i>OFFS</i>	offset
<i>out</i>	boundary output
<i>OUT</i>	output
<i>p</i>	piston
<i>P</i>	at constant pressure
<i>pc</i>	piston cylinder
<i>Pe</i>	Peclet
<i>per</i>	period
<i>pmax</i>	piston, maximum
<i>omin</i>	piston, minimum
<i>P/P</i>	pressure profile
<i>Fr</i>	Prandtl
<i>ps</i>	piston stop
<i>r</i>	regenerator
<i>R</i>	right hand
<i>ra</i>	radial
<i>rcas</i>	regenerator casing
<i>Re</i>	Reynolds
<i>rconv</i>	regenerator convergence
<i>rough</i>	roughness
<i>rw</i>	regenerator wall

s	gas spring
(s)	system of particles
sin	sinusoidal
ss	steady-state
St	Stanton
Su	Sutherland
T	at constant temperature
TOT	total
V	at constant volume
w	wall
wi	wire
x	axial
xr	radial component in axial coordinate direction
xx	axial component in axial coordinate direction
x <sup>θ</sup>	angular component in axial coordinate direction
Y	ordinate
He	helium
H <sub>2</sub>	hydrogen
n	momentum control volume
NC	compression space Lagrangian mass/energy control volume adjacent to transfer space
NE	expansion space Lagrangian mass/energy control volume adjacent to transfer space
NHL	last heater mass/energy control volume
NKF	first cooler mass/energy control volume
NRF	first regenerator mass/energy control volume
NRL	last regenerator mass/energy control volume
NT	last transfer space mass/energy control volume
(.5V)	mass/energy control volume centroid
Δt	time increment
*	distinguishing indicator
γ	compression space combined Eulerian/Lagrangian control volume
ε	expansion space combined Eulerian/Lagrangian control volume
X	friction

$\theta$  angular displacement  
 $\xi$  porosity  
 $\sigma$  wetted  
 $\omega$  angular velocity

SUPERSCRIPTS

(t) turbulent  
T transpose  
s previous time step  
\* distinguishing indicator  
' fluctuating component  
^ per unit mass  
· time rate of change

## CHAPTER 1

### I N T R O D U C T I O N

#### 1.1 MOTIVATIONAL BACKGROUND

At the beginning of 1977, under the leadership of Professor Costa J. Rallis, the Stirling engine research program at the University of the Witwatersrand was entering a dynamic growth phase. Urieli was completing his landmark doctoral thesis on the numerical simulation of Stirling cycle machines (Ur77) while Berchowitz was preparing an experimental test rig for validating a modified version of the Urieli simulation model (Be78). As an impressionable graduate student, the author joined this effort by commencing a research project on liquid-piston Stirling engines which later became the subject of a master's dissertation (Go79).

As Berchowitz's research matured, many questions were raised about the philosophy underpinning the Urieli simulation model. Predominantly, these queries related to the importance of a mathematically rigorous description of Stirling machine fluid dynamics as well as to the significance of momentum in the variable volume spaces. At the termination of his research, Berchowitz demonstrated via his experimental data that these queries remained largely unresolved.

During the course of the liquid-piston engine research, a novel liquid-piston, free-displacer Stirling engine (LPPDSE) was developed and tested (Go79, GR79). The LPPDSE was designed using a numerical simulation of the displacer and piston dynamics coupled to simplified

adiabatic and/or isothermal descriptions of the working fluid thermodynamics. The dynamic/thermodynamic coupling emerged as the primary factor enabling a successful simulation to be developed. A comparison of the simulated and experimental performance data later showed significant discrepancies between the simulated and measured operating frequencies. This was ascribed to a lack of physical correspondence between the experimental and simulated dynamic/thermodynamic coupling mechanisms which were radically different from each other.

Hence the need for an accurate coupled dynamic/thermodynamic design analysis for free-piston Stirling machines clearly became apparent. To be useful for innovative or non-standard free-piston designs (such as that of the LPPDSE), such an analysis must be self-contained, avoiding the necessity of stipulating displacer and piston motions. Very often, such dynamic motions may not be precisely predetermined. This is true for the LPPDSE in particular, owing to the discontinuous, non-linear motion of its displacer. Berchowitz and Wyatt-Mair (BW79) explored the coupled dynamic/thermodynamic analysis issue by applying classical control theory to a standard beta-configuration, free-piston Stirling engine. Their approach, however, requires the specification of predefined harmonic piston and displacer motions.

The queries raised by the experimental evaluation of the Urieli simulation model and the deficiencies of the LPPDSE design methodology originally motivated the research described in this thesis. These issues were later recognised by the Stirling research community at large, substantiating the relevance of and the need for the research undertaken. This research spans a period of eight years, from 1979 to

1987. During its evolution, the research has benefitted from an interaction with several diverse Stirling machine projects. These projects have ranged from the design of a linear alternator dynamometer control system for the Oak Ridge National Laboratory (GL85), to the development of a two-dimensional fluid dynamics component simulation of the Space Power Demonstrator Engine for NASA (the United States National Aeronautics and Space Administration) (Go87.1). As such, this thesis provides an evolutionary link between the original simulation and analysis work of Urieli and Berchowitz and the recent advent of two-dimensional Stirling machine simulation models.

## 1.2 AN HISTORICAL PERSPECTIVE

The ideal Stirling cycle devised by either James or Robert Stirling in 1816 (Ko72) is depicted in figure 1.1.

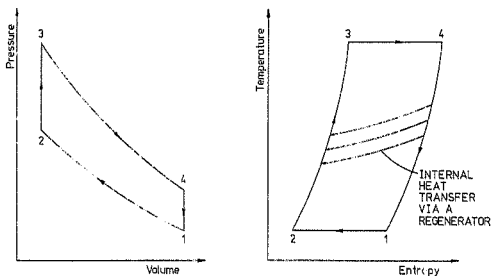


Figure 1.1 The ideal Stirling cycle

The cycle consists of four ideal processes executed in clockwise sequence. An isothermal compression of the working fluid occurs during process 1-4. Thereafter, in process 2-3, the working fluid is transferred isochorically from the compression to the expansion spaces. This is followed by an isothermal expansion phase 3-4 during which work is extracted from the expansion space. The working fluid is then transferred isochorically back to the compression space, closing the cycle. Heat is absorbed from the working fluid by a regenerator during process 4-1 and returned to the fluid during process 2-3. Therefore, providing that the regenerator is perfect (that is, all the heat absorbed is later released), the ideal Stirling cycle conforms externally to the Carnot cycle and is thus capable of yielding the maximum theoretical (or Carnot) efficiency for a heat engine.

The evolution of the ideal Stirling cycle, its thermodynamic analysis and its application to practical energy conversion machinery have been thoroughly documented in the literature, perhaps most notably by Walker (Wa73). The relatively recent acceptance of the Stirling machine as a viable thermal energy conversion device is reflected by the inclusion of the Stirling cycle as a discrete topic in several standard thermodynamics texts (such as that authored by Wark (Wa77)). The reader is referred to these texts (or any of several others) to obtain background information on the fundamentals of Stirling cycle machine hardware and analysis.

The development of the Stirling machine fluid dynamic simulation may be broadly traced with reference to figure 1.2.

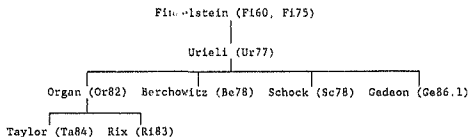


Figure 1.2 Stirling machine fluid dynamic simulation development

In a series of papers published between 1960 (F160) and 1975 (F175), Finkelstein described a computerised procedure for solving the mass and energy conservation equations for Stirling machine working space boundary conditions. No momentum balance is explicitly included in Finkelstein's approach (Be78) so that working fluid inertia is ignored. In these circumstances, the mass fluxes at the expansion and compression space ports are computed via a pressure drop correlation. A further consequence of Finkelstein's method is that the kinetic energy of the working fluid is not included in the energy conservation equations.

Urieli advanced Finkelstein's simulation methodology by applying momentum, mass and energy conservation balances to the working space of a simplified, alpha (or in-line) Stirling engine with horizontally opposed expansion and compression space cylinders (Ur77). Differential formulations of the conservation equations are applied using a one-dimensional, nodal, spatial discretisation scheme. These discretised equations are integrated temporally over a cycle via an explicit numerical algorithm. The integration process is repeated for several cycles until cyclic steady-state equilibrium is achieved.

Berchowitz refined the analytic derivation of Urieli's simulation model and applied it to an experimental test rig (Se78). A comparison between the experimental and simulated data yielded a mean discrepancy of approximately 20% for the indicated works and external heat transfers. In addition, the experimentally observed relative phase angles between the expansion and compression space pressure profiles did not correspond with those simulated. This discrepancy was attributed to the exclusion of momentum in the variable volume spaces in the Urieli model.

Schock (Sc78) applied a variant of the Urieli simulation methodology to a beta-configuration, free-piston Stirling engine. A principal difference between the Schock and Urieli models is Schock's use of weighted-average velocities to determine advective enthalpy and momentum transport between nodes. In contrast, Urieli invokes a staggered grid discretisation of the momentum equation coupled with an 'upwind differencing' scheme (Ro82) to determine inter-nodal advective transport.

Organ criticised the nodal simulation approach spawned by Urieli (Or82) for introducing arbitrary discontinuities into the flow field and not including the effects of information propagation. As a solution to these deficiencies, Organ proposed a 'method of characteristics' simulation methodology commonly applied to compressible gas aerodynamic flows (Sh54). He demonstrated the method for a particular alpha-configuration Stirling machine with the restriction of an assumed isothermal working space. Taylor pursued this approach and attempted to overcome the isothermal limitation by using the method of characteristics to solve a full set of mass,

momentum and energy conservation equations for Stirling machine working space boundary conditions (Ta84). Rix (R183), in an alternate development of Organ's simulation philosophy, applied a Lagrangian spatial discretisation approach to modelling Stirling machine fluid dynamics. However, the method is demonstrated only for a geometrically simple case in which transient momentum effects are ignored.

The method of characteristics approach to Stirling machine simulation eliminates arbitrary fluid discontinuities and models information propagation phenomena. The Lagrangian discretisation method *per se* also eliminates arbitrary discontinuities, but evidently does not describe information propagation effects. However, to the author's knowledge, neither simulation approach has been successfully applied to a complete and unabridged fluid dynamic analysis of a geometrically complex, non-laboratory Stirling machine.

Several other variations of the Urieli simulation model have been proposed over the years. A recent notable addition has been made by Gedeon (Ge86.1). Using a global, temporally implicit integration scheme, Gedeon manages to converge his simulation model rapidly towards the cyclic steady-state. However, this scheme reportedly mandates an extremely coarse temporal resolution (typically 1e. than ten increments per cycle). As such, Gedeon's approach does not seem to specifically address the issues raised either by Berchowitz or by Organ.

The historical record of the development of coupled dynamic/thermodynamic free-piston Stirling engine analyses does not readily lend itself to an hierarchical interpretation. A pioneering effort in this area may be ascribed to Berchowitz and Wyatt-Mair (BW79) who based their approach (as noted in section 1.1) on applying a classical control theory analysis to a particular free-piston machine. Their analysis relies upon the stipulation of harmonic kinematic motions, a concept which had been advocated previously by Rauch (Ra75). Several other researchers have expanded upon the defined harmonic motion control theory analysis, notably Chen and Griffen (CG84, CG86) and Cichy and Carlini (CC84).

7) An alternative to the control theory approach is the phasor diagram methodology reported by Fokker and van Eekelen (FE78). The phasor diagram method has been adapted to various engine configurations including a liquid-piston machine (We83). However, all these control theory and phasor diagram methods are still reliant upon the specification of defined engine kinematics.

This abbreviated historical perspective is amplified where appropriate in later chapters. Nevertheless, limitations and qualifications have been noted in both the areas of fluid dynamic simulation and coupled dynamic/thermodynamic analysis. These limitations and qualifications demonstrate the validity of and the need for the Stirling cycle machine research which is the subject of this thesis.

### 1.3 THE THESIS STATEMENTS AND OBJECTIVES

The limitations of the coupled dynamic/thermodynamic analyses of free-piston Stirling cycle machines are addressed by an application of modern control theory in the guise of a state space analysis. This approach is postulated to yield a closed-form solution to the relevant differential equations without the necessity of stipulating defined kinematic motions. The closed-form solution is achieved via the derivation of a single equation inter-linking all the machine design parameters. This equation defines what is termed a 'hypersurface' in the parameter space (explained in section 2.2). Such a hypersurface equation permits individual parameters to be manipulated in a systems context allowing an assessment of the feasibility of the design to be made. Furthermore, a single equation representation enables optimisation studies to be carried out effectively because the synergistic effects of varying individual parameters are automatically accounted for. Lastly, a design parameter set satisfying the hypersurface equation enables closed-form solutions for the piston and displacer motions to be obtained as dependent functions of the design parameters themselves.

Hence, the formal thesis for the coupled dynamic/thermodynamic Stirling machine analysis research may be expressed as follows:

#### First Thesis Statement

A parameter space stability boundary hypersurface is a sufficient and unique characterisation of the coupled dynamics and thermodynamics of a free-piston Stirling cycle machine.

A physically rigorous approach is adopted to address the limitations in existing Stirling machine fluid dynamic simulations. The fundamental postulate is that the fluid dynamic processes occurring within a Stirling machine may be represented adequately by a continuum mechanics description of the working fluid. Coupling this description with the solid body conservation laws for mass, momentum and energy, enables the relevant fluid conservation balances to be derived without recourse to the less generalised Navier-Stokes approach. These balances are cast in total temporal derivative form within an integral, volume-averaged structure.

After time-averaging, the integral balances are reduced to a format amenable to numerical solution by the application of a turbulence model. A spatial discretisation scheme is defined enabling the reduced integral balances to be applied naturally to a multi-dimensional space without empirical manipulation. Finally, information propagation hypotheses are presented in terms of an implicit numerical integration scheme. Only at this juncture is the resultant simulation model applied rigorously to a particular Stirling machine description.

This overall simulation approach may be summarised by a formal thesis statement as follows:

Second Thesis Statement

The volume- and time-averaged cyclic equilibrium working fluid behaviour of a Stirling cycle machine may be determined along a spatial integration path in a continuum.

The primary objective of the thesis research is to substantiate the first and second thesis statements. Secondary objectives include:

- the development of a practical and accurate free-piston Stirling machine design procedure which enables an effective design optimisation to be performed rapidly
- the creation of a simulation model which may be implemented on a microcomputer without any loss of detail or accuracy. In other words, the microcomputer implementation should be indistinguishable from a mainframe computer implementation in all respects, except possibly that of execution speed.

#### 1.4 LIMITATIONS AND CRITERIA

An experimental data validation criterion is used to demonstrate substantiation of the thesis statements. This criterion mandates the selection of appropriate Stirling machines for which adequate experimental results are available. These machines preferentially must be real (as opposed to hypothetical or generic) devices representative of useful Stirling hardware and not specialised laboratory configuration prototypes. In selecting such machines, no attempt was made to screen out candidates which possess working space geometries not readily amenable to numerical description. The field of qualified candidate machines for which well-founded, published experimental data are available is somewhat restricted. Nevertheless, two such Stirling machines have been identified, namely, the Sunpower RE-1000 free-piston and General Motors GPU3 disciplined piston engines. These engines have been extensively tested by NASA and the

test results are available in the public domain. The RE-1000 and GPU3 engine test results are used as the validation criteria for substantiating the first and second thesis statements respectively.

No particular constraints are imposed upon the substantiation of the first thesis statement. However, the fluid dynamic simulation development is restricted as follows:

1. Only the time-averaged working fluid properties are simulated; predictions of turbulent fluctuating properties are not produced by the simulation model.
2. The focus of the simulation model is directed towards the prediction of cyclic steady-state or equilibrium behaviour directly. In particular, the information propagation hypotheses developed are not directly suitable for predicting transient extra-cyclic (as opposed to transient intra-cyclic) phenomena.
3. A strictly one-dimensional spatial discretisation is used to apply the simulation model.

These limitations are established principally for pragmatic reasons. The prediction of transient, fluctuating working fluid properties under oscillating turbulent flow conditions presents a difficult problem within the context of Stirling engine geometrical boundary conditions. This class of problem is usually addressed by very large scale, state-of-the-art research computer programmes, although typically on a single component basis only. As such, from a systems perspective, these programmes are apparently not readily capable of tackling the inter-related complexities of a Stirling machine working space, at least in the sense of producing the required transient property fluctuations. Furthermore, these simulation programmes are

commonly implemented on supercomputers, a resource not available for conducting the thesis research. Hence, the exclusion of turbulent fluctuating property predictions from the simulation model is a practical necessity.

Focussing the simulation model on the direct prediction of cyclic steady-state behaviour is rather less of a limitation than an advantage. All the experimental validation data are measured under cyclic steady-state conditions only. In addition, as most Stirling machines generally operate under steady-state or quasi-steady-state conditions, there is little practical need for extra-cyclic transient simulation. This must clearly be distinguished from the simulation of intra-cyclic transient effects at the cyclic steady state. A further advantage of the cyclic steady-state restriction is a considerable saving in computation. This facilitates the use of numerical simulation for practical Stirling machine analysis purposes.

Probably the most contentious limitation is the one-dimensional application of the simulation model. All the simulation models reviewed in section 1.2 have also been applied in one-dimension only, either because of the restrictions imposed by their analytic formulations, or simply because two-dimensional simulation was considered impractical. A two-dimensional spatial implementation of a method of characteristics simulation can become quite complex, if not intractable, when applied to geometrical boundary conditions typifying real Stirling hardware.

However, no analytic restrictions apply to the simulation model proposed in this thesis since the model is developed within a multi-dimensional framework. Thus the choice of a one-dimensional application is motivated by a desire to maintain continuity with previous Stirling machine simulation research. This predicates an evolutionary approach in which it is necessary to first substantiate the second thesis statement in one dimension before considering a two-dimensional substantiation. In a pragmatic context, two- or three-dimensional Stirling machine simulations require larger computer resources than are commonly available. This tends to make the use of such simulations economically unattractive for practical design and analysis purposes. Although the restriction of the thesis research to a one-dimensional context is therefore somewhat arbitrary, it enables the validation process to suggest whether and where multi-dimensional effects are significant in the simulation of Stirling cycle machine fluid dynamics.

As alluded to in section 1.1, the simulation model has been successfully applied in two dimensions. This application incorporates a two-dimensional heater in an otherwise one-dimensional discretisation of the NASA Space Power Demonstrator Engine (Go87.1). This research has been performed as part of another project and is not included in this thesis.

#### 1.5 PHILOSOPHICAL CONSIDERATIONS

In performing any research, the philosophy of the researcher becomes woven into the fabric of the work. Of particular note in this regard

is the choice of an integral conservation balance formulation rather than the more frequently adopted differential formulation approach. This choice stems from a conviction that, in reality, differential conservation balances are physically meaningful only on a volume-averaged basis. The concept of intensive working fluid properties which literally exist at a point is a mathematical abstraction appropriate to a continuum only. This abstraction appears to be at odds with the observed probabilistic particulate nature of matter. In the latter model, intensive properties such as density and temperature only have physical meaning for a region of space. Within a given spatial region, intensive fluid properties are the statistically averaged manifestation of the behaviour of the enclosed particles. Hence a physically appropriate application of differential conservation balances suggests that they be volume-averaged prior to numerical discretisation. This volume-averaging produces a set of equations which emulate the characteristics of integral balances but are not as generalised or as convenient to implement numerically.

Integral balances directly produce volume-averaged working fluid properties that are readily and unambiguously interpreted in a numerically discrete spatial context. This avoids some of the difficulties associated with differential analyses such as the assumption of fluid property interpolation profiles between distinct points. Finally, simulation models based on integral analyses may be more readily scaled geometrically than their differential counterparts.

For all these reasons, the simulation model is based upon directly derived integral conservation balances. Nevertheless, it is acknowledged that this choice is more of a personal bias than a rigorous continuum mechanics necessity, as demonstrated by the many successful differential equation based simulations reported in the literature (Ro82).

Significant importance in developing the simulation model has been placed on its ability to be executed on a standard sixteen bit microcomputer (stated as a secondary thesis objective), particularly in terms of the one-dimensional application structure used. This stems from an observation that the practical utility of computer based analytical techniques is in inverse proportion to the cost of the hardware required to implement them. In advocating a microcomputer based simulation implementation, no reduction in the accuracy, completeness or capacity of the simulation model is tolerated. The capabilities of the model should be independent of the computer hardware used for its implementation. Hence a reduction in execution speed is the only penalty in a microcomputer implementation compared with a conventional mainframe or minicomputer implementation. However, the simulation model must still be capable of practical usage on a microcomputer notwithstanding the execution speed limitation. This predates an efficient and well-structured numerical integration algorithm which minimises the arithmetic computation requirements. These implementation objectives have guided the development of the simulation model to a significant (although not predominant) extent.

## 1.6 THESIS ORGANISATION

The thesis is organised into nine chapters and seven appendices in three volumes. The first five chapters are grouped together in volume I while volume II contains the remaining chapters and the first appendix. The balance of the appendices together with the list of references form the contents of volume III.

Chapter 2 and its associated appendices A and B are devoted to the coupled dynamic/thermodynamic analysis of free-piston Stirling engines and substantiation of the first thesis statement. The development of the fluid dynamic simulation model and the substantiation of the second thesis statement comprise the remainder of the thesis.

A continuum mechanics derivation of the conservation balances forms the subject of chapter 3 and appendix C. Chapter 4 and appendix D describe the reduction of the conservation balances via the inclusion of a turbulence model. Thereafter, a staggered spatial mesh discretisation scheme is developed for applying the reduced conservation balances to Stirling machine working spaces. Chapter 5 contains a rigorous application of the reduced and discretised conservation balances to a one-dimensional Stirling engine system model. The information propagation hypotheses are presented and the resulting numerical algorithm is developed.

Empirical considerations influencing the simulation model are described in chapter 6 and the validation protocol mandated thereby is discussed. Chapter 7 and appendix E are devoted to the application of the simulation model to the General Motors GPU3 engine within the

framework of the validation protocol. Appendices F and G contain listings of the simulation programmes, flowcharts describing the algorithms used as well as additional graphics and tabular output results supporting the discussion in chapter 7.

A brief synoptic description of some additional validation of the simulation model performed using the NASA Space Power Demonstrator Engine is described in chapter 8. Finally, a summary and conclusions are given in chapter 9.

## 1.7 CONVENTIONS USED

### 1.7.1 Operators

The hierarchy of operators implemented consistently throughout the thesis is shown in table 1.1. Some examples of the use of operator hierarchy are:

$$a + bc/d \ln e^3 = a + \left\{ (bc) / [dx(\ln(e^3))] \right\}$$

$$a \cdot \nabla \cdot b = a \cdot (\nabla \cdot b)$$

It is important to note that:

$$a/b + c = (a/b) + c \neq \frac{a}{b+c}$$

but:



$$aDbc/de = (ax(Db)xc) / (dxe)$$

but:

$$aD(b+c)(d+e) = ax\{D(b+c)\}x(d+e)$$

Also:

$$ddc \int (a+b)da = ddc \left( \int (a+b)da \right)$$

(The variables  $a, b, c, d, e, a, b, A,$  and  $B$  have no significance here in terms of the notation presented and are used as examples only.)

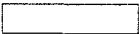
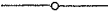
#### 1.7.2 References

The Rallis system of reference designation is used. Each publication is designated by four characters: two Roman letters followed by two numerals. The numerals denote the year of publication of the reference which, if prior to 1900, is denoted by four numerals. Single authors are denoted by the first two letters of the author's surname with the first and second letters being in upper and lower case respectively. If there are two or more authors, then the letters denote the surname initials of the first two authors, both being in upper case. If the name of the author is unknown, three letters denoting the name of the journal are used instead. In cases where two or more references have the identical four character designations, they are distinguished by a numeral preceded by a period, for example Ab86.1 and Ab86.2. The references are listed in alphabetical sequence according to the name or names of the authors.

1.7.3 Flowcharts

The conventions shown in table 1.2 are used in all the computer programme flowcharts presented.

Table 1.2 Computer programme flowchart conventions

Description	Symbol Convention
control statement	
execution statement	
decision statement	
algorithm flow line break location	
entrance from location A	
exit to location A	
subsidiary algorithm block demarcator	
entry to subsidiary algorithm block	
exit from subsidiary algorithm block	

## CHAPTER 2

### A STATE SPACE ANALYSIS OF FREE-PISTON STIRLING CYCLE MACHINES

#### 2.1 INTRODUCTION

When designing Stirling cycle machines in general, and free-piston configurations in particular, a critical issue in achieving a working piece of hardware and optimising its performance is the interaction between the dynamics and fluid dynamics of the machine. In the case of kinematic or disciplined piston machines, the dynamics of the engine (piston displacements and relative phase angles) are generally precisely determinable from purely geometrical considerations. However, if not externally controlled, the operating frequency of kinematic machines is dependent upon the kinetic / fluid dynamic interaction. Free-piston or Beale machines, in contrast, are typified by coupled fluid and piston dynamics mandating cognisance of their interaction to achieve a successful design. This is even more pertinent when designing and developing novel Stirling machine configurations, as demonstrated during the development of a prototype liquid-piston, free-displacer Stirling engine (LPFDSE) (Go79, GR79).

The LPFDSE was designed and analysed using a coupled dynamic/thermodynamic computer simulation programme linking the dynamics of the liquid piston and free displacer to the thermodynamics of the working fluid. Several working space configurations were evaluated using the Schmidt (Sch871) and ideal pseudo-Stirling analyses (Be78, WK65). Specifically, permutations of adiabatic (ideal

pseudo-Stirling) and isothermal (Schmidt) expansion and compression spaces were separated by an isothermal heater, regenerator and cooler assembly of variable geometry. In comparing the experimental and simulated operating frequencies for all the permutations evaluated, the simulation consistently over-predicted the operating frequency by an average of 69%. Furthermore, the convergence of the numerical solution to a closed steady-state cycle was critically dependent on the bounded interval chosen for the seed convergence parameters. Thus the solution would converge only if the initial estimate of the convergence parameters (liquid column velocity and acceleration) fell within the empirically determined 'correct' range. It was concluded that the frequency prediction anomaly could be ascribed to a lack of correspondence between the simulated and experimental configurations as well as to an inadequate numerical representation of the liquid column dynamics. The initial condition sensitivity emphasized the importance of matching the impedance of the liquid column dynamics to those of the working fluid dynamics, an effect noted by West for the Fluidyne engine (Ge76, We71). Thus, from both design and experimental perspectives, the issue critical to the successful operation of LPFDSE was shown to be the dynamic / fluid dynamic interaction.

These observations, although specific to the LPFDSE, are representative of the issues that face the free-piston Stirling machine designer in general. The essential issue devolves to developing a methodology for choosing a set of engine parameters which will produce a performance optimised design. Much effort has been expended on developing fluid dynamic and thermodynamic analyses (Ur83) for design purposes. In the case of free-piston machines though, these analyses usually require the stipulation of the machine kinematics (piston and displac:

motions) as boundary conditions. Thus the issues of dynamic / fluid dynamic coupling are avoided or dealt with indirectly by treating the dynamics and fluid dynamics separately. Since this approach can be both tedious and expensive, it may impede the creativity of the design process.

In this context, several workers have developed methodologies for analysing the combined dynamics/thermodynamics of free-piston Stirling engines in particular. Notably, Berchowitz and Wyatt-Mair (BW79) used classical control theory to solve the combined dynamic and isochermal thermodynamic (Schmidt analysis) equations in closed form by assuming that the piston and displacer motions can be described by complex sinusoidal functions. A similar harmonic motion assumption was invoked by Rauch (Ra75) to estimate the frequency response and dynamic performance of a free-piston engine. However, in this case, the component dynamics and thermodynamics were decoupled by treating the working gas as a linear spring. Cichy and Carlini (CC84) have used essentially the same methodology to perform a 'frequency dynamic' analysis by casting the engine dynamics in state space form. The thermodynamics are decoupled from the dynamics by assuming a sinusoidal working space pressure variation. Rauch (Ra80) also has used a decoupled approach to obtain a more precise estimate of working fluid behaviour (including, for example, regenerator pressure drops) by assuming harmonically varying thermodynamic parameters. West (We83) adapted the phasor diagram approach to elegantly represent the combined dynamics and thermodynamics of the liquid-piston Fluidyne engine, although once again, it was apparently necessary to assume sinusoidal piston motions. Phasor diagrams also have been applied to solid piston Stirling engines by Fokker and van Eekelen (FV78).

All of these methodologies share the same difficulty, namely the a priori assumption of given piston and displacer motions or thermodynamic parameter variations. This mitigates against an independent assessment of the stability of the engine operation, which can be critical in the case of free-piston engines subject to variable loading. Under such conditions, the operating envelope can be quite narrowly bounded by the tendency of the piston and/or displacer to knock against the engine casing under light loading and stall under heavy loading. These defined parameter methodologies do not provide any means of assessing the validity of the analytical assumptions made. These assumptions are particularly important when they result in the exclusion of fluid dynamic irreversibilities which can materially affect the predicted performance. The significance of these irreversibilities has been shown by Chen *et al* (CC84) using extrinsic second law or entropy calculations, although the analysis follows the aforementioned precedents by assuming harmonic piston and displacer motions.

An investigation into an alternate approach aimed at addressing some of these issues was undertaken by the author in 1979. This approach is based on the state space analysis concepts of modern control theory and, in particular, on the stability theorems of Lyapunov (Ha63). The methodology enables the combined dynamics and thermodynamics to be described as a unitary system. Closed form solutions defining the engine operation may be obtained without recourse to any assumed thermodynamic parameter profiles or kinematic motions. The analysis was first presented by way of a case study in 1980 (Go80) while the theoretical foundations of the methodology were presented in 1983

(Go83). The following description elucidates the completed development of the state space analysis and includes refinements of and extensions to the already presented methodology, particularly with regard to an assessment of fluid dynamic irreversibilities.

## 2.2 STATE SPACE ANALYSIS FUNDAMENTALS

The state of a dynamic system such as a free-piston Scirling machine (FPSM) may be defined by paraphrasing Ogata (Og67) as:

'... the smallest collection of numbers which must be specified at time  $t=t_0$  in order to be able to predict uniquely the behaviour of the system for any time  $t \geq t_0$ .'

Thus suppose that there are  $m$  variables  $y_i$  necessary to describe the state of the system. The set of  $m$  state variables then can be considered as the  $m$  components of a state vector  $\mathbf{y}$ . Thereby, the state space is defined as an  $m$ -dimensional space in which the  $y_i$  are coordinates. Any point in the state space at time  $t$  is known as a representative point (Og67) such that the locus of the representative point over a time interval  $\Delta t$  is termed a trajectory.

In order to apply the state space concept to an FPSM, a definition of stability for a system which is inherently oscillatory must be developed. Let the system of equations describing FPSM operation be given in terms of the state column vector  $\mathbf{y}$  such that:

$$\dot{\mathbf{y}} = \mathbf{f}(\mathbf{y}, t) \quad (2.1)$$

This equation is quite general as it is always possible to represent  $m$ th order temporal derivatives by a threaded series of first order temporal derivatives. Hence for a particular variable  $\psi$ , if:

$$y_i = \partial^i \psi / \partial t^i$$

and:

$$y_{i+1} = \partial^{i+1} \psi / \partial t^{i+1}$$

then:

$$\dot{y}_i = y_{i+1} \quad (2.2.1)$$

and:

$$\dot{y}_{i-1} = \partial^{i+2} \psi / \partial t^{i+2} \quad (2.2.2)$$

The equilibrium state of the system  $y_{eq}$  is defined by:

$$f(y_{eq}, t) = 0 \text{ for all } t \quad (2.3)$$

$y_{eq}$  is a stable equilibrium if for each number  $\epsilon > 0$  there exists a real number  $\alpha = \alpha(\epsilon, t_0)$  so that:

$$\| y_0 - y_{eq} \| < \alpha \rightarrow \| f(t; y_0, t_0) - y_{eq} \| \leq \epsilon \quad (2.4)$$

This may be illustrated in terms of Figure 2.1 for a particular second order state space.

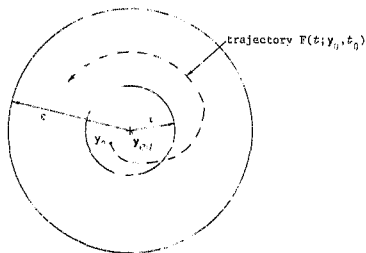


Figure 2.1 Stable equilibrium condition

Equation (2.4) signifies that an equilibrium is stable if no trajectory  $F(t; y_0, t_0)$  originating from  $y_0$  exceeds a given displacement  $c$  with respect to the equilibrium  $y_{eq}$ . Further, the magnitude of  $c$  is such that it constrains  $y_0$  to be within a given displacement  $\alpha$  from  $y_{eq}$ .

The equilibrium state  $y_{eq}$  of equation (2.3) is asymptotically stable if equation (2.4) holds and:

$$\| F(t; y_0, t_0) - y_{eq} \| \rightarrow 0 \text{ as } t \rightarrow \infty \quad (2.5)$$

As illustrated by Figure 2.2, this equation indicates that an equilibrium is asymptotically stable if all trajectories beginning within a displacement  $\alpha$  from  $y_{eq}$  tend towards the equilibrium as time progresses.

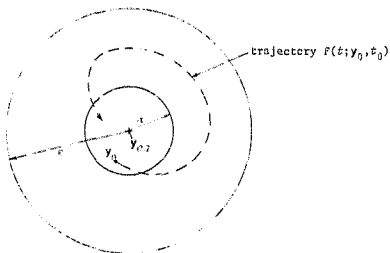


Figure 2.2 Asymptotically stable equilibrium condition

Asymptotic stability is a requirement for FPSM operation. Specifically, this means that an equilibrium condition  $y_{eq}$  must be reached about which the state vector oscillates with constant amplitude. In general,  $y_{eq}$  need not be unique since a particular engine may shift its equilibrium state in response to changing boundary conditions (such as piston loading). This suggests that the operating stability condition for an FPSM oscillating with constant amplitude about its equilibrium state may be defined by stipulating that for each  $\epsilon > 0$  there exist real numbers  $\alpha = \alpha(\epsilon, t_0)$  and  $\beta = \beta(\epsilon, t_0)$  so that as  $t \rightarrow \infty$ :

$$\|y_0 - y_{eq}\| \leq \alpha \implies \|F(t; y_0, t_0) - y_{eq}\| = \|F(r, \beta)\| \leq \epsilon \quad (2.6)$$

As shown by Figure 2.3, equation (2.6) denotes that a system exhibiting asymptotic stability will achieve stable oscillatory behaviour in the temporal limit irrespective of the origin of the trajectory.

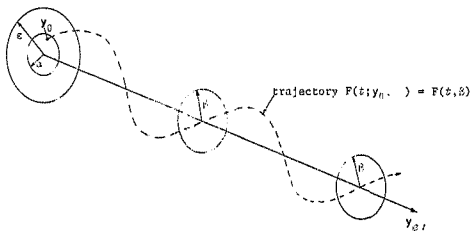


Figure 2.3 Operating stability condition

Hence, at the operating stability point, a FPSM will oscillate without apparent damping so that the energy dissipated by all forms of loading is exactly equal to the net thermal energy supplied to the working fluid.

The immediate objective of the state space analysis is the determination of the conditions under which an arbitrary FPSM may achieve operating stability.

For convenience, the analysis is simplified by transforming the origin of the system to the point of equilibrium by defining:

$$z = y - y_{eq} \quad (2.7)$$

Substituting into equation (2.1):

$$\dot{z} = f(z, t) \quad (2.8)$$

Expanding in a Taylor series (TM72):

$$\dot{z} = E + Bz + G(z)z \quad (2.9)$$

where E is a non-vanishing constant at the origin and B is the Jacobian matrix given by:

$$B_{ij} = \left[ \left[ \frac{\partial F_i}{\partial z_j} \right]_{j=1, n} \right]_{i=1, m} \quad (2.10)$$

The reduced equation, or first approximation of equation (2.9), is given by ignoring the non-linear higher order terms  $G(z)z$  so that:

$$\dot{z} = E + Bz \quad (2.11)$$

This equation may be solved by Laplace transformation as shown in appendix A, yielding the solution:

$$z = z^{-1} \{ (\lambda I - B)^{-1} \} \{ z(0) + B^{-1}E \} \cdot B^{-1}E \quad (2.12)$$

where  $z(0)$  denotes the initial conditions at time  $t = 0$ . The characteristic equation for equation (2.12) is given by:

$$\det(\lambda I - B) = 0 \quad (2.13)$$

The utility of the state space analysis is dependent on the conditions under which the linearised approximation represented by equation (2.11) is a valid substitute for equation (2.8). In turn, this determines whether the solution given by equation (2.12) is adequate for approximating the thermodynamic performance of a given FPSM and thereby constructing useful design optimisation indices. The question of linearisation adequacy is also relevant to the harmonic and/or assumed kinematic motion analyses reported in the literature, since all these approaches seemingly assume that the linearised

approximation is valid.

Lyapunov's theorem on stability in the first approximation (Ha63) provides a means of assessing the validity of the linearised equation. The theorem may be stated as follows:

'If the stability behaviour of the differential equation of the first approximation (or reduced equation) is significant, then the equilibrium of the complete differential equation has the same stability behaviour as the equilibrium of the reduced equation.'

A determination of whether the stability behaviour of the reduced equation is significant may be made by examining the eigenvalues  $\lambda_i$  of the characteristic equation (2.13). The stability behaviour is significant if the characteristic equation is non-singular and the real parts of all the eigenvalues are negative, or:

$$\text{significant behaviour} \Rightarrow \det(\lambda I - B) \neq 0 \text{ and } \text{Real}(\lambda_i) < 0 \quad (2.14)$$

If, however, any simple eigenvalue or the real part of any complex eigenvalue is zero, then the stability behaviour depends on the higher order terms  $G(z)$ . This is termed the critical case (Ha63).

Equation (2.14) allows a physical interpretation of the validity of equation (2.11) as an approximation for equation (2.8). Compliance with the significant behaviour restriction ensures that the approximated equations have the same qualitative behaviour as the full equations but not necessarily the same quantitative behaviour. Hence an FPSM described by a set of linearised equations satisfying equation (2.14) has the same operational behaviour as an FPSM described using

the full equations, although the quantitative performance (work output) of the machines may be different. The linearised equations, therefore, may be used to determine whether a particular machine will 'work' or not as well as how well it will work on a relative basis, although the numerical accuracy of the predictions is undefined. From the results of the linear harmonic analysis described by Chen and Griffin (CG84), it is evident that the prediction accuracy of the state space analysis depends primarily on the number of state variables chosen rather than on whether or not the higher order terms  $G(z)z$  in equation (2.9) are neglected.

Supposing that equation (2.11) exhibits significant stability behaviour, the conditions for achieving the operational stability represented by equation (2.6) can be developed. These conditions may be represented conveniently by considering the stability domain in the parameter space. The parameter space is defined as the smallest collection of numbers describing a particular FPSM such that every set of parameters is associated with a unique trajectory in the state space. If there are  $m$  such parameters, then the set of  $m$  parameters may be considered as the  $m$  components of a parameter vector  $b$ . Thus the parameter space is defined as a  $m$ -dimensional space in which the components of  $b$  are coordinates. Typical FPSM parameters include lengths, diameters and regenerator matrix porosities as well as working fluid temperatures and charge pressures. The distinction as to whether a given quantity is treated as a parameter or a state variable depends on the nature of  $f$  in equation (2.8). If, for example, the expansion space is assumed to be isothermal, then the expansion space temperature is considered a parameter. Conversely, if the expansion space is treated as being adiabatic, then its

temperature is a state variable.

If the system behaviour is continuously dependent on  $b$ , then equation (2.8) may be modified so that:

$$\dot{z} = f(z, b, c) \quad (2.15)$$

Since the differential equations of the first approximation for an FPSM are either autonomous (explicitly independent of  $c$ ) or periodic, equation (2.11) becomes:

$$\dot{z} = E + B(b, c)z \quad (2.16)$$

Those parameter values for which equation (2.15) has significant behaviour form the stability domain in the parameter space (Ha63). The stability domain is bounded by a hypersurface called the stability boundary which is characterised by equation (2.16) having critical behaviour. Physically this means that any FPSM with a parameter vector  $b$  which falls on the stability boundary hypersurface will be neutrally stable at its state space equilibrium  $z_{eq}$ . Hence in order to achieve stable engine operation, it is necessary to exceed the stability boundary so that the resulting amplitude of oscillation is bounded by  $\beta$  as defined for equation (2.6). If  $b$  lies on the stability boundary, let  $b + c$  be a neighbouring point outside the boundary. Equation (2.15) then becomes:

$$z = f(z, b, c) + f^*(z, b, c, c) \quad (2.17)$$

where  $f^* = 0$  for  $c = 0$ .

Under these conditions, the following theorem proved by Hahn (Ha63) applies:

'If the equilibrium [of equation (2.17)] is asymptotically stable for  $b$  located on the stability boundary [that is,  $z_{eq}$  for equation (2.15) is asymptotically stable], then the maximum deviation of the motion from the equilibrium caused by crossing the boundary can be kept arbitrarily small only if the distance  $|c|$  from the boundary is kept sufficiently small.'

After the stability boundary is crossed, the system may be forced into stable oscillation by a small perturbation  $c$  since, by the above theorem, the smallness of the oscillation depends continuously on the magnitude of  $c$ . This assertion was validated experimentally for the liquid-piston Stirling engine (Go79) when  $c$  is taken to represent the bounce space charge pressure or the heater wall temperature. Similar effects have been demonstrated for a wide variety of solid free-piston Stirling engines.

The analytical framework presented provides a *modus operandi* for using the state space analysis as a means of achieving a closed form solution for the operational behaviour of an FPSM. The procedure may be summarised by the following sequence:

1. Select a state space vector to describe a given FPSM and express the governing differential equations in the state space form of equation (2.8).
2. Determine the constant vector  $E$  and the Jacobian  $B$  (using equation (2.10)) in the reduced equation (2.11).

3. Develop the determinant  $\det(\lambda I - B)$  and determine whether it is singular. Depending on the nature of the singularity (that is, exactly how many and which eigenvalues are zero), a judgement on the validity of the reduced equation may be made. In particular, if the singularity conforms to a 'special case' (Kr63), the reduced equation is still valid, otherwise the state space method proposed is inadmissible.
4. Express the characteristic equation (2.13) in terms of the parameter vector  $b$ . The parameter space stability boundary then may be found conveniently by arbitrarily choosing any eigenvalue to be complex so that:

$$\lambda^* = a + jb \quad (2.18)$$

At least one pair of complex conjugate eigenvalues must exist if oscillatory motion under operating stability conditions is to be experienced. Substituting equation (2.18) into the characteristic equation yields two substituent equations, one each for the real and imaginary parts respectively. The stability boundary is defined by  $a = 0$  (that is, the real part of the eigenvalue is zero). This enables the two substituent equations to be solved simultaneously, so eliminating  $b$  (the imaginary part of the eigenvalue). The single equation thus produced is an analytic description of the stability boundary hypersurface expressed in terms of the components of the parameter vector  $b$ .

5. Solution of the stability boundary hypersurface equation enables a set of compatible parameters to be chosen. When substituted into the characteristic equation, these parameters permit the imaginary part of the complex eigenvalue  $\lambda^*$  and the balance of

- the eigenvalues  $\lambda_i$  to be found. An examination of the eigenvalues  $\lambda_i$  in accordance with equation (2.14) determines whether the particular parameter set chosen will enable operating stability to be achieved. In particular, if any of the remaining eigenvalues  $\lambda_i$  has a non-negative real part, then that particular parameter set will not result in a working FPSM configuration.
6. The complete eigenvalue set may be used to perform the Laplace transformation necessary to solve equation (2.12). The oscillatory steady-state solution is extracted as a particular case by considering the limit  $t \rightarrow \infty$ .
  7. A set of physically meaningful initial conditions  $x(0)$  may be chosen by considering the physical compatibility constraints of the FPSM being considered. Appropriate constraints are a specification of strokes or a stipulation that pistons may not oscillate beyond the confines of their cylinders.
  8. The state space vector solution thus obtained enables the indicated and mechanical work outputs of a particular FPSM to be determined independently. Their difference is an indication of the irreversibilities necessary to achieve the operating stability condition.
  9. An optimisation index such as the mechanical power output may then be defined as a means of determining the optimality of a given parameter vector  $b$ .

The symbolic expression of this generalised procedure is most clearly shown by considering particular FPSM examples. Thus in order to fully demonstrate the procedure, both a 'special case' and a 'normal' FPSM configuration are presented in the following sections as case studies.

In closing, particular note of the form of the governing differential equations (2.8) must be taken. As thoroughly documented in the literature (UB84) and demonstrated later in chapter 3, a description of the dynamics and fluid dynamics of Stirling cycle machines generally may be cast in the form of equation (2.8). However, this equation does not conform to that of a typical control system owing to the absence of a distinct control input term (Og67). Thus the inclusion of a control term in the state space analysis (advocated, for example, by Cichy *et al* (CC84)) cannot be physically justified unless a control mechanism is actually included in the FPSM configuration as, for example, described in reference GL85.

## 2.3 APPLICATION OF THE STATE SPACE ANALYSIS TO A BACK-TO-BACK FREE-PISTON STIRLING ENGINE

### 2.3.1 Introduction

The configuration of the back-to-back, free-piston Stirling engine (FPSE) apparently originates in William Beale's patent disclosure describing the free-piston Stirling engine concept. Two examples of the back-to-back engine configuration reported by Beale (Be69) are a 'refrigerator-heat engine' and a 'double ended fluid piston or gamma-configuration of the back-to-back liquid-piston or gamma-configuration of the back-to-back proposed by Rallis and a working prototype was demonstrated by *et al* (LL79). A solid piston version of a gamma-configuration engine is also reported to have achieved self-sustaining operation (Ra86).

The particular version of the back-to-back FPSE used for this case study is described in figure 2.4. The engine consists of two back-to-back Beale or beta-configuration engines which share a common power piston. Work output is conceptualised as being via a linear alternator of the moving permanent magnet type (LT84, LT85). This may be achieved, for example, by incorporating samarium cobalt permanent magnets in the power piston construction while building the field coils into the piston cylinder casing. The displacer pistons in the working spaces on either side of the power piston are connected via a tube which passes through the center of the power piston. An annular heat exchanger is formed in each working space by the gap between the displacer and its cylinder wall. The cylinder wall may be grooved with a spiral Whitworth thread for improved heat transfer (FC67). Heat is added externally to the displacer cylinder walls at their outer ends and is removed via externally mounted cooling jackets at the inner or power piston side ends. The displacer cylinder walls between the heater and cooler portions are externally wrapped with thermal insulation and function as the regenerators.

The particular back-to-back FPSE configuration used is convenient as a case study in view of its inherent simplicity which results in a parameter vector with as few as 19 components. A practical version of such an engine would probably necessitate the use of external heat exchangers as described by Beale (Be69), as well as a significantly more complex linear alternator design than the idealisation depicted in figure 2.4.

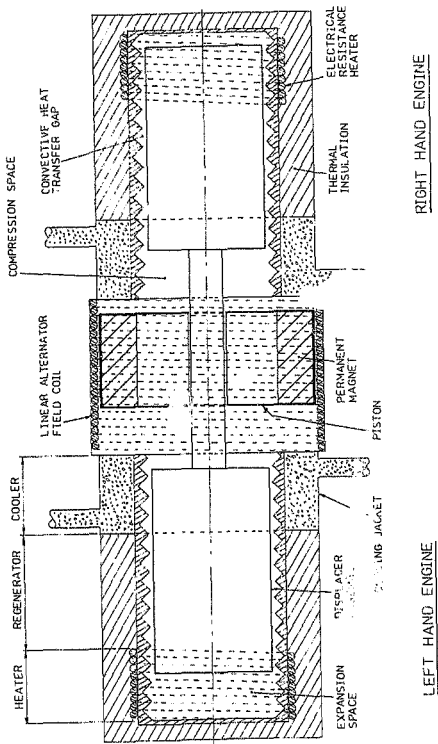


Figure 2.4 Schematic of the back-to-back free-piston Stirling engine

### 2.3.2 Back-to-Back FPSE State Space Analysis

The application of the state space analysis to the back-to-back FPSE is performed using the sequential methodology described at the end of section 2.2 above. Generally, only the final analytical results are included here; the derivational details are given in section A.1 of appendix A.

#### 1. *State space vector selection and formulation of the governing differential equations*

A complete list of the assumptions used to describe the engine being considered is given in section A.1.1. The most important assumptions are an isothermal treatment of the expansion and compression spaces and a constant, linear temperature profile in the regenerator. A four component state vector enables a complete description of the engine operator to be specified. This is the smallest state vector with which any FPSE may be described. The state vector is given by:

$$z = \begin{bmatrix} x_p \\ \dot{x}_p \\ x_d \\ \dot{x}_d \end{bmatrix} = \begin{bmatrix} \text{piston displacement} \\ \text{piston velocity} \\ \text{displacer displacement} \\ \text{displacer velocity} \end{bmatrix} \quad (2.19)$$

The 19 parameters comprising the parameter vector are listed in table 2.1 and depicted in figure 2.5. In view of the thermodynamic symmetry assumed for the working spaces, the origin or equilibrium position of the displacer assembly motion is located at the center of either displacer cylinder, while the power piston motion has its origin at

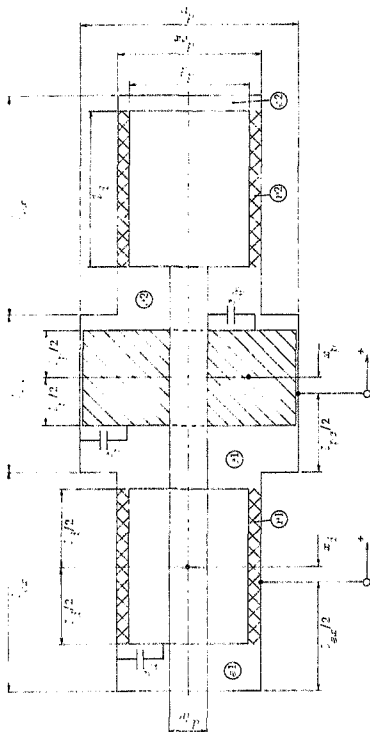


Figure 2.5 Back-to-back free-piston Stirling engine parameters

the center of the power piston cylinder.

Using the threaded temporal derivative formulation of equations (2.2), the governing differential equations may be expressed as:

$$\dot{z}_1 = z_2 \quad (2.20.1)$$

$$\begin{aligned} \dot{z}_2 = H_{TOT} R (A_p - A_{dr}) & \left[ 1 / (\alpha + z_3 (A_{ex} / T_e - (A_{ex} - A_{dr}) / T_c) + z_1 (A_p - A_{dr}) / T_c) \right. \\ & \left. - 1 / (\alpha - z_3 (A_{ex} / T_e - (A_{ex} - A_{dr}) / T_c) - z_1 (A_p - A_{dr}) / T_c) \right] / H_p \\ & + (c_{dp} z_4 - z_2 (c_p + c_{dp})) / H_p \end{aligned} \quad (2.20.2)$$

$$\dot{z}_3 = z_4 \quad (2.20.3)$$

$$\begin{aligned} \dot{z}_4 = H_{TOT} F A_{dr} & \left[ 1 / (\alpha + z_3 (A_{ex} / T_e - (A_{ex} - A_{dr}) / T_c) + z_1 (A_p - A_{dr}) / T_c) \right. \\ & \left. - 1 / (\alpha - z_3 (A_{ex} / T_e - (A_{ex} - A_{dr}) / T_c) - z_1 (A_p - A_{dr}) / T_c) \right] / H_d \\ & + (c_{dp} z_2 - z_4 (c_d + c_{dp})) / H_d \end{aligned} \quad (2.20.4)$$

where:

$$\alpha = \bar{V}_e / T_e + V_r / T_r + \bar{V}_c / T_c \quad (2.20.5)$$

and:

$$H_{TOT} = P_{crg} (\bar{V}_e + V_r + \bar{V}_c) / RT_c \quad (2.20.6)$$

Table 2.1 Back-to-back FPSE parameter vector components

Component	Symbolic description
Displacer piston face area	$A_d$
Displacer rod area	$A_{dr}$
Displacer piston length	$l_d$
Displacer assembly mass	$M_d$
Displacer assembly damping coefficient	$c_d$
Displacer assembly/piston interface damping coefficient	$c_{dp}$
Displacer amplitude of oscillation	$x_{dmax}$
Power piston gross face area	$A_p$
Power piston length	$l_p$
Power piston mass	$M_p$
Power piston loading coefficient	$c_p$
Power piston amplitude of oscillation	$x_{pmax}$
Displacer cylinder area	$A_{ex}$
Displacer cylinder length	$l_{ex}$
Power piston cylinder length	$l_{pc}$
Expansion space isothermal temperature	$T_e$
Compression space isothermal temperature	$T_c$
Working fluid charge pressure	$P_{crg}$
Working gas constant	$R$

## 2. Determination of E and B in the reduced equation

Since the engine is oriented orthogonally to the gravity vector:

$$E = 0$$

(2.21)

The Jacobian B is given by:

$$B = \begin{bmatrix} 0 & 1 & 0 & 0 \\ B_{21} & B_{22} & B_{23} & B_{24} \\ 0 & 0 & 0 & 1 \\ B_{41} & B_{42} & B_{43} & B_{44} \end{bmatrix} \quad (2.22)$$

where the elements of  $B$  are given in terms of the parameter vector components by equations (A.19) in appendix A.

### 3. Development of the determinant of $(\lambda I - B)$ and investigation of its characteristics

The determinant of  $(\lambda I - B)$  may be expressed using the elements of  $B$  given in equation (2.22) by:

$$\begin{aligned} \det(\lambda I - B) = & \lambda^4 - \lambda^3(B_{22} + B_{44}) + \lambda^2(B_{22}B_{44} - B_{24}B_{42} - B_{21} - B_{43}) \\ & + \lambda(B_{22}B_{43} - B_{23}B_{42} + B_{21}B_{44} + B_{24}B_{41}) + B_{21}B_{43} \\ & - B_{23}B_{41} \end{aligned} \quad (2.23)$$

Using equations (A.19) to evaluate the coefficients of the  $\lambda$ -terms shows that the coefficient of the  $\lambda^0$  term is zero, or:

$$B_{21}B_{43} - B_{23}B_{41} = 0 \quad (2.24)$$

Hence equation (2.23) becomes:

$$\begin{aligned} \det(\lambda I - B) = & \lambda(\lambda^3 - \lambda^2(B_{22} + B_{44}) + \lambda(B_{22}B_{44} - B_{24}B_{42} - B_{21} - B_{43}) \\ & + B_{22}B_{43} - B_{23}B_{42} + B_{21}B_{44} + B_{24}B_{41}) \end{aligned} \quad (2.25)$$

Thus the determinant is singular when  $\lambda = 0$ .

However, the nature of the singularity conforms to a special case discussed by Krasovskii (Kr63) who proved the following theorem:

'If all the eigenvalues in the neighbourhood of the origin have negative real parts excepting one simple eigenvalue which is zero, then the equilibrium of the reduced equation [equation (2.11)] is asymptotically stable.'

Hence the state space analysis is admissible for the back-to-back FPSE.

4. *Analytic description of the stability boundary hypersurface in the parameter space*

From equation (2.25), the characteristic equation may be expressed in terms of condensed coefficients as:

$$\lambda^3 + K_3\lambda^2 + K_2\lambda + K_1 = 0 \quad (2.26)$$

Choose a particular complex eigenvalue:

$$\lambda_1 = -a + jb \quad (2.27)$$

Substituting (2.27) into (2.26) yields two equations in  $a$  and  $b$  which may be solved simultaneously. Setting  $a = 0$  in these equations then gives:

$$K_1 = K_2K_3 \quad (2.28)$$

which defines the stability boundary hypersurface.

Expressing (2.28) in terms of the parameter vector components yields:

$$2H_{TOT}R[(A_{ex}/T_e - (A_{ex}-A_{dx})/T_c)(A_{dx}c_p + A_p c_{dp}) + (A_p - A_{dx})(A_p(c_d + c_{dp}) - A_{dx}c_d)/T_c]/H_d H_p \alpha^2$$

$$+ (c_p + c_{dp})/H_p + (v_d + c_{dp})/H_d \left[ (c_{dp}(c_d + c_p) + c_d c_p)/H_d H_p + 2H_{TOT}R[(A_p - A_{dx})^2/H_p T_c + A_{dx}(A_{ex}/T_e - (A_{ex}-A_{dx})/T_c)/H_d]/\alpha^2 \right] \quad (2.29)$$

where  $\alpha$  and  $H_{TOT}$  are given by equations (2.20.5) and (2.20.6) respectively.

#### 5. Solution of the stability boundary hypersurface equation

Any parameter in equation (2.29) can be expressed quadratically in terms of the other parameters. Thus a complete description of the stability boundary hypersurface is achievable analytically. However, an analytic approach is not convenient numerically, particularly when generalising to hypersurface equations of higher than biquadratic order for which no analytic solutions seem to exist (Us48). Thus a physically significant dependent parameter methodology is used to develop a generalised solution procedure for a hypersurface equation of arbitrary order.

In this methodology, the power piston loading coefficient  $c_p$  is chosen to be the dependent parameter such that variations in the remaining independent parameters are evaluated by solving for  $c_p$ . As  $c_p$  determines the nature of the loading on the engine, its numerical value gives immediate insight into the viability of a particular parameter set in enabling operating stability to be achieved. In terms of  $c_p$ , equation (2.29) has the quadratic form:

$$K_1 c_p^2 + K_2 c_p + K_3 = 0 \quad (2.30.1)$$

where, for the sake of clarity, the coefficients are expressed by the threaded sequence:

$$K_1 = K_0/H_p \quad (2.30.2)$$

$$K_2 = K_5 K_6 + K_7/H_p - 2K_4 M_{TOT} R A_{dr} / \alpha^2 H_d H_p \quad (2.30.3)$$

$$K_3 = K_5 K_7 - 2M_{TOT} R [K_4 A_p c_{dp} + (A_p - A_{dr})(A_p (c_d + c_{dp}) - A_{dr} c_d) / T_c] / \alpha^2 H_d H_p \quad (2.30.4)$$

$$K_4 = A_{ex} / T_e - (A_{ex} - A_{dr}) / T_c \quad (2.30.5)$$

$$K_5 = c_{dp} / H_p + (c_d + c_{dp}) / H_d \quad (2.30.6)$$

$$K_6 = (c_d + c_p) / H_d H_p \quad (2.30.7)$$

$$K_7 = c_{dp} c_d / H_d H_p + 2M_{TOT} R (A_p - A_{dr})^2 / H_p T_c + K_4 A_{dr} / H_d \alpha^2 \quad (2.30.8)$$

The solution of equation (2.30) for the roots  $c_{p1}$  and  $c_{p2}$  has the following physical significance:

- a. if both  $c_{p1} < 0$  and  $c_{p2} < 0$  then the engine will not achieve self-sustaining operation since external work must be done on the power piston to sustain oscillation
- b. if  $K_2^2 - 4K_1 K_3 < 0$  then the roots are imaginary and the parameter set is physically incompatible
- c. if  $c_{p1} > 0$  or  $c_{p2} > 0$ , self-sustaining operation as an engine is possible.

Supposing that the given parameter set satisfies the third condition so that self-sustaining operation is possible, the numerical values of the coefficients in equation (2.26) may be determined. The angular operating frequency is given in terms of the imaginary part of equation (2.27) by (see section (A.1.1)):

$$b = (B_{22}B_{44} - B_{24}B_{42} - B_{21} - B_{43})^{0.5} \quad (2.31)$$

If  $b$  is imaginary, then, once again, the given parameter set is physically incompatible. Also, if  $b$  is zero, then no perturbation  $c$  (from equation (2.17)) will result in operating stability being achieved.

Substituting a positive value of  $b$  into equation (2.27) (with  $a = 0$ ) results in the complex conjugate pair of eigenvalues  $\lambda_{1,2} = \pm jb$ . Dividing equation (2.26) by the factor product  $(\lambda^2 + b^2)$  and noting the identity of equation (2.28) gives the third eigenvalue:

$$\lambda_3 = B_{22} + B_{44} \quad (2.32)$$

If  $\lambda_3 \geq 0$  then, by Lyapunov's first theorem (equation (2.14)), the behaviour of the reduced equation (2.11) is not significant and the analysis is inadmissible.

#### 6. Solution of the reduced state space equation

From equations (2.21) and (2.22) the reduced equation for the back-to-back FPSE is given by:

$$\dot{z} = Bz \quad (2.33)$$

which has a solution given from equation (2.12) by:

$$z = \mathcal{L}^{-1}\{(\lambda I - B)^{-1}\}z(0) \quad (2.34)$$

The generalised methodology used to evaluate this equation and, in particular, to perform the required matrix inversion, is given in section A.3 of appendix A. For the set of eigenvalues  $\lambda_{1,2} = \pm jb$  and  $\lambda_3 < 0$ , equation (2.34) becomes:

$$z = (2|Z_1| \cos(bt + \phi_1) + Z_3 \exp(\lambda_3 t)) z(0) \quad (2.35.1)$$

where:

$$Z_1 = (B + jbI)(B - \lambda_3 I) / 2jb(-\lambda_3 + jb) \quad (2.35.2)$$

$$Z_3 = (B^2 + b^2 I) / (\lambda_3^2 + b^2) \quad (2.35.3)$$

$$\phi_1 = \tan^{-1} \{ \text{Imag}(Z_1) / \text{Real}(Z_1) \} \quad (2.35.4)$$

The steady-state solution as  $t \rightarrow \infty$  is given by:

$$z_{ss} = 2|Z_1| \cos(bt + \phi_1) z(0) \quad (2.36)$$

since  $\lambda_3 < 0$ .

#### 7. Selection of the initial conditions

Since the engine must oscillate about its equilibrium position by definition (equations (2.7) and (2.17)),  $z(0)$  may be defined in terms of equation (2.19) as:

$$z(0) = \begin{bmatrix} 0 \\ \dot{x}_p(0) \\ 0 \\ \dot{x}_d(0) \end{bmatrix} \quad (2.37)$$

where the piston and displacer velocities at the equilibrium position are unknown. These unknowns may be determined from geometrical compatibility considerations by requiring that the piston and displacer oscillate within the confines of their respective cylinders. This may be accomplished by specifying steady-state piston and

displacer amplitude limits ( $x_{pmax}$  and  $x_{dmax}$  respectively) as listed in table 2.1. As shown in figure 2.6,  $x_{pmax}$  and  $x_{dmax}$  occur at angular positions of  $\theta_{pmax}$  and  $\theta_{dmax}$  respectively.

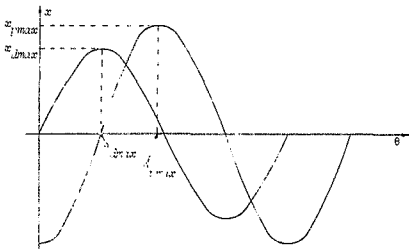


Figure 2.6 Piston and displacer motions

Substituting equation (2.37) into equation (2.36) with  $\theta = \omega t$  produces:

$$x_p = \sum_{j=1}^4 2|(Z_1)_{1j}| \cos(\theta + (\phi_1)_{1j}) z(0)_j \quad (2.38.1)$$

$$x_d = \sum_{j=1}^4 2|(Z_1)_{3j}| \cos(\theta + (\phi_1)_{3j}) z(0)_j \quad (2.38.2)$$

Since  $x_{pmax}$  and  $x_{dmax}$  are maxima,  $\theta_{pmax}$  and  $\theta_{dmax}$  may be found by differentiating the right hand sides of equations (2.38) and equating the resultant expressions with zero. This produces:

$$\theta_{pmax} = \tan^{-1} \left[ - \left( \sum_{j=1}^4 |Z_1|_{1j} |z(0)_j \sin(\phi_1)_{1j} \right) / \left( \sum_{j=1}^4 |Z_1|_{1j} |z(0)_j \cos(\phi_1)_{1j} \right) \right] \quad (2.39.1)$$

$$\theta_{dmax} = \tan^{-1} \left[ - \left( \sum_{j=1}^4 |Z_1|_{3j} |z(0)_j \sin(\phi_1)_{3j} \right) / \left( \sum_{j=1}^4 |Z_1|_{3j} |z(0)_j \cos(\phi_1)_{3j} \right) \right] \quad (2.39.2)$$

In terms of figure 2.6, the phase angle by which the displacer assembly leads the power piston is given by  $\theta_{pmax} - \theta_{dmax}$ .

Substituting equations (2.39) into equations (2.38) and setting  $x_p = x_{pmax}$  and  $x_d = x_{dmax}$  enables physically compatible piston and displacer equilibrium position velocities to be determined from the following matrix equation:

$$\begin{bmatrix} F_{11} & F_{12} \\ F_{21} & F_{22} \end{bmatrix} \begin{bmatrix} \dot{x}_p(0) \\ \dot{x}_d(0) \end{bmatrix} = \begin{bmatrix} x_{pmax} \\ x_{dmax} \end{bmatrix} \quad (2.40)$$

where the coefficient matrix F is given by:

$$F_{11} = 2|Z_1|_{12} | \cos(\theta_{pmax} + (\phi_1)_{12}) | \quad (2.41.1)$$

$$F_{12} = 2|Z_1|_{14} | \cos(\theta_{pmax} + (\phi_1)_{14}) | \quad (2.41.2)$$

$$F_{21} = 2|Z_1|_{32} | \cos(\theta_{dmax} + (\phi_1)_{32}) | \quad (2.41.3)$$

$$F_{22} = 2|Z_1|_{34} | \cos(\theta_{dmax} + (\phi_1)_{34}) | \quad (2.41.4)$$

The matrix equation (2.40) cannot be solved directly since there are four unknowns and only two independent equations. Hence the following iterative solution procedure is adopted:

- a. Guess  $\theta_{pmax}$ ,  $\theta_{dmax}$ .
- b. Use matrix equation (2.40) to solve for  $\dot{x}_p(0)$  and  $\dot{x}_d(0)$ .
- c. Substitute these  $\dot{x}_p(0)$  and  $\dot{x}_d(0)$  into equations (2.39) to produce  $\theta_{pmax}^*$  and  $\theta_{dmax}^*$ .
- d. If  $|\theta_{pmax}^* - \theta_{pmax}|$  and  $|\theta_{dmax}^* - \theta_{dmax}|$  are small enough, the last values of  $\dot{x}_p(0)$  and  $\dot{x}_d(0)$  computed are the solution. Otherwise set  $\theta_{pmax} = \theta_{pmax}^*$  and  $\theta_{dmax} = \theta_{dmax}^*$  and iterate from step b.

The iteration procedure converges, that is a solution for  $\dot{x}_p(0)$  and  $\dot{x}_d(0)$  exists, only if  $\det(F) > 0$ . The physical implications of this restriction are discussed below in terms of the thermodynamic engine performance.

#### 8. Thermodynamic performance determination

The values of  $\dot{x}_p(0)$  and  $\dot{x}_d(0)$  determined enable a combination of equations (2.37) and (2.38) to produce the following expressions for the state variables:

$$\begin{aligned} x_p = & 2 \{ |(Z_1)_{12} \dot{x}_p(0) \cos(br + (\phi_1)_{12}) \\ & + |(Z_1)_{14} \dot{x}_d(0) \cos(br + (\phi_1)_{14}) \} \end{aligned} \quad (2.42.1)$$

$$\begin{aligned} \dot{x}_p = & 2 \{ |(Z_1)_{22} \dot{x}_p(0) \cos(br + (\phi_1)_{22}) \\ & + |(Z_1)_{24} \dot{x}_d(0) \cos(br + (\phi_1)_{24}) \} \end{aligned} \quad (2.42.2)$$

$$\begin{aligned} x_d = & 2 \{ |(Z_1)_{32} \dot{x}_p(0) \cos(br + (\phi_1)_{32}) \\ & + |(Z_1)_{34} \dot{x}_d(0) \cos(br + (\phi_1)_{34}) \} \end{aligned} \quad (2.42.3)$$

$$\begin{aligned} \dot{x}_d = 2 \{ & |(z_1)_{42}| \dot{x}_p(0) \cos[br + (\phi_1)_{42}] \\ & + |(z_2)_{44}| \dot{x}_d(0) \cos[br + (\phi_1)_{44}] \} \end{aligned} \quad (2.42.4)$$

In turn, these equations enable the net instantaneous indicated power output for the back-to-back FPSE to be given by:

$$\dot{W}_{TOT} = P_1(\dot{V}_{e1} + \dot{V}_{c1}) + P_2(\dot{V}_{e2} + \dot{V}_{c2}) \quad (2.43)$$

where the subscripts 1 and 2 denote the left and right hand sides of the engine respectively.

Since the working spaces are assumed to be isothermal:

$$\dot{Q}_{IN} = P_1 \dot{V}_{e1} + P_2 \dot{V}_{e2} \quad (2.44.1)$$

$$\dot{Q}_{OUT} = P_1 \dot{V}_{c1} + P_2 \dot{V}_{c2} \quad (2.44.2)$$

Hence no additional independent performance information may be obtained by considering cyclic heat transfers.

Substituting equations (2.42) into equation (2.43) produces the result:

$$\dot{W}_{TOT} = -2\beta M_{TOT} R I \dot{x}_d (A_{dr} + \dot{x}_p (A_p - A_{dr})) / (\alpha^2 - \beta^2) \quad (2.45.1)$$

where:

$$\beta = x_d (A_{ex} / F_a + (A_{ex} - A_{dr}) / T_a) + x_p (A_p - A_{dr}) / T_c \quad (2.45.2)$$

and  $\alpha$  is given by equation (2.20.5)

As this equation is not readily amenable to analytic integration, a simpler, although approximate, analytically tractable expression may

be obtained by expressing the pressures  $P_1$  and  $P_2$  as Taylor series (TM72). Ignoring second order and higher terms in these series results in the linearised expression:

$$\dot{W}_{TOT} = -2\beta H_{TOT} R (\dot{x}_d A_{dr} + \dot{x}_p (A_p - A_{dr})), \alpha^2 \quad (2.46)$$

where  $\alpha$  and  $\beta$  are unchanged from equation (2.45).

Using a simple numerical algorithm (such as Simpson's rule (Ge70)) for equation (2.45) or standard analytical procedures for equation (2.46), the cyclic indicated work is given by:

$$W_{TOT} = \int_0^{2\pi/b} \dot{W}_{TOT} dt \quad (2.47)$$

The net instantaneous power dissipated mechanically is given by:

$$\dot{W}_{DIS} = c_p \dot{x}_p^2 + c_{dp} (\dot{x}_d - \dot{x}_p)^2 + c_d \dot{x}_d^2 \quad (2.48)$$

which may be integrated analytically to produce the cyclic mechanical dissipation:

$$W_{DIS} = \int_0^{2\pi/b} \dot{W}_{DIS} dt \quad (2.49)$$

Similarly, the gross power output produced by the piston is given by:

$$\dot{W}_{OUT} = c_p \dot{x}_p^2 \quad (2.50)$$

which yields the analytic cyclic integral:

$$W_{OUT} = \int_0^{2\pi/b} \dot{W}_{OUT} dt \quad (2.51)$$

The analytical cyclic integrals of  $\dot{W}_{TOT}$ ,  $\dot{W}_{DIS}$  and  $\dot{W}_{OUT}$  may be expressed as a sum of the product combinations of two state vector components. Hence these integrals have a form which may be described by:

$$\begin{aligned} W = & (4\pi/b) \sum K_{ij} \{ |(Z_1)_{i2}| \cos(\phi_1)_{i2} \dot{x}_p(0) + |(Z_1)_{i4}| \cos(\phi_1)_{i4} \dot{x}_d(0) \\ & \times |(Z_1)_{j2}| \cos(\phi_1)_{j2} \dot{x}_p(0) + |(Z_1)_{j4}| \cos(\phi_1)_{j4} \dot{x}_d(0) \\ & + |(Z_1)_{i2}| \sin(\phi_1)_{i2} \dot{x}_p(0) + |(Z_1)_{i4}| \sin(\phi_1)_{i4} \dot{x}_d(0) \\ & \times |(Z_1)_{j2}| \sin(\phi_1)_{j2} \dot{x}_p(0) + |(Z_1)_{j4}| \sin(\phi_1)_{j4} \dot{x}_d(0) \} \quad (2.52) \end{aligned}$$

where  $i$  and  $j$  denote any two state vector components (including cases for which  $i = j$ ) and  $K$  represents a constant.

The cyclic indicated, dissipation and gross power outputs are given respectively by:

$$\dot{W}_{TOT} = 2\pi \dot{W}_{TOT}/b \quad (2.53.1)$$

$$\dot{W}_{DIS} = 2\pi \dot{W}_{DIS}/b \quad (2.53.2)$$

$$\dot{W}_{OUT} = 2\pi \dot{W}_{OUT}/b \quad (2.53.3)$$

By the conservation of energy postulate, the cyclic indicated and dissipation work outputs must be exactly equal or:

$$\dot{W}_{TOT} = \dot{W}_{DIS} \quad (2.54)$$

Since the reduced equation (2.11) is used as the basis of the state space analysis, equations (2.42) represent *de facto* linearised solutions. Hence equation (2.48) also produces a linearised instantaneous dissipation power. Equation (2.45), however, is developed from first principles (see section A.3) and does not produce a linearised result. Therefore a comparison of  $\dot{W}_{TOT}$  produced by

equation (2.45) with  $W_{DIS}$  always shows a small error, whereas use of the linearised  $W_{TOT}$  produced by equation (2.46) results in an exact equality with  $W_{DIS}$ . Since equation (2.46) produces a more conservative estimate of  $W_{TOT}$  than equation (2.45) and also maintains an exact energy balance, it is preferred for use in the state space analysis.

Equation (2.54) holds strictly on the parameter space stability boundary hypersurface determined by setting the real part of the complex eigenvalue  $\lambda^*$  to zero (that is,  $\alpha = 0$  in equation (2.18)). However, if equation (2.40) does not yield a solution for a physically compatible set of initial conditions on this hypersurface (indicated by a negative  $\det(F)$ ), then the given parameter set will not produce an operating stability condition for the given  $x_{pmax}/x_{dmax}$  combination chosen. This means that the dependent piston loading coefficient  $c_p$  produced by equation (2.30) is too large to enable the chosen amplitudes to be obtained. Intuitively, this is reasonable in the light of a large body of generic FPSE experimental data which show that the piston and displacer amplitudes are dependent on the engine load for a given net cyclic heat input. This situation may be ameliorated by reducing  $c_p$  to a value at which  $\det(F) = 0$ . A zero  $\det(F)$  defines an upper limit for  $c_p$  below which oscillatory motion with the desired amplitudes may be obtained. In effect, this defines a new hypersurface in the parameter space which may be termed the operating hypersurface as illustrated by figure 2.7.

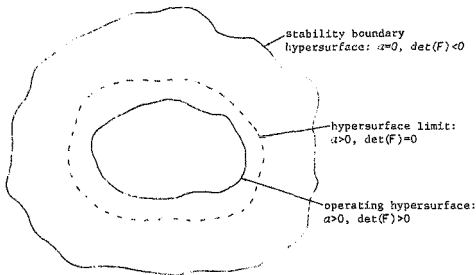


Figure 2.7 Operating hypersurface in the parameter space

On a given operating hypersurface,  $\alpha$  is greater than zero and so the operating hypersurface lies within the stability boundary. Under these conditions  $W_{TOT} > W_{DIS}$  and the motion would be unstable by definition (equation (2.5)). For stable oscillation, however,  $\alpha$  must equal zero on the operating hypersurface; a condition which can be achieved by adding an amount of irreversible dissipation exactly equal to  $(W_{TOT} - W_{DIS})$  to the system. This additional dissipation is a measure of the irreversibility required in but excluded from the governing differential equations (2.20) by assumption. In other words, a set of governing equations which include the required irreversibilities would shift the stability boundary to coincide with the operating hypersurface so that, for a given set of piston and displacer amplitudes,  $\alpha = 0$  and  $\det(F) > 0$  simultaneously.

This process gives a useful indication of the magnitude of the error in the indicated work output as a result of using a given set of thermodynamic or fluid dynamic assumptions. In this case, the relevant assumption is the treatment of the working spaces as being isothermal.

#### 9. Selection of an optimisation index

Considering the isothermal nature of the working spaces and the manner in which the dissipation is defined,  $w_{OUT}$  or  $\dot{w}_{OUT}$  are suitable optimisation indices depending on the desired engine application. In the case of the back-to-back engine where the oscillating frequency may be largely controlled by the engine pressurisation, a key parameter is the available cyclic work output at a given frequency. Thus, perhaps arbitrarily,  $w_{DIS}$  is selected here as the optimisation index.

#### 2.3.3 Numerical Results

The application of the state space analysis to the back-to-back FPSE is embodied in a computer programme entitled 'SYMENG', the listing and algorithmic details of which are given in appendix B. The quantitative results of the analysis are presented firstly in terms of a baseline parameter vector and thereafter as a sequence of variations of several of the parameter vector components in turn. Finally, an attempt at determining an optimised parameter set is described.

### 2.3.3.1 Baseline Engine Performance

The baseline parameter set is almost identical to that used in the initial analysis of the back-to-back FPSE (Go80) and is given in table 2.2. There is no particular justification for choosing the values listed for the baseline case other than the intuition of physical significance and the pragmatism of convenient numerical magnitudes. The actual parameters used in the computer programme correspond to the parameter vector components given in table 2.1 although particular components are represented in a more convenient form such as diameters replacing areas and strokes replacing amplitudes. In addition, the parameter descriptions have been clarified and abbreviated to conform with the label length restrictions of the graphics programme used to process the results (LOTUS 123). In compliance with the boundary hypersurface equation solution methodology, the piston loading coefficient is not included in the baseline parameter set.

Table 2.2 Back-to-back FPSE baseline parameter vector

Parameter Component	Value
Displacer diameter	35 mm
Displacer rod diameter	16 mm
Displacer length	80 mm
Displacer mass	150 g
Displacer damping coefficient	6 kg/s
Displacer/piston damping coefficient	3 kg/s
Displacer stroke	9 mm
Piston diameter	44,5 mm
Piston length	30 mm
Piston mass	1,5 kg
Piston stroke	19 mm
Displacer cylinder diameter	37 mm
Displacer cylinder length	90 mm
Piston cylinder length	50 mm
Expansion space temperature	330°C
Compression space temperature	27°C
Charge pressure	10 bars
Working fluid	Helium

Table 2.3 Back-to-back FPSE baseline parameter set performance

Selected loading coefficient:	26,2 kg/s
Rejected loading coefficient:	$-2,9 \times 10^5$ kg/s
Frequency of oscillation:	42,4 Hz
Non-steady-state term damping coefficient:	$-79,5 \text{ s}^{-1}$
Displacer/piston phase angle advance:	$-0,16^\circ$
lic indicated work:	5,69 J
Cyclic output work:	3,77 J
Cyclic output power:	159,68 W
Additional dissipation work:	0 J

The performance of the engine described by the baseline parameter set is reflected by the data listed in table 2.3. The selected and rejected loading coefficients correspond respectively to the roots  $c_{p1}$  and  $c_{p2}$  of equation (2.30). Since  $c_{p1} > 0$  and  $c_{p2} < 0$ , the engine is capable of self-sustaining operation. The root  $c_{p2}$  legitimately may be ignored since its large negative value is not physically meaningful in comparison with the value of  $c_{p1}$ . The predicted frequency of oscillation of 42,4 Hz is compatible with the dynamics of a spring/mass system corresponding to the piston being acted upon by two opposing gas springs with the stiffness equivalent of a 10 bar pressurisation. The negative non-steady-state term damping coefficient (which corresponds to  $\lambda_3$  in equation (2.32)) determines that the state space analysis is admissible. Consequently, the steady-state solution of equation (2.36) may be inferred from equation (2.35). The piston leads the displacer by a small phase angle of  $0,16^\circ$ . This may appear paradoxical in the light of the accepted notion that a significant piston/displacer phase angle is necessary for an FPSE to achieve self-sustaining operation. While this is

undeniably true when the displacer and piston strokes are nearly equal, in the baseline parameter configuration the piston stroke is specified as being more than double the displacer stroke. The resulting ratio between the expansion and compression space volume variations produces out-of-phase pressure profiles in each half of the engine. The pressure differential thus established drives the displacer and so maintains self-sustaining operation. Since it is the phase relationship between the pressure differential and the displacer motion which is cardinal to the back-to-back FPSE operation, a given parameter set may yield displacer/piston phase angles which appear to be incongruous.

This highlights one of the subtleties inherent in the state space analysis approach, namely, the necessity of stipulating piston and displacer stroke limits in order to achieve a discrete closed form solution. Essentially this is accomplished by converting the initial value problem of equation (2.35) into the boundary value problem of equations (2.42) where the 'initial' conditions are such that the piston and displacer oscillations meet given boundary constraints. These boundary constraints are artificial parameters since their values are implicitly contained in the full solution of equation (2.35). Such a solution may only be obtained from independent initial conditions at time  $t = 0$  using numerical techniques. Thus use of piston and displacement stroke limits as independent parameters (without prior knowledge of their physical viability) makes multiple engine performance evaluations using a range of geometrically compatible stroke limits mandatory. Nevertheless, the analytic procedure used to find the steady-state solution directly is physically admissible. This is demonstrated for the RE-1000 FPSE in

section 2.4.3 where prior experimental knowledge of the piston and displacer strokes is available.

The net cyclic indicated work done is low in comparison with existing Stirling FPSE hardware of similar size, although this is not significant in view of the arbitrariness of the baseline parameter set which is far from optimised (see table 2.4). The cyclic output work is 34% less than the indicated work, indicating that the work absorbed by the displacer in a back-to-back engine can be significant. Nevertheless, an output power of about 160 W for a non-optimised configuration is encouraging.

Perhaps the most significant attribute of the back-to-back FPSE configuration is its ability to operate on the stability boundary since the additional dissipation work required is zero. This means that  $\det(F) > 0$  for equation (2.40) without the necessity of reducing the piston linking coefficient  $c_p$  from its maximum theoretical value. Apparently, the engine is inherently capable of operating on the stability boundary hypersurface since, over the entire numerical test sequence, no cases where  $\det(F) \leq 0$  on the stability boundary have been encountered. Considering this phenomenon from an available energy or exergy perspective, the back-to-back FPSE seems to have the capability of maximising the energy yield from isothermal working spaces. However, this maximum need not be congruent with the realisation of an ideal Stirling thermodynamic cycle *per se* since with a  $-0.16^\circ$  displacer/piston phase advance, the gas displacement parts of the cycle are far from isochoric. Therefore, even in a demonstrably non-ideal practical implementation of the Stirling cycle, the back-to-back FPSE may have an intrinsic advantage compared with other Stirling

machine configurations.

### 2.3.3.2 Baseline Parameter Variations

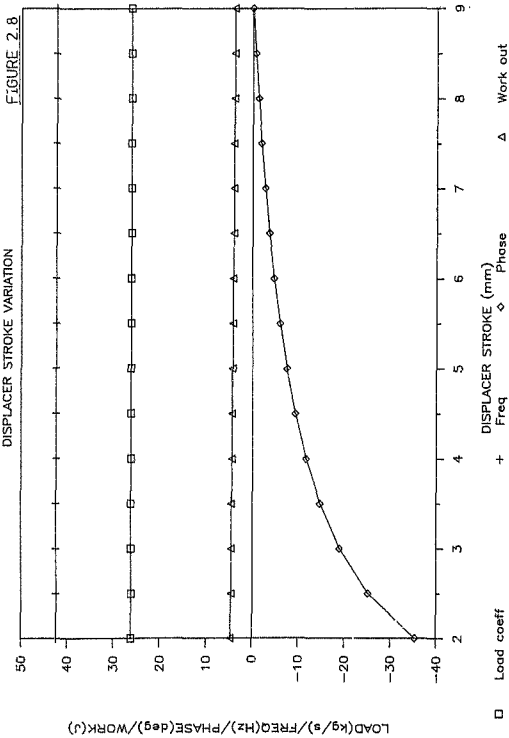
In addition to the piston and displacer stroke variations, the parameter variation profiles discussed are limited to those which show either definite performance optima or effects critical to the engine operation. Each parameter variation is depicted in two graphs. The first graph shows the behaviour of the piston loading coefficient, operating frequency, displacer/piston phase advance and piston work output (which is the optimisation parameter). The second graph depicts the indicated and output power characteristics. As each parameter is varied, the remaining parameters are held constant at their baseline values.

The displacer stroke variation is depicted in figures 2.8 and 2.9 while figures 2.10 and 2.11 show the piston stroke variation. Both figures 2.8 and 2.10 reveal that the piston loading coefficient and operating frequency maintain their baseline values and are independent of the operating strokes. This is anticipated analytically in the case of the back-to-back FPSE, since both equation (2.30) for the loading coefficient and equation (2.31) for the operating frequency are independent of the amplitudes of oscillation.

Figure 2.8 indicates that as the displacer stroke is increased from a minimum of 2 mm to a maximum of 9 mm (which gives a 0,5 mm clearance prior to an end-stop impact), the cyclic output work decreases from 4,6 to 3,8 J corresponding to an output power range (from figure 2.9) of 197 to 160 W. However, over the stroke range, the displacer/piston phase advance increases from  $-15$  to  $-0,2^\circ$ . Conversely, as the piston

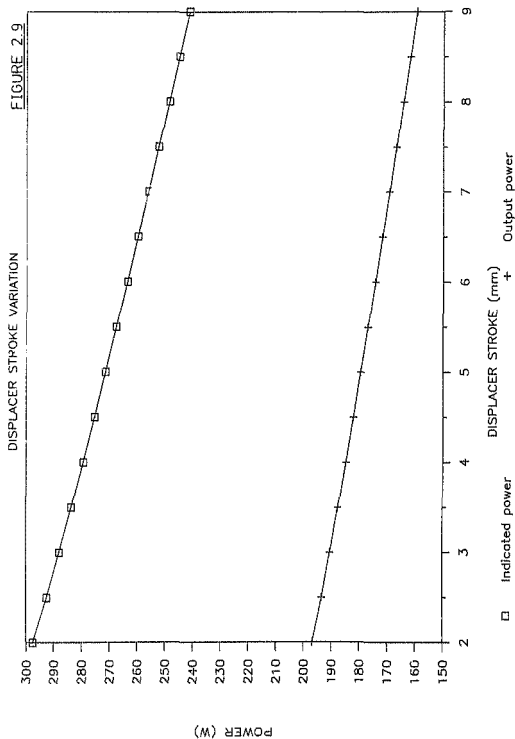
# BACK-TO-BACK FPSE PERFORMANCE

DISPLACER STROKE VARIATION



# BACK-TO-BACK FPSE POWER OUTPUT

FIGURE 2.9



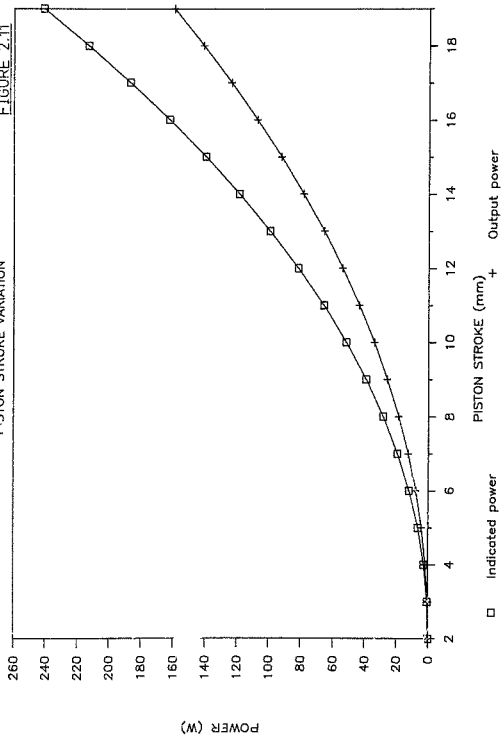
POWER (W)



# BACK-TO-BACK FPSE POWER OUTPUT

PISTON STROKE VARIATION

FIGURE 2.11



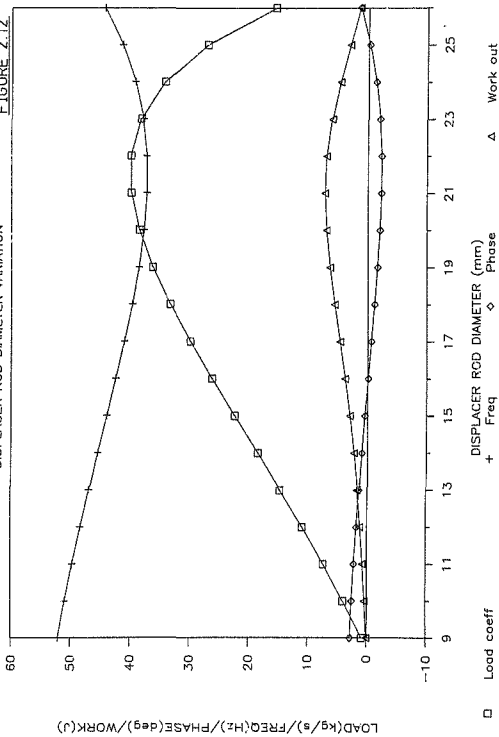
stroke is increased from 2 to 19 mm (which also gives a 0,5 mm end-stop impact clearance), the phase advance decreases from  $9,5$  to  $-0,2^\circ$ . Since the maximum strokes in each case correspond to the baseline parameters, this behaviour demonstrates the influence of the strokes on the phase angle and thereby on the expansion/compression space volume ratio. This ratio, which determines the pressure differential across the displacer, is continuously adjusted to maintain self-sustaining operation. When the displacer and piston strokes are equal at 9 mm, the displacer leads the piston by  $4,7^\circ$  which is intuitively reasonable for a back-to-back configuration. Figure 2.11 also reveals that as the piston stroke is increased, both the indicated and output power increase non-linearly from a negligible value (0,1 W at 2 mm), behaviour typical of an FPSE. At the maximum stroke, approximately 82 W is dissipated by the displacer. At a 9 mm stroke, the dissipation is reduced to 13 W although, in both cases, the dissipation is 34% of the indicated power (the same as the baseline percentage). However, as the displacer stroke is varied, the displacer related dissipation is reduced from 101 W at 2 mm to 82 W at 9 mm while remaining at 34% of the indicated power. The overall constancy of this fraction is consistent with the constancy of the damping and loading coefficients.

It can be argued that the most critical parameter in achieving an operational back-to-back FPSE is the displacer rod area or diameter. The displacer rod area determines the net driving force on the displacer assembly at any point in the cycle and hence whether the timing of the gas displacement will allow a positive indicator or pressure-volume diagram to be achieved. As shown in figure 2.12, the displacer rod diameter is limited to a range of about 9 to 26 mm. Exceeding this range results in the piston loading coefficient

# BACK-TO-BACK FPSE PERFORMANCE

DISPLACER ROD DIAMETER VARIATION

FIGURE 2.12

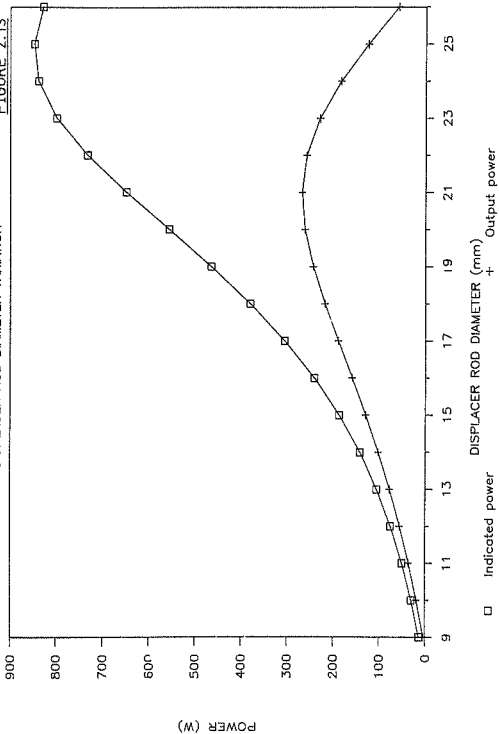


becoming negative, so excluding operation as an engine. A maximum cyclic work output of 7,2 J is achieved for a rod diameter of approximately 21 mm, a 92% increase over the baseline case. At the optimum, the displacer/piston phase angle advance is close to its minimum of  $-2,4^\circ$ , that is, the piston leads the displacer. This is perhaps surprising because the back-to-back FPSE was conceptualised on the basis of a classical Stirling pressure-volume diagram. However, in view of the baseline 2:1 piston/displacer stroke ratio, the result is consistent with those reported above. At the output work optimum, the frequency is at a minimum of 37,2 Hz which defines the lower bound of a 14,9 Hz variation range. These phase angle and frequency characteristics are the inverse of those of conventional FPSE configurations such as the RE-1000 engine (see figure 2.28 for comparison). The power output characteristics are shown as a function of the displacer rod diameter in figure 2.13. The output power reaches a maximum of 268 W at the optimum 21 mm rod diameter while the indicated power peaks at 848 W for a rod diameter of 25 mm. Therefore, as the driving force on the displacer is increased by increasing the displacer rod area, the additional indicated work is absorbed in overcoming the displacer dissipation at the expense of the piston output. Numerically, at the optimum, the displacer dissipation amounts to 59% of the indicated work while, at a 25 mm rod diameter, the displacer dissipation fraction dilates to 85%. These numbers indicate that the work required to drive the displacer can be substantial, raising the question as to whether the displacer also should be considered as a work extraction site.

# BACK-TO-BACK FPSE POWER OUTPUT

DISPLACER ROD DIAMETER VARIATION

FIGURE 2.13



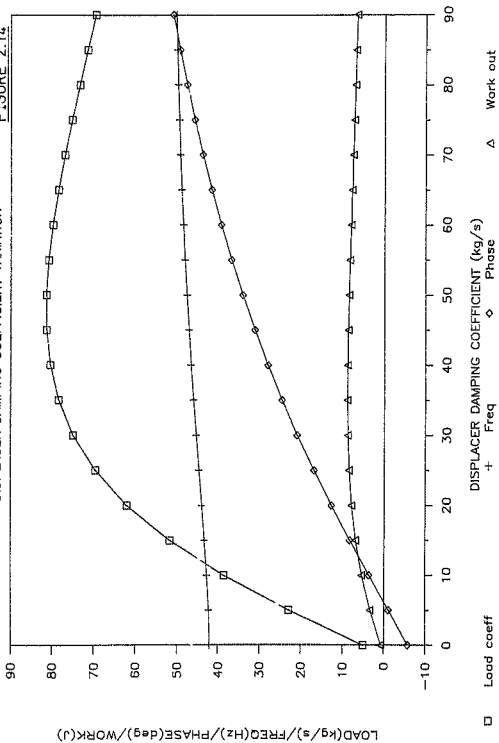
This theme is reiterated by the displacer damping coefficient variation profiles of figures 2.14 and 2.15. At the optimum damping coefficient of 35 kg/s, the work output reaches 8,9 J per cycle while the loading coefficient reaches its maximum of 81,4 kg/s for a displacer damping coefficient of 50 kg/s. Both the frequency and phase angle display monotonically increasing behaviour. Under optimum conditions, the displacer damping factor is 5,8 times larger than the baseline value and produces a phase advance of  $24,6^\circ$  which begins to be more in compliance with observed FPSE behaviour. Based on the speculation that a prototype back-to-back FPSE employing external (as opposed to annular) heat exchangers is likely to have an effective displacer damping coefficient in the 80 kg/s or larger range (such as for the RE-1000 FPSE), the resulting phase angles of  $45^\circ$  or greater are consistent with generic FPSE hardware. Figure 2.15 portrays a maximum output power of 410 W for a 40 kg/s damping coefficient which also yields a maximum indicated power of 655 W. The displacer dissipates 37% of the indicated work which is similar to the 34% baseline value, revealing a typical order of magnitude for the baseline engine.

The effect of varying the displacer mass is displayed in figures 2.16 and 2.17. Essentially, the profiles show that the displacer mass should be kept as small as possible in order to maximise the work and power outputs. A qualification to this assertion arises from the observation that the operating frequency decreases quite rapidly below a 150 g displacer mass. Thus the requirement of a specific frequency of operation may restrict the degree of mass minimisation desirable. In practice, the realisation of even a 400 g displacer may be difficult using conventional materials bearing in mind that, in

# BACK-TO-BACK FPSE PERFORMANCE

DISPLACER DAMPING COEFFICIENT VARIATION

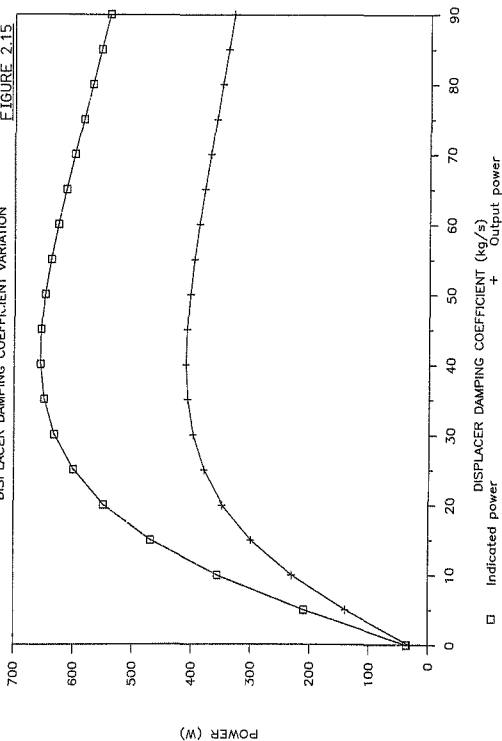
FIGURE 2.14



# BACK-TO-BACK FPSE POWER OUTPUT

DISPLACER DAMPING COEFFICIENT VARIATION

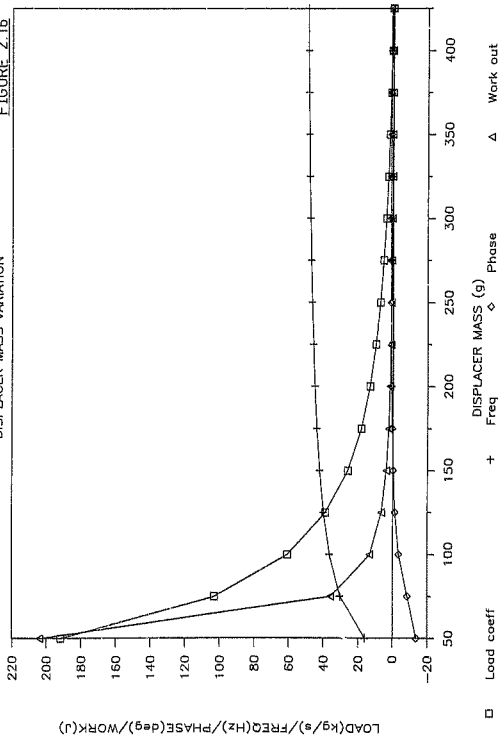
FIGURE 2.15



# BACK-TO-BACK FPSE PERFORMANCE

DISPLACER MASS VARIATION

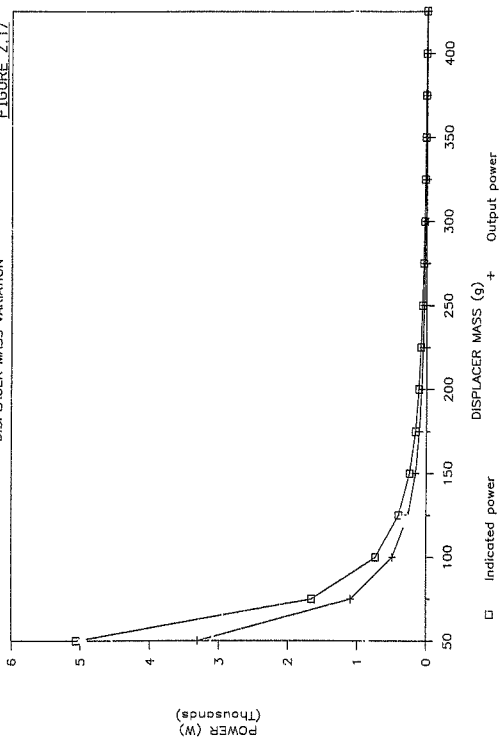
FIGURE 2.16



# BACK-TO-BACK FPSE POWER OUTPUT

DISPLACER MASS VARIATION

FIGURE 2.17



comparison, the RE-1000 FPSE discussed in section 2.4.3 has a single-ended displacer with a mass of 425 g.

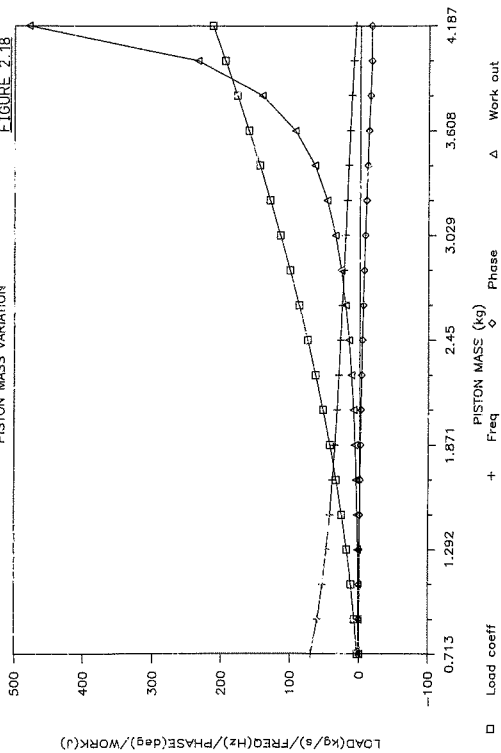
Conversely, figures 2.18 and 2.19 reveal that increasing the piston mass has a dramatic effect on the work and power outputs although the increase in work and power output is achieved at the expense of an operating frequency reduction. Thus for prospective applications such as alternating current electrical power generation, where frequencies of 50 or 60 Hz are desirable, increasing the piston mass must be accompanied by a corresponding increase in engine pressurisation. This serves to offset the drop in frequency by increasing the stiffness of the equivalent gas springs against which the piston oscillates.

Figures 2.20 and 2.21 demonstrate that minimising the piston diameter or area tends to maximise the work and power outputs. The minimum piston diameter chosen is equal to the baseline displacer cylinder diameter and produces the largest cyclic work output of 42.4 J over the diameter range plotted. Decreasing the diameter further to 35 mm results in an imaginary oscillating frequency while increasing the diameter beyond 71 mm produces a negative piston loading coefficient. Keeping the displacer and piston cylinder diameters equal reflects an existing FPSE design trend which in this instance seems to be substantiated. In the case of the back-to-back FPSE, a practical limitation on minimising the piston area arises from the desirability of simultaneously maximising the piston mass. This occurs because, for a given material density, increased mass may only be achieved by increasing the diameter or length of the piston. A diameter increase decreases the work output as shown by figure 2.19 while a length

# BACK-TO-BACK FPSE PERFORMANCE

PISTON MASS VARIATION

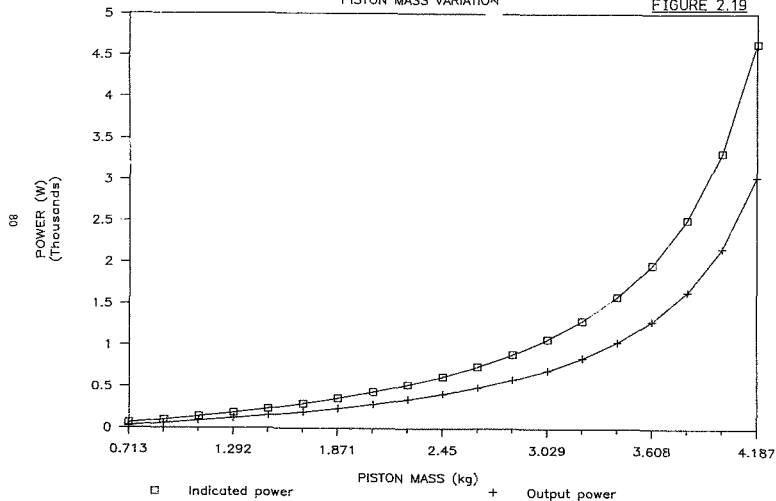
FIGURE 2.18



# BACK-TO-BACK FPSE POWER OUTPUT

PISTON MASS VARIATION

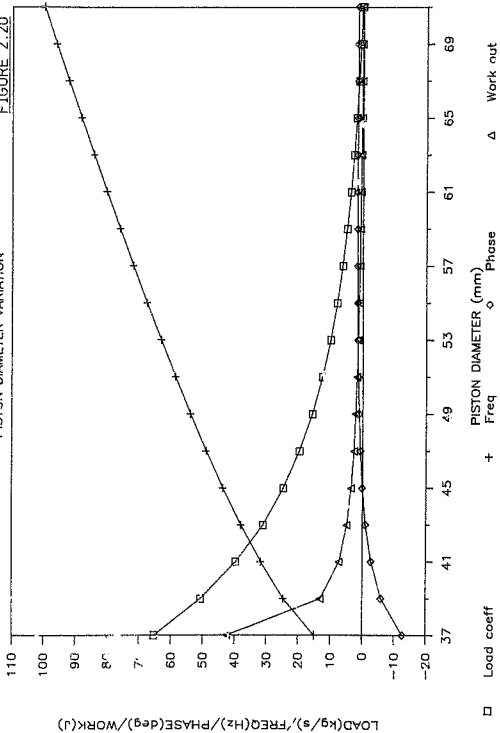
FIGURE 2.19



# BACK-TO-BACK FPSE PERFORMANCE

FIGURE 2.20

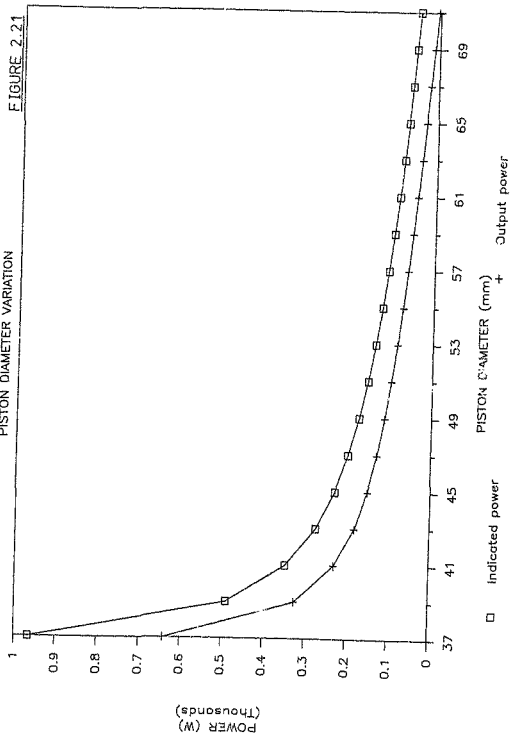
PISTON DIAMETER VARIATION



# BACK-TO-BACK FPSE POWER OUTPUT

PISTON DIAMETER VARIATION

FIGURE 2.21



increase increases the displacer dissipation by providing a greater bearing area. Thus an overall optimised design requires the balancing of these various factors. It may also be noted that the frequency increases with the piston diameter. This is a consequence of an increasing mean working space volume at a constant pressurisation yielding an increasing equivalent gas spring stiffness. At lower piston diameters, therefore, the pressurisation may need to be increased to achieve a desired operating frequency.

Table 2.4 Back-to-back FPSE optimised parameter vector

Parameter Component	Value
Displacer diameter	35 mm
Displacer rod diameter	20 mm
Displacer length	80 mm
Displacer mass	120 g
Displacer damping coefficient	20 kg/s
Displacer/piston damping coefficient	3 kg/s
Displacer stroke	8 mm
Piston diameter	44,5 mm
Piston length	30 mm
Piston mass	2,0 kg
Piston stroke	8 mm
Displacer cylinder diameter	37 mm
Displacer cylinder length	90 mm
Piston cylinder length	50 mm
Expansion space temperature	330°C
Compression space temperature	27°C
Charge pressure	50 bars
Working fluid	Helium

Table 2.5 Back-to-back FPSE optimised parameter set performance

Selected loading coefficient:	253,5 kg/s
Rejected loading coefficient:	$-4,6 \times 10^3$ kg/s
Frequency of oscillation:	53,3 Hz
Non-steady-state term damping coefficient:	$-319,9 \text{ s}^{-1}$
Displacer/piston phase angle advance:	$5,57^\circ$
Cyclic indicated work:	66,53 J
Cyclic output work:	28,8 J
Cyclic output power:	1536,10 W
Additional dissipation work:	0 J

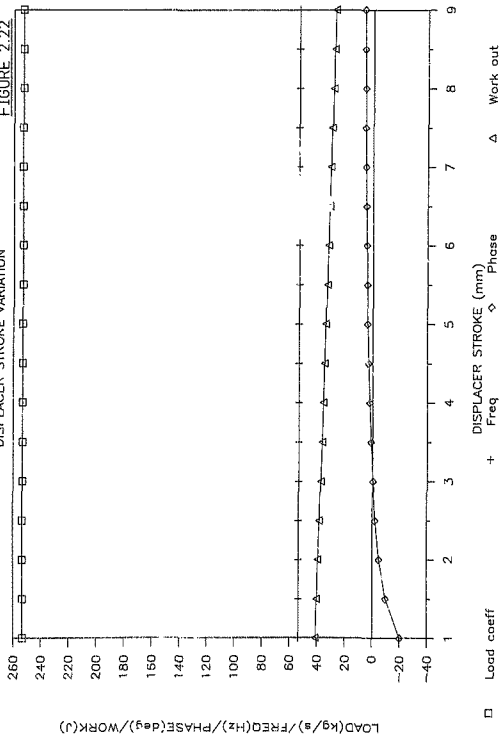
#### 2.3.3.3 Optimised Engine Performance

An attempt to achieve an optimised parameter set has been made using the results discussed above. The optimised parameter set is given in table 2.4 while the corresponding performance results are listed in table 2.5. Of particular note are the 30 g decrease in displacer mass and 20 g increase in piston mass while the displacer rod diameter and damping factor are increased to 20 mm and 20 kg/s respectively. The displacer and piston strokes are kept equal and restricted to 8 mm while the pressurisation is increased five times to 50 bars, which is not unusual for generic FPSE hardware. The remaining parameters are kept at their baseline values. Under these conditions, the predicted output power yield is 1536 W at a frequency of 53 Hz with a displacer/piston phase advance of  $5,6^\circ$ . Figures 2.22 to 2.25, which depict the displacer and piston stroke variations, have the same characteristics as figures 2.7 to 2.10 for the baseline parameter set. The output power decreases from 2,2 to 1,5 kW as the displacer stroke ranges from 1 to 9 mm for a constant piston stroke of 8 mm. Keeping the displacer stroke constant at 8 mm produces an 11 kW power output

# BACK-TO-BACK FPSF. OPTIMISED PERFORMANCE

FIGURE 2.22

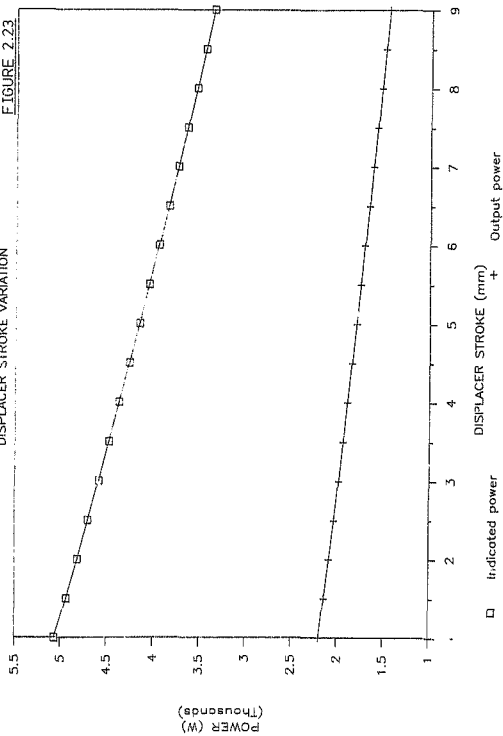
DISPLACER STROKE VARIATION



# BACK-TO-BACK FPSE OPTIMISED POWER YIELD

DISPLACER STROKE VARIATION

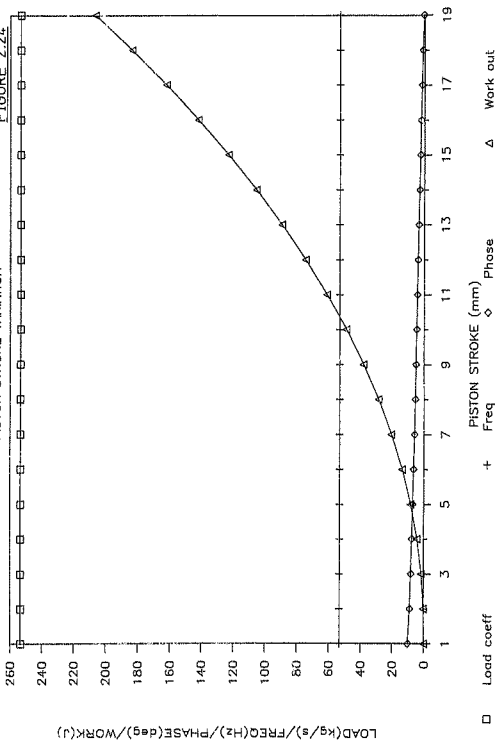
FIGURE 2.23



# BACK-TO-BACK FPSE OPTIMISED PERFORMANCE

FIGURE 2.24

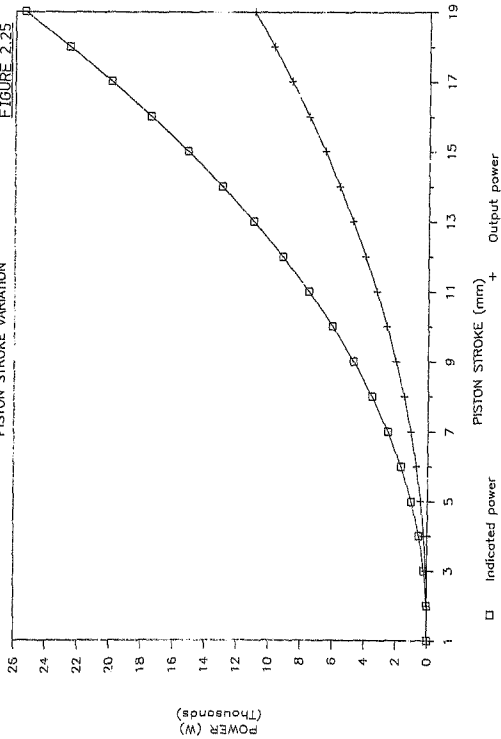
PISTON STROKE VARIATION



# BACK-TO-BACK FPSE OPTIMISED POWER YIELD

PISTON STROKE VARIATION

FIGURE 2.25



for a 19 mm piston stroke, an impressive theoretical yield which may not be achievable in practice. Figure 2.25 demonstrates that, over the entire piston stroke range, 57% of the indicated power output is sacrificed to displacer dissipation under optimum conditions. A clear case for providing the required additional displacer dissipation via a work extraction device may thus be made in this instance.

#### 2.3.3.4 Conclusion

The numerical results for the back-to-back FPSE show the wealth of design information that may be gleaned rapidly and efficiently from an application of the state space analysis. Particular performance characteristics which appear to be unusual, such as the typically small displacer/piston phase angle advance, are highlighted and alternate design strategies, such as using the displacer as a work extraction medium, are suggested. Parametric studies may be used to bound the uncertainties inherent in the design of new and untested hardware. Hence the major performance unknowns not explicitly produced by a steady-state analysis, namely the piston and displacer strokes, may be included in the performance estimates. From a hardware perspective, the characteristics of the back-to-back FPSE and, in particular, its ability to operate on the stability boundary hypersurface under all parametric conditions, make it a configuration worthy of further analytical and experimental study.

2.4 APPLICATION OF THE STATE SPACE ANALYSIS TO THE SUNPOWER  
RE-1000 FREE-PISTON STIRLING ENGINE

2.4.1 Introduction

The RE-1000 free-piston Stirling engine (FPSE) was designed and fabricated at Sunpower Incorporated, Athens, Ohio. Since the engine is intended for research purposes, an internally mounted dashpot power absorbing device precludes the availability of any usable power output. The RE-1000 engine is designed to yield maximum efficiency at a power level of 1 kW using helium working fluid at 70 bars pressurisation, a heater metal tube temperature of 600°C and an engine frequency of 30 Hz. Owing to its extensive testing by the National Aeronautics and Space Administration's (NASA) Lewis research center (Sc83), the specifications of the RE-1000 FPSE have been publically disclosed, making it an ideal case study representing a typical beta-configuration FPSE.

A schematic of the RE-1000 engine is shown in figure 2.26. The displacer slides on a spider mounted guiding rod such that a ground-coupled gas spring is formed within the displacer piston cavity. A radially symmetric external heater, regenerator and cooler are positioned around the displacer cylinder. Thirty-four parallel tubes form the element of an electrical resistance heater, permitting the passage of a low voltage current to supply heat directly to the engine. The heater tubes are joined to an annular cavity created by positioning an external sleeve around the displacer cylinder. Knitted stainless steel 'Metax' mesh is packed into the cavity to form the regenerator. A series of 135 parallel rectangular passages located

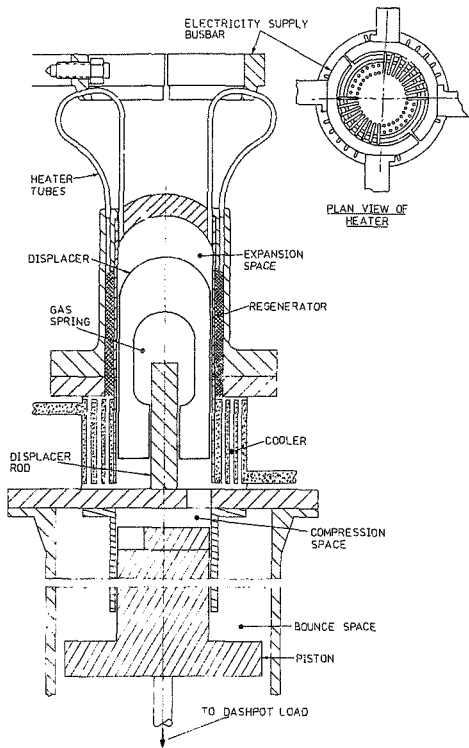


Figure 2.26 Schematic of the RE-1000 free-piston Stirling engine (adapted from a figure reproduced from reference Sc83)

between the regenerator cavity and the compression space constitute the cooler. These passages are formed by press-fitting an aluminium gas passage fin module into the annular cavity below the regenerator, ensuring that the cooling water flows parallel to the working gas. The power piston, which is attached to the dashpot power absorber by a coupling rod, is sprung to ground via a gas spring formed by the bounce space. Clearance seals are used throughout the engine to separate the expansion and compression spaces from each other and from the displacer gas spring and bounce spaces. The motions of the displacer and power piston are centralised by a system of ports which connect the bounce space with the displacer gas spring and with the working space when the displacer and power piston are, respectively, at their mid-stroke positions.

#### 2.4.2 RE-1000 FPSE State Space Analysis

The specifics of the application of the state space analysis to the RE-1000 FPSE are described in section A.2 of appendix A. Since many of the application details are similar to those of the back-to-back FPSE discussed in section 2.3.2, previous elaboration will not be repeated in the following discussion. As before, the application procedure follows the listing sequence described in section 2.2.

##### 1. *State vector solution and formulation of the governing differential equations*

A complete list of the assumptions made in describing the RE-1000 FPSE is given in section A.2.1. The expansion space and heater are considered as being isothermal at one temperature while the

compression space and cooler are isothermal at a lower temperature. The temperature profile in the regenerator is constant and linear between these two temperatures. The displacer gas spring and the bounce space are treated as being adiabatic while the engine is assumed to be positioned vertically so that gravity influences the piston and displacer dynamics. The four component state vector necessary to completely describe the RE-1000 is the same as that for the back-to-back FPSE (given by equation (2.19)).

The parameter vector has 22 components which are listed in table 2.6 and shown in figure 2.27. The displacer and piston are assumed to oscillate about an equilibrium position defined by the alignment of their respective centering ports. It may be noted that the parameter vector does not represent a minimum set; the expansion space dead volume and heater volume could, for example, be combined, as could the cooler volume and compression space dead volume. The deviation from a rigorous minimum is undertaken in the interests of maintaining compatibility with the published RE-1000 data set (Sc83), although prior to implementing the analysis the parameter vector is reduced to a minimum configuration (equations (A.28) to (A.31)).

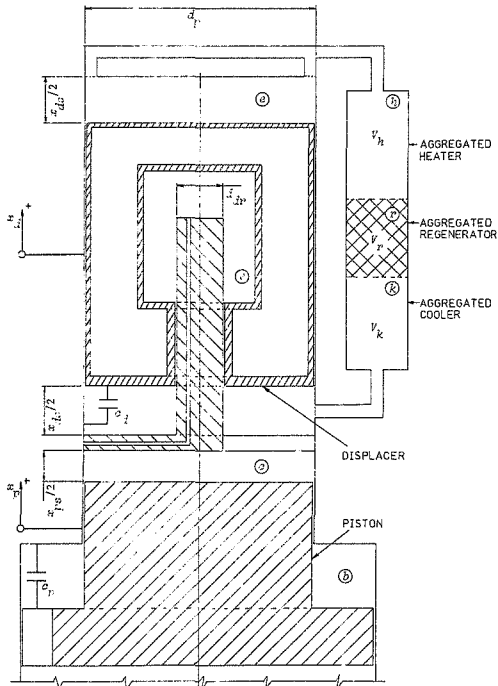


Figure 2.27 RE-1000 free-piston Stirling engine parameters

Table 2.6 RE-1000 FPSE parameter vector components

Component	Symbolic description
Displacer rod area	$A_{dr}$
Displacer gas spring midstroke volume	$\bar{V}_s$
Displacer mass	$H_d$
Displacer damping coefficient	$c_d$
Displacer stroke between stops	$x_{ds}$
Displacer amplitude of oscillation	$x_{dmax}$
Piston bounce space midstroke volume	$\bar{V}_b$
Piston mass	$H_p$
Piston loading coefficient	$c_p$
Piston stroke between stops	$x_{ps}$
Piston amplitude of oscillation	$x_{pmax}$
Expansion space cylinder area	$A_p$
Expansion space dead volume	$(V_e)_{dead}$
Expansion space / heater temperature	$T_e$
Heater volume	$V_h$
Regenerator volume	$V_r$
Cooler volume	$V_k$
Compression space dead volume	$(V_c)_{dead}$
Compression space / cooler temperature	$T_c$
Working fluid charge pressure	$P_{crg}$
Working gas constant	$R$
Working gas ratio of specific heats	$\gamma$

The governing differential equations describing the RE-1000 FPSE in terms of the assumptions made may be stated using the threaded derivative formulation (equations (2.2)) as:

$$\dot{z}_1 = z_2 \quad (2.55.1)$$

$$\dot{z}_2 = A_p \left[ K_b / (\bar{V}_b + z_1 A_p)^{\gamma} - M_{TOT} R / (\alpha + z_3 ((A_p - A_{dr}) / T_c - A_p / T_a) - z_1 A_p / T_c) \right] / H_p - c_p z_2 / H_p - g \quad (2.55.2)$$

$$\dot{z}_3 = z_4 \quad (2.55.3)$$

$$\dot{z}_4 = A_{dr} \left[ K_s / (\bar{V}_s + z_3 A_{dr})^{\gamma} - M_{TOT} R / (\alpha + z_3 ((A_p - A_{dr}) / T_c - A_p / T_a) - z_1 A_p / T_c) \right] / H_d - c_d z_4 / H_d - g \quad (2.55.4)$$

where  $\alpha$  and  $M_{TOT}$  are given by equations (2.20.5) and (2.20.6) respectively and:

$$K_b = (P_{crg} + M_p g / A_p) \bar{V}_b^{\gamma} \quad (2.55.5)$$

$$K_s = (P_{crg} + M_d g / A_p) \bar{V}_s^{\gamma} \quad (2.55.6)$$

## 2. Determination of E and B in the reduced equation

As the engine is oriented in parallel with the gravity vector:

$$E = \begin{bmatrix} 0 \\ -R \\ 0 \\ -g \end{bmatrix} \quad (2.56)$$

The Jacobian B is given by:

$$B = \begin{bmatrix} 0 & 1 & 0 & 0 \\ B_{21} & B_{22} & B_{23} & 0 \\ 0 & 0 & 0 & 1 \\ B_{41} & 0 & B_{43} & B_{44} \end{bmatrix} \quad (2.57)$$

where the elements of B are expressed in terms of the parameter vector components by equation (A.45) in appendix A.

### 3. Development of the determinant of $(\lambda I - B)$ and investigation of its characteristics

Using the elements of B,  $\det(\lambda I - B)$  may be expressed as:

$$\begin{aligned} \det(\lambda I - B) = & \lambda^4 - \lambda^3(B_{22} + B_{44}) + \lambda^2(B_{12}B_{44} - B_{21} - B_{43}) \\ & + \lambda(B_{22}B_{43} + B_{21}B_{44}) + B_{21}B_{43} - B_{23}B_{41} \end{aligned} \quad (2.58)$$

Expanding the coefficients of the  $\lambda$ -terms in terms of the parameter vector components (equation (A.47)) shows that the state space analysis is unconditionally applicable, that is, no special case stipulations need be invoked.

### 4. Analytic description of the stability boundary hypersurface in the parameter space

Developing the characteristic equation using condensed coefficients from equation (2.54) produces:

$$\lambda^4 + K_4\lambda^3 + K_2\lambda^2 + K_1\lambda + K_0 = 0 \quad (2.59)$$

Substituting a particular complex eigenvalue given by equation (2.2) and solving the resultant equation for the real and imaginary parts simultaneously produces on the stability boundary hypersurface (where  $a = 0$ ):

$$K_3K_2 - K_1(K_2 - K_1/K_3) \quad (2.60)$$

In terms of the parameter vector components, the stability boundary hypersurface defining equation becomes:

$$A_p^2 A_{dx} \gamma (c_p / H_p + c_d / H_d) [K_s A_{dx} (\gamma K_b / \bar{V}_b^{\gamma+1} + M_{TOT} R / T_c \alpha^2) / \bar{V}_s^{\gamma+1} - K_b M_{TOT} R (A_p \cdot A_{dx}) / T_c - A_p / T_e] / \alpha^2 \bar{V}_b^{\gamma+1}]$$

$$\begin{aligned} & \left[ M_{TOT} R \cdot d A^4 p / T_c - c_p A_{dx} (A_p \cdot A_{dx}) / T_c - A_p / T_e \right] / \alpha^2 + \gamma (c_p A_{dx}^2 K_s / \bar{V}_s^{\gamma+1} + c_d A_p^2 K_b / \bar{V}_b^{\gamma+1}) \left[ c_p c_d / H_p H_d + \gamma (A_p^2 K_b / \bar{V}_b^{\gamma+1} H_p + A_{dx}^2 K_s / \bar{V}_s^{\gamma+1} H_d) + M_{TOT} R [A_p^2 / T_c H_p - A_{dx} (A_p \cdot A_{dx}) / T_c - A_p / T_e] / H_d \right] / \alpha^2 - \left[ M_{TOT} R [c_d A_p^2 / T_c - c_p A_{dx} (A_p \cdot A_{dx}) / T_c - A_p / T_e] / \alpha^2 + \gamma (c_p A_{dx}^2 K_s / \bar{V}_s^{\gamma+1} + c_d A_p^2 K_b / \bar{V}_b^{\gamma+1}) \right] / (c_p H_d + c_d H_p) \end{aligned} \quad (2.61)$$

where  $M_{TOT}$ ,  $\alpha$ ,  $K_b$ , and  $K_s$  are given respectively by equations (2.20.5), (2.20.6), (2.51.5) and (2.51.6).

### 5. Solution of the stability boundary hypersurface equation

Using the dependent parameter methodology described for the back-to-back PFSE, equation (2.61) forms a cubic polynomial when expressed in terms of the piston loading coefficient  $c_p$ . This polynomial may be expressed as:

$$K_1 c_p^3 + K_2 c_p^2 + K_3 c_p + K_4 = 0 \quad (2.62.1)$$

where the coefficients are given by the following threaded sequence:

$$K_1 = -K_5 c_d / H_p \quad (2.62.2)$$

$$K_2 = K_6 H_d + K_5 (K_3 - c_d^2 / H_d) \quad (2.62.3)$$

$$K_3 = K_7 H_d + c_d H_p K_8 + 2K_5 A_p^2 c_d K_8 \quad (2.62.4)$$

$$K_4 = K_7 c_d H_p + A_p^2 c_d^2 K_8^2 \quad (2.62.5)$$

$$K_5 = A_{dx} (\gamma K_s A_{dx} / \bar{V}_s^{\gamma+1} + M_{TOT} R K_{11} / \alpha^2) \quad (2.62.6)$$

$$K_6 = (K_9 - K_9 A_p^2 c_d^2 / M_d) / M_p - K_2 K_{10} \quad (2.62.7)$$

$$K_7 = K_9 c_d / M_d - A_p^2 c_d K_6 K_{10} \quad (2.62.8)$$

$$K_8 = M_{TOT} R / T_c \alpha^2 + \gamma K_b / \bar{V}_b^{\gamma+1} \quad (2.62.9)$$

$$K_9 = A_p^2 A_{dx} (\gamma K_s A_{dx} K_8 / \bar{V}_s^{\gamma+1} - \gamma K_b M_{TOT} R K_{11} / \alpha^{2\gamma+1}) \quad (2.62.10)$$

$$K_{10} = A_p^2 K_8 / M_p + A_{dx} (\gamma K_s A_{dx} / \bar{V}_s^{\gamma+1} - K_{11} M_{TOT} R / \alpha^2) / M_d \quad (2.62.11)$$

$$K_{11} = (A_p - A_{dx}) / T_c - A_p / T_e \quad (2.62.12)$$

Equation (2.62.1) may be solved analytically using Cardan's formulae (Us48). These formulae enable the extraction of a simple root, factoring equation (2.62.1) into the form:

$$(c_p - \beta_1)(c_p^2 + \beta_2 c_p + \beta_3) = 0 \quad (2.63)$$

The physical significance of the roots  $c_{p1}$ ,  $c_{p2}$  and  $c_{p3}$  may be interpreted in the light of the experimental behaviour of the RE-1000 FPSE (Sc83) as follows:

- If  $\beta_2^2 - 4\beta_3 > 0$  then the loading coefficient is non-discrete and the engine may operate at more than one loading state simultaneously. As this is physically incompatible with the requirements of the operating stability condition, the parameter set is inadmissible.
- If  $\beta_1 < 0$  and  $\beta_2^2 - 4\beta_3 < 0$  then the machine will not achieve self-sustaining operation as an engine, but may operate as a heat pump.
- If  $\beta_1 > 0$  and  $\beta_2^2 - 4\beta_3 < 0$ , self-sustaining operation as an engine is possible.

Supposing that the last condition is true, the coefficients in equation (2.60) may be evaluated and the angular frequency of oscillation can be found from:

$$b = \{(B_{22}B_{43} + B_{21}B_{44}) / -(B_{22} + B_{44})\}^{0.5} \quad (2.64)$$

As for the back-to-back FPSE, if  $b$  is imaginary then the parameter set is physically incompatible. If  $b$  is zero then operating stability will not be achieved.

Substituting a positive value of  $b$  into equation (2.27) produces a quadratic factor  $(\lambda^2 + b^2)$ . Dividing equation (2.52) by this factor and invoking equation (2.60) produces the remaining eigenvalues given by:

$$\lambda_{3,4} = 0.5(B_{22} + B_{44}) \pm 0.5\{(B_{22} + B_{44})^2 - 4(B_{22}B_{44} - B_{21} \cdot B_{43} + (B_{22}B_{43} + B_{21}B_{44}) / (B_{22} + B_{44}))\}^{0.5} \quad (2.65)$$

If  $\lambda_{3,4}$  are complex conjugates and their real part is non-negative, or if they are simple and either eigenvalue is non-negative, then, by Lyapunov's first theorem (equation (2.14)), the behaviour of the reduced equation (2.11) is not significant and the analysis is inadmissible.

#### 6. Solution of the reduced state space equation

The reduced equation for the RE-1000 FPSE is given by equation (2.11) since, by equation (2.56),  $E$  is non-zero. Thus the general solution of equation (2.12) is valid in this case. Using the methodology described in section A.3 for a particular set of admissible eigenvalues  $\lambda_{1,2} = \pm jb$ ,  $\lambda_3$  and  $\lambda_4$ , equation (2.12) becomes:

$$z = \{2|Z_1| \cos(bt + \phi_1) + Z_3 \exp(\lambda_3 t) + Z_4 \exp(\lambda_4 t)\} (z(0) + B^{-1}E) - B^{-1}E \quad (2.66.1)$$

where:

$$Z_1 = (B + j\omega I)(B - \lambda_3 I)(B - \lambda_4 I) / 2jb(-\lambda_3 + j\omega)(-\lambda_4 + j\omega) \quad (2.66.2)$$

$$Z_3 = (B^2 I + b^2 I)(B - \lambda_4 I) / (\lambda_3^2 + b^2)(\lambda_3 - \lambda_4) \quad (2.66.3)$$

$$Z_4 = -(B^2 I + b^2 I)(B - \lambda_3 I) / (\lambda_4^2 + b^2)(\lambda_3 - \lambda_4) \quad (2.66.4)$$

$$\phi_1 = \tan^{-1} \{ \text{Imag}(Z_1) / \text{Real}(Z_1) \} \quad (2.66.5)$$

As  $t \rightarrow \infty$  the steady state solution is given by:

$$z_{ss} = \{2|Z_1| \cos(bt + \phi_1)\} (z(0) + B^{-1}E) - B^{-1}E \quad (2.67)$$

#### 7. Selection of the Initial conditions

The method used to determine the initial conditions is identical to that elaborated for the back-to-back FPSE. Since the piston and displacer by definition oscillate about their equilibrium positions,  $z(0)$  is defined by equation (2.37). This produces the following expressions for  $x_p$  and  $x_d$ :

$$x_p = -(B^{-1}E)_1 + \sum_{j=1}^4 2|(Z_1)_{1j}| \cos(\theta + (\phi_1)_{1j}) \{z(0) + B^{-1}E\}_j \quad (2.68.1)$$

$$x_d = -(B^{-1}E)_3 + \sum_{j=1}^4 2|(Z_1)_{3j}| \cos(\theta + (\phi_1)_{3j}) \{z(0) + B^{-1}E\}_j \quad (2.68.2)$$

where  $\theta = bt$ .

The angular displacements at which  $x_p$  and  $x_d$  are at their maximum may be found from:

$$x_{pmax} = \tan^{-1} \left\{ \frac{4}{\sum_{j=1}^4 |(Z_1)_{1j}| |z(0) + B^{-1}E_j \sin(\phi_1)_{1j}|} \right. \\ \left. / \left( \sum_{j=1}^4 |(Z_1)_{1j}| |z(0) + B^{-1}E_j \cos(\phi_1)_{1j}| \right) \right\} \quad (2.69.1)$$

$$x_{dmax} = \tan^{-1} \left\{ \frac{4}{\sum_{j=1}^4 |(Z_1)_{3j}| |z(0) + B^{-1}E_j \sin(\phi_1)_{3j}|} \right. \\ \left. / \left( \sum_{j=1}^4 |(Z_1)_{3j}| |z(0) + B^{-1}E_j \cos(\phi_1)_{3j}| \right) \right\} \quad (2.69.2)$$

Substituting equation (2.69) into equations (2.68) produces the piston and displacer equilibrium position velocity matrix equation:

$$\begin{bmatrix} F_{11} & F_{12} \\ F_{21} & F_{22} \end{bmatrix} \begin{bmatrix} \dot{x}_p(0) \\ \dot{x}_d(0) \end{bmatrix} = \begin{bmatrix} x_{pmax} + (B^{-1}E)_1 + \sum_{j=1}^4 \alpha_j \\ x_{pmin} + (B^{-1}E)_3 + \sum_{j=1}^4 \beta_j \end{bmatrix} \quad (2.70.1)$$

where:

$$\alpha_j = 2 |(Z_1)_{1j}| (B^{-1}E)_j \cos(\theta_{pmax} + (\phi_1)_{1j}) \quad (2.70.2)$$

$$\beta_j = 2 |(Z_1)_{3j}| (B^{-1}E)_j \cos(\theta_{dmax} + (\phi_1)_{3j}) \quad (2.70.3)$$

and the coefficient matrix F is given by equations (2.41).

Using the same iterative method of solution described for the back-to-back FPSE, a solution for  $\dot{x}_p(0)$  and  $\dot{x}_d(0)$  may be found if  $\det(F) > 0$ .

The phase angle by which the displacer leads the piston is given at

convergence by  $\theta_{pmax} - \theta_{dmax}$ .

### 8. Thermodynamic performance determination

Using the values of  $\dot{x}_p(0)$  and  $\dot{x}_d(0)$  found from equation (2.70), the state variables are given by the components of equation (2.67). In turn these state variable solutions yield the net instantaneous indicated power output given by:

$$\dot{W}_{TOT} = P(\dot{y}_e + \dot{y}_c) \quad (2.71)$$

which, after substitution of the state vector components and relevant parameters, produces the non-linearised form:

$$\begin{aligned} \dot{W}_{TOT} = & -M_{TOT} R (\dot{x}_d A_{dr} + \dot{x}_p A_p) / [\alpha + x_d \{(A_p - A_{dr}) / T_c - A_k / T_e\} \\ & - x_p A_p / T_c] \end{aligned} \quad (2.72)$$

where  $\alpha$  is given by equation (2.20.5). The linearised pressure version becomes:

$$\dot{W}_{TOT} \approx -M_{TOT} R (\dot{x}_d A_{dr} + \dot{x}_p A_p) [x_d \{(A_p - A_{dr}) / T_c - A_p / T_e\} - x_p A_p / T_c] / \alpha^2 \quad (2.73)$$

The net instantaneous power dissipated mechanically is given by:

$$\dot{W}_{DIS} = c_p \dot{x}_p^2 + c_d \dot{x}_d^2 \quad (2.74)$$

while the gross power output produced by the piston is limited to:

$$\dot{W}_{OUT} = c_p \dot{x}_p^2 \quad (2.75)$$

The cyclic integrals of  $\dot{W}_{TOT}$ ,  $\dot{W}_{DIS}$  and  $\dot{W}_{OUT}$  are given respectively by equations (2.47), (2.49) and (2.51) while the cyclic power outputs are given by equations (2.53).

Invoking the same arguments cited for the back-to-back FPSE, the linearised equation for  $\dot{W}_{TOT}$  is also preferred here. Thus the cyclic integrals of  $\dot{W}_{TOT}$ ,  $\dot{W}_{DIS}$  and  $\dot{W}_{OUT}$  may be expressed in a format similar to that of equation (2.52) as:

$$\begin{aligned}
 W = & (2\pi/b) \sum K_{ij} \left[ (B^{-1}E)_i (B^{-1}E)_j + 2 \left[ \sum_{k=1}^4 |(Z_1)_{ik}| \cos(\phi_1)_{ik} (z(0) + B^{-1}E)_k \right] \right. \\
 & \times \left[ \sum_{k=1}^4 |(Z_1)_{jk}| \cos(\phi_1)_{jk} (z(0) + B^{-1}E)_k \right] + 2 \left[ \sum_{k=1}^4 |(Z_1)_{ik}| \sin(\phi_1)_{ik} \right. \\
 & \left. \left. \times (z(0) + B^{-1}E)_k \right] + \left[ \sum_{k=1}^4 |(Z_1)_{jk}| \sin(\phi_1)_{jk} (z(0) + B^{-1}E)_k \right] \right] \quad (2.76)
 \end{aligned}$$

where  $i$  and  $j$  are any two state vector components (including cases for which  $i=j$ ) and  $K$  is a constant.

The significance of a negative  $\det(F)$  in terms of the indicated and dissipation cyclic work is the same as that for the back-to-back FPSE. Hence the discussion given previously (in section 2.3.2) elucidating this significance is also applicable to the RE-1000 FPSE.

#### 9. Selection of an optimisation index

Once again, either  $\dot{W}_{OUT}$  or  $\dot{W}_{DIS}$  are useful optimisation indices because the assumption of isothermal working spaces does not yield any independent heat transfer information. As the RE-1000 is intended as a research engine, more attention seems to have been focussed on the power delivered to the dashpot loading device (Sc83) and hence  $\dot{W}_{OUT}$  is selected as the optimisation index.

### 2.4.3 Numerical Results

A computer programme entitled 'RE1000' embodies the application of the state space analysis to the RE-1000 FPSE. Details of the algorithms used as well as a programme listing are given in appendix B. The numerical results are focussed on using the available experimental data for substantiating the validity of the state space analysis. Initially, a baseline parameter vector is established by calibrating the results of the analysis against the nominal design performance test data supplied by Sunpower Incorporated prior to the engine being accepted by NASA Lewis. Thereafter, a comparison between the state space analysis and NASA experimental results is made over a representative segment of the engine's performance map. Finally, a series of variations of several of the more prominent parameters affecting the power output is presented to provide an assessment of the optimality of the baseline parameter set.

#### 2.4.3.1 Baseline Engine Performance

The baseline parameter set listed in table 2.7 reflects a more detailed definition of the heater, regenerator and cooler geometries than given in table 2.6. This results from an effort to maintain correspondence between the geometrical data reported by NASA (Sc83) and the interactive data entry procedure incorporated in the RE-1000 computer programme. As for the back-to-back FPSE, data entry is clarified by using diameters in preference to areas and strokes in preference to amplitudes. All the geometrical parameters quoted in table 2.7 are those supplied by NASA while the parameters defining the engine operating state (displacer and piston strokes, charge pressure and working space temperatures) correspond to those defining the

Sunpower acceptance test point (Sc83). Only the displacer damping coefficient is obtained by calibrating the state space analysis performance results against these test data. The approximate value of the damping coefficient had been previously established using a simulation employing isothermal working spaces (GL85, LT85). In conformity with its dependent status, the piston damping coefficient is not included in the parameter set used to implement the state space analysis numerically.

Table 2.7 RE-1000 FPSE baseline parameter set

Parameter	Value
Displacer rod diameter	16,63 mm
Displacer gas spring midstroke volume	31,79 cm <sup>3</sup>
Displacer mass	426 g
Displacer damping coefficient	80 kg/s
Displacer stroke between stops	40,4 mm
Displacer stroke	25,5 mm
Piston bounce space midstroke volume	20500 cm <sup>3</sup>
Piston mass	6,2 kg
Piston stroke between stops	42 mm
Piston stroke	23,2 mm
Expansion space cylinder diameter	57,23 mm
Expansion space dead volume	11,62 cm <sup>3</sup>
Expansion space / heater temperature	567,41°C
No. of heater tubes	34
Heater tube inside diameter	2,362 mm
Heater tube length	177,876 mm
Heater dead volume	13,11 cm <sup>3</sup>
Regenerator annular gap outer diameter	71,8 mm
Regenerator annular gap inner diameter	60,7 mm
Regenerator length	56,368 mm
Regenerator matrix porosity	75,9 %
No. of cooler passages	135
Cooler passage width	0,508 mm
Cooler passage depth	0,376 mm
Cooler length	79,19 mm
Cooler dead volume	8,08 cm <sup>3</sup>
Compression space dead volume	55,98 cm <sup>3</sup>
Compression space / cooler temperature	40°C
Charge pressure	70 bars
Working fluid	Helium

The performance of the RE-1000 FPSE described by the baseline parameter set at the calibration point is listed in table 2.8.

Table 2.8 RE-1000 RFSE baseline parameter set performance

	Analytical	Experimental
Stability boundary hyper-surface loading coefficient	1148,7 kg/s	-
Operating hypersurface loading coefficient	405,0 kg/s	-
Frequency of oscillation	29,9 Hz	31,2 Hz
Non-steady-state term damping coefficients	$-126,6 \pm j129,0$	-
Displacer/piston phase angle advance	$49,6^\circ$	$47,6^\circ$
Cyclic indicated power	1766,2 W	1100 W
Cyclic output power	1000,0 W	1000 W
Power dissipated by displacer	227,2 W	-
Additional dissipation power	539,0 W	0 W
det(F)	$0,66018 \times 10^{-5} \text{ s}^2$	-

Using the previously determined displacer damping coefficient of 70 kg/s as a starting point (GL85, LT85), the damping coefficient was varied to obtain the closest agreement between the analytical and experimental frequency of operation and displacer/piston phase angle advance. Thereafter the magnitude of det(F) was altered to equalize the experimental and analytical power outputs. This in turn changed the operating frequency and phase angle mandating another adjustment to the displacer damping coefficient. Iterating these adjustments produced the converged calibration state described by table 2.8 defined by a displacer damping coefficient of 80 kg/s and a value for det(F) of  $0,7 \times 10^{-5} \text{ s}^2$ .

It may be observed immediately that, unlike the back-to-back FPSE, the RE-1000 engine is not capable of achieving self-sustaining operation on the stability boundary hypersurface, a characteristic which is consistent over the entire numerical test sequence. As noted in section 2.3.2 with reference to the discussion of figure 2.7, the operating hypersurface lies within the stability boundary hypersurface and is defined by  $\det(F) > 0$ . However, the magnitude of  $\det(F)$  is indeterminate without additional boundary condition data, thus predicating that, under design conditions, the limiting case defined by  $\det(F) = 0$  must be used initially. The availability of the power output experimental data for the RE-1000 engine in this case permits a value of  $\det(F)$  to be chosen so as to enable a precise calibration of the analysis in output power terms. The small magnitude of  $\det(F)$  of order  $10^{-6}$  is consistent with that of the back-to-back FPSE which yielded values in the range of  $1 \times 10^{-7}$  to  $2 \times 10^{-6} \text{ s}^2$  on the stability boundary hypersurface. Of primary significance from a validity perspective, though, is the existence of a physically credible  $\det(F)$  which enables the achievement of a calibration.

The conditions governing the solution of equation (2.63) are satisfied since the stability boundary hypersurface loading coefficient is positive while the remaining roots are imaginary. A 763,7 kg/s difference separates the stability boundary and operating hypersurfaces indicating that the RE-1000 operates well within the limits defining the maximum utilisation of the energy available from a thermodynamic cycle with isothermal working spaces. Of the 666,2 W separating the analytical and experimental indicated works, 539 W or 81% is devoted to additional irreversible dissipation which shows the extent of the error made in using an isothermal analysis to describe

the RE-1000 FPSE fluid dynamics. Corresponding to the eigenvalues  $\lambda_{3,4}$  in equations (2.62), the non-steady-state term damping coefficients are a complex conjugate pair with negative real parts. This confirms the admissability of the state space analysis for the baseline parameter set and the validity of the steady-state solution given by equation (2.67). At the calibration point, the analytical frequency differs from that experimentally measured by 1% while the discrepancy in the phase advance is 4.2%. In view of the assumptions made in describing the RE-1000, particularly with regard to treating the piston loading and displacer damping as being linearly dependent on velocity, these discrepancies are considered to be acceptable. The displacer loading (which incorporates all the gas dynamic dissipation) is intuitively non-linear while, physically, a dashpot piston load tends to be proportional to the square of the velocity. Thus for the relatively large calibration point piston and displacer strokes of 23,2 and 25,5 mm respectively, the errors accrued from the linear loading and damping assumptions are likely to be significant. This argument may be substantiated by noting that the phase angle errors in particular should increase with increasing strokes, a characteristic which is demonstrated by the NASA-Lewis / state space analysis data comparison discussed below.

#### 2.4.3.2 Comparison with Experimental Data

The comparison of the state space analysis and NASA experimental data for the RE-1000 FPSE is summarised in table 2.9. The experimental data used comprise a consecutive series of tests designated by the numerical sequence 598-617. These data, which were kindly supplied by Mr. J. Schreiber of NASA-Lewis in November 1984, were labelled as being preliminary and, as such, had not been published.

Table 2.9 RE-1000 FPSE state space analysis / experimental data comparison

NASA Test No.	Pliston Stroke (mm)	Displ. acer Stroke (°C)	Exp Space Temp (°C)	Comp Space Temp (°C)	Comp Space Mean Pres (bar)	Output Power (W)	det(F) ( $\% \times 10^5$ )	Frequency (Hz)		Phase (degrees)		Indicated Power (U)	
								Experi-mental	State space	Experi-mental	State space	Experi-mental	State space
598	17.8	21.8	556.0	45.7	70.26	709.0	0.460444	29.9	29.3	54.7	54.3	739.0	1198.0
599	20.0	23.6	503.3	49.4	70.19	839.0	0.500289	29.8	29.5	55.4	53.6	878.0	1419.0
600	22.1	25.2	562.2	53.5	70.31	976.0	0.546299	29.9	29.6	56.1	52.7	1021.0	1639.8
601	23.8	26.5	557.6	57.1	70.21	1077.0	0.566293	29.9	29.6	57.1	52.5	1125.0	1816.4
602	25.8	27.2	554.8	61.6	70.36	1216.0	0.600978	29.9	29.8	57.1	51.6	1282.0	1909.5
603	18.0	21.7	519.9	47.8	70.35	662.0	0.446352	29.8	29.5	56.2	56.0	686.0	1153.1
604	20.0	23.4	517.6	51.0	70.19	776.0	0.4796	29.8	29.5	57.0	55.4	808.0	1346.7
605	21.9	24.8	514.6	54.2	70.37	866.0	0.525498	29.8	29.7	57.7	54.6	907.0	1530.7
606	24.0	26.5	509.2	60.2	70.42	1004.0	0.538745	29.9	29.7	58.8	54.5	1045.0	1721.5
607	26.0	26.9	507.3	63.2	70.52	1095.0	0.594506	29.7	29.8	58.5	53.1	1137.0	1852.4
608	17.9	21.4	470.7	49.4	70.51	612.0	0.405918	30.1	29.5	58.8	58.5	656.0	1071.0
609	19.9	23.0	468.9	51.4	70.34	693.0	0.459008	29.9	29.6	59.1	57.6	721.0	1248.7
610	21.9	24.5	464.7	55.7	70.34	784.0	0.491082	29.9	29.6	59.6	56.9	821.0	1419.0
611	23.9	25.5	462.7	59.3	70.65	890.0	0.534319	30.2	29.7	61.4	57.7	923.0	1509.4
612	25.9	25.9	458.5	63.5	70.58	971.0	0.577963	30.1	29.7	61.6	54.6	996.0	1657.9
613	17.9	21.1	423.2	48.4	70.54	545.0	0.389443	30.1	29.5	60.6	60.7	567.0	993.2
614	19.9	22.4	421.8	51.3	70.38	622.0	0.446817	30.1	29.5	61.6	59.2	649.0	1132.6
615	21.9	23.8	418.7	54.8	70.62	700.0	0.485644	30.1	29.6	62.3	58.3	730.0	1289.2
616	23.9	25.1	415.4	58.9	70.59	777.0	0.512406	30.2	29.6	62.9	57.8	798.0	1435.4
617	25.8	25.6	412.4	62.8	70.52	834.0	0.554744	30.0	29.6	62.7	56.6	850.0	1517.8

Table 2.9 RE-1000 FPSE state space analysis / experimental data comparison

NASA Test No.	Piston Stroke (mm)	Displ-acer Stroke (mm)	Exp Space Temp (°C)	Comp Space Temp	Comp Space Mean Pres (bar)	Output Power (W)	dot(f) (s <sup>-2</sup> x10 <sup>5</sup> )	Frequency (Hz)		Phase (degrees)		Indicated Power (W)	
								Exper-imental	State space	Exper-imental	State space	Exper-imental	State space
598	17,8	21,8	566,0	45,7	70,26	709,0	0,460444	29,9	29,3	54,7	54,3	739,0	1198,0
599	20,0	23,6	563,3	49,4	70,19	839,0	0,508280	29,8	29,5	55,4	53,4	870,0	1419,9
600	22,1	25,2	562,2	53,5	70,31	976,0	0,546299	29,9	29,6	56,1	52,7	1021,0	1639,8
601	23,0	26,5	557,6	57,1	70,21	1077,0	0,566293	29,9	29,6	57,1	52,5	1125,0	1816,4
602	25,8	27,2	554,8	61,6	70,56	1216,0	0,609978	29,9	29,8	57,1	51,6	1262,0	1969,5
603	18,0	21,7	519,9	47,8	70,35	662,0	0,446352	29,8	29,5	56,2	56,0	686,0	1153,1
604	20,0	23,4	517,6	51,0	70,19	776,0	0,4796	29,8	29,5	57,0	55,4	808,0	1346,7
605	21,9	24,8	514,6	54,2	70,37	866,0	0,525498	29,8	29,7	57,7	54,6	907,0	1530,7
606	24,0	26,3	509,2	60,2	70,42	1006,0	0,536745	29,9	29,7	58,8	54,5	1045,0	1721,5
607	26,0	26,9	507,3	63,2	70,52	1095,0	0,594506	29,7	29,8	58,5	53,1	1137,0	1892,4
608	17,9	21,4	470,7	49,4	70,51	612,0	0,405918	30,1	29,5	58,8	58,5	636,0	1071,0
609	19,9	23,0	468,9	51,4	70,34	693,0	0,458908	29,9	29,6	59,1	57,4	721,0	1248,7
610	21,9	24,5	464,7	55,7	70,34	784,0	0,491082	29,9	29,6	59,6	56,9	821,0	1419,0
611	23,9	25,5	462,7	59,3	70,65	890,0	0,534319	30,2	29,7	61,4	55,7	923,0	1569,4
612	25,9	25,9	458,5	63,3	70,58	971,0	0,577983	30,1	29,7	61,6	54,6	996,0	1657,9
613	17,9	21,1	423,2	48,4	70,54	545,0	0,389443	30,1	29,5	60,6	60,7	567,0	993,2
614	19,9	22,4	421,8	51,3	70,38	622,0	0,446817	30,1	29,3	61,6	59,2	649,0	1132,6
615	21,9	23,8	418,7	54,8	70,62	700,0	0,485644	30,1	29,6	62,3	58,3	730,0	1289,2
616	23,9	25,1	415,4	58,9	70,59	777,0	0,512406	30,2	29,6	62,9	57,8	798,0	1435,4
617	25,8	25,6	412,4	62,8	70,52	834,0	0,554744	30,0	29,6	62,7	56,6	850,0	1517,8

Subsequently, tests 598-602 have been published in final form in reference SC86. The data published in reference SC83 reveals significant deviations from the nominal performance specification owing to prior physical defects in the engine and its instrumentation. Only after some considerable testing, rebuilding and modification by NASA was the engine restored to its performance specification as reflected by the baseline calibration results. Hence, the original choice of unpublished data was motivated by a desire to use test data garnered on the engine as restored to its acceptance test specification.

The experimental data set covers four nominal heater temperatures, ranging from 450°C to 600°C in 50°C increments. At each heater temperature, the piston stroke is varied over a nominal 18 to 26 mm range. The test results used as variable inputs for the state space analysis are the piston and displacer strokes, expansion and compression space gas temperatures and the mean cyclic pressure in the compression space. These parameters ostensibly enable the greatest degree of correlation between the actual and state space analysis approximated fluid dynamic operating states. All the remaining parameters, including the displacer loading coefficient, are kept constant. At each test point,  $\det(F)$  is varied so as to match the experimental and analytical power outputs to at least two decimal places, hence the reporting of six significant figures for  $\det(F)$ . Three performance parameters are then compared to examine the validity of the state space analysis, namely, the operating frequency, displacer/piston phase advance and cyclic indicated power. Since the analytic indicated power is known from independent theoretical considerations to be a considerable over-estimate of that measured,

only the frequency and phase angle comparisons are practically significant as validation indices.

Over the entire performance map, the largest discrepancy in operating frequency encountered is 2% (test no. 598) while the largest discrepancy in phase angle amounts to 11.4% (test no. 612). For all four heater temperatures, as the piston and displacer strokes increase, the phase angle discrepancy increases in compliance with the assumption of linear loading and damping forces. Considering the smallest piston strokes only (nominally 18 mm), the maximum phase angle discrepancy is reduced to 0.7% over the test map. Examining the phase angle trend indicates that, for all heater temperatures, as the piston stroke increases the state space phase angle decreases while the experimental phase angle increases. This may be attributed to an increase in  $\det(F)$  with increasing piston stroke to maintain experimental and analytic output power equality (while the displacer damping coefficient is kept constant). Varying the displacer damping coefficient to better the linear approximation of the actual displacer damping as the displacer stroke changes yields a much closer agreement between the analytic and experimental phase angles over the entire piston stroke range. No consistent trend is exhibited by the experimental operating frequencies, behaviour which is matched by the state space frequencies.

Both the experimental and analytic indicated powers increase with piston stroke for the four heater temperatures considered. The discrepancies between the analytical and experimental results are tabulated in table 2.10. In all cases, the analytic indicated powers are greater than their experimental counterparts.

Table 2.10 Comparison of the indicated power discrepancies

Heater Temperature ( $^{\circ}\text{C}$ )	Indicated Power Discrepancy (%)	
	Average	Maximum
600	60.4	62.1
550	66.2	68.8
500	70.2	73.2
450	77.0	79.9

Both the average and maximum discrepancies increase with a decreasing heater temperature. This trend is consistent with the notion that the error resulting from an isothermal working space assumption (compared with actual non-isothermal conditions) increases with a decreasing hot side temperature. This occurs since the irreversible dissipation, as a proportion of the available energy, increases with decreasing expansion space / heater temperatures for approximately constant compression space / cooler temperatures.

Within the constraints of the assumptions made, the comparison between the analytic and experimental data for the RE-1000 FPSE demonstrates the validity of the state space analysis in predicting the output power, operating frequency and piston/displacer phase angle advance with worst case discrepancy of less than 12%. This is achieved with the availability of sufficient empirical boundary condition data to define the operating boundary hypersurface. The magnitude of the parameter defining the operating hypersurface (namely,  $\det(F)$ ) seems to be consistent within an order of magnitude for both the RE-1000 and back-to-back engines. This establishes a pragmatic baseline standard for use in applying the state space analysis to untested FPSE designs

which cannot operate on the stability boundary hypersurface.

A limiting case defined by  $\det(F) = 0$  (which determines the maximum theoretical output power yield) may, however, always be evaluated, thus establishing an upper bound on the design performance expectation. It is this capability of the state space analysis methodology which is fully substantiated by the analytical/experimental performance data comparison and, therefore, which endows the analysis with its practical utility as a design tool

#### 2.4.3.3 Baseline Parameter Variations

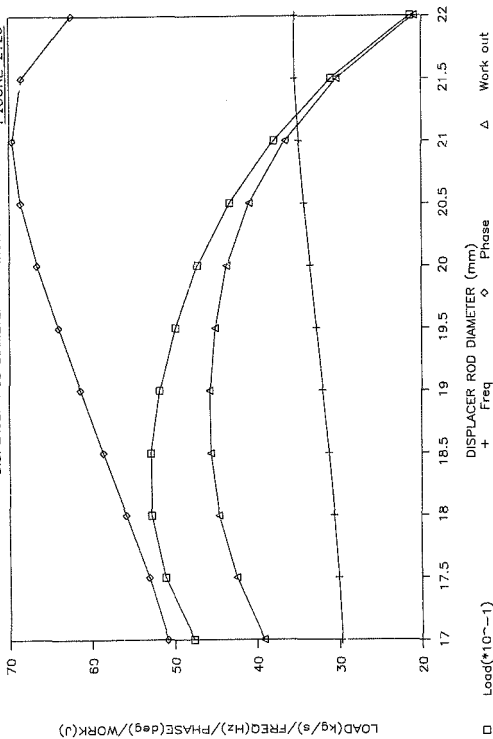
Six parameter variations are presented as a framework within which the optimality of the RE-1000 FPSE baseline parameter set may be reviewed. In each case, only the designated parameter is varied; all the remaining parameters are held constant at their baseline values. Furthermore, over the entire variation sequence,  $\det(F)$  maintains its baseline calibration value. As for the back-to-back FPSE, each parameter variation is presented in two graphs. The first graph depicts the displacer loading coefficient, frequency, displacer/piston phase advance and output work. The second graph shows the indicated, output and additional dissipation powers. In compliance with the discussion in section 2.4.2, the output power is used as the optimisation index.

Figures 2.28 and 2.29 reflect the influence of the displacer guiding rod diameter on the engine performance. This parameter is arguably the most critical from a design optimisation perspective (Sc83), a characteristic shared with the back-to-back FPSE. A maximum power output of 1478 W is attained for a displacer rod diameter of 19,5 mm

# RE-1000 FPSE PERFORMANCE

DISPLACER ROD DIAMETER VARIATION

FIGURE 2.2B



LOAD (kg/s)/FREQ(Hz)/PHASE(deg)/WORK(J)

□ Load ( $\times 10^{-1}$ )

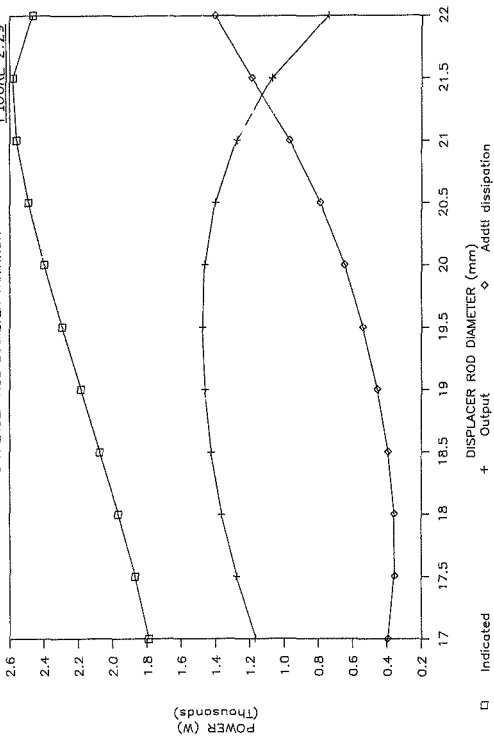
+ Freq

△ Work out

# RE-1000 FPSE POWER OUTPUT

DISPLACER ROD DIAMETER VARIATION

FIGURE 2.29



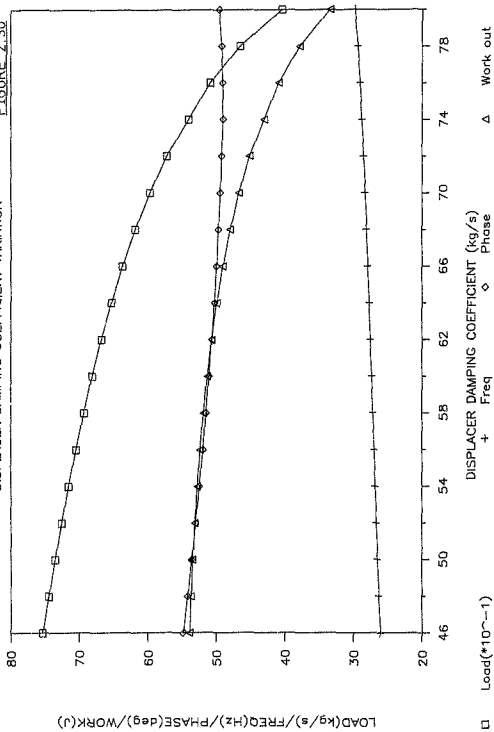
while the maximum work output occurs at a 19 mm displacer diameter. However, the minimum additional dissipation power of 358 W occurs at a diameter of 17,5 mm while the maximum indicated power is experienced at a 21,5 mm displacer diameter. Self-sustaining operation for the baseline parameter set is achievable only within a 16,5 to 22,5 mm range; no operating states for the given piston strokes exist outside these bounds. Thus the narrow 6 mm diameter range for which self-sustaining operation may apparently be achieved is indicative of the precision required in the design of RE-1000 style engine configurations. The baseline value of 16,63 mm would appear to be 2,87 mm smaller than optimum although the overall accuracy of the state space analyses of 12% does not warrant the conclusion that the baseline value is an inappropriate choice, particularly if a 30 Hz operating frequency at a 70 bar pressurisation is desired. Figure 2.28 shows a 5,6 Hz increase in frequency over the diameter variation range while the phase angle falls within an 18,7 degree interval, peaking at 69,6 degrees for a 21 mm displacer rod diameter. The piston loading coefficient and work output decrease at the range extremities, the decrease being more substantial at the upper limit.

The variation in displacer damping coefficient is depicted in figures 2.30 and 2.31. As for the displacer rod diameter, no operating states for the given piston and displacer strokes are possible outside a 45 to 81 kg/s displacer damping coefficient range. A maximum power output of 1421 W is achieved for a 54 kg/s damping coefficient while the minimum additional dissipation of 95 W occurs at a 58 kg/s damping coefficient. However, the output power optimum is not particularly notable, as the output power is within 1,6% of the optimum value over a 46 to 62 kg/s damping coefficient range. Of more interest is the

# RE-1000 FPSE PERFORMANCE

DISPLACER DAMPING COEFFICIENT VARIATION

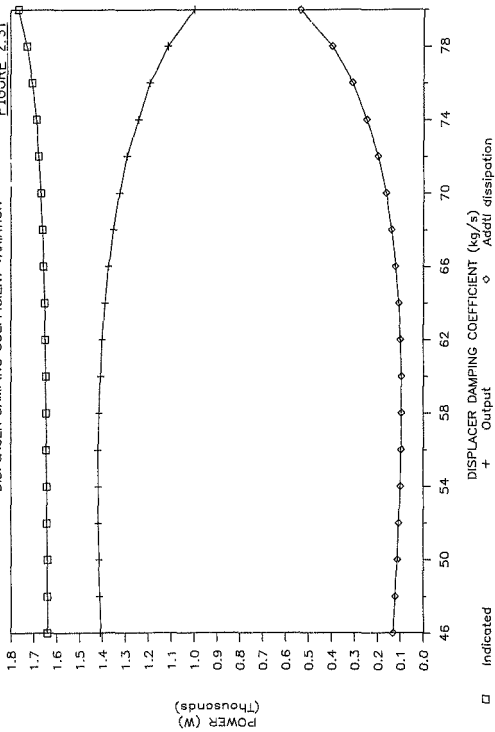
FIGURE 2.30



# RE-1000 FPSE POWER OUTPUT

FIGURE 2.31

DISPLACER DAMPING COEFFICIENT VARIATION



□ Indicated

+ Output

◇ Addtl dissipation

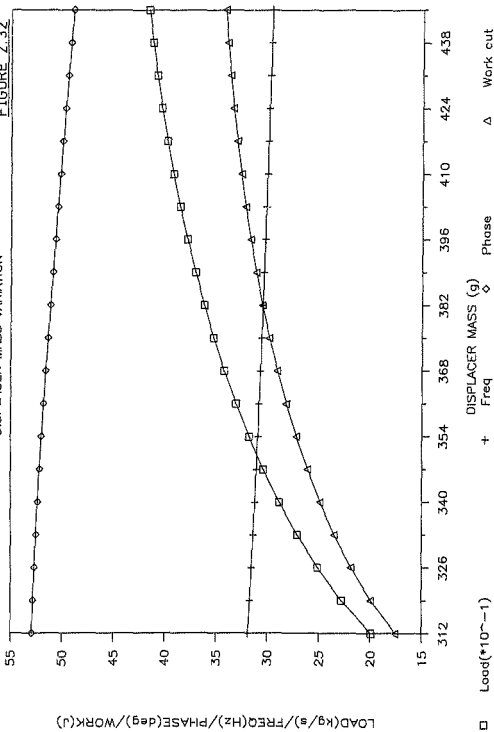
observation that, at the calibration value of 80 kg/s, the output power is at a minimum, as is the phase angle, while the operating frequency is maximised. The contrast between the optimum and baseline displacer damping coefficients is indicative of a fundamental dilemma facing the FPSE designer, namely, a desire to achieve a required level of displacer dissipation to optimise performance while simultaneously not being able to manipulate the dissipation in a design sense. This arises because the fluid dynamic dissipation cannot be controlled precisely. In particular, the frictional dissipation in the regenerator matrix (which is the principal fluid flow related irreversibility) may be manipulated with the least amount of precision. Such dissipation may be included in the state-space analysis using an approach based upon one proposed by Chen and Griffin (CG86), although at some increase in analytic complexity. Practically, it usually materialises that even though every effort is made to reduce the displacer related dissipation, the value obtained is still greater than the optimum, a situation exemplified by the RE-1000 FPSE. The operating frequency experiences a 3.8 Hz rise over the damping coefficient range while the phase angle advance spans a  $6^\circ$  interval, neither variation being substantial in a relative sense.

The displacer mass variation given in figures 2.32 and 2.33 shows that the output power increases monotonically with displacer mass, behaviour which is the inverse of that exhibited by the back-to-back FPSE. Furthermore, the additional dissipation power decreases as the output power increases. This behaviour, however, is limited to the 312 to 445 g range plotted, no operating states for the given displacer and piston strokes being possible beyond these confines. Thus the baseline value of 426 g for the displacer mass is an

# RE-1000 FPSE PERFORMANCE

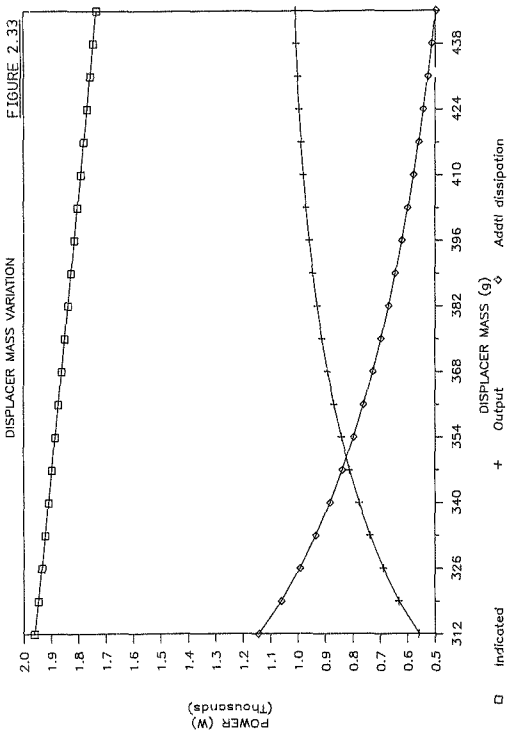
DISPLACER MASS VARIATION

FIGURE 2.32



# RE-1000 FPSE POWER OUTPUT

FIGURE 2.33



appropriate choice. In addition, the necessity of minimising displacer mass is not a critical constraint, permitting some design flexibility. Both the piston loading coefficient and output work increase over the displacer mass variation range, while the frequency and phase angle decrease uniformly over 2,3 Hz and  $4^\circ$  intervals respectively.

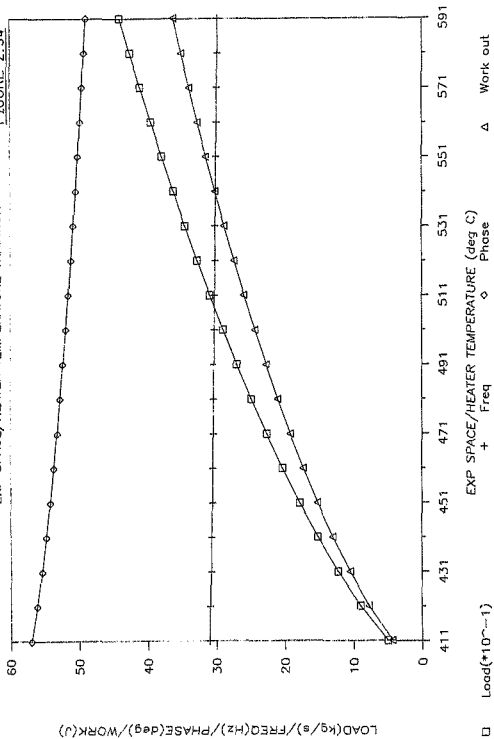
As expected, the requirement of constant displacer and piston strokes limits the expansion space / heater temperature range for which operating states exist. For the baseline parameter set, this range is limited to about 405 to 600°C as shown in figures 2.34 and 2.35. As the hot end temperature increases, the output power increases and the additional dissipation power decreases, both variations being monotonic. The indicated power also increases with temperature, although the gradient is significantly less than that of the output power increase. Hence the baseline expansion space / heater temperature of 567,4°C enables 93% of the maximum power output to be achieved within the given stroke limits. The operating frequency is minimally influenced by the hot end temperature, experiencing a 1,3 Hz drop as the temperature increases. The phase angle also decreases with increasing temperature, although the 8,1° phase angle drop indicates a more marked dependence on temperature.

The behaviour of the engine as the compression space / cooler temperature is varied (shown in figures 2.36 and 2.37) is the inverse of that for the expansion space / heater temperature variation. The temperature range enabling operation for the given displacer and piston strokes spans about 80°C between 30°C and 116°C, which is more restricted than the corresponding 200°C hot end temperature range.

# RE-1000 FPSE PERFORMANCE

EXP SPACE/HEATER TEMPERATURE VARIATION

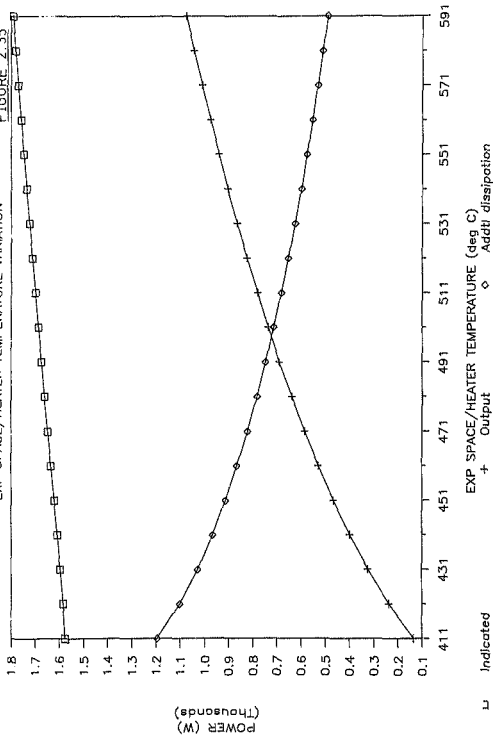
FIGURE 2.34



# RE-1000 FPSE POWER OUTPUT

FIGURE 2.35

EXP SPACE/HEATER TEMPERATURE VARIATION

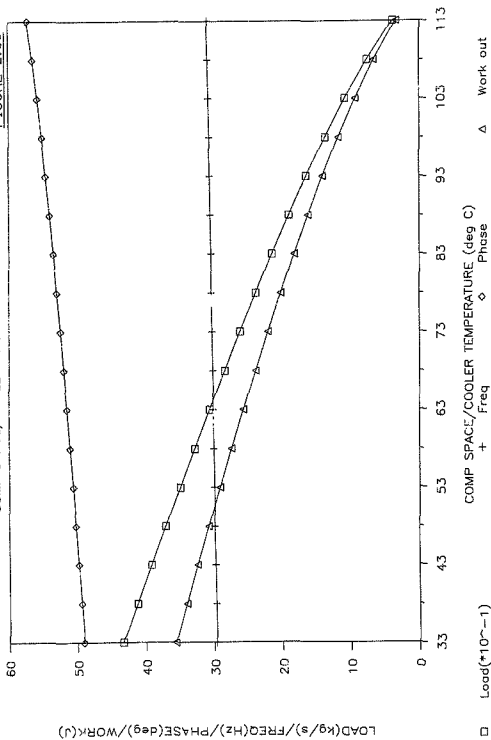


Indicated

# RE-1000 FPSE PERFORMANCE

FIGURE 2.36

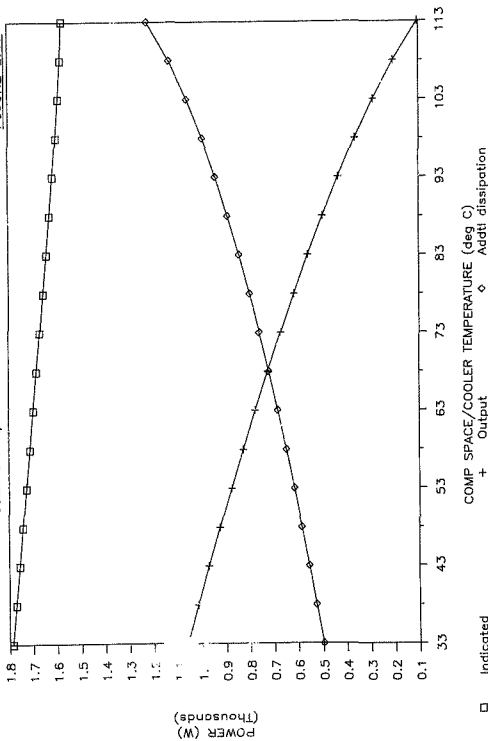
COMP SPACE/COOLER TEMPERATURE VARIATION



# RE-1000 FPSE POWER OUTPUT

FIGURE 2.37

COMP SPACE/COOLER TEMPERATURE VARIATION



□ Indicated

+ Output

◇ Addtl dissipation

Increasing the compression space / cooler temperature causes a reduction in output power and an increase in additional dissipation power. Concomitantly, the indicated power experiences a relatively gradual drop. Hence the baseline cold end temperature of  $40^{\circ}\text{C}$  is close to the allowable minimum for the given stroke limits and therefore is appropriately optimised. The operating frequency and phase angle advance characteristics are mirror images of those shown in figure 2.34 for the hot end temperature variation. Over the temperature range plotted, the frequency and phase angle undergo a 1,3 Hz and  $8,2^{\circ}$  increase respectively.

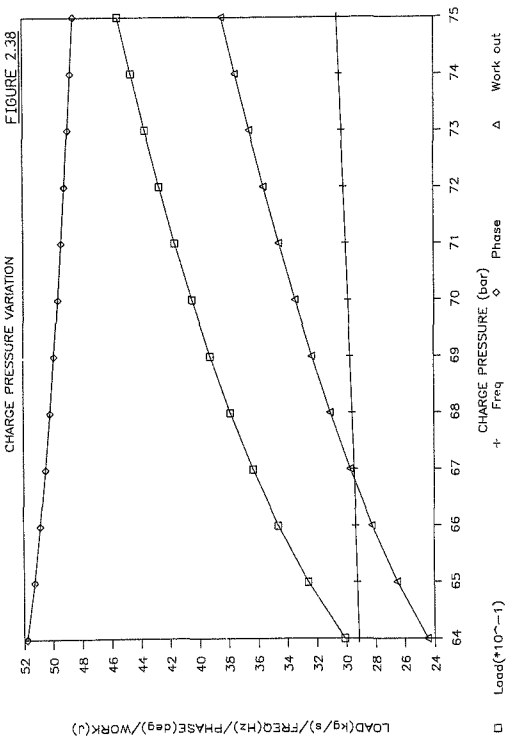
The permissible charge pressures (for which operating states at the given stroke limits exist) may range between 11 and 13 bars as depicted in figures 2.38 and 2.39. The baseline charge pressure falls centrally within this range, indicating that the remaining baseline parameters as a whole have been well-configured to achieve the design performance. In compliance with generic Stirling engine hardware, as the charge pressure is increased, both the indicated and output powers increase while the additional dissipation power decreases. Increasing the charge pressure also increases the stiffness of the equivalent gas springs thus resulting in an expected frequency rise. Figure 2.38 shows that the frequency increases marginally by 1,4 Hz over the charge pressure range plotted. As the charge pressure increases, the phase angle advance decreases by  $3,24$  degrees while both the output work and piston loading coefficient increase monotonically. These characteristics are in harmony with the aforementioned observations.

#### 2.4.3.4 Conclusion

Generally the six parameter variations discussed reveal that the

# RE-1000 FPSE PERFORMANCE

FIGURE 2.38



# RE-1000 FPSE POWER OUTPUT

CHARGE PRESSURE VARIATION

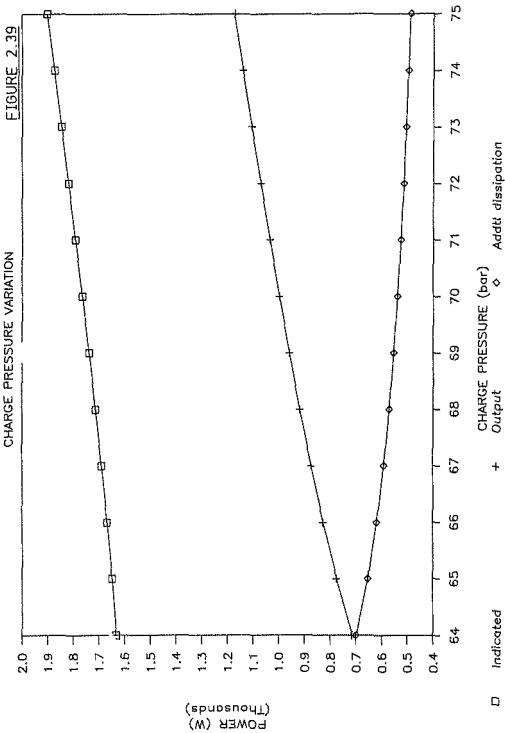


FIGURE 2.39

baseline parameter set describing the RE-1000 FPSE represents an adequate state of optimisation with respect to the design performance specification. Perhaps some additional fine-tuning of the displacer guiding rod diameter and further effort at reducing the fluid dynamic dissipation may be justifiable. When modelling the RE-1000 FPSE using isothermal working spaces, it is evident that the state space analysis inadequately assesses the fluid dynamic irreversibilities which have a significant impact on the overall performance. However, it is worth repeating that this is a restriction imposed by the assumptions made rather than an intrinsic limitation of the state space analysis methodology presented *per se*.

## 2.5 CLOSURE

The derivation of the state space analysis and its application to the back-to-back and RE-1000 free piston Stirling engines establish the validity of the first thesis statement (section 1.3), namely, that 'a parameter space boundary hypersurface is a sufficient and unique characterisation of the combined dynamics and thermodynamics of an FPSE'. The application examples demonstrate the two possible parameter space hypersurfaces that may arise when describing any physically realisable FPSE, namely, one which is located on the stability boundary hypersurface and another, defined as the operating hypersurface, which occurs within the stability boundary. Unambiguous analytic criteria for locating the position of the stability boundary hypersurface and the limiting position of the operating hypersurface are established as well as a means of determining which hypersurface is appropriate for a given FPSE configuration. A comparison of the

state space analytical predictions with experimental performance data for the RE-1000 FPSE demonstrate the numerical validity of the state space analysis and quantify the hypersurface criterion defining self-sustaining FPSE operation. The parameter variations described for the back-co-back and RE-1000 engines exemplify the usefulness of the analysis as a design tool without the limitations imposed by defined piston and displacer motions (which are characteristic of many design analyses presented in the literature).

Given a means of reliably translating fluid dynamic dissipation data into a linearised approximation, the state space analysis shows an overall accuracy of 12% in predicting the combined dynamic/thermodynamic output performance of a representative piece of FPSE hardware, even within the limiting confines of the particular assumptions made. Although the case studies analysed have been restricted to fourth order state spaces, there is no theoretical limit on the order of the state space vector. Hence the introduction of working fluid temperatures and velocities as state variables would enable a much more comprehensive description of the fluid dynamic dissipation to be built into the analysis. Hereby, a considerable refinement in prediction accuracy with respect to the indicated and additional dissipation works and powers would be attainable.

Ultimately, however, the state space methodology, while eminently suitable as a design tool, cannot replace a full fluid dynamic simulation for the purpose of obtaining a complete understanding of the detailed operation of a free-piston Stirling engine. Thus a dual track approach yields an optimum design/analysis mix. The state space methodology may be used to design and optimise a new configuration and

defines the working space geometry and kinematic boundary conditions. These defined boundary conditions make the subsequent use of a full fluid dynamic simulation as cost-effective and productive as possible. Within this context, the remainder of the thesis is devoted to an examination and development of a fluid dynamic analysis of the working spaces of Stirling cycle machinery in general.

## CHAPTER 3

### A CONTINUUM MECHANICS DESCRIPTION OF COMPRESSIBLE FLUID FLOW

#### 3.1 INTRODUCTION

Traditionally, the postulates expressing the conservation of mass, momentum and energy have been inferred from empirical evidence gleaned from macroscopic experiments. In this century, through the dynamic growth of nuclear physics, the proliferation of microscopic experimentation has yielded new perspectives on the physical universe. These perspectives cannot be inferred purely from macroscopic observation. Hence the intuitive formulation of microscopic or differential conservation postulates based on macroscopic observations philosophically seems open to question.

Although extensively used and well-founded in the literature, as typified by standard reference works such as that of Schlichting (Sc79), this approach is not fundamental in the sense that it predicates an intuitive transformation of macroscopic conservation onto the microscopic plane. This process has resulted in considerable argument amongst the Stirling machine research community (Be78, Or82, Sc78, Ta84, Ur77) as to what constitutes the 'correct' set of conservation equations for use in Stirling machine analysis. Semantically, the argument seems to be spurious, since the conservation equations applicable to Stirling machine boundary conditions must be identical to those used for every other set of boundary conditions in the physical universe provided that the

conservation basis is held invariant.

Hence the essence of the formulation of the conservation equations does not reside in the mechanics of symbolism but rather in the definition of a set of postulates which can be experimentally demonstrated to represent the physical universe adequately depending on the scale of observation. This 'postulational' approach is described in Tisza (T166) in his discussion of the evolution of the concepts of thermodynamics. Callen (Ca60) uses this approach to develop the physical theories of equilibrium thermostatics and irreversible thermodynamics. In summarising the efficacy of the postulational approach, Tisza makes the following critical observation:

'First, and most important, we claim no absolute validity for our postulational basis. The validity of the postulates and the usefulness of the primitive concepts are only tentative and have to be justified by the experimental verification of the implications of the theory.'

Thus the postulational approach used to develop a symbolic description of the fluid dynamics of Stirling cycle machines ultimately can be justified only by the extent to which the results produced can be given validity by experimental observation.

### 3.2 THE GENERALISED TRANSPORT EQUATION

The first postulate is based on the classical concept that matter is uniformly distributed through space (R181). Even though this

postulate is known to be unrealistic in terms of the particulate, discontinuous nature of matter, its usefulness lies in the simplicity with which macroscopic phenomena may be described. The following statement of the first postulate is adopted:

Postulate I Matter is continuous and distributed uniformly within an arbitrary bounded space.

This statement is more restrictive than those usually offered (S181, ZH76) since the uniform and continuous distribution of matter is postulated only within a space delineated by boundaries. Thus the unbounded continuity of matter is not included in the definition which admits the existence of discontinuities at the space boundaries. This permits discontinuous physical phenomena such as shock waves and phase change interfaces to be accommodated within the piecewise continuum model postulated. The particular characteristics of a continuum necessary to give quantitative meaning to postulate I are stated in section C.1 of appendix C and may be summarised as follows:

1. A control volume may be used to delineate an arbitrary bounded space such that discontinuities may be completely demarcated by control volume boundaries.
2. Continuity within the control volume is maintained by representing the behaviour of a continuum with smooth functions which may be repeatedly differentiated (ZH76).
3. The physical *appropriateness* of the continuum description is ensured by limiting the largest particle motion considered to be much greater than the molecular mean free path (ZH76).

Having defined a continuum in postulate I, the essential requirement is to describe the temporal variation of intensive properties within the control volume from macroscopically observable external conditions. If, for example, the mass density of a cohesive material body is denoted by  $\rho$ , the total mass of the body may be expressed as:

$$M_{(m)} = \int_V \rho dV \quad (3.1)$$

Thus the rate of change of mass of the body is given by:

$$dM_{(m)}/dt = ddt \int_V \rho dV \quad (3.2)$$

In order to determine how the density of the body varies with time, it is necessary to interchange the differentiation and integration operations on the right hand side of equation (3.2).

The derivation of the equations describing how this process may be performed is presented in appendix C, section C.2. A generalised scalar, vector or tensor quantity  $\psi$  is defined by:

$$\psi = \psi(\mathbf{x}, t) \quad (3.3)$$

The total temporal derivative of the quantity  $\psi$  for a cohesive material body is then denoted by:

$$ddt \int_V \psi dV \quad (3.4)$$

The derivation in section C.2 produces:

$$\frac{d}{dt} \int_{V_{(m)}} \psi dV = \int_{V_{(m)}} (\partial\psi/\partial t) dV + \int_{A_{(m)}} \psi(\mathbf{v} \cdot \mathbf{n}) dA \quad (3.5)$$

Equation (3.5) indicates that the total change of  $\psi$  for the entire material body is a function of the change of  $\psi$  at each fixed point within the body plus the transport of  $\psi$  at the boundaries of the body. This equation, which is known as the 'transport theorem' (S181), places no restrictions on the nature of the body other than that it be regarded as an autonomous entity within a given volume  $V_{(m)}$  and that it have the characteristics of a continuum. In particular, the degree of cohesiveness is arbitrary, implying that equation (3.5) is applicable to a body irrespective of its state, whether it be solid, liquid or gas. Hence the body may be generalised to a system of particles with any cohesiveness. This allows equation (3.5) to be applied if the volume occupied by the system of particles is identical to that of the body and the normal component of the velocity of the particles at the boundary of the system is equal to the normal component of the boundary velocity of the body. Thus:

$$V_{(s)} = V_{(m)}, \quad A_{(s)} = A_{(m)}, \quad \text{and} \quad \mathbf{v}_{(s)} = \mathbf{v} \quad (3.6)$$

Therefore from (3.5) and (3.6):

$$\frac{d}{dt} \int_{V_{(s)}} \psi dV = \int_{V_{(s)}} (\partial\psi/\partial t) dV + \int_{A_{(s)}} \psi(\mathbf{v}_{(s)} \cdot \mathbf{n}) dA \quad (3.7)$$

Equation (3.7) is known as the 'generalised transport theorem' (S181) and, in essence, is the symbolic realisation of the first postulate. The transport theorem of equation (3.5) provides the means by which the macroscopic conservation postulates may first be transformed into their microscopic or differential counterparts. Thereafter, the

generalised transport theorem permits the differential conservation postulates to be applied to a system of particles such as that comprising the working fluid of a Stirling cycle machine.

### 3.3 THE DIFFERENTIAL CONSERVATION EQUATIONS

Three postulates of macroscopic conservation have classically been cited (BS60, Sc79, Sl81), namely those of mass, momentum and energy. On a differential basis, these conservation postulates may be expressed in two ways depending on the observer's frame of reference. In the Lagrangian frame, the observer moves with the body while in the Eulerian frame, the observer remains stationary relative to the fixed stars. A Lagrangian temporal derivative is denoted in terms of equation (3.3) by  $D\psi/Dt$  (usually termed the substantial time derivative (BS60)) while the Eulerian temporal derivative is given by the partial derivative form  $\partial\psi/\partial t$ . As both forms of the differential conservation equations are useful, both are given in the course of the following discussion.

#### 3.3.1 Conservation of Mass

The macroscopic conservation of mass of an arbitrary material body is expressed by the following postulate (Sl81):

Postulate II The mass of an autonomous material body is independent of time.

Symbolically, from equation (3.2), this may be expressed as:

$$d \int_{V(m)} \rho dV = 0 \quad (3.8)$$

Choosing  $\psi = \rho$  in the transport theorem, the following equation describing the differential conservation of mass in a Eulerian frame of reference is derived in section C.3.1 of appendix C:

$$\partial \rho / \partial t = -(\nabla \cdot \rho \mathbf{v}) \quad (3.9)$$

In a Lagrangian frame of reference this becomes:

$$D\rho/Dt = -\rho(\nabla \cdot \mathbf{v}) \quad (3.10)$$

Equations (3.9) and (3.10) describe how the intensive property 'density' varies at every point in a body.

### 3.3.2 Conservation of Momentum

The macroscopic conservation of momentum of an arbitrary material body is expressed by the following postulate which is referred to classically as Euler's first law (S181):

Postulate III The time rate of change of the momentum of an autonomous material body relative to the fixed stars is equal to the sum of the forces acting on the body.

In general, three kinds of forces may act on a material body, namely:

- contact forces on the surface of the body
- external forces resulting from the body being located in a force field (for example, gravitational, electrostatic, or magnetic)

fields)

mutual forces resulting from the interaction between the particles comprising the material body (such as mutual gravitational forces between any two substituent portions of the body).

Thus denoting the contact forces per unit area by  $s$  and the external and mutual forces by  $f$ , postulate III may be symbolically expressed as:

$$d\dot{c} \int_V \rho v dV = \int_{A_{(M)}} s dA + \int_V \rho \hat{f} dV \quad (3.11)$$

In this case, selecting  $\psi = \rho v$  (the momentum per unit volume) in the transport theorem (equation (3.5)), the following Eulerian differential momentum conservation equation is derived in appendix C (section C.3.2):

$$\partial(\rho v)/\partial t + \nabla \cdot (\rho v v) = \nabla \cdot T - \nabla P + \rho \hat{f} \quad (3.12)$$

The first term on the left hand side denotes the temporal variation of the intensive property 'momentum per unit volume', while the second term is a dyadic product which describes the differential advection of momentum. The first and second terms on the right hand side represent the contact forces resultant from the shear stresses and thermodynamic pressure respectively, while the last term describes the mutual and external forces at each point in the body.

In the derivation of equation (3.12), the sign convention adopted for determining the extra shear stress tensor  $T$  is such that  $T$  represents the stress acting at any point within a material body. Thus invoking

Stokes hypothesis (Sc79), the extra shear stress for a Newtonian fluid may be expressed in terms of the deformation tensor D as (S181):

$$T = 2\mu D - (2\mu\nabla \cdot \mathbf{v}/3)\mathbf{I} \quad (3.13.1)$$

where:

$$D = 0.5(\nabla\mathbf{v} + (\nabla\mathbf{v})^T) \quad (3.13.2)$$

In the case of gaseous fluids, equation (3.13.1) may be modified to include the 'bulk viscosity' (BS60) as follows:

$$T = 2\mu D + \{(\lambda - 2\mu/3)(\nabla \cdot \mathbf{v})\}\mathbf{I} \quad (3.14)$$

A manipulation of equation (3.12) described in section C.3.2 results in the Lagrangian form:

$$\rho D\mathbf{v}/Dt = \nabla \cdot T - \nabla P + \rho \mathbf{f} \quad (3.15)$$

It may be noted that the right hand sides of equations (3.12) and (3.15) are identical while the left hand side is reduced to the substantive derivative of velocity only. This is consistent with the notion that, in a Lagrangian system, an observer moving with the particle velocity will not perceive any advection of momentum.

### 3.3.3 Conservation of Energy

The conservation of energy postulate for a material body is not as clearly defined in the literature as is the case for mass and momentum. Most authors (Ca60, Sc79, Wa77, ZH26) adopt the first law of thermodynamics as their postulational basis, namely (ZH76):

$$d(\text{total stored energy}) = \delta Q + \delta W$$

(3.16)

In the context of this work, equation (3.16) is not specific enough for a macroscopic material body since, in particular, the nature of  $W$  (the work done), which is usually considered in thermodynamic terms, is not precisely stated. Furthermore, the meaning of 'total stored energy' is also imprecise in a postulational sense since there may exist forms of energy as yet unobserved which do not obey equation (3.16). Thus the following formulation advocated by Slattery (S181) for the macroscopic conservation of energy of an arbitrary material body is preferred:

Postulate IV The time rate of change of the internal and kinetic energy of an autonomous material body relative to the fixed stars is the sum of the rate at which forces acting on the body do work on the body and the rate of energy transmission to the body.

In this context, the internal energy  $U$  is defined in equilibrium thermodynamic terms using the postulational relationship  $U = U(E, V, \Gamma_i)$  (Ca60) where  $\Gamma_i$  represents the mole numbers of the  $i$  chemical species constituting the material body.

The forces acting on the body are the contact, external and mutual forces described for postulate III (section 3.3.2) while the energy transmission to the body has three similar components, namely:

- contact energy transmission through the bounding surface of the body

- external energy transmission (such as that arising from radiation)
- mutual energy transmission resulting from an exchange of energy between any two portions of a material body (such as that caused by mutual radiation).

Thus denoting the contact energy transmission rate per unit area by  $\dot{q}$  and the external and mutual energy transmission rate by  $\dot{E}$ , postulate IV may be expressed symbolically as:

$$\frac{d}{dt} \int_V \rho (\hat{U} + v^2/2) \dots \mathbf{v} \cdot \mathbf{s} dA + \int_V \rho (\mathbf{v} \cdot \hat{\mathbf{E}}) dV + \int_{A_{(M)}} \dot{q} dA + \int_V \rho \hat{E} dV \quad (3.17)$$

The first and second terms on the right hand side represent the work done by the corresponding force terms in equation (3.11).

It may be noted that the intensive conservative property on the left hand side of equation (3.17) is the sum of the internal specific energy  $\hat{U}$  and the kinetic energy per unit mass  $v^2/2$ . The conservation of potential energy is included in the interaction of the first two integrals on the right hand side of equation (3.17) to produce a change in  $(\hat{U} + v^2/2)$ . This is demonstrated in section C.3.3 (appendix C) for the particular case of gravitational potential energy. Under these conditions, the mutual and external force per unit mass term  $\hat{\mathbf{f}}$  may be split into two components such that the forces arising from a gravitational field are accounted for separately. Hence defining the gravitational potential energy per unit mass as a conservative field  $\hat{T}$ ,  $\hat{\mathbf{f}}$  may be expressed as:

$$\hat{\mathbf{f}} = \hat{\mathbf{F}}^* - \nabla \hat{T} \quad (3.18)$$

This allows equation (3.17) to take the form:

$$d d t \int_V \rho (\hat{U} + v^2/2 + \hat{T}) dV = \int_{A_{(M)}} (\mathbf{v} \cdot \mathbf{s}) dA + \int_V \rho (\mathbf{v} \cdot \hat{\mathbf{F}}^a) dV + \int_{A_{(M)}} \dot{q} dA + \int_V \rho \hat{\mathbf{E}} dV \quad (3.19)$$

Thus equation (3.17) implicitly includes the conservation of gravitational potential energy and, by extension, that arising from any other conservative force field.

Choosing the internal plus kinetic energy per unit volume as the transport property by setting  $\psi = \rho(\hat{U} + v^2/2)$  in the transport theorem (equation (3.5)), the following Lagrangian differential energy conservation equation is derived in appendix C (section C.3.3):

$$\rho D(\hat{U} + v^2/2)/Dt - \rho[(\mathbf{v} \cdot \hat{\mathbf{E}}) + \nabla \cdot (\mathbf{T} \cdot \mathbf{v}) - \nabla \cdot (P\mathbf{v}) - \nabla \cdot \dot{q}] \quad (3.20)$$

This equation describes the differential conservation of thermal and mechanical energy. It may be simplified by observing that the differential conservation of mechanical energy may be determined separately using postulate III. Forming the scalar product of equation (3.15) with  $\mathbf{v}$  yields the differential conservation of mechanical energy equation in a Lagrangian frame of reference (section C.3.2):

$$\rho D(v^2/2)/Dt - \nabla \cdot (\mathbf{T} \cdot \mathbf{v}) - (\mathbf{T} : \nabla \mathbf{v}) - (\mathbf{v} \cdot \nabla P) + \rho(\mathbf{v} \cdot \hat{\mathbf{E}}) \quad (3.21)$$

The second term on the right hand side is a tensor scalar product which represents the irreversible conversion of mechanical energy into thermal energy, or dissipation. Subtracting equation (3.21) from equation (3.20) results in the Lagrangian differential conservation of thermal energy equation:

$$\rho \hat{D}\hat{U}/D\tau = \rho \hat{E} + (\mathbf{T}:\nabla\mathbf{v}) - P(\nabla\cdot\mathbf{v}) - \nabla\cdot\hat{q} \quad (3.22)$$

In Eulerian terms, this becomes:

$$\partial(\rho\hat{U})/\partial\tau + \nabla\cdot(\rho\hat{U}\mathbf{v}) = \rho\hat{E} + (\mathbf{T}:\nabla\mathbf{v}) - P(\nabla\cdot\mathbf{v}) - \nabla\cdot\hat{q} \quad (3.23)$$

Equations (3.15) and (3.22) contain the same information in terms of intensive properties as contained by equation (3.20). Thus a conservative differential equation system consisting of equations (3.15) and (3.20) contains a redundancy which is absent from a combination of equations (3.15) and (3.22) and their Eulerian counterparts. Although either equation set is admissible, and both sets must ultimately yield identical results, in this work the former set (equations (3.15) and (3.22), or equations (3.12) and (3.23)) is preferred because of the convenience it affords in describing Stirling machine fluid dynamics.

#### 3.4 THE INTEGRAL BALANCES

The generalised transport theorem of equation (3.7) allows the differential conservation balances to be applied to a system of particles. The resulting integral balances expressing the conservation of mass, momentum and energy for such a system are produced in total temporal derivative form. This formulation is frame indifferent such that the equations may be applied to Eulerian, Lagrangian or combined Eulerian/Lagrangian frames of reference. This frame indifference is demonstrated for each of the integral balances by describing both the Lagrangian and Eulerian forms. These forms are particular cases of the generalised integral balances which correspond

to the combined Eulerian/Lagrangian form. In all cases, the details of the integral balance derivations may be found in section C.4 of appendix C.

### 3.4.1 Conservation of Mass

Identifying the mass per unit volume as the transport property (that is,  $\psi = \rho$ ) in the generalised transport theorem (equation (3.7)) and replacing  $\partial\rho/\partial t$  with equation (3.9) results in:

$$dM_{(S)}/dt = \int_{A_{(S)}} \rho [(\mathbf{v} - \mathbf{v}_{(S)}) \cdot \mathbf{n}] dA \quad (3.24)$$

In this generalised or combined Eulerian/Lagrangian form, the rate of change of mass of a system of particles is equal to the net advection of mass across the boundaries of the system. It should be noted that the advection velocity is the relative velocity between the particles and the boundary itself.

In a Eulerian frame of reference  $\mathbf{v}_{(S)} = 0$ , hence equation (3.24) becomes:

$$dM_{(S)}/dt = \int_{A_{(S)}} (\rho \mathbf{v} \cdot \mathbf{n}) dA \quad (3.25)$$

However, in a Lagrangian frame of reference  $\mathbf{v} = \mathbf{v}_{(S)}$ , which transforms equation (3.24) into:

$$dM_{(S)}/dt = 0 \quad (3.26)$$

Although equation (3.24) has been rigorously derived, it is interesting to note that some authors of Stirling machine analysis have used the particular case of equation (3.25) directly as the postulational basis (Be78, Ur77). This approach is justifiable even though it potentially complicates experimental validation of the relevant equations by introducing additional assumptions at a fundamental level.

### 3.4.2 Conservation of Momentum

Defining the momentum per unit volume ( $\psi = \rho v$ ) as the transport property in equation (3.7) and replacing  $\partial(\rho v)/\partial t$  with equation (3.12) yields the generalised or combined Eulerian/Lagrangian form:

$$\begin{aligned} d(\int_{(V)} \bar{v}H_{(S)})/dt = & \int_{A_{(S)}} \rho v(v - v_{(S)}) \cdot n dA - \int_{A_{(S)}} PndA - \int_{A_{(S)}} (T \cdot n) dA \\ & + \int_{V_{(S)}} \rho \hat{x} dV \end{aligned} \quad (3.27)$$

Thus the rate of change of momentum of a system of particles is equal to the net advection of momentum across the boundaries of the system relative to the system boundary velocity plus the contact, mutual and external forces acting on the system.

In a Eulerian frame of reference  $v_{(S)} = 0$ , which transforms equation (3.25) into:

$$d(\int_{(V)} \bar{v}H_{(S)})/dt = \int_{A_{(S)}} \rho v(v \cdot n) dA - \int_{A_{(S)}} PndA - \int_{A_{(S)}} (T \cdot n) dA + \int_{V_{(S)}} \rho \hat{x} dV \quad (3.28)$$

In a Lagrangian frame of reference  $\mathbf{v} = \mathbf{v}_{(S)}$ , thus equation (3.26) allows equation (3.27) to be expressed as:

$$N_{(S)} \frac{d}{dt} \bar{\mathbf{v}} / dt = - \int_{A_{(S)}} F n dA - \int_{A_{(S)}} (\mathbf{T} \cdot \mathbf{n}) dA + \int_{V_{(S)}} \rho \bar{\mathbf{E}} dV \quad (3.29)$$

In contrast with the approach presented here, equation (3.27) has been used directly in the guise of equation (3.28) as a postulational basis by other Stirling machine analysts (6e78, 6c78).

### 3.4.3 Conservation of Energy

Choosing the internal energy per unit volume as the transport property in the generalised transport theorem (that is,  $\psi = \rho \hat{U}$  in equation (3.7)) and substituting equation (3.23) for  $\delta(\rho \hat{U})/\delta t$  results in the combined Eulerian/Lagrangian formulation:

$$\begin{aligned} d(\int_{(V)} \bar{\rho} \hat{U}_{(S)} / dt) = & \int_{A_{(S)}} (\rho \bar{\mathbf{E}} + (\mathbf{T} \cdot \nabla \mathbf{v}) + (\nabla \cdot \mathbf{T}) \mathbf{P}) dV + \int_{A_{(S)}} (\dot{q} \cdot \mathbf{n}) dA \\ & + \int_{A_{(S)}} \rho \hat{H} ((\mathbf{v} - \mathbf{v}_{(S)}) \cdot \mathbf{n}) dA - \int_{A_{(S)}} \mathbf{P}(\mathbf{v}_{(S)} \cdot \mathbf{n}) dA \end{aligned} \quad (3.30)$$

Thus the rate of change of internal energy of a system of particles is equal to the sum of six components, which in left to right sequence may be described as:

1. the rate of mutual and external energy transmission to the system
2. the rate of irreversible conversion of mechanical into thermal energy within the boundaries of the system

3. the Gibbs free energy and isentropic heat generation rate (Wa77) within the boundaries of the system
4. the net rate of contact energy transmission across the boundaries of the system
5. the net advection of enthalpy across the boundaries of the system relative to the boundary velocity
6. the net rate at which mechanical work is done at the boundaries of the system

Equating  $\nabla_{(S)}$  with zero yields the Eulerian version of equation (3.31):

$$d_{(V)} \bar{U}_{(S)} / dt = \int_{A_{(S)}} \{ \rho \dot{E} + (T:\nabla v) + (v \cdot \nabla P) \} dV + \int_{A_{(S)}} (\dot{q} \cdot n) dA + \int_{A_{(S)}} \rho \dot{H} (v \cdot n) dA \quad (3.31)$$

Since  $\nabla_{(S)} = 0$ , equation (3.31) indicates that in an exclusively Eulerian system with fixed boundaries no mechanical work is done by the system of particles. In contrast, for a Lagrangian system  $\nabla = \nabla_{(S)}$ , which, after invoking equation (3.26), yields:

$$M_{(S)} d_{(V)} \bar{U} / dt = \int_{A_{(S)}} \{ \rho \dot{E} + (T:\nabla v) + (v \cdot \nabla P) \} dV + \int_{A_{(S)}} (\dot{q} \cdot n) dA - \int_{A_{(S)}} P (\nabla_{(S)} \cdot n) dA \quad (3.32)$$

Thus in this frame of reference, the only mode of mechanical energy transmission between adjacent systems of particles is via the action

of mechanical work at the interface between systems.

### 3.5 TURBULENT FLOW INTEGRAL BALANCES

The integral balances of equations (3.24), (3.27) and (3.30) are strictly applicable in the limit as  $\Delta t \rightarrow 0$  (H175). However, when the balances are applied to systems in which  $\Delta t$  is finite, then the balances are precise only for laminar flow conditions. Under turbulent flow conditions, the transport properties may experience random fluctuations with periods less than  $\Delta t$  thus invalidating the instantaneous constancy of the temporal gradients implied by the equations as derived. This limitation is minimized for  $\Delta t \ll \Delta t^*$  where  $\Delta t^*$  is the period of the highest frequency perturbation, as illustrated by figure 3.1 for a generic quantity  $\psi$  defined by equation (3.3).

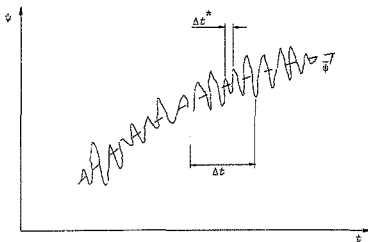


Figure 3.1 Turbulent flow profile

The instantaneous value of  $\psi$  may be represented as the sum of a time-averaged component and a fluctuating component (Sc79):

$$\psi = \bar{\psi} + \psi' \quad (3.33)$$

In terms of the thesis statement, attention is focussed on directly obtaining the time-averaged quantities  $\bar{\psi}$ . This treatment should not be construed as a limitation of the continuum analysis presented but simply a restriction imposed by the scope of this thesis.

The most general approach to obtaining the time-averaged or turbulent energy balances is to perform the averaging process on the integral balances directly (S181). This admits fluctuating control volume geometries such as those occurring in combined Eulerian/Lagrangian systems with non-rigid boundaries. The method used to time-average the integral flow balances (equations (3.24), (3.27) and (3.30)) is described in appendix C (section C.5) and results in the following relationships.

Mass:

$$\frac{d\bar{M}}{dt} = \int_{A_{(S)}} \rho (\mathbf{v} \cdot \mathbf{n}) dA \quad (3.34)$$

Momentum:

$$\begin{aligned} \frac{d(\bar{M} \bar{\mathbf{v}})}{dt} = & \int_{A_{(S)}} \rho \mathbf{v} (\mathbf{v} \cdot \mathbf{n}) dA \cdot \int_{A_{(S)}} \mathbf{P} n dA - \int_{A_{(S)}} (\mathbf{T} \cdot \mathbf{n}) dA \\ & - \int_V \rho \hat{\mathbf{I}} dV \end{aligned} \quad (3.35)$$

Energy:

$$\begin{aligned}
 \frac{d}{dt} \int_{V(s)} \hat{U} dV &= \int_{V(s)} (\rho \hat{E} + (\mathbf{T} : \nabla \mathbf{v}) + (\mathbf{v} \cdot \nabla P)) dV + \int_{A(s)} (\hat{q} \cdot \mathbf{n}) dA \\
 &+ \int_{A(s)} \rho \hat{H} ((\mathbf{v} - \mathbf{v}(s)) \cdot \mathbf{n}) dA - \int_{A(s)} P (\mathbf{v}(s) \cdot \mathbf{n}) dA
 \end{aligned} \tag{3.36}$$

Equations (3.34), (3.35) and (3.36) are by definition also applicable under laminar flow conditions since, from equation (3.33),  $\psi = \bar{\psi}$  when  $\psi' = 0$ .

### 3.6 CLOSURE

In order to implement the integral conservation balances for gaseous fluids such as air, helium and hydrogen which are commonly used as Stirling machine working fluids, an equation of state is required. The equation of state for an ideal gas has the form:

$$PV = nRT \tag{3.37}$$

In keeping with the established practice for Stirling machine analysis (Scl871, Wa73) the ideal gas equation of state is used here. Nevertheless, there are no *intrinsic* restrictions placed on the form of the equation of state; other equations describing the behaviour of real gases, such as that of Redlich and Kwong (RK49), may be used. Generally these equations are significantly more complex than equation (3.37) and are thus not as convenient to use numerically, mainly because of the difficulty in establishing fiduciary pressures and densities at absolute zero (Ca60).

Equations (3.34) through (3.37) thus provide an analytic basis in terms of the continuum model for determining the time-averaged working fluid behaviour of Stirling cycle machines. The equation set is generally applicable to combined Eulerian/Lagrangian, Eulerian or Lagrangian frames of reference in one, two or three dimensions employing arbitrary coordinate systems.

## CHAPTER 4

### THE DISCRETE SIMULATION MODEL

#### 4.1 INTRODUCTION

An examination of the generalised form of the time-averaged integral balances developed in chapter 3 reveals that the equations may not be solved directly using numerical methods for two principal reasons. In the first instance, the time-averaging is performed over groups or ensembles of parameters so that the equations are not expressed in terms of individual time-averaged parameters. The time-averaged ensembles may only be converted into groups of individual time-averaged components with knowledge of the temporal fluctuations of each component. However, as derived, the integral balances are explicitly devoid of any features permitting the determination of the fluctuating transport property components.

Secondly, the total derivative of each of the transport properties defined by the integral balances of mass, momentum and energy is expressed strictly in volume-averaged terms. However, these derivatives are determined by expressions composed of parameters which, in general, are not volume-averaged. In other words, the left and right hand sides of the integral balances are not consistent with respect to volume-averaging. This arises since the rigorous derivation of the integral balances has the consequence that, by definition, the spatial variation of intensive parameters such as density and temperature within any control volume is not described explicitly. Hence, the volume-averaging inconsistency precludes any

literal application of the integral balances as derived.

These impediments are resolved by the postulation of a turbulence model and a volumetric spatial discretisation scheme, respectively. In the following development, the generalised integral balances are cast into numerically soluble form by describing -- then applying the turbulence model and spatial discretisation scheme successively.

#### 4.2 THE TURBULENCE MODEL

As has been stated, a principal difficulty in solving the time-averaged integral balances is the unavailability of the fluctuating components of the transport properties. One of the main thrusts of current fluid dynamics research is to develop numerical and other methodologies for determining or simulating these fluctuating components. In a numerical context, these methodologies have been termed 'higher-level' simulations for turbulent flows by Ferziger (Fe83). He classifies these simulations into two categories, namely, 'large eddy' and 'full' simulations. In a large eddy simulation, the differential conservation balances are averaged over a small volume so that an equation for the large eddies of the turbulent field is derived. Since the small eddies are not explicitly simulated their effect on the large eddies is accounted for by invoking empirical or theoretical correlations. A full simulation attempts to solve the differential conservation balances directly using time-steps small enough so as to track the turbulent fluctuations. However, as Ferziger notes, this approach is limited to low Reynolds numbers in view of its inherently severe computing requirements.

Both of these higher-level simulation approaches are beyond the scope of this thesis which, by stipulation, is limited to determining time-averaged behaviour only. Consequently, the analytic approach adopted for dealing with turbulence falls into the category of 'Reynolds averaged equations' (Fe83). In this context, since the integral balances derived include both time- and volume-averaging, Ferziger makes the following observation:

'... The equations describing the mean field contain averages of products of fluctuating velocities and there are fewer equations than unknowns - the well-known closure problem. In fact, the set of equations can never be closed by further averaging; a closure assumption, or what is the same thing, a turbulence model, has to be introduced. The closure assumption must represent the unknown higher-order average quantities in terms of the lower-order quantities that are computed explicitly.'

The difficulties inherent in developing turbulence models for compressible fluid flow may be attested to by the preponderance of research performed for incompressible fluid flow (Hi75). The usual approach to such modelling is to develop correlation equations which are parametric in particular flow properties and then fit the equations to experimental data. One of the most common correlation equations is the double velocity correlation which may be described in terms of figure 4.1.

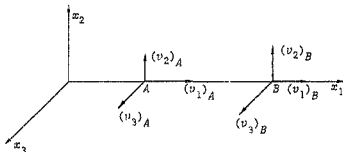


Figure 4.1 Double velocity correlation

The correlation tensor  $Q$  is given by:

$$Q_{A,B} = \overline{v_A' v_B'} \quad (4.1)$$

This correlation has been extensively analysed for spatially homogeneous (the same quantitative turbulence structure in all parts of the flow) and isotropic (no statistical preference for any particular flow direction) incompressible turbulent flow fields. With this as background, Hinze (Hi75) makes the following comment with regard to compressible turbulent flows:

'Now for the incompressible case it was already impossible to obtain complete solutions of the dynamic equations for the double correlation  $(v_i')_A (v_j')_B$ . Needless to say, it will be hopeless for the compressible case.'

Furthermore, the experimental correlations developed have been for relatively simple flow geometries and boundary conditions (Fe83, Hi75, LS72, Sc79). None of these cases appears to be equivalent to the complex geometrical interstices of Stirling cycle machines with oscillating velocity boundary conditions.

These observations crystallize into the central difficulty inherent in the numerical simulation of Stirling cycle machines, namely, that despite their superficial simplicity, Stirling machines have fluid dynamic boundary conditions which elevate a completely rigorous treatment to a plane beyond that of current practical capabilities. This difficulty has not really been given full cognisance in previous numerical analyses of Stirling cycle machines (Be78, Or82, Sc78, Ur77) since the underlying assumptions regarding turbulence necessary to make these analyses tractable are not explicitly stated.

In this work, the minimum set of assumptions constituting a turbulence model which enables the time-averaged solution of the integral balances developed to be achieved is clearly stated. The turbulence model adopted is defined by the following restrictions:

Restriction I

The turbulent flow field is stationary such that:

$$\Delta t_{\text{turbulence characteristic}} \ll \Delta t_{\text{analytical time increment}} \quad (4.2)$$

Restriction II

The turbulent flow field is spatially homogeneous such that:

$$\Delta V_{\text{turbulence characteristic}} \ll \Delta V_{\text{control volume}} \quad (4.3)$$

These observations crystallize into the central difficulty inherent in the numerical simulation of Stirling cycle machines, namely, that despite their superficial simplicity, Stirling machines have fluid dynamic boundary conditions which elevate a completely rigorous treatment to a plane beyond that of current practical capabilities. This difficulty has not really been given full cognisance in previous numerical analyses of Stirling cycle machines (Be78, Or82, Sc78, Ur77) since the underlying assumptions regarding turbulence necessary to make these analyses tractable are not explicitly stated.

In this work, the minimum set of assumptions constituting a turbulence model which enables the time-averaged solution of the integral balances developed to be achieved is clearly stated. The turbulence model adopted is defined by the following restrictions:

Restriction I

The turbulent flow field is stationary such that:

$$\Delta t_{\text{turbulence characteristic}} \ll \Delta t_{\text{analytical time increment}} \quad (4.2)$$

Restriction II

The turbulent flow field is spatially homogeneous such that:

$$\Delta V_{\text{turbulence characteristic}} \ll \Delta V_{\text{control volume}} \quad (4.3)$$

Restriction III

The ergodic hypothesis (H175)<sup>1</sup> is valid for scalar turbulent fields.

Restriction IV

The effect on the mean flow resultant from vector turbulent fields may be modelled.

Restriction V

The control volume boundaries do not experience temporal fluctuations.

Rigorously, equations (4.2) and (4.3) are conflicting conditions for any turbulent flow. This arises since if a turbulent flow field is homogeneous then it is simultaneously a decaying flow field. However, if it is also stationary then the dissipation in the field can only be balanced by a non-homogeneity in order to maintain the decaying characteristic. The following rationale offered by Hinze (H175) for proceeding with the stationary, homogeneous flow field model is adopted here.

... Fortunately, the rate of decay of the mean properties is rather slow with respect to the time scale of the smaller eddies. Therefore, the actual state of non-stationarity is considered not to be a serious drawback in the experimental study of the smaller scale turbulence. For the theoretical study, this makes it possible to apply the concepts and theories of stationary random

---

<sup>1</sup>The ergodic hypothesis states that for a stationary and homogeneous turbulence:

$$\langle \psi^* \rangle = \bar{\psi}^* = \langle \text{ensemble} \rangle \bar{\psi}^*$$

where  $\psi^*$  represents a scalar or a component of a vector. The ensemble average is the average over a number of identical experiments for the same boundary conditions.

processes.'

Thus if the turbulent field is stationary and homogeneous then by the assumed validity of the ergodic hypothesis for any scalar turbulent field property:

$$\langle v \rangle \bar{\psi}_{scalar} = \bar{\psi}_{scalar} \quad (4.4)$$

or, the volume-average of any scalar property is equal to the time-average of that property. But, by definition (equation (3.35)), a time average has no fluctuating component, that is:

$$\bar{\psi}'_{scalar} = 0$$

Hence by equation (4.4), a volume average also has no temporally fluctuating components, or:

$$\langle v \rangle \bar{\psi}'_{scalar} = 0 \quad (4.5)$$

Hence in particular for density and temperature:

$$\langle v \rangle \bar{\rho}' = 0 \quad (4.6.1)$$

$$\langle v \rangle \bar{T}' = 0 \quad (4.6.2)$$

Equations (4.6) constitute two of the explicit restrictions of the turbulence model described in section D.1 of appendix D while equation (4.2) represents a third. Since the ergodic hypothesis is applied to scalar properties only, non-zero temporal fluctuations of vector properties are permitted. Thus, in particular, the velocity field need not necessarily be both stationary and homogeneous. The effects of the velocity fluctuation on the time-averaged flow field properties are, by assumption, included via modelling using empirical

correlations.

The final restriction of the turbulence model may be expressed symbolically as:

$$A'_{(S)} = 0 \quad (4.7.1)$$

which in turn implies that the magnitude of the control volume does not fluctuate, or:

$$V'_{(S)} = 0 \quad (4.7.2)$$

Thus by equation (3.35):

$$A_{(S)} = \bar{A}_{(S)} \quad (4.8.1)$$

$$V_{(S)} = \bar{V}_{(S)} \quad (4.8.2)$$

Equations (4.8) have the further consequence that the unit outward normal does not fluctuate which leads to the result:

$$\bar{\psi} \cdot \bar{n} = \bar{\psi} \cdot \bar{n} \quad (4.8.3)$$

Equations (4.7) and their implications do not place a restriction on the Lagrangian condition  $\mathbf{v} = \mathbf{v}_{(S)}$  as suggested by the generalised transport theorem given by equation (3.7). Under turbulent conditions, this is achieved by setting  $\mathbf{v}_{(S)} = \bar{\mathbf{v}}$  and admitting a turbulent flux as a function of  $\mathbf{v} - \mathbf{v}_{(S)}$  (which is equal to  $\mathbf{v}'$ ) across the Lagrangian boundary. In effect this converts a turbulent Lagrangian boundary into a combined Eulerian/Lagrangian boundary. In the context of Stirling cycle machine numerical analysis, a spatial discretisation scheme may be devised without any loss of convenience such that the case for which  $\mathbf{v}'_{(S)} \neq 0$  does not arise. Thus

equations (4.7) and (4.8) do not result in any further assumption for the particular class of problems being considered.

In applying the turbulence model, it is necessary to introduce the concept of a second order time average or, the time average of a time average. Thus from equation (3.33) and the definition of a time average given by equation (C.52) in appendix C, a second order time average may be formed as follows:

$$\bar{\bar{\psi}} = (1/\Delta t) \int_c^{c+\Delta t} \left[ (1/\Delta t) \int_c^{c+\Delta t} \psi dt' \right] dt \quad (4.9)$$

From the derivation detailed in section D.1 of appendix D it is shown that because equation (4.2) holds by assumption such that:

$$\Delta t_{\text{turbulence characteristic}} / \Delta t_{\text{analytical time increment}} \ll 1$$

then:

$$\bar{\bar{\psi}} = \bar{\psi} \quad (4.10)$$

Hence as a lemma to equation (4.2), the exactness of equation (4.10) is taken to be the sixth restriction of the turbulence model, namely:

Restriction VI

The stationarity of the turbulent flow field is sufficient for the equality of the first and second order time averages, or:

$$\bar{\bar{\psi}} = \bar{\psi} \quad (4.11)$$

Thus by taking the time average of equation (3.33) it immediately follows that:

$$\overline{\bar{\psi}'} = 0 \quad (4.12)$$

The six restrictions of the turbulence model cited are sufficient to reduce the generalised turbulence integral balances to a form in which they are amenable to numerical solution without explicit knowledge of the fluctuating components of the transport properties.

#### 4.3 APPLICATION OF THE TURBULENCE MODEL

The details of the application of the turbulence model to the equation of state (3.37) and the resultant thermodynamics of the working fluid are described in section D.2 of appendix D. Similarly, the reduction of the time-averaged integral balances of equations (3.34) to (3.36) is detailed in section D.3.

##### 4.3.1 Thermodynamics of the Working Fluid

As stated, the equation of state (3.37) is applicable to a finite mass of gas  $M_{(s)}$  occupying a given volume  $V_{(s)}$ . Hence expressing equation (3.37) in volume-averaged terms results in:

$$\overline{p}_{(v)} = \overline{\rho}_{(v)} \overline{R}_{(v)} \overline{T}$$

Taking the time average and applying equation (4.6.1) results in the form:

$$\overline{p}_{(t,v)} = \overline{\rho}_{(t,v)} \overline{R}_{(t,v)} \overline{T} \quad (4.13)$$

Equation (4.13) is often stated in non-volume-averaged form as a necessary assumption in order to solve the compressible turbulent flow

equation set (Sc79), even though, as shown, it is a consequence of the turbulence model adopted.

Equation (4.13) may be expressed in terms of second order time averages and time-averaged fluctuating components using equation (3.33). In this form, equations (4.6), (4.11) and (4.12) may be used to show that:

$$\overline{[v] \dot{P}'} = 0 \quad (4.14)$$

which is intuitively expected.

In terms of the characteristics of an ideal gas, the internal energy and enthalpy are functions of temperature only such that they disappear at absolute zero (Ca60, Wa77). Thus if the specific heats are taken as being constant, the volume-averaged internal energy is described by:

$$\overline{[v] \hat{U}} = \hat{C}_V \overline{[v] \hat{T}} \quad (4.15)$$

while the specific enthalpy takes the form:

$$\hat{H} = \hat{C}_P \hat{T} \quad (4.16)$$

These latter two equations enable the integral energy balance to be expressed in terms of temperature which may then be used as a primary variable.

#### 4.3.2 The Reduced Turbulent Integral Mass Balance

At this stage it is convenient to introduce the mass flux  $g$  into the analysis. This simplifies the numerical solution of the equation set by eliminating the necessity of determining density transport at the control volume boundaries. The mass flux is formed from the product of density and velocity, or:

$$g = \rho v \quad (4.17)$$

Applying equations (4.8) (which result from restriction V) to the mass balance of equation (3.34) and substituting equation (4.17) results in:

$$\frac{d\bar{M}_{(s)}}{dt} = \int_{\bar{A}_{(s)}} \{(\bar{g} - \bar{\rho v}_{(s)}) \cdot n\} dA \quad (4.18)$$

The Eulerian and Lagrangian forms of (4.18) follow the same pattern as those of equation (3.24). It may be noted that, from equation (4.17),  $\bar{g} = \bar{\rho v}_{(s)}$  under Lagrangian conditions. This must be true in any case since, by equations (3.26) and (3.33):

$$dM_{(s)}/dt = 0 \quad \rightarrow \quad d\bar{M}_{(s)}/dt = 0$$

In a combined Eulerian/Lagrangian application, the further reduction of  $\bar{\rho v}_{(s)}$  may be achieved by an appropriate choice of spatial discretisation scheme as described in section 4.5.

#### 4.3.3 The Reduced Turbulent Integral Momentum Balance

Applying equations (4.8) to the right hand side of equation (3.33) and

using equations (4.17) and (4.7.2) respectively to reconstitute and reduce the left hand side yields:

$$d(\overline{\mathbf{g}} \cdot \overline{\mathbf{v}}_{(S)})/dt = \int_{\overline{A}_{(S)}} \{(\overline{\mathbf{g}}\mathbf{v} - \overline{\mathbf{g}}\mathbf{v}_{(S)}) \cdot \mathbf{n}\} d\overline{A} - \int_{\overline{A}_{(S)}} \overline{F}nd\overline{A} - \int_{\overline{A}_{(S)}} (\overline{\mathbf{T}} \cdot \mathbf{n}) d\overline{A} + \int_{\overline{V}_{(S)}} \overline{\rho} \overline{\mathbf{f}} d\overline{V} \quad (4.19)$$

In terms of restriction IV, the effect of the fluctuating velocity field on the time-averaged turbulent field is modelled. This may be achieved by defining the Reynolds stress tensor for a combined Eulerian/Lagrangian field. This definition is a generalisation of the Reynolds stress tensor definition for incompressible Eulerian flow fields usually quoted in the literature (Sc79, Fe83) and is given by:

$$\mathbf{T}^{(t)} = (\overline{\mathbf{g}} \cdot \overline{\mathbf{v}} - \overline{\mathbf{g}} \cdot \overline{\mathbf{v}}_{(S)}) - (\overline{\mathbf{g}}\mathbf{v} - \overline{\mathbf{g}}\mathbf{v}_{(S)}) \quad (4.20)$$

which by invoking equations (4.11) and (4.12) has the functional form:

$$\mathbf{T}^{(t)} = \overline{f(\rho' \mathbf{v}' \mathbf{v}', \rho' \mathbf{v}' \mathbf{v}'_{(S)})} \quad (4.21)$$

The formulation of a correlation equation useful for expressing  $\mathbf{T}^{(t)}$  in terms of  $\overline{\rho}$ ,  $\overline{\mathbf{v}}$  and  $\overline{\mathbf{v}}_{(S)}$  is dependent upon the spatial discretisation scheme adopted in a similar manner to that required for the further reduction of equation (4.18).

Substituting equation (4.20) into (4.19) and collecting terms results in the combined Eulerian/Lagrangian form:

$$d(\overline{v}_j \overline{g} \overline{V}_{(s)})/dt = \int_{\overline{A}_{(s)}} \overline{g} \{ (\overline{v} \cdot \overline{v}_{(s)}) \cdot \mathbf{n} \} d\overline{A} - \int_{\overline{A}_{(s)}} \overline{P} n d\overline{A} \\ - \int_{\overline{A}_{(s)}} \{ (\overline{T} + \overline{T}^{(t)}) \cdot \mathbf{n} \} d\overline{A} + \int_{\overline{V}_{(s)}} \overline{\rho} \overline{E} d\overline{V} \quad (4.22)$$

The Eulerian and Lagrangian forms are similar to those for equation (3.27) with the exception that under Lagrangian conditions, as noted in the discussion of equations (4.7),  $\overline{T}^{(t)}$  does not disappear but takes the form:

$$\overline{T}^{(t)} = -\overline{g} \overline{v}^i \quad (4.23.1)$$

since:

$$\overline{\mathbf{v}}_{(s)} = \mathbf{v} - \mathbf{v}^i \quad (4.23.2)$$

#### 4.3.4 The Reduced Turbulent Integral Energy Balance

Expressing  $\overline{U}$  and  $\overline{H}$  in terms of temperature using equations (4.15) and (4.16) and then applying equation (4.17) and the restrictions of the turbulence model enables equation (3.36) to be reduced to the form:

$$\hat{C}_V d(\overline{v}_j \overline{T} \overline{H}_{(s)})/dt = \int_{\overline{V}_{(s)}} \overline{\rho} \overline{E} + (\overline{T} \cdot \overline{\nabla} \overline{v}) + (\overline{v} \cdot \overline{\nabla} \overline{P}) d\overline{V} + \int_{\overline{A}_{(s)}} (\overline{q} \cdot \mathbf{n}) d\overline{A} \\ + \hat{C}_P \int_{\overline{A}_{(s)}} \{ (\overline{g} \overline{T} - \overline{\rho} \overline{T} \overline{v}_{(s)}) \cdot \mathbf{n} \} d\overline{A} - \int_{\overline{A}_{(s)}} (\overline{P} \overline{\mathbf{v}}_{(s)} \cdot \mathbf{n}) d\overline{A} \quad (4.24)$$

The effect of the fluctuating velocity field on the enthalpy transport is determined by modelling as permitted by restriction IV. In this context, it is important to note that equation (4.6.2) cannot be used

to simplify the time-averaged enthalpy transport given by the third integral on the right hand side of equation (4.24) since the enthalpy transport is not expressed in volume-averaged terms. Thus a generalised turbulent energy flux vector applicable to a combined Eulerian/Lagrangian system may be defined analogously to the Reynolds stress tensor. Likewise, this generalised definition is based upon a definition for a Eulerian field commonly cited in the literature (Sc79, S181) and is given by:

$$q^{(t)} = \hat{C}_p \{ (\overline{gT} - \overline{\rho v_{(s)} T}) - (\overline{g} \overline{T} - \overline{\rho v_{(s)} \overline{T}}) \} \quad (4.25)$$

By equations (4.11) and (4.12), the turbulent flux vector has the functional relationship:

$$q^{(t)} = \hat{E}(\hat{C}_p, \overline{\rho' v' T'}, \overline{\rho' v' \overline{T}'}) \quad (4.26)$$

The development of a suitable correlation equation using  $\tilde{\rho}$ ,  $\tilde{v}$ ,  $\tilde{v}_{(s)}$  and  $\tilde{T}$  is dependent on the spatial discretisation scheme adopted as noted previously.

Substituting (4.25) into (4.24) and collecting terms produces the combined Eulerian/Lagrangian form:

$$\begin{aligned} \hat{C}_p d_{(t,v)} \overline{T} \overline{H}_{(s)} / dt = & \int_{V_{(s)}} \{ \rho \dot{E} + (\overline{T} \cdot \overline{\nabla v}) + (\overline{v} \cdot \overline{\nabla P}) \} dV + \int_{\hat{A}_{(s)}} \{ (\hat{q} + q^{(t)}) \cdot \mathbf{n} \} d\hat{A} \\ & - \int_{\hat{A}_{(s)}} \{ \overline{P v}_{(s)} \cdot \mathbf{n} \} d\hat{A} + \hat{C}_p \int_{\hat{A}_{(s)}} \{ \overline{T} (\overline{g} - \overline{\rho v}_{(s)}) \cdot \mathbf{n} \} d\hat{A} \quad (4.27) \end{aligned}$$

The Eulerian and Lagrangian forms of equation (4.27) are similar to equations (3.31) and (3.32) respectively. The latter form is achieved by noting that, as for equation (4.18), under Lagrangian conditions the last integral on the right hand side of equation (4.27) disappears

because  $\bar{g} = \bar{g}_{(s)}$ . However,  $q^{(b)}$  does not vanish under Lagrangian conditions since by equation (4.23.2) it takes the form:

$$q^{(b)} = \hat{C}_p (\overline{\rho v' T} - \overline{\rho v'} \bar{T}) \quad (4.28)$$

Thus the application of the turbulence model eliminates the need for explicit knowledge of the fluctuating components of the turbulent field. The influence of those fluctuating components required to describe the time-averaged turbulent field is included in the form of empirical correlations which use time-averaged quantities as independent variables.

#### 4.4 THE SPATIAL DISCRETISATION SCHEME

In his comprehensive review of computational fluid mechanics, Roache (Ro82) describes a variety of spatial and temporal discretisation schemes for the numerical application of the differential conservation balances. Generally, these schemes fall into two categories which may be loosely termed 'coincident' and 'staggered' mesh systems respectively. Furthermore, the mesh systems may be applied both spatially and temporally thus yielding a multiplicity of schemes involving combinations of coincident and staggered mesh systems.

In a coincident mesh scheme, the three differential transport properties, namely, density, velocity and temperature, are evaluated at the same time and/or at the same spatial location. However, in a spatially staggered mesh, generally the density and temperature are computed at one set of grid points while the velocities are computed at an offset grid point mesh as shown in figure 4.2 for a particular

two-dimensional case.

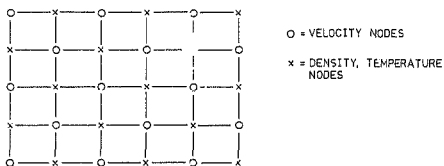


Figure 4.2 Spatially staggered two-dimensional grid

In a temporally staggered mesh, the velocity is computed at a half time step offset from the density and temperature. A realisation of this scheme is shown for a one-dimensional spatially coincident mesh in figure 4.3 and for a spatially staggered mesh in figure 4.4.

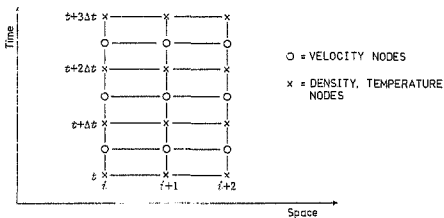


Figure 4.3 Temporally staggered, spatially coincident one-dimensional grid

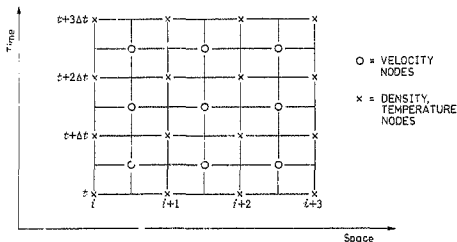


Figure 4.4 Temporally and spatially staggered one-dimensional grid

In recent years, particularly with the advent of commercial general purpose fluid dynamics computer programmes, a tangible consensus appears to have emerged that spatially staggered, temporally coincident discretisation schemes are convenient and useful for fluid flow modelling (Fe83, Pa80). Roache seems to infer that the first use of a version of the spatially staggered mesh may be attributed to Harlow and Fromm (HF64), although its apparent reinvention over the intervening two decades is an attestation of its efficacy.

In the field of Stirling machine analysis, Urieli (Ur77) applied the temporally coincident, spatially staggered grid to a generically simple machine geometry. Schock, by contrast, used a temporally and spatially coincident grid and introduced the concept of volumetrically weighted averages for computing flow rates between grid points (Sc78). Both of these discretisation schemes involve the application of the differential conservation balances in a one-dimensional Eulerian frame of reference.

Although the spatial discretisation scheme used in this work contains elements employed by Urieli and Schock, it has its origins in the mesh structure used in the 'Marker And Cell' (MAC) method of Harlow and Welch (HW65). In particular, the general precepts of a temporally coincident, spatially staggered numerical discretisation scheme suitable for the application of the differential conservation balances are applied to the time-averaged integral balances described in section 4.3. This application admits a three-dimensional space in a combined Eulerian/Lagrangian frame of reference.

#### 4.4.1 The Staggered Control Volume Spatial Discretisation Scheme

As the mass, momentum and energy integral balances are fundamentally based upon the concept of a control volume, the spatial discretisation scheme naturally devolves to partitioning a given space into an assemblage of finite volumes with coincident boundaries. All the intensive parameters are thus expressed in volume-averaged terms so that, by definition, the value of any intensive parameter at a point within a control volume is unknown. The essence of the spatial discretisation scheme involves a method of constructing the control volume grid so that, within any control volume, scalar intensive parameters are assigned a position and vector intensive parameters are assigned a plane respectively. This introduces the concept of a 'volumetric filter' which may be defined for a scalar field as a control volume surrounding a point such that the value of a scalar intensive parameter at that point represents the volume average over the filtered space. Similarly, for a vector field, the volumetric

filter is a region of space split by a plane such that the value of a vector intensive parameter over that plane represents the volume average over the filtered space normalised with respect to the area of the plane. Hence every point or plane in the spatial domain may be associated respectively with a unique scalar or vector volumetrically filtered intensive parameter so that the variation of the volumetrically filtered parameters is spatially continuous.

The methodology employed to construct the spatial discretisation is an adaptation of the staggered grid construction used by Harlow and Welch in the MAC method. The characteristics of the scheme may be illustrated for the sake of clarity by a two-dimensional, Eulerian space using a Cartesian coordinate system as shown in figure 4.5.

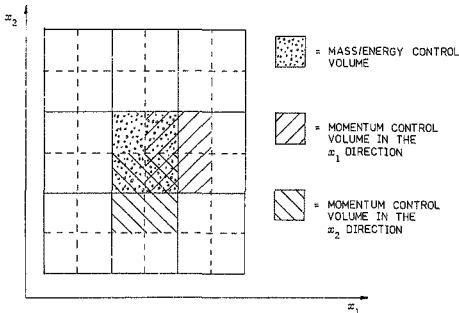


Figure 4.5 Spatial discretisation scheme characteristics

The mass and energy integral balances are applied to a common control volume while the momentum balance is applied to a control volume which is offset horizontally or vertically from the mass/energy control volume depending on the coordinate direction. In this arrangement, the integral momentum balance is split into its vector components so that each component balance is applied to a unique offset control volume. As indicated by the double cross-hatched area in figure 4.5, the net momentum over any volume may be determined by vector addition of the momentum components determined individually for that volume. The net vector momentum field for the entire spatial domain may thus be determined from its vector component fields which are explicitly produced by applying the staggered control volume discretisation methodology. It may also be observed that the volume-averaged intensive parameters corresponding to the mass/energy volumetric filter, namely, density and temperature, are located at a point defined by the intersection of the dashed lines within a mass/energy control volume. However, the volume-averaged intensive parameters corresponding to the momentum volumetric filter, namely, the velocity or mass flux components, are located on the planes bounding the mass/energy control volumes. This latter condition mandates that in a generalised coordinate system where the planar area of a momentum component control volume is non-uniform, the mass/energy control volume boundary areas must be used as the normalisation basis for the volume-averaged values produced by the momentum integral balance.

Generalising these concepts to a three-dimensional space with an arbitrary coordinate system, the characteristics of the staggered control volume grid may be expressed symbolically by denoting the mass/energy control volume as  $V_{(s)}$  and any momentum component control

volume as  $V_{n(s)}$ . Then considering any adjacent mass/energy control volumes  $V_{(s)i}$  and  $V_{(s)i+1}$  in a particular coordinate direction, the following attributes may be defined for the control volume grid.

Attribute I

A momentum control volume straddles every mass/energy control volume boundary and has a magnitude equal to half that of the sum of the adjacent mass/energy control volumes. Symbolically, this may be expressed as:

$$V_{(s)} \cap V_{n(s)} = V_{(s)}/2 \quad (4.29.1)$$

$$V_{(s)i}/2 \cup V_{(s)i+1}/2 = V_{n(s)} \quad (4.29.2)$$

Attribute II

The volume-averaged intensive parameters corresponding to a mass/energy control volume are located at its 'centroid' which is positioned at the intersection of the boundaries of all the surrounding momentum control volumes. Thus  ${}_{(v)}\bar{\psi}$  is located at the centroid so that for each coordinate direction:

$$\int_{-a}^0 \text{Andx} = \int_0^a \text{Andx} \quad (4.29.3)$$

where  $a$  is the location of the centroid.

Attribute III

The volume-averaged intensive parameters corresponding to a momentum control volume are located on the plane separating adjacent mass/energy control volumes. Therefore  ${}_{(v_n)}\bar{\psi}$  is determined by:

$$\int_{V_{n(s)}} \psi dV = \int_{0,5V_{(s)l}} \psi dV + \int_{0,5V_{(s)l+1}} \psi dV \quad (4.29.4)$$

The adjacent mass/energy control volumes may be of arbitrary magnitude, or:

$$V_{(s)l} / V_{(s)l+1} = \alpha \geq 0 \quad (4.29.5)$$

where  $V_{(s)l+1}$  is taken to be non-zero for the sake of reference.

Equation (4.29.3) implies that in the case of a one-dimensional coordinate system, the centroid is defined by a plane separating two adjacent momentum control volumes. In a two-dimensional system, the centroid becomes a line perpendicular to the coordinate surface while only in three dimensions does the centroid become a point.

The concept of the volumetric filter as expressed by the attributes of the spatial discretisation scheme enables all the non-volume-averaged boundary terms in the reduced integral balances to be replaced with volume-averaged terms. The staggered grid arrangement permits the boundary mass fluxes required for the mass and energy balances to be computed explicitly while simultaneously ensuring that the pressures driving the rate of change of momentum are located correctly. Hence the attributes of the discretisation scheme are sufficient to enable the numerical solution of the reduced equation set developed in section 4.3.

#### 4.5 APPLICATION OF THE REDUCED INTEGRAL BALANCES

A detailed description of the manner in which the attributes of the spatial discretisation scheme (equations (4.29)) are used to apply the reduced integral balances of equations (4.18), (4.22) and (4.27) is expounded in appendix D in sections D.4.1 to D.4.3. The following discussion summarises and elucidates the salient features of the application methodology.

##### 4.5.1 Application of the Reduced Integral Mass Balance

Applying attribute III to equation (4.18) and invoking the restrictions of the turbulence model to reduce the time-averaged product term results in the combined Eulerian/Lagrangian form:

$$\frac{d\bar{M}_{(s)}}{dt} = \int_{A_{n(s)}} \{ (\bar{v}_n)_s \bar{\rho} - (\bar{v}_n)_s \bar{\rho} \bar{v}_{n(s)} \} \cdot \bar{n} d\bar{A} \quad (4.30)$$

where the subscript  $n$  denotes that the relevant parameters are associated with the momentum control volume. The Eulerian and Lagrangian forms of equation (4.30) follow the same pattern as those for equation (4.18). In particular, it may be noted that under Lagrangian conditions:

$$(\bar{v}_n)_s \bar{\rho} = (\bar{v}_n)_s \bar{\rho}_{(s)} \quad (4.31.1)$$

since, by definition, the mass/energy control volume boundary velocity is the same as that of the momentum control volume straddling that boundary, or:

$$\bar{v}_{n(s)} = (\bar{v}_n)_s \quad (4.31.2)$$

The transient density field may be extracted from the temporally integrated mass field by applying restriction V of the turbulence model (equation (4.7.2)) which results in:

$${}_{(tV)}\bar{\rho} = \bar{N}_{(s)}/\bar{V}_{(s)} \quad (4.32)$$

Further, by attribute III of the discretisation scheme, the momentum control volume density is given for a pair of adjacent mass/energy control volumes  $i$  and  $i+1$  by:

$${}_{(tV_n)}\bar{p} = (\bar{N}_{(s)i} + \bar{N}_{(s)i+1})/2\bar{V}_{n(s)} \quad (4.33)$$

#### 4.5.2 Application of the Reduced Integral Momentum Balance

The shear stress tensor  $T$  given by equation (3.14) may be expressed in time- and volume-averaged form with respect to a mass/energy control volume by applying the kinetic theory of gases to the commonly used working fluids for Stirling cycle machines, namely, helium, hydrogen and air. Thus in terms of the Sutherland molecular model (Sc79), the viscosity may be expressed as a function of temperature only, or  $\mu = \mu(T)$ . Similarly, Hirschfelder *et al* (HC54) show that, from the kinetic theory of dilute gases, the bulk viscosity is also a function of temperature, or  $\Lambda = \Lambda(T)$ . Hence substituting equation (3.13.2) into (3.14), taking the volume and time averages and simplifying the result by an invocation of the turbulence model restrictions yields:

$${}_{(tV)}\bar{T} = {}_{(tV)}\bar{\mu}(\nabla_{(tV)}\bar{v}) + (\nabla_{(tV)}\bar{v})^T + \{({}_{(tV)}\bar{\Lambda} - 2{}_{(tV)}\bar{\mu}/3)(\nabla_{(tV)}\bar{v})\}I \quad (4.34)$$

In considering the analysis of the fluid dynamics of Stirling cycle machines, the only mutual and external forces operating are those resulting from the influence of an external gravitational field. In most cases (other than the use of Stirling machines in outer space) the gravitational field is constant for a particular location. Hence, considering a terrestrial location for the sake of specificity (although any arbitrary constant gravitational acceleration is acceptable), the mutual and external forces per unit mass are given by:

$$\hat{\mathbf{f}} = -\mathbf{g} \quad (4.35)$$

Applying attributes I and II of the spatial discretisation scheme to equation (4.22) and substituting equations (4.34) and (4.35) produces the combined Eulerian/Lagrangian form:

$$\begin{aligned} d(\langle \mathbf{t}_{(S)} \rangle \bar{\mathbf{v}}_{n(S)})/dt &= \int_{\bar{A}_{(S)}} \langle \mathbf{t}_{(S)} \rangle \bar{\mathbf{g}}(\langle \mathbf{t}_{(S)} \rangle \bar{\mathbf{v}} \cdot \bar{\mathbf{v}}_{(S)}) \cdot \mathbf{n} d\bar{A} - \int_{\bar{A}_{(S)}} \bar{\mathbf{p}} n d\bar{A} \\ &- \int_{\bar{A}_{(S)}} \langle \mathbf{t}_{(S)} \rangle \bar{\mathbf{T}}^{(2)} \cdot \mathbf{n} d\bar{A} - \bar{\mathbf{h}}_{n(S)} \bar{\mathbf{g}} \\ &- \int_{\bar{A}_{(S)}} \left[ \langle \mathbf{t}_{(S)} \rangle \bar{\mu} (\nabla_{(S)} \bar{\mathbf{v}} + (\nabla_{(S)} \bar{\mathbf{v}})^T) \right. \\ &\left. + (\langle \mathbf{t}_{(S)} \rangle \bar{\lambda} - 2 \langle \mathbf{t}_{(S)} \rangle \bar{\mu} / 3) (\nabla_{(S)} \bar{\mathbf{v}}) \cdot \mathbf{I} \right] \cdot \mathbf{n} d\bar{A} \quad (4.36) \end{aligned}$$

It may be noted that  $\bar{\mathbf{v}}_{(S)}$  is not expressed as a volume average since it represents the motion of the planar boundary separating adjacent momentum control volumes. The Eulerian and Lagrangian forms of equation (4.36) follow the prescription for those of equation (4.22). In particular, under Lagrangian conditions, the Reynolds stress tensor is given by:

$$\overline{[v] \mathbf{T}^{(t)}} = - \overline{[v] \mathbf{S}_{[v]} \overline{\mathbf{v}}'} \quad (4.36.1)$$

since under these conditions the boundary velocity is equal to the time-averaged velocity across the boundary, or:

$$\overline{\mathbf{v}}_{(s)} = \overline{[v] \overline{\mathbf{v}}'} \\ = \overline{[v]} \overline{\mathbf{v}} = \overline{[v]} \overline{\mathbf{v}}' \quad (4.36.2)$$

#### 4.5.3 Application of the Reduced Integral Energy Balance

The application of the reduced integral energy balance of equation (4.27) to the staggered grid requires a greater amount of manipulation than was necessary for the mass and momentum balances. In particular, those terms which are expressed as volume integrands are not readily apparent. Following an argument similar to that used to produce equation (4.34), the time- and volume-averaged dissipation term may be reduced to the following form after application of the turbulence model restrictions:

$$\overline{[v] \langle \mathbf{T} : \nabla \mathbf{v} \rangle} = \overline{[v] \bar{\Lambda}} - 2 \overline{[v] \bar{\mu} / 3} \left\{ \sum_i \overline{(\partial_{[v]} \overline{v}_i / \partial x_i)^2} \right\} - 2 \sum_i \overline{[v] \bar{\mu}} \overline{(\partial_{[v]} \overline{v}_i / \partial x_i)^2} \\ + \sum_i \sum_j \overline{[v] \bar{\mu}} \overline{(\partial_{[v]} \overline{v}_i / \partial x_j + \partial_{[v]} \overline{v}_j / \partial x_i)^2} \quad (4.37)$$

where  $i$  and  $j$  represent coordinate direction indices.

Further simplification of this expression requires the definition of a dissipation tensor similar in nature to the Reynolds stress tensor. Generally, equation (4.37) is approximated using an empirical correlation (Sc79) owing to the complexities involved in establishing

a formal correlation in the form of equation (4.1) for Stirling machine boundary conditions. Thus it is convenient to define a dissipation term  $\phi$  such that:

$$\langle_{(tV)} \bar{\phi} = \langle_{(tV)} \overline{(\mathbf{x}:\nabla\mathbf{v})} \quad (4.38)$$

The volume integral of the  $(\mathbf{v}\cdot\nabla P)$  term is reduced by applying the turbulence model restrictions to its volume average so resulting in:

$$\langle_{(tV)} \overline{(\mathbf{v}\cdot\nabla P)} = \langle_{(tV)} \overline{\mathbf{v}\cdot\nabla} \langle_{(tV)} \bar{P} \rangle \quad (4.39)$$

The pressure gradient in equation (4.39) is expressed in terms of the staggered grid by a finite difference approximation between the centroids of adjacent mass/energy control volumes. This results in a pair of finite difference pressure gradients occurring for each coordinate direction in a mass/energy control volume, a situation requiring a careful numerical interpretation.

The numerical evaluation of equation (4.38) may be accomplished directly in two or three dimensions using time and volume averages. However, in a one-dimensional system, which necessarily requires an empirical correlation to account for significant three-dimensional dissipation effects, the physical significance and numerical application of this equation becomes problematic. An interpretation of the equation which has been demonstrated numerically to yield a successful solution is described in chapter 5.

The boundary time-averaged heat flux term may be evaluated in the context of the staggered grid spatial discretisation scheme by invoking Fourier's law of thermal conduction (S181). After

appropriate volume- and time-averaging, this process produces:

$$\langle \bar{q} \rangle_{(tV_n)} = - \langle \bar{K} \bar{\nabla} \rangle_{(tV_n)} \bar{T} \quad (4.40)$$

As for equation (4.39), the temperature gradient centered over the momentum control volumes is determined by a finite difference approximation between the centroids of the constituent mass/energy control volumes. In this case, the approximation is natural since the temperature gradient is single-valued over each momentum control volume. However, the boundary thermal conductivity  $\langle \bar{K} \rangle_{(tV_n)}$  is determined using a weighting procedure involving the conductivities of the adjacent mass energy control volumes as discussed in section 4.6.3.

The final issue arising in the application of the discretisation scheme involves the determination of the mechanical work done at the boundaries of a mass/energy control volume. As this term does not represent the flux of a transport property, the pressure acting on each side of a boundary is the volume-averaged pressure (in discretised terms) associated with the mass/energy control volume in the direction of the unit inward normal ( $-\mathbf{n}$ ) for that side. Thus after invoking the restrictions of the turbulence model, the mechanical work rate  $\dot{W}$  for a discretised mass/energy control volume may be expressed as:

$$\dot{W} = \int_{\bar{A}_{(S)}} \bar{P} \langle \bar{\nabla} \rangle_{(tV)} \cdot \mathbf{n} d\bar{A}$$

But since the volume-averaged pressure is constant over the control volume boundaries:

$$\dot{W} = \langle_{(tV)} \bar{P} \int_{\bar{A}_{(S)}} (\bar{v}_{n(S)} \cdot \bar{n}) d\bar{A} \quad (4.41)$$

Applying the generalised transport theorem of equation (3.7) with  $\phi = 1$ , time-averaging and invoking equations (4.7) gives:

$$d\bar{V}_{(S)}/dt = \int_{\bar{A}_{(S)}} (\bar{v}_{n(S)} \cdot \bar{n}) d\bar{A}$$

or in discretised terms for a mass/energy control volume:

$$d\bar{V}_{(S)}/dt = \int_{\bar{A}_{n(S,i)}} (\bar{v}_{n(S,i)} \cdot \bar{n}) d\bar{A}$$

Hence substituting into equation (4.41) results in:

$$\dot{W} = \langle_{(tV)} \bar{P} d\bar{V}_{(S)}/dt \quad (4.42)$$

which represents the classical equilibrium thermodynamics expression for the rate of performing mechanical work (Ca60, Wa77).

In the light of the above discussion, attribute III of the spatial discretisation scheme may be applied to equation (4.27) to produce the final combined Eulerian/Lagrangian form:

$$\begin{aligned} \hat{C}_V d(\langle_{(tV)} \bar{T} \bar{H}_{(S)} \rangle) / dt = & \bar{V}_{(S)} \langle_{(tV)} \bar{\rho} \bar{E} + \langle_{(tV)} \bar{\Phi} + \langle_{(tV)} \bar{\nabla} \cdot \langle_{(tV)} \bar{P} \rangle - \langle_{(tV)} \bar{P} d\bar{V}_{(S)}/dt \\ & - \int_{\bar{A}_{n(S)}} \langle_{(tV_n)} \bar{\kappa} (\bar{\nabla}_{(tV_n)} \bar{T} \cdot \bar{n}) d\bar{A} - \int_{\bar{A}_{n(S)}} \langle_{(tV_n)} \bar{q}^{(t)} \cdot \bar{n} \rangle d\bar{A} \\ & + \hat{C}_P \int_{\bar{A}_{n(S)}} \langle_{(tV_n)} \bar{T} (\langle_{(tV_n)} \bar{B} - \langle_{(tV_n)} \bar{\rho} \bar{\nabla}_{n(S)} \rangle \cdot \bar{n}) d\bar{A} \quad (4.43) \end{aligned}$$

The Eulerian and Lagrangian forms of this equation are similar to those of equation (4.27). In particular, under Lagrangian conditions, the advection flux term (the last term on the right hand side) disappears as a consequence of the argument expressed by equation (4.31). The turbulent flux vector then takes the form:

$$\langle v_n \rangle q^{(t)} = \hat{C}_P \left( \overline{\overline{\rho_{(v_n)} \nabla' \cdot (v_n) T}} - \overline{\overline{\rho_{(v_n)} \nabla' \cdot (v_n) T}} \right) \quad (4.44)$$

Thus the staggered grid, volumetrically filtered discretisation scheme enables all the parameters in the reduced integral balances to be expressed in volume-averaged terms. This makes the equations consistent with respect to volume- and time-averaging so permitting their numerical solution without the intrusion of implicit or hidden closure assumptions.

#### 4.6 THE IMPLICIT CONTROL VOLUME BOUNDARY TERMS

In order to implement equations (4.36) and (4.43) numerically, expressions for determining the control volume boundary terms which are not explicitly available must be found. For the momentum control volume these terms are  $\langle v_n \rangle \bar{g}$ ,  $\langle v_n \rangle \bar{\nabla}$  and  $\nabla \langle v_n \rangle \bar{\nabla}$ , while for the mass/energy control volume the only additional unknown term is  $\langle v_n \rangle \bar{T}$ . Furthermore, the determination of the advective term in the momentum equation is not obvious since the mass flux  $\langle v_n \rangle \bar{g}$  is a transport parameter which must be normalised with respect to the momentum control volume area across which the averaged flux  $\langle v_n \rangle \bar{g}$  flows.

These unknown terms may be found conveniently by splitting the analysis into three sections. The first section deals with the mass flux and velocity gradient within a mass/energy control volume, while the second section describes the mass flux advected across the momentum control volume boundaries. The third section develops a formulation for determining the advected temperature on the mass/energy control volume boundaries.

#### 4.6.1 Mass/Energy Control Volume Mass Flux and Velocity Gradient

The details of the analysis for determining the mass flux and velocity gradient in the mass/energy control volume are given in appendix D, section D.5. The analysis is initiated by noting that, since volume is distributive over density, the rate of change of density may be split arbitrarily into three substituents such that each substituent may be associated with a boundary mass flux vector component. Thus for the three coordinate directions  $j$ , from equation (4.30):

$$\begin{aligned} d\bar{v}_{(s)}/dt &= \sum_{j=1}^3 d(\rho_{(s)} \bar{v}_{(s)})/dt \\ &= \sum_{j=1}^3 \int_{\bar{A}_{n(s),j}} \{ (\rho_{(s)} \bar{v}_{(s)}) \cdot \bar{n} \} \cdot \bar{n} d\bar{A} \end{aligned} \quad (4.45)$$

Consider a generalised, combined Eulerian/Lagrangian mass/energy control volume in any coordinate direction  $j$  as shown in figure 4.6. Let the control volume be split into left and right hand components by a plane of area  $A$  moving with velocity  $v_{(s)}$  at a displacement  $x$  from the arbitrary defined boundary entrance plane. A mass flux  $g$  with velocity  $v$  flows across the bifurcating plane. The entrance boundary

area  $A_{nL}$  is Lagrangian and consists of a piston moving with a velocity  $v_{n(s)}$  while the exit boundary is Eulerian with an area  $A_{nR}$  across which flows a mass flux  $g_{nR}$ . The control volume has a length  $\Delta l$  such that the centroid of the control volume occurs at  $\Delta l_{(sV)}$ .

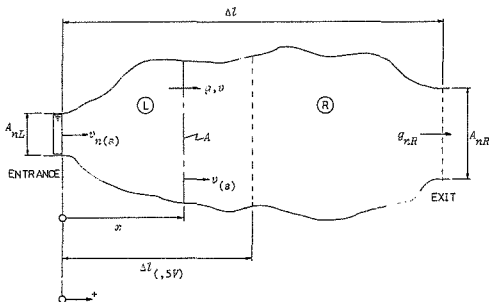


Figure 4.6 One-dimensional mass/energy control volume

By equation (4.32), the time- and volume-averaged density is single-valued over the entire control volume which is spatially fixed. Thus, dropping the overbar and  $j$  subscript notation for the sake of simplicity:

$$\rho_L = \rho_R = \rho \quad (4.46.1)$$

which results in:

$$d\rho_L/dt = d\rho_R/dt \quad (4.46.2)$$

Applying equation (4.45) in single coordinate direction form to the left and right hand components of figure 4.6 separately, rearranging the resultant expressions to isolate the temporal derivatives of the total density, substituting into equation (4.46.2) and simplifying produces:

$$(\rho v_{n(s)} A_{nL} - Ag)/V_L = (Ag - g_{nR} A_{nR})/V_R$$

Expressing the left and right hand averages in terms of length-averaged areas results in:

$$g = \{_{(1)} \bar{A}_R (\Delta l - x) \rho v_{n(s)} A_{nL} + \{_{(1)} \bar{A}_L x g_{nR} A_{nR}\} / AV_{(s)} \quad (4.47)$$

From equation (4.17) it can be shown (see the development of equation (D.56)) that:

$$_{(1, v)} \bar{g} = \{_{(1, v)} \bar{v}\} \bar{v} \quad (4.48)$$

which allows the velocity across plane A to be given from (4.47) by:

$$v = \{_{(1)} \bar{A}_R (\Delta l - x) \rho v_{n(s)} A_{nL} + \{_{(1)} \bar{A}_L x g_{nR} A_{nR}\} / AV_{(s)} \rho \quad (4.49)$$

Differentiating with respect to x gives the velocity gradient:

$$\partial v / \partial x = \{_{(1)} \bar{A}_L g_{nR} A_{nR} - \{_{(1)} \bar{A}_R \rho v_{n(s)} A_{nL}\} / AV_{(s)} \rho \quad (4.50)$$

In conformity with the attributes of the volumetric filter, the velocity gradient is constant over the control volume while the averaged velocity and mass flux at any plane within the control volume is displacement dependent.

At the control volume centroid defined in terms of attribute II (equation (4.29.3)) by  $V_L = V_R$ , the mass/energy control volume velocity and velocity gradient may be expressed in full notation for each

coordinate direction  $i$  from equations (4.49) and (4.50) by:

$${}_{(tV)}\bar{v}_i = ({}_{(tV_n)}\bar{\rho}_i \bar{v}_{n(s)} \bar{A}_{n(s)} i + {}_{(tV_n)}\bar{g}_{i+1} \bar{A}_{n(s)} i + 1) / 2 {}_{(tV)}\bar{\rho} \bar{A}_{(s)} \quad (4.51.1)$$

$$\begin{aligned} (\delta_{{}_{(tV)}} \bar{v} / \delta x)_i &= ({}_{(tV_n)}\bar{g}_{i+1} \bar{A}_{n(s)} i + 1) / \Delta l_{(s)} V_i \\ &\quad - ({}_{(tV_n)}\bar{\rho}_i \bar{v}_{n(s)} \bar{A}_{n(s)} i) / (\Delta l_{(s)} V_i) / 2 {}_{(tV)}\bar{\rho} \bar{A}_{(s)} \end{aligned} \quad (4.51.2)$$

where  $i$  and  $i+1$  represent adjacent momentum control volumes in the  $i$ th coordinate direction.

Furthermore, it is shown in section D.5 that the velocity of the centroid is given by:

$$\bar{v}_{(s)} i = \bar{v}_{n(s)} i \bar{A}_{n(s)} i / 2 \bar{A}_{(s)} \quad (4.52)$$

In the case of a fully Eulerian control volume  $v_{(s)} i = 0$  and equations (4.51) are applicable with the following alteration:

$${}_{(tV_n)}\bar{\rho}_i \bar{v}_{n(s)} i \rightarrow ({}_{(tV_n)}\bar{g}_i \quad (4.53)$$

#### 4.6.2 The Boundary Advection of Momentum

In the light of the attributes of the staggered grid discretisation scheme and, in particular, the area normalisation requirement for the averaged momentum, the interpretation of the momentum advection term in equation (4.36) is not self-evident. Superficially, it might be concluded that equations such as (4.47) and (4.49) for  ${}_{(tV)}\bar{g}$  and  ${}_{(tV)}\bar{v}$  may be used to determine completely the boundary advection of momentum. However, such an approach is not transportive in nature and therefore violates the physical meaning of the generalised transport theorem. Roache (Ro82) discusses the importance of maintaining the

transportive property in numerical terms and demonstrates that under certain conditions, failure to ensure transportivity results in numerical instability. In the context of Stirling machine analysis, these difficulties were encountered by Urieli who overcame them by using the well known 'upwind differencing method' for determining the boundary momentum flux (CI52). However, this method is only first order accurate (Ro82) and is justified by an *a posteriori* numerical stability analysis.

The approach adopted here is based on a methodology developed by Spalding and Patankar (Pa80) in which the momentum balance is reduced to a steady-state, one-dimensional Eulerian form amenable to analytic solution. The solution thus obtained (the details of which may be found in section D.6 of appendix D) is used as the basis for determining the discretised nature of the boundary momentum advection.

Following the methodology used to develop equation (4.36), by applying equation (4.22) to a mass/energy control volume and ignoring mutual and external forces and turbulent momentum fluxes, the momentum balance may be expressed as:

$$d(\langle \bar{v} \rangle_{(S)})/dt = \int_{\bar{A}_{(S)}} \langle \bar{v} \rangle_{(S)} \bar{v} \cdot \bar{n} d\bar{A} - \int_{\bar{A}_{(S)}} \langle \bar{v} \rangle_{(S)} \bar{T} \cdot \bar{n} d\bar{A} \quad (4.54)$$

Consider a Eulerian mass/energy control volume in any coordinate direction  $i$  as shown in figure 4.7. Let the control volume have a length  $\Delta l$  and an entrance area  $A$  across which there is a diffusion  $r$  and a mass flux  $g$  with velocity  $v$ . At the exit plane, the area, diffusion, mass flux and velocity are incrementally larger than their corresponding terms at the entrance plane by  $\Delta A$ ,  $\Delta r$ ,  $\Delta g$  and  $\Delta v$

respectively.

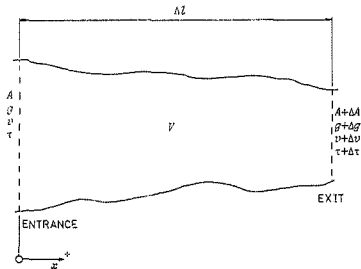


Figure 4.7 One-dimensional, Eulerian mass/energy control volume

Expressing the volume in terms of a length-averaged area and substituting the entrance and exit plane boundary conditions into equation (4.54) in one-dimensional form results in the following expression (which is simplified by dropping the time average overbar notation):

$$d(\int_{(1)} \bar{A} g \Delta l) / dt = (g v \cdot r) A - [(g + \Delta g)(v + \Delta v) - (r + \Delta r)(A + \Delta A)] \quad (4.55)$$

Applying equation (D.49) in one dimension to the boundary conditions of figure 4.7 results in an expression for  $d\rho/dt$ . Thus using equation (4.48) to decompose the mass flux  $g$  on the left hand side of equation (4.55) into velocity and density components allows a simplifying substitution for  $d\rho/dt$ . After ignoring second and third order of smallness terms, this produces:

$$\int_{(1)} \bar{A} \rho \Delta l \, dv/dt + g \Delta A \Delta v = \Delta(rA)$$

Substituting equation (4.34) in one-dimensional form for  $v$ , treating the bulk viscosity of the common Stirling machine working fluids as being zero or vanishingly small (HC54) and noting that  ${}_{(tv)}\bar{\mu}$  is constant over a mass/energy control volume results in:

$${}_{(1)}\bar{\rho}\Delta l \, dv/dt + gA\Delta v = 4\mu\Delta(A\partial v/\partial x)/3 \quad (4.56)$$

Applying equation (4.51.2) in Eulerian terms to the boundary conditions of Figure 4.7 and substituting the result into equation (4.56) produces in the limit as  $\Delta l \rightarrow 0$ :

$$\rho Adv/dt + v\partial(gA)/\partial x = (4\mu/3\rho)\partial^2(gA)/\partial x^2 \quad (4.57)$$

since  ${}_{(tv)}\bar{\rho}$  is constant over a spatially fixed mass/energy control volume.

Considering equation (4.57) in steady-state form enables the following analytic solution to be found:

$$(gA) = \{ (gA)_{nR} - (gA)_{nL} \} \{ \exp(N_{Pe} x/L) - 1 \} / \{ \exp(N_{Pe}) - 1 \} + (gA)_{nL} \quad (4.58.1)$$

where  $N_{Pe}$  is the Peclet number defined at the centroid of a finite mass/energy control volume of length  $l$  by:

$$N_{Pe} = 3\rho v l / 4\mu \quad (4.58.2)$$

and the  $L$  and  $R$  subscripts represent the control volume boundary values.

Denoting the net boundary momentum flow (advection plus diffusion) across a single momentum control volume boundary as  $G$ , equations (4.58) result in the following expressions:

if  $N_{Pe} = 0$  then:

$$G = (4\mu/3\rho l)\{(gA)_{nL} - (gA)_{nR}\} \quad (4.59.1)$$

if  $N_{Pe} \neq 0$  then:

$$G = v\{(gA)_{nL} + \{(gA)_{nL} - (gA)_{nR}\}(\exp(N_{Pe}) - 1)\} \quad (4.59.2)$$

Under steady-state laminar flow conditions in one-dimension, equations (4.59) provide an exact solution for the net boundary momentum flow. Some authors, notably Patankar and Spalding (Pa80), seem to suggest using these equations for all cases even under transient flow conditions, despite the steady-state assumption made in their derivation. However, such an approach is not considered warranted for Stirling machine boundary conditions which can be highly transient, particularly at machine operating frequencies which have already approached 100 Hz (S186) in certain prototype configurations.

However, equations (4.59) do provide a physically meaningful methodology for determining the boundary advected momentum flux. Consider a plot of the net momentum flux  $G$  as a function of the Peclet number  $N_{Pe}$  as shown in figure 4.8. Since the Peclet number expresses the ratio between the advection and diffusion of momentum across a momentum control boundary, figure 4.8 shows that even at very low Peclet numbers the advection term dominates. At a zero Peclet number there is no advection while in the intermediate range, the momentum flux is partly diffusive and partly advective. Furthermore, from equation (4.59.2) the net momentum flow exhibits the following behaviour in the limit:

$$\text{As } N_{Pe} \rightarrow \infty, G \rightarrow v(gA)_{nL} \quad (4.60.1)$$

$$\text{As } N_{Pe} \rightarrow -\infty, G \rightarrow v(gA)_{nR}$$

$$(4.60.2)$$

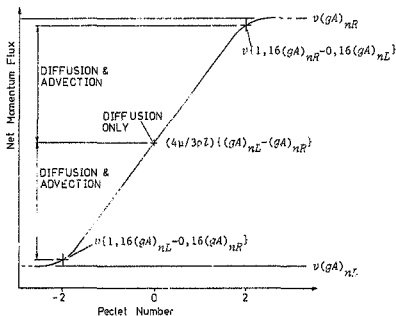


Figure 4.8 Net momentum flux dependence on the Peclet number

Thus figure 4.7 and equations (4.60) establish a physically meaningful model which may be used to determine the boundary advection of momentum. In keeping with the transient nature of the problem being considered, the diffusion is included separately as a discretised term and is not lumped together with the advection flux in a single term. Considering the spatially discretised momentum balance of equation (4.36) and the definition of the Peclet number given by equation (4.58.2), the independent parameter determining the value of the advected mass flux in a given coordinate direction is the relative boundary velocity defined by:

$$v^* = \frac{v}{(tv)} \bar{v} - \bar{v} \quad (4.61.1)$$

Hence for a particular coordinate direction  $i$ :

If  $v_i^* \geq 0$  then:

$$\int_{\bar{A}_{(S)}} \langle \bar{v} \rangle \bar{g}(\bar{v}^* \cdot \bar{n}) d\bar{A} \Big|_i = (v_i^* \langle \bar{v} \rangle \bar{g} \bar{A}_{N(S)})_i \quad (4.61.2)$$

and if  $v_i^* < 0$  then:

$$\int_{\bar{A}_{(S)}} \langle \bar{v} \rangle \bar{g}(\bar{v}^* \cdot \bar{n}) d\bar{A} \Big|_i = -v_i^* \langle \bar{v} \rangle \bar{g} \bar{A}_{N(S)} \Big|_{i+1} \quad (4.61.3)$$

where  $i$  and  $i+1$  denote adjacent momentum control volumes.

Equations (4.61) intrinsically perform the area normalisation required for equation (4.36) as mandated by the attributes of the discretisation scheme. This occurs since the transportive term is  $gA$  (or the mass flow rate) which is independent of the momentum control volume boundary area. Hence the advected mass flux depends only on the averaged mass flux  $\langle \bar{v} \rangle \bar{g}$  flow area which, by definition, is the normalising area.

It is noteworthy that equations (4.61) represent a convoluted integral version of the 'second upwind differencing' method proposed by Gentry, Martin and Daly (GM66). An analysis of this method shows that, while it is clearly transportive (as with the classical or first upwind difference), it is also second-order accurate for the advection field (Ro82). Hence, although the advection is determined on a physical basis, it also has a mathematical justification.

#### 4.6.3 The Boundary Advection of Energy

The determination of the energy advection term for the discretised integral energy balance of equation (4.43) is less problematic than that for the equivalent term in the momentum balance. This arises since the only term at issue is the advected temperature  $(v_n) \bar{T}$  and there is no requirement for any area normalisation.

The approach adopted (detailed in section D.7 of appendix D) is similar to that used in section 4.6.2 above and thus will only be described in outline below.

Consider a constant area Eulerian momentum control volume of length  $\Delta l_n$  in any coordinate direction  $i$  as shown in figure 4.9.  $\Delta l_n$  is composed of the lengths  $\Delta l_i$  and  $\Delta l_{i+1}$  which locate the centroids of the adjacent mass/energy control volumes. Let the averaged mass flux  $\bar{v}_n$  flow across the boundary normalising area  $A_n$  which is taken to be the constant cross-sectional area for the control volume. The temperatures in the adjoining mass/energy control volumes are given by  $T$  and  $T+\Delta T$  respectively. This constant area approach is justified by noting that only the boundary  $A_n$  is active in the energy transport between adjacent mass/energy control volumes.

Applying equation (4.43) to a constant area Eulerian momentum control volume (by exchanging mass/energy and momentum control volumes) and ignoring all non-boundary and turbulent flux terms results in:

$$\hat{C}_V d(\bar{v}_n \bar{T} \bar{H}_{n(s)}) dt = - \bar{v}_n \bar{\kappa} \int_{A_{n(s)}} (\bar{v}_{(lv)} \bar{T} \cdot \bar{n}) d\bar{A} + \hat{C}_P (\bar{v}_n \bar{g} \cdot \bar{n}) \int_{A_{n(s)}} \bar{T} d\bar{A} \quad (4.62)$$

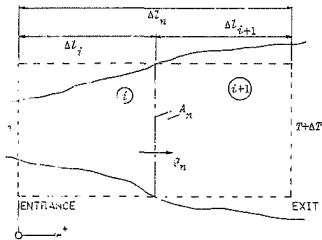


Figure 4.9 Normalised Eulerian momentum control volume

Substitution of equation (4.33) into (4.62), applying the one-dimensional boundary conditions of figure 4.9 and dropping the overbar notation produces, for a constant cross-sectional area:

$$\hat{C}_V \Delta l_n d(T/\rho_n)/dt = \kappa_n \Delta(\delta T/\delta x) - \hat{C}_P g_n \Delta T \quad (4.63)$$

since the volume is given by:

$$V_n = A_n \Delta l_n$$

Dividing equation (4.63) by  $\Delta l_n$ , ignoring the temporal derivative and taking the limit as  $\Delta l_n \rightarrow 0$  results in the steady-state differential equation:

$$\hat{C}_P g_n \delta T/\delta x = \kappa_n \delta^2 T/\delta x^2 \quad (4.64)$$

Since equation (4.64) has the same form as the steady-state version of equation (4.57) it has a similar solution given by:

$$T = \langle T_R - T_L \rangle \{ \exp(N_{Pe} x/l) - 1 \} / \{ \exp(N_{Pe}) - 1 \} + T_L \quad (4.65.1)$$

where  $N_{Pe}$  is the Peclet number at the boundary between two finite mass/energy control volumes whose centroids are separated by a length  $l$ . Under these conditions,  $N_{Pe}$  is redefined (compared with equation (4.58.2)) as:

$$N_{Pe} = \hat{C}_p \bar{S}_n l / \kappa_n \quad (4.65.2)$$

The  $L$  and  $R$  subscripts denote the temperatures at the boundaries of the momentum control volume.

Denoting the net boundary energy flow (advection plus diffusion) across a single mass/energy control volume as  $G$ , equations (4.65) produce the following expressions:

if  $N_{Pe} = 0$  then:

$$j = \kappa_n A_n (T_L - T_R) / l \quad (4.66.1)$$

if  $N_{Pe} \neq 0$  then:

$$G = g_n \hat{C}_p A_n [T_L + \langle T_L - T_R \rangle / \{ \exp(N_{Pe}) - 1 \}] \quad (4.66.2)$$

Using an argument analogous to that used in section 4.6.2 to produce equations (4.61) from equations (4.59), a physically meaningful model for the determination of the boundary enthalpy flux may be developed. As before, in keeping with the transient nature of the Stirling machine analysis problem, the diffusion of energy across a boundary is included separately as a discretised term and not lumped together with the enthalpy advection flux in a single term. From the form of the

advection term in equation (4.43) as well as the definition of the Peclet number in equation (4.65.2), the independent parameter determining the value of the advected enthalpy flux in a given coordinate direction is the relative boundary mass flux given by:

$$g^* = (\rho_{(i,v,n)} \bar{g} - \rho_{(i,v,n)} \bar{v}_n \bar{v}_{n(s)}) \quad (4.67.1)$$

Hence for a particular coordinate direction  $i$ :

If  $g_i^* \geq 0$  then:

$$\left[ \int_{\bar{A}_{n(s)}}^{\bar{A}_{(i,v,n)}} \bar{T}(g^* \cdot n) d\bar{A} \right]_i = (g_{(i,v)}^* \bar{A}_{n(s)})_i \bar{T}_{i-1} \quad (4.67.2)$$

and if  $g_i^* < 0$  then:

$$\left[ \int_{\bar{A}_{n(s)}}^{\bar{A}_{(i,v,n)}} \bar{T}(g^* \cdot n) d\bar{A} \right]_i = (g_{(i,v)}^* \bar{T} \bar{A}_{n(s)})_i \quad (4.67.3)$$

where  $i-1$  and  $i$  denote adjacent mass/energy control volumes.

From a numerical analysis perspective, equations (4.67) represent the integral version of the upwind differencing scheme. In this case, since the attributes of the staggered grid permit the explicit determination of the boundary mass flux, the upwind differencing and second upwind differencing schemes are operationally equivalent and hence equations (4.67) also maintain second order accuracy for the advection field.

The discretised boundary diffusion of heat as described by equation (4.40) requires the determination of a boundary thermal conductivity which is also used in the Peclet number definition (equation (4.65.2)). This boundary conductivity is evaluated as the harmonic

mean of the thermal conductivities in the mass/energy control volumes associated with any momentum control volume. As detailed in section D.7, the boundary thermal conductivity is given by:

$$\overline{\kappa}_{(iV)_n} = \frac{(\Delta l_{(i,SV),i} + \Delta l_{(i,SV),i+1}) \overline{\kappa}_i \overline{\kappa}_{i+1}}{(\overline{\kappa}_{i+1} \Delta l_{(i,SV),i} + \overline{\kappa}_i \Delta l_{(i,SV),i+1})} \quad (4.68)$$

where  $i$  and  $i+1$  denote adjacent mass/energy control volumes in the  $i$ th coordinate direction and  $\Delta l_{(i,SV)}$  denotes a centroid location as depicted in figure 4.6.

#### 4.7 CLOSURE

Both from the standpoint of rigour and that of the available experimental evidence for Stirling cycle machines, none of the assumptions made in developing the turbulence model or the spatial discretisation scheme can be unequivocally or directly substantiated. Nevertheless, all of the claimed experimental validation of existing Stirling machine numerical analyses has traditionally been used as a means of justifying the assumption practice. This is contradictory in the sense that, strictly, the fictitiousness of assumptions in deviating from physical reality should mitigate against the achievement of 'validation'. However, the prevalent resort to an empiricism which forces validation can be justified pragmatically only if such an empiricism is acknowledged unambiguously. Thus the proceeding application of the discrete simulation model developed is undertaken in the spirit of using the validation process as a means of testing the consequences of the turbulent model and spatial discretisation scheme in as objective a manner as possible.

## CHAPTER 5

### NUMERICAL APPLICATION TO STIRLING CYCLE MACHINES

#### 5.1 INTRODUCTION

As the numerical analysis of Stirling cycle machinery has evolved from the purely analytic techniques espoused by Schmidt (Sc1871) to the plethora of computerised numerical methods surveyed by Urieli (Ur83), three distinct approaches may be discerned. The first approach, initially promulgated by Finkelstein (Fi60) and refined by Urieli (Ur77) and Schock (Sc78), divides a Stirling machine working space into an arbitrary number of fixed control volumes or 'nodes' to which the partial differential equations of mass, momentum and energy conservation are applied in Eulerian form. The resulting set of equations are solved in what Organ (Or82) has termed an 'ad hoc' fashion in which the partial differential equations are treated as total or ordinary differential equations and temporally integrated using explicit numerical algorithms.

One of the principal objections to the 'ad hoc' nodal approach made by Organ (Or82) is that:

'(These) numerical schemes draw no distinction between the respective speeds of propagation of pressure information, of temperature information and of the integration process itself.'

This criticism should not be interpreted to imply a generalisation that control volume based numerical schemes are inherently incapable of accurately modelling compressible gas flow, as such a generalisation would manifestly be repudiated by the large number of compressible gas flow control volume based numerical schemes reviewed by Roache (Ro82). In particular, approaches such as the 'Implicit Continuous-fluid Eulerian' (ICE) method of Harlow and Amsden (HA71) and the more esoteric 'Flux-Corrected Transport' (FCT) methods of Book, Boris and Hain (BB75) are examples of successful methods used to simulate physical situations in which the accurate modelling of information propagation is cardinal. However, in the sense that the nodal Stirling numerical simulation schemes treat partial temporal differentials as total differentials and violate physical continuity by imposing artificial discontinuities on the working fluid domain as a result of the discretisation process, Organ's criticism is warranted. Organ proposed a second approach to Stirling machine simulation, namely the 'method of characteristics' solution described by Shapiro (Sh54). This approach has been applied in one dimension to a hypothetical isothermal Stirling engine with gradually varying area changes (Or82). Taylor (Ta84) has extended the one-dimensional method of characteristics solution to include a non-isothermal working fluid flow field.

While undoubtedly providing a physically accurate description of the information propagation effects in a compressible flow field, the method of characteristics approach has not been widely implemented for a large array of problems owing to the difficulties inherent in its application to geometrically complex boundary conditions such as those found in Stirling machine working spaces. As an example, Taylor

(Ta84) noted initially that in the context of a one-dimensional Stirling machine analysis:

'Attempts ... to allow for the sudden changes in cross-sectional area, usually encountered in a Stirling engine, have led to instabilities in the solution.'

Thus in the context of simulating generalised compressible fluid flows, including turbulence effects in two or three dimensions, the method of characteristics becomes cumbersome with excessive computational requirements, even by 'supercomputer' standards. Perhaps for this reason it is unusual to find the method of characteristics a part of the simulation of turbulent compressible flows such as those occurring in Stirling machine working spaces (Is83).

Furthermore, both the characteristics and nodal approaches as presented by Taylor and Urieli respectively utilise explicit integration algorithms which have a time step magnitude limitation imposed by the requirement of satisfying the Courant criterion (CF67). In essence, the Courant criterion requires that the integration time increment be chosen such that information may propagate at most across a single control volume in a nodal simulation or a single spatial grid interstice in a characteristics simulation. This ensures that in the characteristics case the solution remains stable (Ta84) while, for a nodal simulation, the information propagation rate error is bounded. In both approaches, maintaining compliance with the Courant criterion necessitates the capability of using a unique integration time increment at every node or grid point in the flow field. Usually the tendency in explicit algorithms is to choose the smallest integration

time increment determined within the flow field as the universal time increment. In the case of a characteristics simulation involving geometrical complexities (such as the discontinuous flow area changes found in Stirling machines), this mandates the use of iterative 'indirect marching' methods requiring a grid point interpolation which is a potential source of inaccuracy. The minimum time increment selection in a nodal simulation leads to what Roache has termed 'phase' and 'dispersion' errors in the simulated pressure field in particular (Ro82). In this regard also, Organ's criticism of nodal methods is appropriate.

The salient issue in the context of Stirling machine fluid dynamic simulation is that even in a one-dimensional implementation, compliance with the Courant criterion results in both the nodal and method of characteristics solutions requiring large amounts of computation on a unit cycle basis. Coupled to this is the notion that ultimately only the cyclic steady-state or equilibrium solution is of interest. This mandates that many cycles be simulated prior to the steady-state being achieved, so compounding the computation problem. Therefore the principal difficulty with the method of characteristics approach *per se* is one of practical implementation in view of its excessive computational requirements, particularly in the presence of complex geometrical boundary conditions.

A third approach to Stirling machine simulation is described by Rix (R183). This approach seeks to overcome the entropy advection deficiencies of the nodal methodology which arise from the imposition of arbitrary discontinuities on the temperature field. The method is based upon a Lagrangian rather than a Eulerian system model of the

entire working space. However, Rix only demonstrates this method for a case in which transient momentum conservation is ignored. Changing the frame of reference cannot, by definition, have any effect on the physical laws describing the working fluid dynamics. Therefore, the working fluid behaviour determined by an observer moving with the fluid (Lagrangian system) may be converted into the behaviour determined by an observer who is stationary with respect to the fluid flow (Eulerian system) and vice versa by an appropriate coordinate system transformation.

In particular, for any property  $\psi$ , from equation (C.9):

$$\psi_{Lagrange} = \psi_{Eulerian} + \int_{\Delta t} (\mathbf{v} \cdot \nabla \psi) dt \quad (5.1)$$

Hence, provided  $\mathbf{v}(t)$  and  $\psi(t)$  are known functions, no improvement in physical accuracy for a wholly Lagrangian analysis is apparent. However, in the classical nodal simulation approach, the problem is that over any time increment  $\Delta t$  the functions  $\mathbf{v}(t)$  and  $\psi(t)$  are unknown and are assumed either to be constant at their starting values (Pa80) or to be approximated by the characteristics of the integration algorithm as shown in figure 5.1.

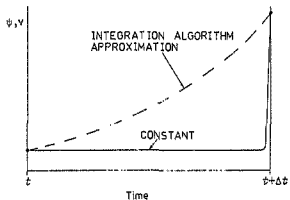


Figure 5.1 Incremental property profile of the explicit integration algorithm

A wholly Lagrangian simulation avoids this difficulty since, by definition (equations (3.26), (3.29), and (3.32)), the control volume boundary mass fluxes are always zero. However, as the Lagrangian approach of Rix and the classical nodal approach both employ control volume spatial discretisations, the difficulty with the Eulerian approach may not be attributed to the discretisation scheme but rather to the characteristics of the explicit integration process used. The degree to which the difficulty may be resolved thus depends on the effectiveness of the chosen explicit integration scheme in approximating the  $\psi(t)$  and  $v(t)$  profiles over  $\Delta t$ . It should, however, be noted that in order for these algorithms to be effective,  $\Delta t$  must be constrained so that the approximations of  $\psi(t)$  and  $v(t)$  produced are physically credible. This constraint is usually defined numerically in terms of the truncation error with its attendant stability implications. Almost without exception in compressible flow situations, such a truncation error constraint is satisfied by the a

*a priori* requirement of satisfying the Courant criterion.

Acknowledging the integration algorithm restriction, the choice of using Lagrangian or Eulerian frames of reference is usually boundary condition dependent, as some boundary conditions are more amenable to a Lagrangian than a Eulerian treatment (No64). In any event, the wholly Lagrangian approach advocated by Rix is also seemingly a candidate for Organ's '*ad hoc*' criticism in that, unlike the method of characteristics which rigorously yields total temporal derivatives, Rix's method is based on the integration of substantive temporal derivatives. In this sense, the method devolves to a transformed version of the nodal method, thus predicating that the two methods share the same '*ad hoc*' deficiency. Nevertheless, use of such a Lagrangian system can be advantageous in overcoming at least one of the deficiencies in the classical nodal approach (Ur77), namely, in eliminating the assumption of zero momentum in the expansion and compression spaces. However, in view of the complex heat exchanger and regenerator geometries of actual Stirling machines, Lagrangian methods are not practically convenient throughout the working space. Thus a combined Eulerian/Lagrangian (CEL) system in which the variable volume spaces are treated as Lagrangian and the constant volume spaces as Eulerian potentially offers a better utilisation of the Lagrangian analysis concept suggested by Rix.

## 5.2 NUMERICAL ALGORITHM SELECTION

Coalescing the attributes of the nodal, method of characteristics and Lagrangian approaches to Stirling machine fluid dynamic simulation, an

idealised methodology may be defined. In this methodology, the tractability of the control volume approach is combined with the information propagation accuracy of the method of characteristics solution and the flexibility of the Lagrangian scheme in accomodating non-stationary boundary conditions. The foundation of such an idealised scheme must be based *inter alia* on a rigorous analytic treatment of the conservation equations which yields a formul ion devoid of the 'ad hoc' deficiencies of existing control volume approaches. In particular, the formulation must be cast in frame-of-reference indifferent, total temporal derivative terms such that no arbitrary discontinuities are imposed upon the temperature and pressure fields. Within the limitations of the turbulence and discretisation models proposed in chapter 4, the theoretical development of chapters 3 and 4 ostensibly does provide a conservation equation formulation with the necessary attributes, although no absolutism of any kind is claimed or warranted for this formulation.

The selection of a numerical algorithm to apply the integral conservation equation set to Stirling machine boundary conditions may be made on a physical basis since each algorithm has definite implications in terms of accurately modelling information propagation. A summary of the relevant numerical algorithms is tabulated hierarchically in table 5.1.

Table 5.1 Stirling machine numerical algorithm hierarchy

Algorithm	Physical Implication
Implicit - implicit mass, momentum and energy conservation.	Transient solution under cyclic equilibrium conditions only.
Hybrid implicit/explicit - explicit momentum, implicit mass and explicit or implicit energy conservation.	Transient solution under cyclic equilibrium conditions only with numerically restricted integration time increment.
Pressure domain splitting, hybrid implicit/explicit - explicit momentum and explicit or implicit energy conservation, implicit mass conservation with characteristically determined local field limits.	Transient solution with numerically restricted integration time increment.
Method of characteristics, explicit - explicit mass, momentum and energy conservation.	Transient solution, governed by Courant criterion.
Explicit - explicit mass, momentum and energy conservation.	Transient solution with phase and dispersion errors, governed by Courant criterion.

Table 5.1 is arranged such that the physically unrestricted transient algorithms are located centrally and are bounded by restricted explicit and implicit algorithms. The traditional approach to Stirling machine simulation as discussed above has been to progress from the bottom of table 5.1 upwards, while in this work, the approach adopted is to move from the top of table 5.1 downwards.

When compared with the more traditional explicit algorithms (Sc78, Ur77), an implicit numerical algorithm has several advantages to recommend it in the context of one-dimensional, Stirling machine fluid dynamic simulation. These advantages may be cited as follows:

1. Numerical stability independent of the 'stiffness' of the total temporal derivative equations to be solved.

2. Computation times on a unit cycle basis which are significantly lower than explicit algorithms owing to a reduced computational volume and ability to accommodate large time increments.
3. Reduction in the number of simulated machine cycles needed to achieve numerical convergence at the steady-state.

Moreover, in physical terms, implicit and hybrid implicit/explicit methods have advantages over purely explicit methods in that, when properly formulated, they permit a physically discrete accounting of information propagation and advection effects in a manner which is independent of Courant criterion restrictions. This may be understood by considering the incremental time step profile of any transport property  $\psi$  in an implicit process depicted by figure 5.2.

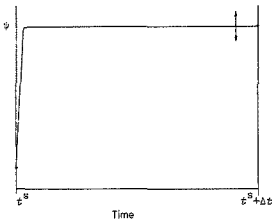


Figure 5.2 Incremental property profile of an implicit integration algorithm

In this case,  $\psi(t)$  is effectively assumed to be constant at its final value over the time increment  $\Delta t$ , but the final value is a variable determined by the requirement that the mass, momentum and energy conservation balances are satisfied simultaneously over the entire

flow field at time  $t^* + \Delta t$ . Thus knowledge of  $\psi(t)$  over  $\Delta t$  is not mandatory in order to guarantee that the conservation criteria are satisfied without advective anomalies.

The structure of an implicit algorithm must account properly for information propagation both on a cyclic equilibrium as well as on a transient basis. Such a structure depends upon the analytical methodology used to formulate the conservation of mass equation so that it implicitly defines the pressure field. This methodology is described in section 5.5, and yields pressure field equations of the form:

$$\sum_{j=i-m}^{i+m} K_{ij} \bar{v}_j = \alpha_i \quad (5.2)$$

where  $i$  denotes the individual mass/energy control volumes of which the flow field is comprised and  $m$  is dependent on the dimensionality of the problem. In a cyclic equilibrium solution, equation (5.2) is applied to the entire flow field, while in a transient solution equation (5.2) is applied to a series of pressure domains, one for each mass/energy control volume as illustrated (for a particular two-dimensional Eulerian field) in figure 5.3. Each pressure domain has an extent determined by the information propagation characteristics  $\sum \mathbf{f}(\mathbf{v}_a \mathbf{T})_i$  where  $(v_a)_i$  is the sonic velocity within each mass/energy control volume comprising a particular pressure domain. Hence by this process of partitioning, the 'pressure domain splitting' (PDS) algorithm may be structured to yield a transient information propagation simulation. This simplified explanation ignores the complexities arising from defining the pressure domain boundaries under supersonic or sonic flow conditions (that is, when  $|\mathbf{v}|_i \geq (v_a)_i$ ).

since such an explanation is beyond the limits set by the thesis statement. However, it may be mentioned that under these conditions the PDS algorithm essentially devolves to a standard approach such as the 'region-to-region' method (Jo69).

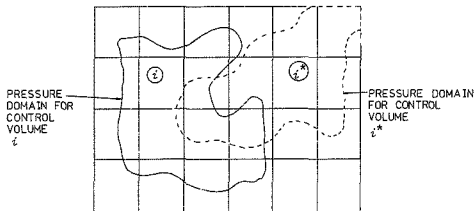


Figure 5.3 Structure of the pressure domain splitting algorithm

Applying equation (5.2) to the entire flow field (or treating the flow field as a unitary pressure domain) enables the cyclic equilibrium solution to be obtained directly. Two approaches to obtaining the equilibrium solution may be hypothesized:

1. *Infinite information propagation*

This hypothesis may be justified by the notion that, at cyclic equilibrium, sufficient time has passed such that every point in the flow field has received information from every other point in the flow field for all instants over the cyclic period. This concept is graphically illustrated by Organ (Or82) who depicts a Mach line net for about 1.25 cycles after the initiation of the oscillation of an alpha-configuration Stirling engine as shown in the reproduction denoted as figure 5.4. The infinite information

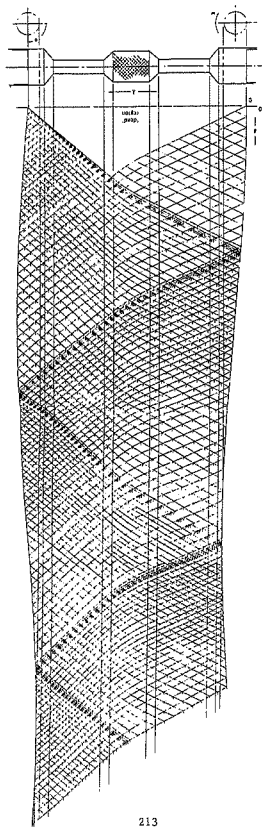


Figure 5.4 Alpha-configuration Stirling engine Mach line net for 4000 rpm (extracted from reference Or82)

propagation hypothesis may be implemented by arbitrarily selecting an integration time increment which is much less than the smallest information propagation time characteristic of a particular machine. The time characteristic may be defined as the interval required for a pressure wave to exactly traverse the unitary pressure domain once. Henceforward, the infinite information propagation hypothesis is distinguished by referring to its implementation as the 'equilibrium algorithm'.

2. *Characteristically determined integration time increments*

Here, the integration time increment is treated as a dependent variable which is instantaneously equal to the machine time characteristic. In this instance, the equilibrium solution produces the spatially limiting case of the pressure domain splitting algorithm and as such yields an approximation to the full information propagation transient solution. The implementation of the characteristically determined integration time increment hypothesis is termed the 'unitary pressure domain (UPD) algorithm'.

The validity of the unitary pressure domain and cyclic equilibrium algorithms is limited strictly to Stirling machine configurations which never experience sonic or supersonic conditions at any time during their operation. This is apparently not a restriction of consequence for a representative sample of the Stirling engine hardware constructed to date. Over this hardware map (SS86) the largest Mach numbers encountered have been much less than 0,5 (Se86) while both algorithms have been successfully tested to threshold Mach numbers of at least 0,85 (Go87.1). As intuitively expected, both

algorithms fail for Mach numbers of unity or greater.

However, the assertion that most Stirling engine hardware experiences low cyclic maximum Mach numbers is by no means definite. The maximum Mach numbers referred to have been determined for each piece of Stirling hardware at the minimum flow area (usually the heater/regenerator interface) where the peak cyclic flow velocities are inferred to occur. Yet Organ (Or84) has argued, based on single screen experimental data, that the flow in the regenerator may choke at upstream Mach numbers in the range  $0,2 < N_{Ma} < 0,5$  for regenerator matrix porosities in the range  $0,4 < \xi < 0,8$ , a porosity range spanning most Stirling machines. Should this be true then the consequent existence of a weak shock front in the regenerator militates against the use of the equilibrium or UPD algorithms, so mandating the use of the PDS algorithm.

Referring once again to table 5.1, it may be observed that, in addition to the pressure domain splitting and implicit cyclic equilibrium algorithms, a hybrid implicit/explicit version of the cyclic equilibrium algorithm is also described. This hybrid algorithm, even though numerically restricted, becomes useful when considering two- and three-dimensional flow fields with relatively fine control volume spatial discretisations. Under these conditions, the computational effort in the fully implicit method mandated by the repeated inversion of very large square matrices may become comparable with or greater than the effort involved in using partially explicit, numerically restricted algorithms. This statement also takes cognisance of the particular difficulties arising from Stirling machine boundary conditions which yield 'stiff' differential equations

(Sh82), so predicating the use of iterative explicit algorithms (Ge67) which can become fairly complex (Bu64).

Thus in the light of the foregoing discussion and in accordance with the thesis statement which stipulates that only cyclic equilibrium solutions are of relevance, attention is restricted here to the development and application of the fully implicit algorithm under cyclic equilibrium conditions only. The remainder of this chapter is therefore devoted to transforming the time-averaged and spatially discretised integral conservation balances developed in chapter 4 into a form amenable to solution by an implicit numerical algorithm. Although this development is undertaken in one-dimensional terms (as required by the constraints elucidated in section 1.4), the methodology may be applied readily in two or three dimensions. Such multi-dimensional applications are in some respects simpler than the one-dimensional case discussed, since they avoid some of the convolutions necessary to apply uni-dimensional empirical correlations in a volume-averaged setting.

In presenting the development of the implicit numerical algorithm, a complete listing of all the relevant equations as actually implemented in the simulation programmes is given. Unavoidably, such an approach results in a certain amount of tedium but eliminates any loss of rigour in translating analytical symbolism into numerical details.

### 5.3 THE ONE-DIMENSIONAL SIMULATION SYSTEM MODEL

The system model depicted in figure 5.5 is a literal one-dimensional application of the discretisation scheme described by equations (4.29) to a Stirling machine working space. The working space is divided into three sub-regions termed the expansion, transfer and compression spaces respectively. In turn, the expansion and compression spaces, which are defined as having constant cross-sectional flow areas, are split further into purely Lagrangian and combined Eulerian/Lagrangian (CEL) zones. A single CEL mass/energy control volume provides the interface between the purely Lagrangian and Eulerian control volumes bordering the Eulerian/Lagrangian zone. Each Lagrangian mass/energy control volume is denoted by a numerical sequence which increases from the piston inwards towards the transfer space. This produces what may cursorily appear to be a needlessly complex mirror image numbering sequence in the expansion and compression spaces. However, in view of the structure of the Eulerian/Lagrangian interfacing scheme discussed later, this notation yields the most effective computer programme structure. In both the expansion and compression spaces, the Lagrangian momentum control volumes (whose centroids are depicted by the single chain dashed lines) are numbered so that the numerical indices denoting any mass/energy control volume and its piston side momentum control volume are identical. The properties of the first momentum control volume in both the expansion and compression spaces describe the kinematics of the pistons, so defining the momentum boundary conditions for the entire flow field.

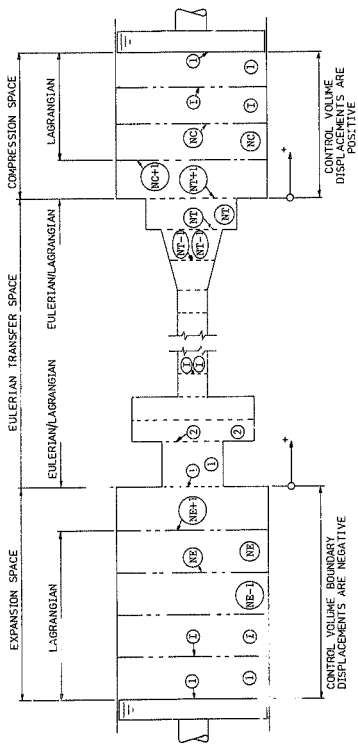


Figure 5.5 One-dimensional Stirling machine working space system model

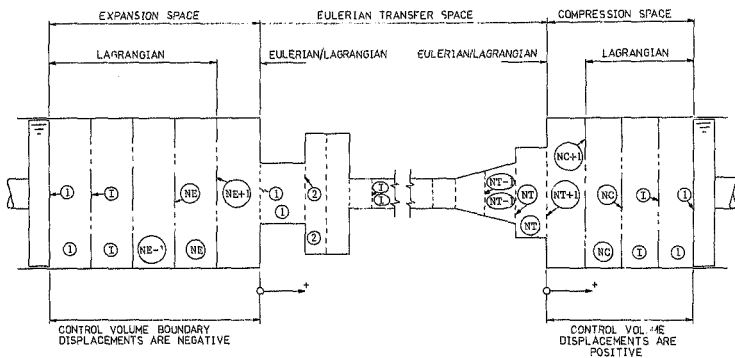


Figure 5.5 One-dimensional Stirling machine working space system model

There are  $NE/NC^i$  mass/energy and  $NE+1/NC+1$  momentum control volumes instantaneously in the expansion and compression spaces respectively. The universal sign convention defines positive to be in the direction from the expansion space to the compression space. In addition, zero piston displacements are defined for both variable volume spaces to occur at their junctions with the transfer space. Therefore, momentum control volume positions will appear as negative and positive values in the expansion and compression spaces respectively. The momentum control volume velocities and displacements in both spaces adhere to the universal sign convention such that positive vectors are directed towards the right.

Separating the expansion and compression spaces is a Eulerian transfer space comprising the heater, regenerator and cooler as well as any intermediate ducting. The mass/energy control volume discretisation of the transfer space may be arbitrary with the restriction that discontinuous changes in flow area occur at mass/energy control volume boundaries. The momentum control volume straddling the left hand boundary of a given mass/energy control volume has the same numerical index as the given mass/energy control volume. This results in the transfer space having an aggregate of  $NT$  mass/energy control volumes and  $NT+1$  momentum control volumes. In terms of the universal sign convention cited above, all mass fluxes and velocities in the transfer space are positive when vectored towards the right (or compression space end). The 'entrance' to and 'exit' from a particular control volume are defined to be coincident with its left and right boundaries

---

<sup>i</sup>Non-boldface upright capitals refer to computer programme nomenclature which is introduced directly into the notation in order to simplify the symbolism and allow the programme listings to be interpreted more readily.

respectively.

In the following discussion as well as in the computer simulation programmes, the sign conventions discussed above are meticulously applied throughout and thus will no longer be alluded to explicitly.

#### 5.4 THE REDUCED AND DISCRETISED ONE-DIMENSIONAL INTEGRAL BALANCES

The one-dimensional conservation balances as well as their associated boundary advection terms are a simplification of the generalised equations developed in sections 4.5 and 4.6. Henceforward, the nomenclature is simplified where appropriate by ignoring the overbar averaging nomenclature and reducing all the vector terms to their one-dimensional form which, in terms of the adopted system sign convention, need not be referred to using bold-faced symbols. As the system model involves Eulerian, Lagrangian and combined Eulerian/Lagrangian control volumes, the one-dimensional conservation equations are given in all the forms necessary for a complete description of the Stirling machine fluid dynamic system.

##### 5.4.1 One-Dimensional Integral Mass Balance

From equation (4.30), the Eulerian version of the integral mass balance is given by:

$$dM_i/dt = (g_{n'n}^A)_i - (g_{n'n}^A)_{i+1} \quad (5.3)$$

where, as before, the subscript  $n$  refers to those parameters occurring at a momentum control volume centroid.

From equation (4.18), under Lagrangian conditions, the integral mass balance becomes:

$$dM_i/dt = 0 \quad (5.4)$$

while for the combined Eulerian/Lagrangian control volumes in the expansion and compression spaces (which are denoted henceforward by the Greek subscripts  $\epsilon$  and  $\gamma$  respectively):

$$dM_\epsilon/dt = -(g_n A_n)_1 \quad (5.5.1)$$

$$dM_\gamma/dt = (g_n A_n)_{N+1} \quad (5.5.2)$$

#### 5.4.2 One-Dimensional Integral Momentum Balance

The one-dimensional Eulerian version of equation (4.36) is complicated by the properties of the system model. In particular, the non-uniform flow areas and the necessity of including the multi-dimensional characteristics of the stress tensors into a uni-dimensional mould mandate that equation (4.36) be applied with careful adherence to local geometrical boundary conditions.

Consider a momentum control volume straddling a flow area discontinuity between two mass/energy control volumes  $i$  and  $i+1$  as depicted in figure 5.6.

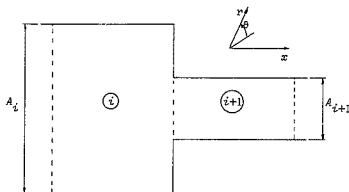


Figure 5.6 Flow area discontinuity

Since the area difference  $A_i - A_{i+1}$  constitutes a rigid boundary, the surface integral of pressure from equation (4.36) yields:

$$\begin{aligned}
 - \int_{A_{(S)}} \bar{p} n d\bar{A} &= P_i A_i - P_i (A_i - A_{i+1}) - P_{i+1} A_{i+1} \\
 &= A_{i+1} (P_i - P_{i+1})
 \end{aligned} \tag{5.6}$$

In other words the net pressure force acting on the momentum control volume is given by the volume-averaged pressure differential acting on the centroidal area  $(A_n)_{i+1}$ .

Since only a uni-dimensional variation of velocity  $v$  is permitted, the full stress tensor incorporated into equation (4.36) may be simplified considerably and expressed in terms of the cylindrical coordinate system of figure 5.6 as:

$$\begin{aligned}
 [{}_{(t,v)} \bar{\mu} (\nabla_{(t,v)} \bar{v} + (\nabla_{(t,v)} \bar{v})^T) + \{({}_{(t,v)} \bar{\Lambda} - 2 {}_{(t,v)} \bar{\mu} / 3) (\nabla_{(t,v)} \bar{v}) \cdot \mathbf{I}\}]_i \\
 = \\
 [ (4\mu/3 + \Lambda) \partial v / \partial x + \mu \{ (\partial v / \partial \theta) / r + \partial v / \partial r \}]_i
 \end{aligned} \tag{5.7}$$

From equations (4.34) and (4.36), the total stress tensor, including the Reynolds stresses, may be expressed as:

$$\int_{\bar{A}_{(s)}} \{ (\{t\}_v) \bar{T} + \{v\} \bar{T}^{(t)} \} \cdot \bar{n} dA = \int_{A_A} \{ (\{t\}_v) \bar{T} + \{v\} \bar{T}^{(t)} \} \cdot \bar{n} dA + \int_{A_B} \{ (\{t\}_v) \bar{T} + \{v\} \bar{T}^{(t)} \} \cdot \bar{n} dA \quad (5.8.1)$$

where:

$$A_A = \bar{A}_{(s)ent,ext} \quad (5.8.2)$$

$$A_B = \bar{A}_{(s)} - \bar{A}_{(s)ent,ext} \quad (5.8.3)$$

Examining equations (5.7) and (5.8) with reference to figure 5.6, it may be noted that:

$$\{ (\{t\}_v) \bar{T} + \{v\} \bar{T}^{(t)} \}_{xx} \cdot \bar{n} = 0 \text{ on } A_B \quad (5.9.1)$$

and:

$$\{ (\{t\}_v) \bar{T} + \{v\} \bar{T}^{(t)} \}_{xr, x\theta} \cdot \bar{n} = 0 \text{ on } A_A \quad (5.9.2)$$

Hence substituting equation (5.7) into equation (5.8) and simplifying in terms of equations (5.9) produces:

$$\int_{\bar{A}_{(s)}} \{ (\{t\}_v) \bar{T} + \{v\} \bar{T}^{(t)} \} \cdot \bar{n} dA = \int_{A_A} [ \{ (4\mu/3 + \lambda) \partial v / \partial x + \tau_{xx}^{(t)} \} \cdot \bar{n} ] dA + \int_{A_B} [ \{ \mu ( (\partial v / \partial \theta) / r + \partial v / \partial r ) + \tau_{xr, x\theta}^{(t)} \} \cdot \bar{n} ] dA \quad (5.10)$$

In terms of the one-dimensional system model  $\partial v / \partial \theta$  and  $\partial v / \partial r$  are explicitly indeterminate and thus must be expressed, via an empirical

correlation, as a function of  $v$  (BS60). The Reynolds stress tensor components  $\tau_{XR, X\theta}^{(b)}$  are also explicitly indeterminate and must likewise be expressed empirically in terms of  $v$ . It is convenient to combine these correlations and express them as the single relationship  $\Omega(v)$ . Hence the second integral on the right hand side of equation (5.10) becomes:

$$\int_{A_B} \left\{ [\mu(\partial v/\partial \theta)/r + \partial v/\partial r] + \tau_{XR, X\theta}^{(b)} \cdot \mathbf{n} \right\} dA$$

$$= (\Omega(v)A_\sigma)_i + (\Omega(v)A_\sigma)_{i+1} \quad (5.11.1)$$

where:

$$(A_\sigma)_i + (A_\sigma)_{i+1} = \bar{A}_{(s)} - \bar{A}_{(s)ent, ext} \quad (5.11.2)$$

represents the solid surface bounding the two mass/energy control volume segments comprising a momentum control volume.

Following an argument offered by Schlichting (Sc79),  $\tau_{XX}^{(b)}$  is ignored since, by an order-of-magnitude analysis, it is significantly less than  $\tau_{XR, X\theta}^{(b)}$ . Thus from equations (5.10) and (5.11):

$$\int_{A_{(s)}} \{ (\rho v)_i \mathbf{T} + (\rho v)_i \mathbf{T}^{(b)} \cdot \mathbf{n} \} dA = \int_{A_A} \{ ((4\mu/3 + \lambda)\partial v/\partial x) \cdot \mathbf{n} \} dA$$

$$+ (\Omega(v)A_\sigma)_i + (\Omega(v)A_\sigma)_{i+1} \quad (5.12)$$

Hence, reducing equations (4.36) to one-dimensional form and substituting equations (5.6) and (5.12), the Eulerian form becomes:

$$d(g_n v_n)_i / dt = (g v A)_{i-1} - (g v A)_i + (A_n)_i (P_{i-1} - P_i) - (M_n)_i g$$

$$- \{ ((4\mu/3 + \lambda)\partial v/\partial x) A \}_{i-1} + \{ ((4\mu/3 + \lambda)\partial v/\partial x) A \}_i$$

$$- (\Omega(v)A_\sigma)_{i-1} - (\Omega(v)A_\sigma)_i$$

Substituting equations (4.50) and (4.61):

$$\begin{aligned}
 d(g_n v_n)_i / dt = & v_{i-1} (gA)_{i-1}^* - v_i (gA)_i^* + (A_n)_i (P_{i-1} - P_i) - (H_n)_i g \\
 & - (\rho(v)A_\sigma)_{i-1} + (A(4\mu/3+A)/H)_{i-1} (g_n A_n)_{i-1} - (g_n A_n)_i \\
 & - (\rho(v)A_\sigma)_i - (A(4\mu/3+A)/H)_i (g_n A_n)_i - (g_n A_n)_{i+1} \quad (5.13.1)
 \end{aligned}$$

where  $(gA)_j^*$  are determined such that for  $j = i-1$  and  $j = i$ :

$$\text{if } v_j \geq 0 \text{ then: } (gA)_j^* = (g_n A_n)_j \quad (5.13.2)$$

$$\text{if } v_j < 0 \text{ then: } (gA)_j^* = (g_n A_n)_{j+1} \quad (5.13.3)$$

and  $v_j$  is given by:

$$v_j = ((g_n A_n)_j + (g_n A_n)_{j+1}) / 2\rho_j A_j \quad (5.13.4)$$

Equation (5.13.1) is applicable to the Eulerian momentum control volume at the junction of the expansion and transfer spaces with the modifications described by equations (5.14).

When  $j = i-1 = c$ :

$$\text{if } v_c \geq 0 \text{ then: } (gA)_c^* = \rho_c (v_n A_n)_{nE+1} \quad (5.14.1)$$

$$\text{if } v_c < 0 \text{ then: } (gA)_c^* = (g_n A_n)_1 \quad (5.14.2)$$

Since the centroid of the  $c$  mass/energy control volume constitutes a moving boundary, from equations (4.51.1) and (4.36),  $v_c$  is given by:

$$v_c = (\rho_c (v_n A_n)_{nE+1} + (g_n A_n)_1) / 2\rho_c A_c - 0.5(v_n)_{nE+1} \quad (5.14.3)$$

and hence by inference:

$$\rho_c (v_n A_n)_{nE+1} + (g_n A_n)_1 \quad (5.14.4)$$

Similarly, for the Eulerian momentum control volume at the compression/transfer space interface, equation (5.13.1) applies with the changes given by equations (5.15).

When  $j = i = \gamma$ :

$$\text{if } v_\gamma \geq 0 \text{ then: } (gA)_\gamma^* = (g_{n'n})_{\gamma\tau+1} \quad (5.15.1)$$

$$\text{if } v_\gamma < 0 \text{ then: } (gA)_\gamma^* = \rho_\gamma (v_{n'n})_{\gamma\tau+1} \quad (5.15.2)$$

where:

$$v_\gamma = \{\rho_\gamma (v_{n'n})_{\gamma\tau+1} + (g_{n'n})_{\gamma\tau+1}\} / 2\rho_\gamma A_\gamma - .5(v_n)_{\gamma\tau+1} \quad (5.15.3)$$

hence:

$$\rho_\gamma (v_{n'n})_{\gamma\tau+1} \rightarrow (g_{n'n})_{j+1} \quad (5.15.4)$$

The Lagrangian form of equation (4.36) may be expressed using the structure of equation (3.28). In terms of the system model (Figure 5.5) the Lagrangian form is used only in a constant flow area environment. This permits the simplified result:

$$\begin{aligned} d(M_n v_n)_i / dt &= (A_n)_i (P_{i-1} - P_i) - (\Omega(v)A_\sigma)_{i-1} - (\Omega(v)A_\sigma)_i - (M_n)_i g \\ &\quad + (A(4\mu/3+\lambda)/l)_{i-1} \{(v_n)_{i-1} - (v_n)_i\} \\ &\quad - (A(4\mu/3+\lambda)/l)_i \{(v_n)_i - (v_n)_{i+1}\} \end{aligned} \quad (5.16)$$

The form  $d(M_n v_n)_i / dt$  of equation (3.28) is preferred to  $(M_n)_i (dv_n / dt)_i$  given by equation (3.29) in order to accommodate the NE+1 and NC+1 momentum control volumes in the expansion and compression spaces respectively (see figure 5.4). In terms of equations (4.33) and (5.5), these particular control volumes will in general have  $d(M_n)_i / dt \neq 0$ .

Equation (5.16) is applicable to the NE+1 momentum control volume in the expansion space with the replacement (determined from equation (4.50)):

$$\langle \rho_e \langle v_n^A \rangle_{NE+1} - \langle g_n^A \rangle_1 \rangle / H_e \rightarrow \langle \langle v_n \rangle_1 - \langle v_n \rangle_{I+1} \rangle / l_1 \quad (5.17.1)$$

and the addition of an advective term on the right hand side so that:

$$\langle \text{RHS of (5.16)} \rangle - v_e \langle g \rangle_e^* \rightarrow \langle \text{RHS of (5.16)} \rangle \quad (5.17.2)$$

where  $\langle g \rangle_e^*$  is given by equations (5.14).

Similarly, for the NC+1 momentum control volume in the compression space equation (5.16) applies with the replacement:

$$\langle \langle g_n^A \rangle_{NT+1} - \rho_e \langle v_n^A \rangle_{NC+1} \rangle / H_e \rightarrow \langle \langle v_n \rangle_{I-1} - \langle v_n \rangle_1 \rangle / l_{I-1} \quad (5.18.1)$$

and the addition:

$$\langle \text{RHS of (5.16)} \rangle + v_e \langle g \rangle_e^* \rightarrow \langle \text{RHS of (5.16)} \rangle \quad (5.18.2)$$

where  $\langle g \rangle_e^*$  is given by equations (5.15).

#### 5.4.3 One-Dimensional Integral Energy Balance

In translating the generalised integral energy balance of equation (4.43) into a one-dimensional Eulerian form, difficulties similar to those encountered above for the dissipation and turbulence terms arise, namely, the inclusion of essentially multi-dimensional phenomena in a uni-dimensional structure. Thus in terms of the uni-dimensional velocity  $v$ , from equations (4.37) and (4.38), the

dissipation is given in cylindrical coordinates by:

$$\langle \epsilon_{(t,v)} \bar{\Phi} \rangle_I \sim \left[ (4\mu/3 + \Lambda) (\partial v / \partial x)^2 + \mu \{ (\partial v / \partial x)^2 \{ (\partial v / \partial \theta) / r \}^2 \} + F(\langle \epsilon_{(t,v)} \bar{\mu}, \langle \epsilon_{(t,v)} \bar{v} \rangle, x, \theta, r) \right]_I \quad (5.19)$$

where the function F represents an empirical evaluation of the dissipation resultant from the temporally fluctuating component of the volume-averaged velocity. As for equation (5.7),  $(\partial v / \partial x)$  and  $(\partial v / \partial \theta)$  are not explicitly determinable and hence it is convenient to combine these terms with the functional term F into a single empirical relationship  $\Phi^*(v)$ . Equation (5.19) then becomes:

$$\langle \epsilon_{(t,v)} \bar{\Phi} \rangle_I = (4\mu/3 + \Lambda) (\partial v / \partial x)^2 + \Phi^*(v) \quad (5.20)$$

The non-advective heat flux and turbulent heat flux surface integral terms in equation (4.43) may be combined and repartitioned into flow and non-flow surface area components as follows:

$$\begin{aligned} & \int_{\bar{A}_{n(s)}} \{ \langle \epsilon_{(t,v_n)} \bar{\kappa} \bar{v}_{(t,v_n)} \bar{T} + \langle \epsilon_{(t,v_n)} \bar{q}^{(t)} \rangle \cdot \bar{n} \} dA \\ & - \\ & \int_{A_A} \{ \langle \epsilon_{(t,v_n)} \bar{\kappa} \bar{v}_{(t,v_n)} \bar{T} + \langle \epsilon_{(t,v_n)} \bar{q}^{(t)} \rangle \cdot \bar{n} \} dA \\ & + \int_{A_B} \{ \langle \epsilon_{(t,v_n)} \bar{\kappa} \bar{v}_{(t,v_n)} \bar{T} + \langle \epsilon_{(t,v_n)} \bar{q}^{(t)} \rangle \cdot \bar{n} \} dA \end{aligned} \quad (5.21.1)$$

where:

$$A_A = \bar{A}_{n(s)ent,ext} \quad (5.21.2)$$

$$A_B = \bar{A}_{n(s)} - \bar{A}_{n(s)ent,ext} \quad (5.21.3)$$

In a one dimensional field, the second integral on the right hand side of equation (5.21.1) (which describes the heat transfer between the solid portions of the boundary and the control volume fluid) is dependent on  $\partial T/\partial x$ ,  $\partial T/\partial \theta$  and  $v(x, \theta)$  as well as on their temporally fluctuating components. As none of these terms are explicitly available, it is customary to lump all the solid boundary / fluid heat transfer effects into a single convective heat transfer term (BS60). This term incorporates an empirically determined heat transfer coefficient as follows:

$$\int_{A_B} \{ (\rho v_n) \bar{v} \bar{T} + (v_n) \bar{q}^{(t)} \} \cdot n \, dA = h(A_n)_s (T_s - T_o) \quad (5.22)$$

where  $h$  is the empirical heat transfer coefficient and  $(A_n)_s$  denotes the solid surface bounding a mass/energy control volume. By analogy with the momentum balance, following Schlichting (Sc79):

$$(v_n) \bar{q}^{(t)} \approx q_{x\theta}^{(t)} \quad (5.23)$$

or the turbulent flux  $q_x^{(t)} \ll q_{x\theta}^{(t)}$  by an order-of-magnitude analysis and may thus be ignored.

Hence combining equations (5.21), (5.22) and (5.23) and substituting the result together with equation (5.20) into equation (4.43) yields the one-dimensional Eulerian form:

$$\begin{aligned} \hat{C}_v d(TN)_I / dc = N_I \hat{E}_I + V_I \{ (4\mu/3 + \lambda) (\partial v / \partial x)^2 + \Phi^*(v) \}_I + (Vv\partial P / \partial x)_I \\ + \{ h(A_n)_s (T_w - T) \}_I + (\kappa_{n'n})_{I+1} (\partial T_n / \partial x)_{I+1} \\ + \hat{C}_p (g_n T_n A_n)_I - \hat{C}_p (g_n A_n T_n)_{I+1} - (\kappa_{n'n})_I (\partial T_n / \partial x)_I \end{aligned} \quad (5.24)$$

The discretisation of all the gradients in equation (5.24) is quite natural in terms of the system model with the exception of the  $(\partial P/\partial x)_i$  gradient. As mentioned previously in the discussion of equation (4.39), an approach which has proved to be numerically successful is developed with reference to figure 5.7 for the particular case of a constant area mass/energy control volume.

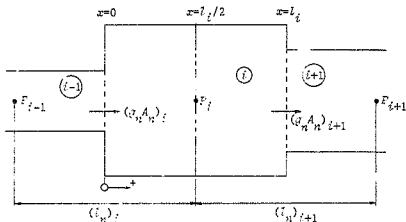


Figure 5.7 Pressure gradient discretisation

As there are two pressure gradients existing in the mass/energy control volume, the aggregate effect may be obtained by integrating  $v(\partial P/\partial x)$  in two parts as follows:

$$\begin{aligned} \langle v \partial P / \partial x \rangle_i &= A_i \left[ \int_0^{l_i/2} v(x) (P_i - P_{i-1}) / (l_n)_i dx \right. \\ &\quad \left. + \int_{l_i/2}^{l_i} v(x) (P_{i+1} - P_i) / (l_n)_{i+1} dx \right] \end{aligned}$$

Substituting equation (4.49) for  $v(x)$  and rearranging:

$$\begin{aligned}
 (Vv\partial P/\partial x)_i &= (A_i/\rho_i v_i) \{ (P_i - P_{i-1}) / (I_n)_i \int_0^{I_i/2} \{ (g_n A_n)_i (I_i - x) + (g_n A_n)_{i+1} x \} dx \\
 &+ (P_{i+1} - P_i) / (I_n)_{i+1} \int_{I_i/2}^{I_i} \{ (g_n A_n)_i (I_i - x) + (g_n A_n)_{i+1} x \} dx \}
 \end{aligned}$$

Integrating and simplifying produces:

$$\begin{aligned}
 (Vv\partial P/\partial x)_i &= (I_i/8\rho_i) \{ (P_i - P_{i-1}) \{ 3(g_n A_n)_i + (g_n A_n)_{i+1} \} / (I_n)_i \\
 &+ (P_{i+1} - P_i) \{ (g_n A_n)_i + 3(g_n A_n)_{i+1} \} / (I_n)_{i+1} \} \quad (5.25)
 \end{aligned}$$

This equation is a paradigmatic expansion of  $(Vv\partial P/\partial x)_i$  although the algebra may become quite complex when  $A_i$  is an arbitrary function of  $x$ . As the constant area case is most prevalent, equation (5.25) is used henceforward for exemplifying the algorithm development.

Substituting equations (4.50), (4.67), (4.68) and (5.25) into equation (5.24) yields the final Eulerian form:

$$\begin{aligned}
 \dot{C}_v^* d(T_n)_i / dt &= H_i \dot{E}_i + (4\mu/3 + A)_i \{ (g_n A_n)_{i+1} - (g_n A_n)_i / \rho_i^2 \} / v_i + (V\Phi^*(v))_i \\
 &+ (I_i/8\rho_i) \{ (P_i - P_{i-1}) \{ 3(g_n A_n)_i + (g_n A_n)_{i+1} \} / (I_n)_i \\
 &+ (P_{i+1} - P_i) \{ (g_n A_n)_i + 3(g_n A_n)_{i+1} \} / (I_n)_{i+1} \\
 &+ [h(A_n)_e (T_w - T)]_i + \hat{C}_p (g_n A_n)_i (T_n)_i^* - \hat{C}_p (g_n A_n)_{i+1} (T_n)_{i+1}^* \\
 &+ (A_n)_i (T_{i-1} - T_i) 2\kappa_{i-1} / (\kappa_i I_{i-1} + \kappa_{i-1} I_i) \\
 &- (A_n)_{i+1} (T_i - T_{i+1}) 2\kappa_i / (\kappa_{i+1} I_i + \kappa_i I_{i+1}) \} \quad (5.26.1)
 \end{aligned}$$

where  $(T_n)_j^*$  are determined such that for  $j = i$  and  $j = i+1$ :

$$\text{IF } (g_n)_j \geq 0 \text{ then: } (T_n)_j^* = T_{j-1} \quad (5.26.2)$$

$$\text{IF } (g_n)_j < 0 \text{ then: } (T_n)_j^* = T_j \quad (5.26.3)$$

The Lagrangian form of equation (4.43) may be expressed using the structure of equation (3.32). In terms of the system model given by figure 5.4, the Lagrangian form is used in a constant flow area environment only and thus may be simplified to yield:

$$\begin{aligned} \hat{C}_v M_i dT_i/dT = & N_i \hat{E}_i + (4\mu/3+A)_i V_i [(v_{n,i+1} - (v_n)_i)/I_i]^2 \\ & + (V\Phi^*(v))_i + (V_i/8) [(P_i - P_{i-1}) (3(v_n)_i + (v_n)_{i+1}) / (I_n)_i \\ & + (P_{i+1} - P_i) ((v_n)_i + 3(v_n)_{i+1}) / (I_n)_{i+1}] - P_i A_i ((v_n)_{i+1} - (v_n)_i) \\ & + (h(A_n)_o (T_w - T))_i + A_i ((T_{i-1} - T_i) 2\kappa_{i-1} \kappa_i / (\kappa_i I_{i-1} + \kappa_{i-1} I_i) \\ & - (T_i - T_{i+1}) 2\kappa_i \kappa_{i+1} / (\kappa_{i+1} I_i + \kappa_i I_{i+1})) \end{aligned} \quad (5.27)$$

The energy equation in the combined Eulerian/Lagrangian  $c$  mass/energy control volume in the expansion space is given by:

$$\begin{aligned} \hat{C}_v d(TH)_c/dc = & N_c \hat{E}_c + P_c A_c (v_n)_{NE+1} + (4\mu/3+A)_c [(g_n A_n)_1 / \rho_c - (v_n A_n)_{NE+1}]^2 / V_c \\ & + (I_c/8) [(P_c - P_{NE}) (3(v_n A_n)_{NE+1} + (g_n A_n)_1 / \rho_c) / (I_n)_{NE+1} \\ & + (P_1 - P_c) ((v_n A_n)_{NE+1} + 3(g_n A_n)_1 / \rho_c) / (I_n)_1] - \hat{C}_p (g_n A_n)_1 (T_n)_1^* \\ & + (h(A_n)_o (T_w - T))_c + (A_n)_{NE+1} (T_{NE} - T_c) 2\kappa_{NE} \kappa_c / (\kappa_c I_{NE} + \kappa_{NE} I_c) \\ & + (V\Phi^*(v))_c - (A_n)_1 (T_c - T_1) 2\kappa_c \kappa_1 / (\kappa_1 I_c + \kappa_c I_1) \end{aligned} \quad (5.28.1)$$

where  $(T_n)_1^*$  is determined such that:

$$\text{if } (g_n)_1 \geq 0 \text{ then: } (T_n)_1^* = T_c \quad (5.28.2)$$

$$\text{if } (g_n)_1 < 0 \text{ then: } (T_n)_1^* = T_1 \quad (5.28.3)$$

Similarly for the  $\gamma$  mass/energy control volume in the compression space:

$$\begin{aligned}
\hat{C}_V d(T)_T / dc = & N_T \hat{E}_T + (4\mu/3+A_T) \{ (v_{n,n}^A)_{NC+1} - (g_{n,n}^A)_{NT+1} / \rho_T \}^2 / v_T \\
& + (V\Phi^*(v))_T + (I_T/8) \{ (P_T - P_{NT}) \{ 3(g_{n,n}^A)_{NT+1} / \rho_T \\
& + (v_{n,n}^A)_{NC+1} / (I_T)_{NT+1} + (P_{NC} - P_T) \{ (g_{n,n}^A)_{NT+1} / \rho_T \\
& + 3(v_{n,n}^A)_{NC+1} / (I_T)_{NC+1} \} + (h(A_n)_T (T_W - T))_T - P_T A_T (v_{n,n}^A)_{NC+1} \\
& + \hat{C}_P (g_{n,n}^A)_{NT+1} (T_n^*)_{NT+1} + (A_n)_{NT+1} (T_{NT} - T_T) 2\kappa_{NT} \kappa_T / (\kappa_T I_{NT} \\
& + \kappa_{NT} I_T) - (A_n)_{NC+1} (T_T - T_{NC}) 2\kappa_T \kappa_{NC} / (\kappa_{NC} I_T + \kappa_T I_{NC}) \} \quad (5.29.1)
\end{aligned}$$

where  $(T_n^*)_{NT+1}$  is determined such that:

$$\text{if } (g_{n,n}^A)_{NT+1} \geq 0 \text{ then: } (T_n^*)_{NT+1} = T_{NT} \quad (5.29.2)$$

$$\text{if } (g_{n,n}^A)_{NT+1} < 0 \text{ then: } (T_n^*)_{NT+1} = T_T \quad (5.29.3)$$

#### 5.5 THE IMPLICIT NUMERICAL ALGORITHM

The implicit numerical algorithm used has its origins in the implicit Continuous-Fluid Eulerian (ICE) technique of Harlow and Amsden (HA71) and the Semi-Implicit Method for Pressure-Linked Equations, Revised (SIMPLER) of Patankar (Pa80). In turn, this latter method reportedly (Is83) extracts its central idea from a semi-implicit scheme developed by Chorin (Ch68). Although elements of the implicit algorithm are clearly identifiable with the ICE and SIMPLER algorithms and, in particular, the overall iterative approach used conforms to the SIMPLER scheme, the details and sequencing of the algorithm have not been encountered in the literature (Es83, Ro82).

The implicit algorithm is discussed in several sub-sections. Firstly, the necessary implicit pressure, temperature, velocity and mass flux field equations are developed from the one-dimensional integral

balances discussed in section 5.4. As before, the Eulerian, Lagrangian and CEL forms of the relevant equations are listed for the sake of completeness. Thereafter, the algorithm itself is defined in terms of these implicit field relationships. Finally, the methodology used to interface the Eulerian and Lagrangian fields is discussed in terms of the defined algorithmic structure.

#### 5.5.1 The Implicit Pressure, Temperature, Velocity and Mass Flux Field Equations

Central to the implicit algorithm is the methodology by which the implicit pressure field equation (5.2) is extracted from a combination of the conservation of mass and momentum equations. This methodology is in essence similar to that proposed by Harlow and Amsden in the ICE algorithm.

Discretising the left hand side of equation (5.13.1) and invoking equations (5.13.2) and (5.13.3) allows the Eulerian integral momentum balances to be given the form (for  $2 \leq i \leq NT$ ):

$$\langle K_n \mathcal{E}_n \rangle_i = \langle K_{nL} \rangle_i (\mathcal{E}_n)_{i-1} + \langle K_{nR} \rangle_i (\mathcal{E}_n)_{i+1} + \langle A_n \rangle_i (P_{i-1} - P_i) + \langle \alpha_n \rangle_i \quad (5.30.1)$$

where:

$$\beta_L = \langle A_n \rangle_{i-1} \{A(4\mu/3+\lambda)/M\}_{i-1} \quad (5.30.2)$$

$$\beta_R = \langle A_n \rangle_{i+1} \{A(4\mu/3+\lambda)/M\}_i \quad (5.30.3)$$

$$\langle K_{nL} \rangle_i = \beta_L \left[ + v_{i-1} \langle A_n \rangle_{i-1} \right] \text{ if } v_{i-1} \geq 0 \quad (5.30.4)$$

$$\langle K_{nR} \rangle_i = \beta_R \left[ -v_i \langle A_n \rangle_i \right] \text{ if } v_i < 0 \quad (5.30.5)$$

$$\langle K_n \rangle_i = \langle v_n \rangle_i / \Delta t + \beta_L + \beta_R \left[ -v_{i-1} \langle A_n \rangle_i \right] \text{ if } v_{i-1} < 0 \quad \left[ +v_i \langle A_n \rangle_i \right] \text{ if } v_i \geq 0 \quad (5.30.6)$$

$$\langle \alpha_n \rangle_i = \langle v_n^* \beta_n^* \rangle_i / \Delta t - \langle M_n \rangle_i g - \langle \Omega(v) A_o \rangle_{i-1} - \langle \Omega(v) A_o \rangle_i \quad (5.30.7)$$

For the momentum control volume straddling the expansion/transfer space junction (i=1), equation (5.13.1) is coupled with equations (5.14) to produce:

$$\langle K_{nS_n} \rangle_1 = \langle K_{nL} \rangle_1 \langle v_n \rangle_{nE+1} + \langle K_{nR} \rangle_1 \langle g_n \rangle_2 + \langle A_n \rangle_1 \langle P_c - P_1 \rangle + \langle \alpha_n \rangle_1 \quad (5.30.8)$$

where  $\beta_R$  and  $\langle K_{nR} \rangle_1$  are given by equations (5.30.3) and (5.30.5) respectively with i=1 while:

$$\beta_L = (A(4\mu/3+\lambda)/H)_c \quad (5.30.9)$$

$$\langle K_{nL} \rangle_1 = \rho_c \langle A_n \rangle_{nE+1} \beta_L \left[ +v_c \rho_c \langle A_n \rangle_{nE+1} \right] \text{ if } v_c \geq 0 \quad (5.30.10)$$

$$\langle K_n \rangle_1 = \langle v_n \rangle_1 / \Delta t + \langle A_n \rangle_1 \beta_L + \beta_R \left[ -v_c \langle A_n \rangle_1 \right] \text{ if } v_c < 0 \quad \left[ +v_1 \langle A_n \rangle_1 \right] \text{ if } v_1 \geq 0 \quad (5.30.11)$$

$$\langle \alpha_n \rangle_1 = \langle v_n^* \beta_n^* \rangle_1 / \Delta t - \langle M_n \rangle_1 g - \langle \Omega(v) A_o \rangle_{1c} - \langle \Omega(v) A_o \rangle_1 \quad (5.30.12)$$

Similarly, for the momentum control volume straddling the compression/transfer space junction (i=NT+1), equations (5.13.1) and (5.15) are combined to yield:

$$(K_{nR}^n)_{NT+1} = (K_{nL}^n)_{NT+1}(g_n)_{NT} + (K_{nR}^n)_{NT+1}(v_n)_{NC+1} + (A_n)_{NT+1}(P_{NT} - P_T) + (\alpha_n)_{NT+1} \quad (5.30.13)$$

where, in this case,  $\beta_L$  and  $(K_{nL}^n)_{NT+1}$  are given respectively by equations (5.30.2) and (5.30.4) with  $i=NT+1$ , while:

$$\beta_R = \{A(4\mu/3+\lambda)/H\}_T \quad (5.30.14)$$

$$(K_{nR}^n)_{NT+1} = \rho_T(A_n)_{NC+1}\beta_R \left[ -v_T \rho_T(A_n)_{NC+1} \right]_{i \in v_T < 0} \quad (5.30.15)$$

$$(K_n)_{NT+1} = (v_n)_{NT+1}/\Delta c + \beta_L + (A_n)_{NT+1}\beta_R \left[ -v_{NT}(A_n)_{NT} \right]_{i \in v_{NT} < 0} \left[ +v_T(A_n)_{NT+1} \right]_{i \in v_T \geq 0} \quad (5.30.16)$$

$$(\alpha_n)_{NT+1} = (v_n^* v_n^*)_{NT+1}/\Delta c - (M_n)_{NT+1}E - \{N(v)A_n\}_{NT} - \{N(v)A_n\}_T \quad (5.30.17)$$

The Lagrangian integral momentum balances are obtained from equation

(5.16) which may be manipulated to yield, for  $2 \leq i \leq NE$  or  $2 \leq j \leq$

NC:

$$(K_n v_n)_i = (K_{nL}^n)_i (v_n)_{i-1} + (K_{nR}^n)_i (v_n)_{i+1} + (A_n)_i (P_{i-1} - P_i) + (\alpha_n)_i \quad (5.31.1)$$

where:

$$(K_{nR}^n)_i = \{A(4\mu/3+\lambda)/l\}_i \quad (5.31.2)$$

$$(K_{nL}^n)_i = \{A(4\mu/3+\lambda)/l\}_{i-1} \quad (5.31.3)$$

$$(K_n)_i = (M_n)_i/\Delta c + (K_{nL}^n)_i + (K_{nR}^n)_i \quad (5.31.4)$$

$$(\alpha_n)_i = (v_n^* v_n^*)_i/\Delta c - (M_n)_i E - \{N(v)A_n\}_{i-1} - \{N(v)A_n\}_i \quad (5.31.5)$$

The integral momentum balance for the (NE+1) control volume in the expansion space is determined from the combination of equations (5.16) and (5.17) resulting in:

$$\begin{aligned} \langle K_{n'n} \rangle_{NE+1} = & \langle K_{nL} \rangle_{NE+1} \langle v_n \rangle_{NE} + \langle K_{nR} \rangle_{NE+1} \langle g_n \rangle_1 + \langle A_n \rangle_{NE+1} (P_{NE} - P_e) \\ & + \langle \alpha_n \rangle_{NE+1} \end{aligned} \quad (5.31.6)$$

where  $\langle K_{nL} \rangle_{NE+1}$  is defined by equation (5.31.3) with  $l = NE+1$  and:

$$\beta_R = \{A(4\mu/3+A)/M\}_e \quad (5.31.7)$$

$$\langle K_{nR} \rangle_{NE+1} = \langle A_n \rangle_1 \beta_R \left[ -v_e \langle A_n \rangle_1 \right] \text{ if } v_e < 0 \quad (5.31.8)$$

$$\begin{aligned} \langle K_n \rangle_{NE+1} = & \langle H_n \rangle_{NE+1} / \Delta t + \langle K_{nL} \rangle_{NE+1} + \rho_e \langle A_n \rangle_{NE+1} \beta_R \\ & \left[ + v_e \rho_e \langle A_n \rangle_{NE+1} \right] \text{ if } v_e \geq 0 \end{aligned} \quad (5.31.9)$$

$$\langle \alpha_n \rangle_{NE+1} = \langle H_{n'n}^2 \rangle_{NE+1} / \Delta t - \langle H_n \rangle_{NE+1} g - \{ \Omega(v) A_\sigma \}_{NE} - \{ \Omega(v) A_\sigma \}_e \quad (5.31.10)$$

Similarly for the compression space, the (NC+1) control volume integral momentum balance is obtained from equations (5.16) and (5.18) which combine to produce:

$$\begin{aligned} \langle K_{n'n} \rangle_{NC+1} = & \langle K_{nL} \rangle_{NC+1} \langle g_n \rangle_{NT+1} + \langle K_{nR} \rangle_{NC+1} \langle v_n \rangle_{NC} + \langle A_n \rangle_{NC+1} (P_T - P_{NC}) \\ & + \langle \alpha_n \rangle_{NC+1} \end{aligned} \quad (5.31.11)$$

where  $\langle K_{nR} \rangle_{NC+1}$  is defined by equation (5.31.2) with  $j = NC+1$  and:

$$\beta_L = \{A(4\mu/3+A)/M\}_T \quad (5.31.12)$$

$$\langle K_{nL} \rangle_{NC+1} = \langle A_n \rangle_{NT+1} \beta_L \left[ + v_T \langle A_n \rangle_{NT+1} \right] \text{ if } v_T \geq 0 \quad (5.31.13)$$

$$\begin{aligned}
 (X_n)_{NC+1} &= (X_n)_{NC+1}/\Delta t + \rho_\gamma (A_n)_{NC+1} \beta_L + (X_{nR})_{NC+1} \\
 &\left[ -v_\gamma \rho_\gamma (A_n)_{NC+1} \right]_{iE} v_\gamma < 0
 \end{aligned}
 \tag{5.31.14}$$

$$(\alpha_n)_{NC+1} = (H_n^* v_n^*)_{NC+1}/\Delta t - (H_n)_{NC+1} B - (\Omega(v)A_p)_\gamma - (\Omega(v)A_p)_{nR}
 \tag{5.31.15}$$

Discretising the left hand side of equation (5.3) and substituting the equation of state (4.13) produces:

$$(PV/RT - H^*)_{iE}/\Delta t = (g_n A_n)_{iE} - (g_n A_n)_{i+1}
 \tag{5.32}$$

The left hand side of equation (5.32) is implicitly dependent upon the information propagation rate at time  $t^* + \Delta t$  (see figure 5.2) for the mass/energy control volume  $i$ . This may be shown by noting that  $V_i$  is a constant for a Eulerian control volume so that:

$$\begin{aligned}
 PV/RT - H^* &= V(P - RT\rho^*)/RT \\
 &= VRT(\rho - \rho^*)/RT \\
 &= (V/RT)(\partial P/\partial \rho)_T(\rho - \rho^*)
 \end{aligned}
 \tag{5.33}$$

where  $(\partial P/\partial \rho)_T$  is the square of the isothermal speed of sound for a fluid with constant specific heats.

Substituting equation (5.30.1) into equation (5.32) and rearranging produces the implicit Eulerian pressure field relationship:

$$\begin{aligned}
 P_i (V_i/RT)_i \Delta t + (A_n^2/K_n)_i + (A_n^2/K_n)_{i+1} &\cdot P_{i-1} (A_n^2/K_n)_i \\
 - P_{i+1} (A_n^2/K_n)_{i+1} & \\
 - & \\
 H_i^2/\Delta t + (A_n)_i \{ (\beta_n)_{i-1} (K_{nL})_i + (\beta_n)_{i+1} (K_{nR})_i + (\alpha_n)_i \} / (K_n)_i & \\
 - (A_n)_{i+1} \{ (\beta_n)_i (K_{nL})_{i+1} + (\beta_n)_{i+2} (K_{nR})_{i+1} + (\alpha_n)_{i+1} \} / (K_n)_{i+1} &
 \end{aligned}
 \tag{5.34}$$

The Lagrangian pressure field relationship may be found by manipulating equation (5.4) as follows:

$$0 = dM_i/dt \\ = \rho_i dV_i/dt + V_i d\rho_i/dt$$

Since the control volume flow areas in the Lagrangian zones are constant, in advanced time form this becomes:

$$d\rho_i/dt = \rho_i (v_i - v_{i+1})_n / l_i$$

Discretising the left hand side and substituting equation (4.13):

$$(P/RT - \rho^s)_i / \Delta t = \rho_i (v_i - v_{i+1})_n / l_i \quad (5.35)$$

Following a manipulation similar to that used to produce equation (5.33), the implicit dependence of the left hand side of equation (5.35) on the information propagation rate may also be demonstrated. Substituting equation (5.31.1) into equation (5.35) and rearranging yields the implicit Lagrangian pressure field equation:

$$P_i [(1/RT)_i \Delta t + \rho_i \{ (A_n/K_n)_i + (A_n/K_n)_{i+1} / l_i \}] - P_{i-1} \rho_i (A_n/K_n)_i / l_i \\ - P_{i+1} \rho_i (A_n/K_n)_{i+1} / l_i \\ \rho_i^s / \Delta t + \rho_i [ (v_n)_{i-1} (K_{nL})_i + (v_n)_{i+1} (K_{nR})_i + (\alpha_n)_i / (K_n)_i \\ - (v_n)_i (K_{nL})_{i+1} + (v_n)_{i+2} (K_{nR})_{i+1} + (\alpha_n)_{i+1} / (K_n)_{i+1} ] / l_i \quad (5.36)$$

Considering the  $\epsilon$  CEL control volume, using a process similar to that which produced equation (5.35), equation (5.5.1) may be transformed into:

$$(P/RT - \rho^s)_\epsilon / \Delta t = \rho_\epsilon v_{\epsilon\epsilon+1} / l_\epsilon - (g_n^s)_i / V_\epsilon \quad (5.37)$$

Substituting equations (5.30.8) and (5.31.6) into equation (5.37) and rearranging yields the  $z$  control volume pressure field equation:

$$\begin{aligned}
 & P_z \{ 1/RT_z \Delta t + \rho_z (A_N/K_N)_{NE+1}/I_z + (A_N^2/K_N)_1/V_z \} - P_{NE} \rho_z (A_N/K_N)_{NE+1}/I_z \\
 & - P_1 (A_N^2/K_N)_1/V_z \\
 & = \\
 & \rho_z^2/\Delta t + \rho_z \{ (v_N)_{NE} (K_{NL})_{NE+1} + (g_N)_1 (K_{NR})_{NE+1} + (\alpha_N)_{NE+1} \} / (K_N)_{NE+1} I_z \\
 & - (A_N)_1 \{ (v_N)_{NE+1} (K_{NL})_1 + (g_N)_z (K_{NR})_1 + (\alpha_N)_1 \} / (K_N)_1 V_z \quad (5.38)
 \end{aligned}$$

Similarly, the pressure field relationship in the  $\gamma$  CEL control volume is given by:

$$\begin{aligned}
 & P_\gamma \{ 1/RT_\gamma \Delta t + (A_N^2/K_N)_{NT+1}/V_\gamma + \rho_\gamma (A_N/K_N)_{NC+1}/I_\gamma \} \\
 & - P_{NT} (A_N^2/K_N)_{NT+1}/V_\gamma - P_{NC} \rho_\gamma (A_N/K_N)_{NC+1}/I_\gamma \\
 & = \\
 & \rho_\gamma^2/\Delta t + (A_N)_{NT+1} \{ (g_N)_{NT} (K_{NL})_{NT+1} + (v_N)_{NC+1} (K_{NR})_{NT+1} \\
 & + (\alpha_N)_{NT+1} \} / (K_N)_{NT+1} V_\gamma - \rho_\gamma \{ (g_N)_{NT+1} (K_{NL})_{NC+1} + (v_N)_{NC} (K_{NR})_{NC+1} \\
 & + (\alpha_N)_{NC+1} \} / (K_N)_{NC+1} I_\gamma \quad (5.39)
 \end{aligned}$$

The temperature field equation in the Eulerian zone may be determined directly from equations (5.26). Discretising the left hand side of equation (5.26.1) and rearranging yields:

$$K_I^T I_L - (K_L)_I^T I_{L-1} - (K_R)_I^T I_{L+1} = \alpha_I \quad (5.40.1)$$

where the constants are defined by the threaded sequence:

$$\beta_L = 2(A_N)_I \kappa_{I-1} \kappa_I / (\kappa_I I_{I-1} + \kappa_{I-1} I_I) \quad (5.40.2)$$

$$\beta_R = 2(A_N)_{I+1} \kappa_I \kappa_{I+1} / (\kappa_{I+1} I_I + \kappa_I I_{I+1}) \quad (5.40.3)$$

$$(K_L)_I = \beta_L \left[ + \hat{C}_P (g_N A_N)_I \right] \text{ if } (g_N)_I \geq 0 \quad (5.40.4)$$

$$(K_R)_i = \beta_R \left[ -\hat{C}_P(\mathcal{E}_N^A)_i \right]_{iF} (\mathcal{E}_N)_i < 0 \quad (5.40.5)$$

$$K_i = \hat{C}_V M_i / \Delta t + \beta_L + \beta_R + (h(A_N)_\sigma)_i \left[ -\hat{C}_P(\mathcal{E}_N^A)_i \right]_{iF} (\mathcal{E}_N)_i < 0 \\ \left[ + \hat{C}_P(\mathcal{E}_N^A)_{i+1} \right]_{iF} (\mathcal{E}_N)_{i+1} \geq 0 \quad (5.40.6)$$

$$\alpha_i = \hat{C}_V (h^* T^*)_{iF} / \Delta t + M_i \hat{E}_i + (4\mu/3 + \lambda)_i [(\mathcal{E}_N^A)_{i+1} - (\mathcal{E}_N^A)_i] / \rho_i^2 / V_i \\ + (V\Phi^*(v))_i + (I_i / \beta \rho_i) [(P_i - P_{i-1}) (3(\mathcal{E}_N^A)_i + (\mathcal{E}_N^A)_{i+1}) / (I_N)_i \\ + (P_{i+1} - P_i) ((\mathcal{E}_N^A)_i + 3(\mathcal{E}_N^A)_{i+1}) / (I_N)_{i+1}] + (h(A_N)_\sigma T_W)_i \quad (5.40.7)$$

The implicit temperature field equation in the Lagrangian space is similarly defined with the notable addition that the work term  $(P_i dV_i / dt)$  is included in the temperature coefficient term  $K_i$  rather than in the constant term  $\alpha_i$ . This is accomplished by substituting the equation of state (4.13) into the second term on the right hand side of equation (5.27) yielding:

$$P_i A_i [(v_N)_{i+1} - (v_N)_i] = \rho_i R T_i A_i [(v_N)_{i+1} - (v_N)_i] \quad (5.41)$$

Hence, discretising the left hand side of equation (5.27), substituting equation (5.41) and rearranging produces:

$$K_i T_i - (K_L)_i T_{i-1} - (K_R)_i T_{i+1} = \alpha_i \quad (5.42.1)$$

where the constants are redefined by:

$$(K_L)_i = 2A_i \kappa_{i-1} \kappa_i / (\kappa_i^2 I_{i-1} + \kappa_{i-1}^2 I_i) \quad (5.42.2)$$

$$(K_R)_i = 2A_i \kappa_i \kappa_{i+1} / (\kappa_{i+1}^2 I_i + \kappa_i^2 I_{i+1}) \quad (5.42.3)$$

$$K_i = \hat{C}_V M_i / \Delta t + (K_L + K_R)_i + \rho_i R A_i [(v_N)_{i+1} - (v_N)_i] + (h(A_N)_\sigma)_i \quad (5.42.4)$$

$$\alpha_L = \hat{C}_V (H T^*)_{L} / \Delta t + H_L \hat{E}_L + (4\mu/3+A)_L V_L [(v_n)_{L+1} - (v_n)_L] / I_L]^2 + (V \Phi^*(v))_L + (V_L/B) [(P_L - P_{L-1}) \{3(v_n)_L + (v_n)_{L+1}\} / (I_n)_L + (P_{L+1} - P_L) \{(v_n)_L + 3(v_n)_{L+1}\} / (I_n)_{L+1}] + (h(A_n)_\sigma T_w)_L \quad (5.42.5)$$

Similarly, for the CEL  $\epsilon$  control volume, using an equation of state substitution, equation (5.28) may be manipulated to yield:

$$K_\epsilon T_\epsilon - (K_L)_\epsilon T_{NE} - (K_R)_\epsilon T_1 = \alpha_\epsilon \quad (5.43.1)$$

where:

$$(K_L)_\epsilon = 2(A_n)_{NE+1} \kappa_{NE} \kappa_\epsilon / (\kappa_\epsilon I_{NE} + \kappa_{NE} I_\epsilon) \quad (5.43.2)$$

$$\beta_R = 2(A_n)_1 \kappa_\epsilon \kappa_1 / (\kappa_1 I_\epsilon + \kappa_\epsilon I_1) \quad (5.43.3)$$

$$(K_R)_\epsilon = \beta_R \left[ -\hat{C}_P (g_n A_n)_1 \right]_{1\epsilon} (g_n)_1 < 0 \quad (5.43.4)$$

$$K_\epsilon = \hat{C}_V H_\epsilon / \Delta t + (K_L)_\epsilon + \beta_R - \rho_\epsilon R A_\epsilon (v_n)_{NE+1} + (h(A_n)_\sigma)_\epsilon \left[ + \hat{C}_P (g_n A_n)_1 \right]_{1\epsilon} (g_n)_1 \geq 0 \quad (5.43.5)$$

$$\alpha_\epsilon = \hat{C}_V (H^* T^*)_\epsilon / \Delta t + H_\epsilon \hat{E}_\epsilon + (4\mu/3+A)_\epsilon [(g_n A_n)_1 / \rho_\epsilon - (v_n A_n)_{NE+1}]^2 / V_\epsilon + (V \Phi^*(v))_\epsilon + (I_\epsilon/B) [(P_\epsilon - P_{NE}) \{3(v_n A_n)_{NE+1} + (g_n A_n)_1 / \rho_\epsilon\} / (I_n)_{NE+1} + (P_1 - P_\epsilon) \{(v_n A_n)_{NE+1} + 3(g_n A_n)_1 / \rho_\epsilon\} / (I_n)_1] + (h(A_n)_\sigma T_w)_\epsilon \quad (5.43.6)$$

Likewise, for the combined Eulerian/Lagrangian  $\gamma$  control volume, after manipulation, equation (5.29) produces:

$$K_\gamma T_\gamma - (K_L)_\gamma T_{NT} - (K_R)_\gamma T_{NC} = \alpha_\gamma \quad (5.44.1)$$

where:

$$\beta_L = 2(A_n)_{NT+1} \kappa_{NT} \kappa_\gamma / (\kappa_\gamma I_{NT} + \kappa_{NT} I_\gamma) \quad (5.44.2)$$

$$\langle K_L \rangle_\gamma = \beta_L \left[ + \hat{C}_p (\mathcal{E}_N^A)_{NT+1} \right] \text{if } (\mathcal{E}_N^A)_{NT+1} \geq 0 \quad (5.44.3)$$

$$\langle K_R \rangle_\gamma = 2(A_N)_{NC+1} \kappa_\gamma \kappa_{NC} / (\kappa_{NC} I_\gamma + \kappa_\gamma I_{NC}) \quad (5.44.4)$$

$$\begin{aligned} \kappa_\gamma = \hat{C}_v H_\gamma / \Delta t + \beta_L + \langle K_R \rangle_\gamma + \rho_\gamma R A_\gamma \langle v_N \rangle_{NC+1} + \langle h(A_N)_o \rangle_\gamma \\ \left[ - \hat{C}_p (\mathcal{E}_N^A)_{NT+1} \right] \text{if } (\mathcal{E}_N^A)_{NT+1} < 0 \end{aligned} \quad (5.44.5)$$

$$\begin{aligned} \alpha_\gamma = \hat{C}_v (H^* T^*)_\gamma / \Delta t + H_\gamma \hat{E}_\gamma + (4\mu/3+A)_\gamma [ \langle (v_N^A)_{NC+1} - (\mathcal{E}_N^A)_{NT+1} / \rho_\gamma \rangle^2 / \gamma \\ + \langle V\Phi^* \rangle_\gamma + (1_\gamma/B) \{ \langle P_\gamma - P_{NT} \rangle \{ 3(\mathcal{E}_N^A)_{NT+1} / \rho_\gamma + \langle v_N^A \rangle_{NC+1} \} / (1_N)_{NT+1} \\ + \langle P_{NC} - P_\gamma \rangle \{ (\mathcal{E}_N^A)_{NT+1} / \rho_\gamma + 3 \langle v_N^A \rangle_{NC+1} \} / (1_N)_{NC+1} \} \\ + \langle h(A_N)_o T_w \rangle_\gamma \end{aligned} \quad (5.44.6)$$

Finally, the implicit forms of the momentum equations may be determined from the previous discussion. For the Eulerian zone, the implicit mass flux field equations are given by rearranging equations (5.30) as:

$$\langle K_R \mathcal{E}_N \rangle_1 - \langle K_{NL} \rangle_1 \langle v_N \rangle_{NE+1} - \langle K_{NR} \rangle_1 (\mathcal{E}_N)_2 = \langle A_N \rangle_1 (P_e - P_1) + \langle \alpha_N \rangle_1 \quad (5.45.1)$$

$$\begin{aligned} \langle K_R \mathcal{E}_N \rangle_{NT+1} - \langle K_{NL} \rangle_{NT+1} \langle \mathcal{E}_N \rangle_{NT} - \langle K_{NR} \rangle_{NT+1} \langle v_N \rangle_{NC+1} = \langle A_N \rangle_{NT+1} (P_{NT} - P_\gamma) \\ + \langle \alpha_N \rangle_{NT+1} \end{aligned} \quad (5.45.2)$$

and for  $2 \leq l \leq NT$ :

$$\langle K_R \mathcal{E}_N \rangle_l - \langle K_{NL} \rangle_l \langle \mathcal{E}_N \rangle_{l-1} - \langle K_{NR} \rangle_l \langle \mathcal{E}_N \rangle_{l+1} = \langle A_N \rangle_l (P_{l-1} - P_l) + \langle \alpha_N \rangle_l \quad (5.45.3)$$

Similarly, the velocity field equations in the Lagrangian zones are given by rearranging equations (5.31) to produce:

$$\begin{aligned} \langle K_N v_N \rangle_{NE+1} - \langle K_{NL} \rangle_{NE+1} \langle v_N \rangle_{NE} - \langle K_{NR} \rangle_{NE+1} \langle \mathcal{E}_N \rangle_1 = \langle A_N \rangle_{NE+1} (P_{NE} - P_e) \\ + \langle \alpha_N \rangle_{NE+1} \end{aligned} \quad (5.46.1)$$

$$(K_N v_N)_{SC+1} - (K_{NL})_{SC+1} (v_N)_{ST+1} - (K_{NR})_{SC+1} (v_N)_{SC} - (A_N)_{SC+1} (P_{j-1} - P_{SC}) + (\alpha_N)_{SC+1} \quad (5.46.2)$$

and for  $2 \leq i \leq NE$  or  $2 \leq j \leq NC$ :

$$(K_N v_N)_i - (K_{NL})_i (v_N)_{i-1} - (K_{NR})_i (v_N)_{i+1} - (A_N)_i (P_{j-1} - P_i) + (\alpha_N)_i \quad (5.46.3)$$

### 5.5.2 The Implicit Numerical Algorithm Computing Sequence

The algorithm is presented in the form of a sequence of operations required to progress from time  $t^*$  to time  $t^* + \Delta t$ . Peripheral issues such as the establishment of initial conditions, fluid property determinations, data input/output procedures and the like are discussed in appendix F. Machine specific details such as the computation of tube wall or regenerator matrix temperature fields (which are based on thermal conduction considerations and are not intrinsic to the fluid dynamics) are discussed in chapter 7 for the specific hardware simulated. As elucidated in section 5.2, two versions of the algorithm are presented. The equilibrium algorithm based on the infinite information propagation hypothesis is described first followed by the unitary pressure domain (UPD) algorithm embodying the characteristically determined integration time increment hypothesis.

#### 5.5.2.1 Equilibrium Algorithm

Assuming a constant, arbitrarily determined integration time increment  $\Delta t$  which is much less than the smallest time characteristic of a given Stirling machine, the equilibrium algorithm is given by the following

computational sequence:

1. Determine the expansion space and compression space piston kinematics at time  $t^* + \Delta t$ , that is, find  $(x_n, v_n)_{ie}$ ,  $(x_n, v_n)_{ic}$ .
2. Guess the Lagrangian zone velocity fields  $(v_n^*)|_{i-2, NE+1}$  and  $(v_n^*)|_{i-2, NC+1}$  and the Eulerian zone mass flux field  $(g_n^*)|_{i-1, NT+1}$  at time  $t^* + \Delta t$  by setting  $(v_n^*)_i = (v_n^*)_i$  and  $(g_n^*)_i = (g_n^*)_i$ .
3. Explicitly compute the CEL zone control volume masses using equations (5.5) as follows:

$$M_\epsilon = M_\epsilon^* - \Delta t (g_n^* A)_{i-1} \quad (5.47.1)$$

$$M_\gamma = M_\gamma^* + \Delta t (g_n^* A)_{NT+1} \quad (5.47.2)$$

4. Test whether the masses in the  $\epsilon$  and  $\gamma$  CEL control volumes are sufficiently large. If not, reduce the time increment  $\Delta t$  and return to step 3.
5. Explicitly compute the Eulerian zone control volume masses using equation (5.3) as follows:

$$M_i = M_i^* + \Delta t (g_n^* A)_{i-1} - (g_n^* A)_{i+1} \quad (5.47.3)$$

6. Explicitly compute the Lagrangian zone momentum control volume displacements from:

$$(v_n^*)_i = d(v_n^*)_i / dt$$

such that.

$$(x_n)_i = (x_n^s)_i + \Delta t (v_n^s)_i \quad (5.48)$$

7. Determine the density field in all spaces using equation (4.32).
8. Compute the necessary fluid properties such as viscosity and conductivity and calculate the mass/energy control volume velocities using equations (4.51.1) and (4.53). Thereby determine the required empirical coefficients (heat transfer coefficients and friction factors) using appropriate correlation formulae or tabulations.
9. Implicitly solve equations (5.40.1), (5.42.1), (5.43.1) and (5.44.1) to produce the unified temperature field at time  $t^n + \Delta t$ .
10. Implicitly compute all the necessary thermal conduction temperature fields (such as those occurring in tube walls and regenerator matrices) using the advanced time fluid temperatures of step 9 as boundary conditions.
11. Implicitly solve equations (5.34), (5.36), (5.38) and (5.39) as a unified field, using the latest advanced time temperatures to determine the pressure field at time  $t^n + \Delta t$ .
12. Solve equations (5.45) and (5.46) implicitly to produce the unified advanced time velocity and mass flux fields, using the advanced time pressures of step 11.

13. IF: { all  $g_n$  and  $v_n$  are sufficiently converged, or:  

$$\max \left( (1 - |g_n^*/g_n|) \Big|_{i=1, NE+1}, (1 - |v_n^*/v_n|) \Big|_{i=2, NE+1} \right) < \beta \quad (5.49)$$

$$\Big|_{i=2, NC+1}$$
where  $\beta$  is of arbitrary smallness }

THEN:

{ go to step 14. }

ELSE: { set:

$$\beta_{conv}(g_n)_i + (1 - \beta_{conv})(g_n^*)_i \rightarrow (g_n^*)_i \Big|_{i=1, NE+1}$$

$$\beta_{conv}(v_n)_i + (1 - \beta_{conv})(v_n^*)_i \rightarrow (v_n^*)_i \Big|_{i=2, NE+1} \\ i=2, NC+1$$

where  $\beta_{conv}$  is a convergence factor in the range  
 $0 < \beta_{conv} \leq 1$ . Go to step 3. }

14. Test the mass in the  $\epsilon$  CEL control volume as follows:

IF: {  $M_t < (M_t)_{min}$  and  $NE > 1$  }

THEN:

{ Combine the NE an  $\epsilon$  mass/energy control volumes and  
reduce the number of Lagrangian control volumes by 1 or  
 $NE-1 \rightarrow NE$ . Go to next step. }

ELSE IF: {  $M_t > (M_t)_{max}$  }

THEN:

{ Create a new Lagrangian mass/energy control volume  
by partitioning the  $\epsilon$  CEL control volume and increase  
the number of Lagrangian control volumes by 1 or  
 $NE+1 \rightarrow NE$ . Go to next step. }

ELSE: { go to next step. }

15. Repeat step 14 for the  $\gamma$  CEL control volume by replacing  $\epsilon$  with  $\gamma$  and NE with NC.
16. Set  $t^s + \Delta t \rightarrow t^s$  and all necessary  $\psi \rightarrow \psi^s$  (where  $\psi$  = mass, momentum, energy, etcetera) and repeat from step 1.

#### 5.5.2.2 Unitary Pressure Domain (UPD) Algorithm

The UPD algorithm (which is the limiting case of the pressure domain splitting (PDS) algorithms) has the potential for generating very large time increments. This has the advantage of producing a significant increase in computation speed since fewer time increments are required to integrate the equations over a cycle. However, fewer time increments make a fine resolution of the flow field in the Lagrangian spaces impractical using the algorithm described above because of the need to reconfigure expansion and compression space control volumes at almost every time step. It may be noted, though, that this impracticality would not apply to the full PDS algorithm since arbitrary time increments of adequate smallness may be selected to restore the viability of the CEL interfacing scheme described.

The UPD algorithm may be formulated as a subset of the infinite information propagation algorithms since the CEL interfacing steps fall away and the expansion and compression spaces are represented throughout the cycle by the  $\epsilon$  and  $\gamma$  control volumes respectively. Thus the UPD algorithm may be described in terms of steps 1-16 listed in section 5.5.2.1 as follows:

- a. Compute the time increment  $\Delta t$  from:

$$\Delta t = \max \left\{ \sum_i L_i / |v_i - \langle v_a \rangle_i|, \sum_i L_i / |v_i + \langle v_a \rangle_i| \right\}_{i=1, (1, NT), 2}$$

b. Step 1.

c. Guess the Eulerian zone mass flux field  $(g_n^*)_{i=1, NT+1}$  at time  $t^* + \Delta t$  by setting  $\langle g_n^* \rangle_i = \langle g_n^* \rangle_i$ .

d. Execute the following steps omitting all references to the Lagrangian zones: 3, 5, 7-12.

e. IF: { all  $g_n$  are sufficiently converged, or from equation (5.48):

$$\max \left\{ (1 - |g_n^* / g_n|)_{i=1, NT+1} \right\} < \beta$$

THEN:

{ go to step f. }

ELSE: { set:  $\beta_{conv}(g_n)_i + (1 - \beta_{conv})(g_n^*)_i \rightarrow (g_n^*)_i$  |  $i=1, NT+1$   
Go to step a. }

f. Step 16 and repeat from step 1.

In practice, this algorithm has an artificial limitation in the sense that it does not permit precise values for cyclically integrated parameters (such as heat transfers and indicated works) to be computed. This arises because, in general, a given cyclic period will not contain an integral number of time characteristics, or, the end of a cycle and the completion of a pressure pulse traverse will not coincide. Various methods of dealing with this difficulty have been tested including the obvious protocol of interpolating between data points to determine the cyclic closure values. However, the characteristics of the implicit algorithm combined with the relative sparsity of data points produced make the interpolation protocol quite

hazardous and prone to large errors. Thus an alternate approach has been developed in which the average time increment over an entire cycle is used to generate the nearest integral number of increments to be used in the next cycle, or:

$$\text{no. of increments} = \text{integer} (t_{\text{per}} / (\Delta t)_{\text{average}} + 0.5)$$

This approach, while eliminating the numerical cyclic integral errors, has been demonstrated to yield small discrepancies in closure temperatures and pressures under oneous boundary conditions (Go87.1). Hence, in physical terms, the cyclic integral values produced by the time increment approximation are not exact UPD values. The cyclic integral errors seem to be proportional to the operating frequency such that at 100Hz, the errors reach values of about 2-3% (Go87.1). If necessary, this discrepancy must be taken into account when comparing experimental results with those simulated by the UPD algorithms.

### 5.5.3 Discussion of the Implicit Algorithm

The structure of the implicit algorithm described above is the result of a prolonged trial and error development process. Hence the principal justification for the algorithm's structure is its demonstrated efficacy under a wide range of generalised fluid dynamic boundary conditions including, for example, its application to a generalised cavity flow problem in two-dimensions (Go85). Since myriad different approaches to solving the given equation set are theoretically possible, the selection process necessarily depends on criteria such as computational speed, ease of implementation and data

storage requirements. Hence for Stirling machine boundary conditions, the implicit algorithm described above outperformed the SIMPLER algorithm in all categories, notably in computational speed. This is attributable to the implicit algorithm's significantly faster rate of convergence, that is, fewer iterations are required to satisfy equation (5.49) than needed by the SIMPLER algorithm. However, this improvement in performance is only substantial under conditions in which the various coefficient matrices are inverted using non-iterative techniques such as Gaussian elimination or Crout reduction (Ge70). In a one-dimensional context this is not a limitation, since all the implicit field equations may be cast in the following tri-diagonal matrix (TDMA) form:

$$\begin{bmatrix}
 K_{11} & K_{12} & 0 & \cdot & \cdot & \cdot & 0 \\
 K_{21} & K_{22} & K_{23} & \cdot & \cdot & \cdot & 0 \\
 0 & \cdot & \cdot & \cdot & \cdot & \cdot & \cdot \\
 \cdot & \cdot & \cdot & \cdot & \cdot & \cdot & \cdot \\
 \cdot & \cdot & \cdot & \cdot & \cdot & \cdot & 0 \\
 0 & \cdot & \cdot & K_{m-1,m-2} & K_{m-1,m-1} & K_{m-1,m} & \cdot \\
 0 & \cdot & \cdot & 0 & K_{m,m-1} & K_{m,m} & \cdot
 \end{bmatrix}
 \begin{bmatrix}
 \psi_1 \\
 \cdot \\
 \cdot \\
 \cdot \\
 \cdot \\
 \cdot \\
 \psi_m
 \end{bmatrix}
 =
 \begin{bmatrix}
 \alpha_1 \\
 \cdot \\
 \cdot \\
 \cdot \\
 \cdot \\
 \cdot \\
 \alpha_m
 \end{bmatrix}
 \quad (5.50)$$

The coefficient matrix  $[K]_{ij}$  may readily and rapidly be inverted using Gaussian elimination techniques such that only the elements in the three non-zero diagonals need be stored.

An essential difference between the implicit and SIMPLER algorithms, however, is in the treatment of the temperature field equation. In the SIMPLER algorithm, steps 8 and 9 which produce the temperature

field are performed after steps 12 and 13 in which the velocity and mass flux fields are determined. Furthermore, the temperature field equations in the CEL and Lagrangian zones do not apparently (Pa80) include the indicated work term within the coefficient matrix (using the substitution of equation (5.41)), but rather incorporate the indicated work in the constant term. Since the piston motions drive the flow in a Stirling machine, the driving impetus is thus not as directly involved in the convergence process in the SIMPLER algorithm as it is in the implicit algorithm. This offers an explanation for the inferior convergence performance of the SIMPLER algorithm under Stirling machine boundary conditions. One other difference between the two algorithms is the use of equations (5.47) and (5.48) to explicitly determine the Eulerian masses and Lagrangian displacements respectively, a procedure which is not explicitly included in the SIMPLER algorithm as reported in reference Pa80. The above comparative discussion is strictly relevant to a one-dimensional, compressible fluid flow situation. In two or three dimensions, as well as under incompressible flow conditions, the two algorithms as described are not comparable. Compressible flows in more than one-dimension yield coefficient matrices  $[K]_{ij}$  (in equation (5.50)) which are no longer tri-diagonal. The non-iterative inversion of these matrices may not always be computationally tractable. Under such circumstances, iterative inversion schemes such as Gauss-Seidel iteration (Ge70) or Stone's 'strongly implicit method' (St68) are required. Modifications to the presented implicit algorithm are needed to implement these iterative schemes, whereas no modification of the published SIMPLER algorithm (Pa80) is necessary. Furthermore, unlike the SIMPLER algorithm, the implicit algorithm as described may not be applied to incompressible flows.

In summary, the *modus operandi* of the implicit algorithm is an iterative determination of the mass flux and velocity fields such that all other unknowns may be determined as functions of the iterated parameters. At first examination, such an iterative, implicit approach would seem to be incapable of yielding superior computational performance to a non-iterative, explicit scheme such as that described by Urieli (Ur77) and Berchowitz (Be78). In practice, however, particularly when meeting the physically mandated Courant criterion, these explicit schemes are about an order of magnitude slower than the iterative implicit algorithm described (Go87.1). Furthermore, if the particular Stirling machine boundary conditions yield a sufficiently 'stiff' set of differential equations, explicit algorithms are prone to instabilities caused by truncation errors. The implicit algorithm does not suffer from this disadvantage.

These observations are corroborated by Annand (An68) who compared the use of iterative and non-iterative (fourth order, explicit Runge-Kutta) integration schemes for modelling a diesel cycle in a reciprocating engine. The iterative method showed no evidence of instability and allowed complex two-component effects to be accurately modelled, attributes not shared by the non-iterative Runge-Kutta method. In addition, the iterative method proved to be faster than its non-iterative counterpart.

#### 5.5.4 Combined Eulerian/Lagrangian Control Volume Interfacing

Inherent in the conservation balances incorporated in the implicit algorithm is the capability of interfacing the Eulerian and Lagrangian zones in a way that maintains overall mass, momentum and energy conservation. This is accomplished logistically via the CEL control volumes which enable Lagrangian mass/energy control volumes to be created or destroyed depending on the total amount of mass within the expansion and compression spaces. The destruction of Lagrangian mass/energy control volumes is necessary to prevent Lagrangian momentum control volumes encroaching beyond the confines of the constant flow area cylinders as the pistons move towards the transfer space. Conversely, as the pistons move away from the transfer space, new Lagrangian mass/energy control volumes need to be created in order to maintain the desired level of discretisation. These requirements are fulfilled via steps 4, 15 and 16 of the implicit algorithm. The following discussion of the CEL interfacing methodology is described in terms of the  $x$  expansion space control volume since the identical process applies in mirror image form to the  $y$  compression space control volume.

The constant mass of a Lagrangian mass/energy control volume is determined by dividing the mass of gas contained within the entire cylinder cavity at piston bottom dead center (BDC) by an arbitrary discretisation number  $m_e$  such that the constant or control mass  $M_e$  is given by:

$$M_e = P_{crg} A_e |x_{1e}|_{BDC} / R_{11} \bar{T}_{sw} m_e \quad (5.51)$$

where  $|x_{1e}|_{BDC}$  is the expansion cylinder position at BDC and  $(T_{11})_{\overline{0w}}$  is the length averaged expansion space wall temperature at equilibrium conditions (which may either be estimated or available empirically).

The limits  $(M_e)_{min}$  and  $(I_e)_{max}$  used in step 14 of the algorithm are defined in terms of  $M_e$  such that:

$$(M_e)_{min} = 0.3M_e \quad (5.52.1)$$

$$(M_e)_{max} = 1.3M_e \quad (5.52.2)$$

while the time increment change limit in step 4 is set at:

$$(M_e)_{\Delta t} = 0.1M_e \quad (5.52.3)$$

Consider the case when  $M_e < (h_e)_{min}$  and  $NE > 1$  as shown in figure 5.8.

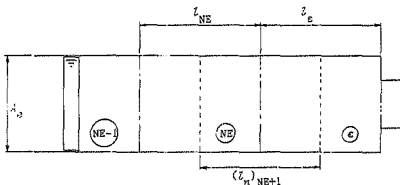


Figure 5.8 Elimination of a Lagrangian mass/energy control volume

The elimination of Lagrangian mass/energy control volume NE is described by the following sequence:

$$M_e \quad M_{NE} \quad \rightarrow \quad M_e \quad (5.53.1)$$

$$(\langle MT \rangle_c + \langle MT \rangle_{NE}) + \langle MT \rangle_c \quad (5.53.2)$$

The state properties of the  $\epsilon$  control volume are recomputed by:

$$T_\epsilon = \langle MT \rangle_c / M_\epsilon \quad (5.53.3)$$

$$P_\epsilon = M_\epsilon RT_\epsilon / A_\epsilon (I_{NE} + I_\epsilon) \quad (5.53.4)$$

Equations (5.53) are mass and energy conservative by inspection.

The elimination of the (NE+1) momentum control volume results in contributions  $\beta_L$  and  $\beta_R$  to the left and right hand moments  $(M_{n,n}^V)_{NE}$  and  $(g_{n,n}^V)_{NE}$ , respectively. From Figure 5.8, the left hand contribution is proportional to the mass of fluid removed from the (NE+1) momentum control volume or:

$$\beta_L = 0.5 I_\epsilon (M_{n,n}^V / I_n)_{NE+1} \quad (5.54)$$

The right hand contribution is also proportional to the mass of fluid removed and is given by:

$$\beta_R = 0.5 I_{NE} (M_{n,n}^V / I_n)_{NE+1} \quad (5.55)$$

But, from equations (4.36), the momentum  $(g_{n,n}^V)_1$  is normalised with respect to the flow area  $(A_n)_1$ , while  $\beta_R$  is normalised with respect to  $A_n$ . Thus  $\beta_R$  must be adjusted to comply with the normalisation of  $(g_{n,n}^V)_1$  so that the momentum added to  $(g_{n,n}^V)_1$  is given by:

$$\beta_R^* = 0.5 I_{NE} (M_{n,n}^V / I_n)_{NE+1} (v_n^*)_{NE+1} \quad (5.56)$$

where  $(v_n^*)_{NE+1}$  is normalised with respect to  $(A_n)_1$ .

This may be accomplished by noting that, from equations (4.17) and (5.3), under constant density, steady-state conditions:

$$A_o \langle v_n \rangle_{NE+1} - \langle A_n \rangle_1 \langle v_n \rangle_{NE+1}$$

Rearranging and substituting into (5.56) yields:

$$\beta_R^* - \beta_R A_o / \langle A_n \rangle_1 \quad (5.57)$$

This result implies that in transferring  $\beta_R$  from  $(M_n v_n)_{NE+1}$  to  $(g_n v_n)_1$ , there is an apparent loss of momentum given by:

$$\beta_R - \beta_R^* = 0.5 I_{NE} \langle M_n v_n / I_n \rangle_{NE+1} \{1 - A_o / \langle A_n \rangle_1\}$$

since  $A_o > \langle A_n \rangle_1$ . However, the magnitude of  $\beta_R - \beta_R^*$  is exactly equal to the external impulse  $fdr$  that is required to reversibly accelerate  $0.5 I_{NE} \langle M_n / I_n \rangle_{NE+1}$  from  $\langle v_n \rangle_{NE+1}$  to  $\langle v_n \rangle_{NE+1}^*$ , so that:

$$fdr + \beta_R - \beta_R^* = 0$$

This ensures that overall momentum is conserved during the momentum control volume elimination process. The elimination of the (NE+1) momentum control volume may thus be described, using equations (5.56) and (5.57), by:

$$(M_n v_n)_{NE} + \beta_L + (M_n v_n)_{NE} \quad (5.58.1)$$

$$(g_n v_n)_1 + \beta_R^* + (g_n v_n)_1 \quad (5.58.2)$$

Equations (5.53) and (5.58) then allow:

$$NE-1 + NE \quad (5.59)$$

When  $M_c > \langle M_c \rangle_{max}$ , the conditions described in figure 5.9 pertain after an additional mass energy control volume is created.

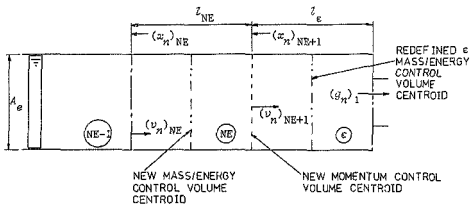


Figure 5.9 Creation of a Lagrangian mass/energy control volume

The creation of an additional Lagrangian mass/energy control volume is an inversion of the elimination process denoted by equations (5.53) and (5.58). The following sequence describes the creation process:

Initially, a new control volume is created by:

$$NE+1 \rightarrow NE \quad (5.60.1)$$

Then:

$$H_e - H_e \rightarrow H_e \quad (5.60.2)$$

$$H_{NE} = H_e \quad (5.60.3)$$

The state properties of the new Lagrangian and  $\epsilon$  mass/energy control volumes are identical, or:

$$T_{NE} = T_e \quad (5.60.4)$$

$$P_{NE} = P_e \quad (5.60.5)$$

Hence the internal energy is redistributed so that:

$$(HT)_{NE} = H_{NE} T_{NE} \quad (5.60.6)$$

$$((MT)_\epsilon - (MT)_{NE}) + (MT)_\epsilon \quad (5.60.7)$$

The mass/energy control volume boundaries and geometries are updated by:

$$I_{NE} = R(MT/P)_\epsilon / A_e \quad (5.60.8)$$

$$(x_N)_{NE+1} = (x_N)_{NE} + I_{NE} \quad (5.60.9)$$

$$I_\epsilon = |(x_N)_{NE+1}| \quad (5.60.10)$$

By inspection, equations (5.60) are mass and energy conservative.

The momentum  $(M_N v_N)_{NE+1}$  of the created momentum control volume comprises contributions  $\beta_L$  and  $\beta_R$  from the left and right hand momenta  $(M_N v_N)_{NE}$  and  $(g_N v_N)_1$  respectively. From figure 5.9, the left hand contribution is proportional to the mass of fluid removed from the NE momentum control volume, or:

$$\beta_L = 0.5 I_\epsilon (M_N v_N / I_N)_{NE} \quad (5.61.1)$$

The right hand contribution is proportional to the volume of fluid removed from the right hand Eulerian momentum control volume so that:

$$\beta_R^* = 0.5 I_{NE} A_e (g_N)_1 \quad (5.61.2)$$

However, from equations (4.36),  $\beta_R^*$  is normalised with respect to the flow area  $(A_N)_1$  while  $(M_N v_N)_{NE+1}$  must be normalised with respect to  $A_e$  so that the right hand side momentum contribution is given by:

$$\beta_R = 0.5 I_{NE} A_e (g_N^*)_1$$

where  $(g_N^*)_1$  is normalised with respect to  $A_e$ . From equation (5.3) under steady-state conditions:

$$(A_n g_n)_1 = A_e (g_n^*)_1$$

which implies that:

$$\beta_R = 0.5 I_{NE} (A_n g_n)_1 \quad (5.62)$$

Since  $A_e > (A_n)_1$ , this suggests an apparent increase in momentum which may be expressed as:

$$\beta_R^* - \beta_R = 0.5 I_{NE} (g_n)_1 (A_e - (A_n)_1)$$

But the magnitude of  $\beta_R^* - \beta_R$  is exactly equal to the reactive impulse  $f_{dc}$  exerted on the walls when  $0.5 I_{NE} A_e (\rho_n)_1$  is reversibly decelerated from  $(v_n)_1$  to  $(v_n^*)_1$ , which results in:

$$\mu_R^* - \beta_R = f_{dc}$$

This ensures that overall momentum is conserved during the momentum control volume creation process. Equations (5.61.2) and (5.62) allow the creation of the NE+1 momentum control volume to be expressed by:

$$(M_n v_n)_{NE} - \beta_L = (M_n v_n)_{NE} \quad (5.63.1)$$

$$(g_n v_n)_1 - \beta_R^* = (g_n v_n)_1 \quad (5.63.2)$$

$$(M_n v_n)_{NE+1} = \beta_L + \beta_R \quad (5.63.3)$$

Finally, as described in the algorithm listing, the time increment adjustment of step 4 is performed for the  $\epsilon$  and  $\gamma$  CEL control volumes simultaneously, since a common time increment for the entire flow field is mandatory. Using the  $\epsilon$  CEL control volume as an example, the sub-algorithmic expansion of step 4 is based upon the substitution of equation (5.52.3) into equation (5.5.1). Hence the global time increment adjustment algorithm may be described by:

IF:  $\left[ H_e < (H_e)_{\Delta t} \text{ or } H_7 < (H_7)_{\Delta t} \right]$

THEN:

$\left[ \min \left\{ (H_e^* - (H_e)_{\Delta t}) \Delta t / (g_{H^*}^* A_{H^*}^*) \right. \right.$   
 $\left. \left. (H_7)_{\Delta t} - H_7^* \right) \Delta t / (g_{H^*}^* A_{H^*}^*)_{N^*+1} \right] + \Delta t.$   
Return to step 3. ]

ELSE: [ go to step 5. ]

#### 5.6 CLOSURE

The foregoing discussion has defined the manner in which the final analytic forms of the reduced integral balances developed in chapter 4 are transformed into a one-dimensional, numerical algorithm suitable for implementation in a computer programme. The transformation has been rigorously accomplished so that the boundary stress tensor  $(\Omega(v))$  and the dissipation  $(\Phi^*(v))$  terms have been included in the discretised equations without change. The equilibrium and UPD algorithms offer a means of bounding the influence of information propagation effects so that the validity of the implicit algorithm per se may be comparatively evaluated.

A final step in implementing the simulation is the incorporation of the necessary empirical correlations which enable the computation of  $\Omega(v)$  and  $\Phi^*(v)$  terms. Additional empiricism is necessary to adequately resolve one-dimensional system description and spatial discretisation effects. These considerations are treated separately in chapter 6 in order to demarcate the boundary between empirical assumption and analytical rigour.

A STATE SPACE AND CONTINUUM MECHANICS  
ANALYSIS OF STIRLING CYCLE MACHINES

---

LOUIS FRANKLIN GOLDBERG

VOLUME II

A thesis submitted to the Faculty of Engineering, University of the  
Witwatersrand, Johannesburg, in fulfilment of the requirements for the  
degree Doctor of Philosophy.

Minneapolis, Minnesota, July 1967

CONTENTS

VOLUME II

	<u>Page</u>
6 EMPIRICAL CONSIDERATIONS IN THE SIMULATION OF STIRLING CYCLE MACHINES.....	262
6.1 INTRODUCTION.....	262
6.2 TWO-DIMENSIONAL EFFECTS IN THE EXPANSION AND COMPRESSION SPACES.....	263
6.3 ADVECTION MODELLING IN THE REGENERATOR.....	265
6.4 EMPIRICAL CORRELATIONS.....	271
6.4.1 Friction and Dissipation Modelling.....	272
6.4.2 Heat Transfer Modelling.....	276
6.4.3 Empirical Correlation Selection.....	277
6.5 VALIDATION PROTOCOL.....	280
7 SIMULATION OF THE GENERAL MOTORS GROUND POWER UNIT 3 STIRLING ENGINE.....	286
7.1 INTRODUCTION.....	286
7.2 DESCRIPTION OF THE GM-GPU3 ENGINE.....	288
7.3 EXPERIMENTAL MEASUREMENTS.....	292
7.4 MODELLING ASSUMPTIONS.....	296
7.4.1 Fluid Dynamics.....	297
7.4.2 Boundary Conditions.....	297
7.4.3 Conduction Heat Transfers at the System Boundary.....	298
7.4.4 Regenerator Matrix Geometry.....	299
7.4.5 One-Dimensional Discretisation.....	300
7.5 EMPIRICAL CORRELATIONS.....	305
7.6 NUMERICAL TOPICS.....	313
7.6.1 Numerical Algorithm Constants.....	314
7.6.2 Cyclic Steady-State Convergence.....	316
7.6.3 Computer Hardware and Software.....	320
7.7 VALIDATION RESULTS.....	323
7.7.1 Baseline Calibration of the Simulation Model.....	327
7.7.2 Baseline Calibration Phase Evaluation of the Simulation Model.....	339
7.7.3 Baseline Simulation of the Experimental Test Map.....	391
7.7.4 Corrected Simulation of the Experimental Test Map.....	411
7.8 CLOSURE.....	431
8 SPACE POWER DEMONSTRATOR ENGINE SIMULATION SUMMARY.....	434
8.1 INTRODUCTION.....	434
8.2 SIMULATION OF THE SPDE.....	434
8.3 CLOSURE.....	443
9 CONCLUSION.....	444
9.1 SUMMARY AND RESEARCH ACHIEVEMENTS.....	444
9.1.1 Coupled Dynamic/Thermodynamic Analysis.....	444

9.1.2	Fluid Dynamic Simulation.....	446
9.2	CONCLUSIONS.....	455
9.2.1	Coupled Dynamic/Thermodynamic Analysis.....	455
9.2.2	Fluid Dynamic Simulation.....	456
9.3	RECOMMENDATIONS FOR FUTURE WORK.....	458

APPENDIX A STATE SPACE ANALYSIS APPLICATION..... 460

A.1	BACK-TO-BACK FREE-PISTON STIRLING ENGINE.....	460
A.1.1	Assumptions.....	460
A.1.2	Geometry.....	461
A.1.3	Thermodynamics.....	462
A.1.4	Dynamics.....	463
A.1.5	State Space Analysis.....	464
A.2	SUNPOWER KE-1000 FREE-PISTON STIRLING ENGINE.....	469
A.2.1	Assumptions.....	469
A.2.2	Geometry.....	471
A.2.3	Thermodynamics.....	472
A.2.4	Dynamics.....	473
A.2.5	State Space Analysis.....	474
A.3	SOLUTION OF THE STATE SPACE EQUATIONS.....	478

## CHAPTER 6

### EMPIRICAL CONSIDERATIONS IN THE SIMULATION OF STIRLING CYCLE MACHINES

#### 6.1 INTRODUCTION

Three areas in which empiricism is necessary to account for the limitations of the simulation model have emerged, namely:

- the effects of a one-dimensional system description
- spatial discretisation issues
- correlations for the boundary stress tensor  $\Omega(v)$  and dissipation  $\Phi^*(v)$  terms.

Some of these effects are inter-related; for example, the  $\Omega(v)$  and  $\Phi^*(v)$  terms necessarily include the effects of a one-dimensional system description. The spatial discretisation issue arises in all the components comprising the working space of a Stirling machine, namely, the heater, regenerator, cooler, expansion and compression space cylinders as well as any connecting ducts, plena or dead volumes. In all cases other than the regenerator, a parametric variation of spatial discretisation is adequate to quantify discretisation effects. Therefore, the spatial discretisation of the regenerator alone requires specific discussion.

Similarly, the effects of the one-dimensional system description are universally relevant, yet they only need be isolated for specific discussion in the expansion and compression spaces. Elsewhere, dimensional effects may be effectively incorporated in a parametric

evaluation of the  $\Omega(v)$  and  $\Phi^*(v)$  terms.

Hence discussion of the empirical considerations is divided into three sections, namely:

- the influence of two-dimensional flows in the expansion and compression spaces
- the effect of spatial discretisation on the modelling of advection in the regenerator
- the selection and implementation of empirical correlations.

Finally, the manner in which a comparison of the numerical predictions with experimental data may be used to assess the validity of the simulation is presented.

## 6.2 TWO-DIMENSIONAL EFFECTS IN THE EXPANSION AND COMPRESSION SPACES

There is a large body of literature, particularly with respect to the flows in internal combustion engine cylinders, that asserts that cylinder flows are strongly multi-dimensional. This is no less true for Stirling machines, although in most cases the radial symmetry of the expansion and compression space cylinders makes a two-dimensional flow description adequate. Two examples of strongly two-dimensional flows which typically occur in Stirling machine working space cylinders are shown in figure 6.1.

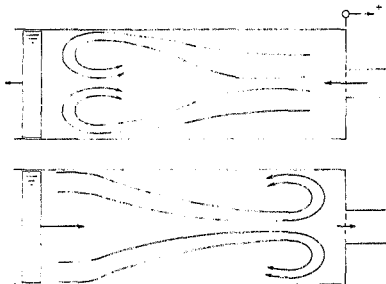


Figure 6.1 Examples of strongly two-dimensional flows in Stirling machine cylinders

The one-dimensional Lagrangian and combined Eulerian/Lagrangian model is not intrinsically capable of describing the recirculating flows which can arise in the expansion and compression spaces. The principal effect of such recirculation becomes apparent in the extent to which the one-dimensional linear or volume-averaged temperature gradients within the cylinders depart from the actual temperature gradients. This in turn affects the enthalpy transported into the transfer space, an effect which can dramatically influence the simulated wall/fluid heat transfer in the heater and cooler.

Within the context of the simulation model, only the spatial discretization of the working space cylinders may be used to quantitatively investigate this effect. The recirculation effect may be bounded above by assuming that a perfectly mixed condition exists within the cylinder over the entire cycle. This may be specified by

setting  $m_e$  and  $m_c$  (the Lagrangian discretisation numbers) in equation (5.51) to unity. Conversely, a completely unmixed condition may be specified by choosing  $m_e$  and  $m_c \gg 1$ . Partially mixed conditions are then characterised by intermediate values of  $m_e$  and  $m_c$ .

The methodology used to accomplish this evaluation is discussed in section 6.5. However, it must be stressed that a one-dimensional parametric evaluation cannot be relied upon to delineate unambiguously the influence of two-dimensional effects in the cylinders. Such a delineation requires the use of a two-dimensional discretisation of the expansion and compression spaces, a topic which is beyond the scope of this work. Nevertheless, the integral balances developed in chapter 4 are relevant for such a two-dimensional application.

Some researchers (Be78) have speculated that ignoring one-dimensional momentum in the expansion and compression spaces may be a significant cause of simulation error. Since the simulation model rigorously includes one-dimensional momentum in these spaces, the aforementioned speculative error is eliminated as a potential source of simulation discrepancies.

### 6.3 ADVECTION MODELLING IN THE REGENERATOR

In view of the very large temperature gradients typically occurring within the matrices of Stirling engine regenerators, the enthalpy advection calculation procedure described by equation (4.67) mandates that a very fine regenerator mass/energy control volume discretisation is necessary to predict the regenerator working fluid temperature

field accurately. As the integral analysis will, by definition, yield the same total internal energy for the working fluid in the regenerator irrespective of the discretisation, the requirement for an accurate temperature field (which is a differential property) is predicated by the physical function of the regenerator. This device is intended to minimise the enthalpy flux between the heater and cooler, enabling the energy transfer portion of the ideal Stirling cycle to be accomplished. During this process, heat is transferred isochorically from the working fluid displacement phase occurring after expansion to that occurring after compression. The efficiency of practical Stirling cycles is thus largely dependent upon the effectiveness of the regenerator in achieving the theoretical ideal.

In view of the very high rates of heat transfer occurring in porous matrices, it has been experimentally validated in several instances (Be78) that the working fluid and matrix temperatures may both be approximated by linear profiles over the entire regenerator. Thus consider the linear working fluid temperature profile in a single regenerator mass/energy control volume depicted in figure 6.2.

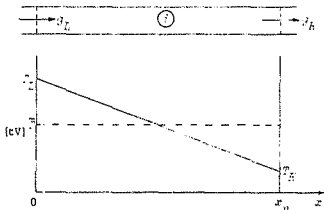


Figure 6.2 Discretisation of a single regenerator mass/energy control volume

The time- and volume-averaged temperature  ${}_{(t,v)}\bar{T}_1$  is approximated by:

$${}_{(t,v)}\bar{T}_1 = (T_L + T_R)/2 \quad (6.1)$$

Hence by equations (4.67):

$$\text{if } g_L < 0 \text{ then: } (T_n)_i = {}_{(t,v)}\bar{T}_i \quad (6.2.1)$$

$$\text{if } g_R > 0 \text{ then: } (T_n)_{i+1} = {}_{(t,v)}\bar{T}_i \quad (6.2.2)$$

Thus the error made in the energy advected to the heater is proportional to  $(T_R - T_L)/2$  while the cooler advection has an error proportional to  $(T_L - T_R)/2$ . This implies that the energy advected to the heater is under-predicted and that advected to the cooler is over-predicted. Generalising this analysis to a regenerator with a discretisation of  $m_c$  control volumes reveals that the heater and cooler advection errors are proportional to  $(T_L - T_R)/2m_c$  and  $(T_R - T_L)/2m_c$  respectively. Hence for prototype Stirling engines where temperature differences across the regenerator may reach values of 400K or more (see chapter 2 for the RE-1000 engine for example), a 1% error for a nominal cooler advection temperature of 300K would require

a regenerator discretisation of 67 control volumes. This is computationally impractical and so mandates an alternate approach.

Before proceeding, it should be noted that small advection errors may be achieved with a relatively coarse spatial discretisation for regenerator mass/energy control volumes with uniform boundary conditions ( $T_L \approx T_R$ ) or nearly uniform boundary conditions ( $|T_L - T_R|$  is small). Furthermore, the advection problem discussed above for the integral energy balance does not arise for the integral momentum balance irrespective of the uniformity of the boundary conditions in view of the characteristics of equations (4.61). These characteristics ensure that the scaling effect of the discretisation on the advection error is avoided because the velocity gradient within any mass/energy control volume is included in computing the momentum transport.

The methodology used to resolve the regenerator discretisation dilemma is adapted from an approach suggested by Gedeon (Ge84). Linear upwind spatial extrapolations of the temperature field lead to a better approximation of the actual advected temperatures within the regenerator, in a manner which is largely independent of the discretisation. The particulars of the method are discussed with reference to figure 6.3.

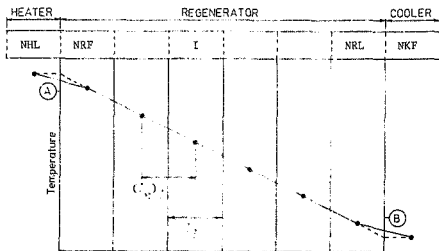


Figure 6.3 Extrapolation of the linear regenerator temperature field

Using the mass/energy control volume temperatures to define a temperature gradient, the upwind extrapolation procedure has the form:

if  $(\mathcal{E}_n)_i \geq 0$  then:

$$(T_n)_i \approx T_{i-1} (1 + 0,5K_r(l/l_n)_{i-1}) + 0,5K_r(l/l_n)_{i-1} T_{i-2} \quad (6.3.1)$$

if  $(\mathcal{E}_n)_i < 0$  then:

$$(T_n)_i \approx T_i (1 + 0,5K_r l_i / (l_n)_{i+1}) - 0,5K_r l_i / (l_n)_{i+1} T_{i+1} \quad (6.3.2)$$

The upwind extrapolation format of these equations is essential in order to maintain the transport properties of equations (4.67). The porous advection coefficient  $K_r$  is introduced as a means of accounting for the deviation of actual regenerator behaviour from the ideal behaviour suggested. Such deviations encompass non-linear matrix temperature profiles and oscillating flow matrix/fluid heat transfer characteristics which make a linear extrapolation of the fluid temperature profile unrealistic.

Equations (6.3) apply at all the regenerator momentum control volume centroids (NRF to NRL+1) with the following exceptions:

$$\text{if } (g_n)_{\text{NRF}} \geq 0 \text{ then: } (T_n)_{\text{NRF}} = T_{\text{NRL}} \quad (6.4.1)$$

$$\text{if } (g_n)_{\text{NRL}+1} < 0 \text{ then: } (T_n)_{\text{NRL}+1} = T_{\text{NKF}} \quad (6.4.2)$$

It may be noted that at momentum control volume centroid NRF+1, the adjacent heater temperature would be used for  $T_{i-2}$  in equation (6.3.1). Similarly at momentum control volume centroid NRL, the cooler control volume temperature  $T_{\text{NKF}}$  is substituted for  $T_{i+1}$  in equation (6.3.2). This is an approximation which is felt to be physically more consistent than the alternative of assuming that  $T_{\text{NRL}}$  occurs at A and  $T_{\text{NKF}}$  occurs at B in figure 6.3. In practice, though, it has been determined that the discrepancy between the two approaches is minimal.

Equations (6.3) are included in equations (5.40), when appropriate, via the following modifications:

if  $(g_n)_i \geq 0$  then:

$$(g_n^A)_i \{1 + 0.5K_r(l/l_n)_{i-1}\} = (g_n^A)_i \quad (6.5.1)$$

$$\alpha_i + 0.5\hat{G}_p(g_n^A)_i K_r(l/l_n)_{i-1} T_{i-2} = \alpha_i \quad (6.5.2)$$

if  $(g_n)_i < 0$  then:

$$(g_n^A)_i \{1 + 0.5K_r l_i / (l_n)_{i+1}\} = (g_n^A)_{i+1} \quad (6.5.3)$$

$$\alpha_i + 0.5\hat{G}_p(g_n^A)_{i+1} K_r(l_i / (l_n)_{i+1}) T_{i+1} = \alpha_i \quad (6.5.4)$$

It may be noted that equations (6.3) are split in equations (6.5) so that the once removed temperatures  $T_{I-2}$  and  $T_{I+1}$  are included in the constant term  $\alpha$  and not in the coefficient matrix  $[K]_{IJ}$ . This maintains the integrity of the tri-diagonal matrix topology while also yielding a faster rate of convergence.

In terms of figure 6.2 and equations (6.2), the scheme of equations (6.3) yields a zero error if  $m_r > 1$  and the working fluid temperature profile is linear so that  $K_r = 1$ . Thus the requirement of an inordinately large number of regenerator control volumes to achieve adequately small advection errors in the presence of a severe boundary condition non-uniformity is eliminated.

#### 6.4 EMPIRICAL CORRELATIONS

As described in section 5.5, the one-dimensional equation set to be solved numerically incorporates a residue of unknowns which may not be determined by further analysis. These unknowns embody most of the modelling assumptions made in deriving the simulation equations. Therefore, the accuracy and reliability of the empirical correlations used to evaluate the residual unknowns is of major significance in determining the extent to which the simulation predictions may be validated by experimental observations.

The manner in which these correlations are included in the simulation is discussed in the following sub-sections. The mathematical form of the  $\Omega(v)$  and  $\Phi^*(v)$  correlations is developed first, followed by a discussion of the correlation selection process.

#### 6.4.1 Friction and Dissipation Modelling

By definition (BS60), the magnitude of the force exerted on a fluid as a result of its motion being constrained by the boundaries of a given space is described by:

$$F_{\sigma} = 0.5A_{\sigma}\chi_{\{L,V\}}\bar{\rho}_{\{L,V\}}\bar{v}^2 \quad (6.6)$$

where  $A_{\sigma}$  is a characteristic boundary area,  $\chi$  is a friction factor and the remaining terms represent a characteristic kinetic energy per unit volume (based on a time- and volume-averaged velocity). It should be emphasised that equation (6.6) is not physically fundamental, but is strictly a definition of  $\chi$ . Thus comparing equations (5.11.1) and (6.6) it is evident that the physical relevance of  $\chi$  is defined by:

$$\begin{aligned} \Omega(v) &= 0.5\chi\rho v|v| \\ &= \mu((\partial v/\partial \theta)/r + \partial v/\partial r) + \tau_{xr,x\theta}^{(t)} \end{aligned} \quad (6.7)$$

$\chi$  is therefore a parametric representation of the laminar and turbulent shear stresses and the turbulent momentum fluxes in the plane orthogonal to the uni-dimensional coordinate direction.

Expressing  $v^2$  as  $v|v|$  maintains the physical relationship between the direction of  $F_{\sigma}$  and  $v$ . Hence, in terms of equation (5.10), it is convenient to signify these laminar and turbulent boundary effects as the combined boundary stress tensor  $T^*$  so that:

$$\int_{A_B} (T^* \cdot \cdot n) dA = 0.5\chi\rho v|v|A_{\sigma} \quad (6.8)$$

where  $A_B$  is given by equation (5.8.3). Typically, dimensional analysis (BS60) allows  $\chi$  to be expressed as a function of the Reynolds number  $N_{Re}$  as well as various parameters describing particular physical characteristics of the confining boundary or wall, such as its roughness (Sc79). Hence:

$$\chi = f(N_{Re}, l_{rough}) \quad (6.9)$$

where  $l_{rough}$  is a measure of the relative protuberance of surface irregularities into the flow stream.

Using the definition of the friction factor  $\chi$  given by equation (6.6), a means of representing the dissipation  $\Phi^*(v)$  as a one-dimensional correlation may be developed.

From equations (5.19) and (5.20):

$$\Phi^*(v) = \mu \{ (\partial v / \partial r)^2 + \{ (\partial v / \partial \theta) / r \}^2 \} + F_{\{x, r, \theta\}} \bar{\mu}_{\{x, r, \theta\}} \bar{v}' \quad (6.10)$$

Therefore,  $\Phi^*(v)$  is comprised of the following contributions:

- the laminar and turbulent dissipation resulting from the shear stresses and advection fluxes in the  $r$  -  $\theta$  orthogonal to the uni-dimensional coordinate direction
- the dissipation caused by the turbulent advection fluxes in the uni-dimensional coordinate direction.

The approach used to develop an empirical expression for equation (6.10) (which is included in the dissipation term  $\{v\Phi^*(v)\}_z$  in equations (5.27), (5.28) and (5.29)) is a more generalised implementation of an analysis suggested by Bird, Stewart and Lightfoot (BS60, §7.4). By equation (4.38) and the tensor identity of equation

(C.28), for any mass/energy control volume  $V$ :

$$\dot{\Phi}^*(V) = \int_V [\nabla \cdot (\mathbf{T} \cdot \mathbf{v})^* - (\mathbf{v} \cdot \nabla \cdot \mathbf{T})^*] dV$$

Applying the divergence theorem to the first term on the right hand side:

$$\dot{\Phi}^*(V) = \int_{A_A} [(\mathbf{T} \cdot \mathbf{v} \cdot \mathbf{n})^*] dA + \int_{A_B} [(\mathbf{T} \cdot \mathbf{v} \cdot \mathbf{n})^*] dA - \int_V (\mathbf{v} \cdot \nabla \cdot \mathbf{T})^* dV \quad (6.11)$$

where  $A_A$  and  $A_B$  are given by equations (5.21.2) and (5.21.3) respectively.

By equation (4.34)  $\mathbf{T}$  is symmetrical, and, in terms of the one-dimensional system model:

$$\mathbf{v} \cdot \mathbf{n} = 0 \text{ on } A_B$$

Thus equation (5.48) becomes:

$$\dot{\Phi}^*(V) = \int_{A_A} [(\mathbf{v} \cdot \mathbf{T} \cdot \mathbf{n})^*] dA - \int_V (\mathbf{v} \cdot \nabla \cdot \mathbf{T})^* dV \quad (6.12)$$

But from equations (5.9), (5.12) and (6.10):

$$\text{on } A_A, \mathbf{T}^* = \int_{[V]} \bar{\mathbf{T}}^{(k)} = 0$$

Thus equation (6.12) may be approximated by:

$$\dot{\Phi}^*(V) = \int_V (\mathbf{v} \cdot \nabla \cdot \mathbf{T})^* dV$$

Now if a volume of magnitude  $\beta$  exists such that:

$$V \leq \beta = \int_{[LV]} \bar{\nabla} \cdot \mathbf{f}(V) \quad (6.13)$$

or, if  $V$  is small enough to prevent the volume-averaged velocity from being affected severely by the discretisation then:

$$\Phi^*(v)V \approx -v \int_V (v \cdot T^*) dV$$

Applying the divergence theorem to the relevant coordinate directions noted for equation (6.10):

$$\Phi^*(v)V \approx v \int_{A_B} (T^* \cdot -n) dA$$

which after substitution of equation (6.8) in the mass/energy control volume context produces the final result:

$$\Phi^*(v)V \approx 0.5 \chi_p v^2 |v| (A_B). \quad (6.14)$$

This equation is the same result produced by Bird, Stewart and Lightfoot with the exception that it is very strongly qualified by equation (6.13). Consequently the use of equation (6.14) requires an adequate level of spatial discretisation to satisfy equation (6.13) in at least an asymptotic sense so that the computational requirements are not exacerbated. Such caution is particularly warranted when considering Stirling machine regenerators whose porous characteristics endow them with very large shear stress gradients. This lack of scalability of the dissipation model is one of the principle practical difficulties in implementing the one-dimensional simulation, a difficulty which may be resolved ultimately by eschewing a one-dimensional approach in favour of two- or three-dimensional treatments.

5.4.2 Heat Transfer Modelling

Equation (5.22) serves as the definition of the heat transfer coefficient  $h$  (BS60) such that:

$$\dot{Q}_e = h(A_B)(T_w - T) \quad (6.15)$$

where, from equation (5.22),  $\dot{Q}_e$  is the effective heat exchange between the wall and the fluid as a function of the fluid velocity  $v$ , or:

$$\dot{Q}_e = \int_{A_B} (v_n \cdot \nabla T)_{n=0} + (v_n \cdot \nabla T)_{n=1} + (v_n \cdot \nabla T)_{n=2} + \dots \cdot n \cdot dA \quad (6.16)$$

with  $A_B$  defined by equation (5.21.3).

Under zero flow conditions,  $h$  is a pure conduction term. For laminar flows, the existence of radial and circumferential velocity gradients creates combined conduction and advection heat transfer in the plane orthogonal to the uni-dimensional coordinate direction; hence the term 'convection' coefficient. Lastly, when the flow is turbulent, the existence of the turbulent advective fluxes  $(v_n) q^{(t)}$  adds a turbulence component to  $h$ . Hence expressing  $h$  as a function of the velocity as well as other parameters  $\psi_i$ :

$$h = f(v, \psi_i) \quad (6.17)$$

enables all possible flow conditions to be covered in a one-dimensional correlation treatment.

### 6.4.3 Empirical Correlation Selection

In their comprehensive review of the literature pertaining to oscillating flows in the context of Stirling machine boundary conditions, Seume and Simon (SS86) point out that one-dimensional correlations for shear stress and heat transfer are not strictly appropriate in a physical sense. Nevertheless, without recourse to two- or three-dimensional simulation, the necessity of using one-dimensional correlations cannot be avoided. They propose one-dimensional correlations of the form:

$$\tau = f((N_{Re})_{\omega}, (N_{Re})_{max}, x_{max} / \sum l) \quad (6.18.1)$$

$$h = F((N_{Re})_{\omega}, (N_{Re})_{max}, x_{max} / \sum l) \quad (6.18.2)$$

where:

$$(N_{Re})_{\omega} = \text{Womersley number} = \omega \mu d^2 / \rho \quad (6.18.3)$$

$$(N_{Re})_{max} = \text{Reynolds number based on velocity amplitude} \\ = |v_{max}| \rho d / \mu \quad (6.18.4)$$

$$x_{max} / \sum l = \text{relative amplitude of fluid displacement, or: (the} \\ \text{streamwise maximum distance of travel of a fluid element} \\ \text{between flow reversals) / (total heat exchanger length)} \quad (6.18.5)$$

$(N_{Re})_{\omega}$  and  $(N_{Re})_{max}$  arise from a normalisation of the differential equation (3.12) while the  $(x_{max} / \sum l)$  ratio derives from the 'critical length ratio' concept suggested by Organ (Or75). Under conditions where the Mach numbers are small, equations (6.18) may be adequate, although there is at least some experimental and anecdotal evidence

(Or84) to suggest that the inclusion of the Mach number  $N_{Ma}$  as a correlation parameter may be essential, particularly in regenerators.

From a simulation perspective, equations (6.18) may not be sufficiently generalised because they are dependent on global steady-state equilibrium parameters such as  $\omega$ ,  $x_{max}$  and  $v_{max}$  which, by definition, cannot be determined on a local transient basis as required by equations such as (5.13) and (5.24). Thus the author has suggested (Go87.1) the use of an acceleration based non-dimensional parameter as a suitable means of improving the simulation applicability of equations (6.18).

Concomitant with the effects of oscillating flow and compressibility, Stirling machines operate in a regime ranging from laminar to fully developed turbulent flow. In addition to the turbulence effects discussed in section 4.2, there is seemingly a large void in the understanding of laminar to turbulent flow transition processes, particularly under Stirling machine boundary conditions (SS86). Since such transitions may occupy a significant portion of the cycle, ignorance of these processes militates against the use of existing oscillating flow correlations which do not specifically encompass transition phenomena.

Thus, from the perspective of a one-dimensional simulation, there do not appear to be any generalised oscillating flow correlations which are appropriate for Stirling machine boundary conditions. Hence, in order to implement a simulation, recourse to the pseudo-steady-state assumption for using existing non-transient correlations becomes mandatory. This approach has been used by most Stirling analysts

(Be78, Or82, Sc78, Ur77), although always with the appropriate qualifications. In essence, the pseudo-steady-state assumption dictates that, instantaneously, steady-state heat transfer and friction factor correlations produce approximately the same result as strictly transient correlations. Physically, the validity of such an assumption is dependent on the local transient acceleration; consequently, the assumption becomes progressively worse with increasing acceleration. In addition, under reversing flow conditions, the pseudo-steady-state assumption yields demonstrably incorrect results (Uc56), even when the flow is laminar, since the core and boundary layer flows have opposing velocity directions. However, in mitigation, it has been argued that on a cyclic integral basis, the use of the pseudo-steady-state assumption yields fairly accurate results for the indicated work done as well as for the net boundary heat transfers. This is based on the notion that, since the flow is periodic, errors resulting from flow in a particular direction are cancelled by the errors occurring during flow in the opposite direction.

There are a plethora of steady-state correlations for friction factors and heat transfer coefficients based upon analytical as well as experimental data available in literature. In the context of this work, chiefly in the interests of standardisation, the experimental correlations compiled by Kays and London (KL64) are used exclusively. These correlations have seemingly become a *de facto* standard in Stirling machine simulation and thus their use here aids in a comparative assessment of the simulation results produced with those of other workers. This choice does not imply that the Kays and London correlations are always the most appropriate for particular

geometrical conditions. However, in view of the errors inherent in all steady-state correlations under oscillating flow conditions, differences between particular steady-state correlations are likely to be of less significance. Hence the argument for using a well-defined and reproducible set of correlations carries greater weight than an attempt to locate tailored correlations whose improved efficacy may be relatively marginal. In any event, the assessment of such an improvement, even if quantitative, may be spurious when cognisance is taken of the omnipresent errors which are generic to steady-state correlations under oscillating flow conditions.

#### 6.5 VALIDATION PROTOCOL

In view of the empirical uncertainties that have emerged during the simulation model development, a parametric evaluation of the simulation model is mandatory. This is justified not only by the unavailability of definitive friction factor and heat transfer correlations, but also by the limitations of a one-dimensional system description in the presence of multi-dimensional effects. The major advantage of a parametric approach is that it enables observed discrepancies between experimental and simulation data to be bounded. This is an effective method of isolating deficiencies in the simulation model in a physically relevant manner since, very often, arbitrary or unbounded correction procedures can produce spurious agreement between experimental and simulation results.

The choice of parametric variables is governed by the empiricism incorporated into the simulation model. Five such empiricisms have emerged as being necessary. These are:

1. The spatial discretisation of Lagrangian expansion and compression spaces ( $m_e$  and  $m_c$ ).
2. The spatial discretisation of the Eulerian transfer space (defined by NH, NR, NK for the heater, regenerator and cooler respectively).
3. The porous advection coefficient in the regenerator ( $K_r$ ).
4. Correlations for the friction factor  $\chi$ .
5. Correlations for the heat transfer coefficient  $h$ .

The first three empiricisms are directly capable of parametric implementation. A parametric variation of the friction factor for a given correlation may be accomplished conveniently by defining a multiplier  $K_\chi$ , so that from equation (6.9):

$$\chi = K_\chi f(Re, l_{rough}) \quad (6.19)$$

Similarly, a parametric variation of the heat transfer coefficient for a particular correlation may be determined by defining  $K_{ht}$ , changing equation (6.17) to:

$$h = K_{ht} E(v, \psi_1) \quad (6.20)$$

The parametric variation coefficient set so defined ( $m_e$ ,  $m_c$ , NH, NR, NK,  $K_r$ ,  $K_{ht}$ ,  $K_\chi$ ) and the UPD and equilibrium algorithms are the ingredients for creating the required validation protocol. Thus for every experimental point used, a maximum of 16 parametric variations may be performed by varying a single parameter at a time while hundreds more variations may be defined by varying more than a single

parameter at once. Such an approach predicates an inordinately large amount of computation especially if every simulation is run to cyclic convergence (defined by acceptably small cyclic energy balance closure errors - see section 7.6.2). Furthermore, a complete parametric map at each test point usually incurs significant redundancy since certain parametric variations may be irrelevant physically for a particular engine configuration. Simplifications can be made by noting that, for example, a variation of the spatial discretisation parameters in the transfer space (NH, NR, NK) need only be performed once, since the geometrical boundary conditions in the transfer space are invariant for a particular Stirling machine. These issues are coalesced into the validation protocol defined in table 6.1 and applied in chapter 7. This protocol has been found to enable all the required parametric variations to be accomplished in a physically meaningful manner without an exorbitant amount of computation.

The validation is accomplished in three phases:

1. *Baseline calibration phase*

The baseline calibration phase determines the appropriate or optimum level of spatial discretisation in the transfer, expansion and compression spaces using baseline values for  $K_r$ ,  $K_x$  and  $K_{hc}$ . The optimum is determined to be the minimum level of discretisation which produces an acceptably small change in cyclic integral parameters (such as indicated work output and overall heat transfer) per unit change in discretisation. Initially, the optimum transfer space discretisations are determined by simulating single cycles from rest conditions. Thereafter, using the established transfer space discretisations.

Table 6.1 Parametric validation protocol

Simulation Run Type	Experimental Test Data	Parametric Coefficients Held Constant <sup>a</sup>	Parametric Coefficients Varied	Algorithm <sup>b</sup>	
				UPD	Equil.
Baseline calibration	Single representative data point	$K_r = 0; K_\chi = 1;$ $K_{ht} = 1$ $m_e = m_c = 1$	NH		S
			NK		S
			NR		S
		$K_r = 0; K_\chi = 1;$ $K_{ht} = 1;$ $NH^*; NR^*; NK^*$	$m_e; m_c$ (such that $m_e = m_c$ )		C C C
Baseline	Series of data points	$K_r = 0; K_\chi = 1;$ $K_{ht} = 1; NH^*;$ $NR^*; NK^*; m_e^*;$ $m_c^*$	none	C	C
Corrected	Series of data points	$NH^*; NR^*; NK^*;$ $m_e^*; m_c^*$	$K_r; K_\chi; K_{ht}$ (as appropriate to match experimental and simulated data)	C	C

Notes:

- a. The asterisk superscript denotes an optimum value chosen from a previous step in the validation sequence.
- b. S = single cycle simulation from rest conditions.  
C = multiple cycle simulation until cyclic convergence is achieved.

the effects of varying the expansion and compression space discretisations are determined from cyclically converged simulation results. An effective simplification is accomplished by choosing the same discretisation in both the expansion and compression spaces since separate variations were found to produce little additional information. The entire calibration run sequence is performed for a single experimental data point which should be chosen arbitrarily. In all cases, the coefficients  $K_r$ ,  $K_x$  and  $K_{hc}$  are set at their baseline values which are chosen to exclude the influence of the regenerator advection model ( $K_r = 0$ ) and to produce no modifications to the nominal friction factor and heat transfer correlations selected ( $K_x = K_{hc} = \dots$ ). All the spatial discretisation evaluation simulations are performed using the equilibrium algorithm since its cyclic integrals are less prone to numerical error (see section 5.5.2.2) while  $m_e$  and  $m_c$  are always unity for the UPD algorithm.

## 2. *Baseline simulation validation phase*

Keeping the optimum discretisation determined in the calibration phase constant, the second or baseline simulation phase is implemented. In this phase as well,  $K_r$ ,  $K_x$  and  $K_{hc}$  are held constant at their assigned baseline values, excluding the influence of the regenerator advection model and maintaining the heat transfer coefficients and friction factors at their nominal values. Both the UPD and equilibrium algorithms are cycled to convergence for a series of experimental data points defining the experimental performance map of the particular Stirling machine chosen for the validation exercise.

3. *Corrected simulation validation phase*

Finally, all the baseline simulation runs are repeated in the third or corrected simulation phase. In this phase, however,  $K_x$ ,  $K_y$  and  $K_{ht}$  are varied simultaneously in order to match the simulated and experimental data. The precise method of coefficient variation cannot be specified a priori because the variation sequence is dictated by specific machine characteristics, the experimental test boundary conditions and the behaviour of the simulation itself.

Since the purpose of the parametric validation approach is to endow the simulation evaluation exercise with as much objectivity as possible, other than the variations listed in table 6.1, no alterations of any kind are made to the geometrical description of a given test machine or to any aspects of the equation set comprising the simulation model. Furthermore, the validation protocol permits a comprehensive assessment of the relative importance of information propagation and empirical correlation dependent effects, an assessment which remains as one of the principal controversies surrounding Stirling machine simulation. As the final form of the derived integral balances is the literal form in which they are solved numerically, the validation protocol tests the simulation model in an environment in which numerical and boundary condition dependent effects may be isolated. Thus the validation protocol not only provides a well founded evaluation basis but also serves as a means of highlighting simulation model deficiencies related to a one-dimensional discretisation.

## CHAPTER 7

### SIMULATION OF THE GENERAL MOTORS GROUND POWER UNIT 3 STIRLING ENGINE

#### 7.1 INTRODUCTION

The General Motors ground power unit 3 (GM-GPU3) was obtained by the NASA (United States National Aeronautics and Space Administration) Lewis Research Center for the specific purpose of obtaining experimental data for validating Stirling cycle machine computer simulations. The GM-GPU3 engine was originally built for the United States Army in 1965 as part of a 3-KW engine-generator set designed for portable electric power generation.

In the context of this work, the GM-GPU3 is a suitable choice for evaluating the validity of the simulation model developed for the following reasons:

1. Using helium and hydrogen as working fluids, the GM-GPU3 may operate in a 15 to 60 Hz speed range with a pressurisation from 10 to 70 bars. As a single cylinder, piston/displacer, beta-configuration engine, the GM-GPU3 has an overall working space topology which is typical of a broad range of free- and disciplined-piston Stirling machines. Hence use of the GM-GPU3 as a validation test case enables the simulation to be assessed for a representative Stirling machine under realistic boundary conditions.

2. Since the engine employs a mechanical linkage to move the pistons, the momentum boundary conditions (piston and displacer positions and velocities) may be defined precisely, so avoiding the potential inaccuracies resulting from assumed piston and displacer motions. This assumption is a prevalent practice in simulating free piston engine fluid dynamics since it permits complicating dynamic coupling effects to be ignored.
3. The working space geometry and mechanical linkage of the GM-GPU3 are adequately defined in reference Th79, enabling the engine to be described analytically in one-dimensional terms.
4. The experimental test data available in references Th79 and Th81 define a GM-GPU3 performance map covering a broad range of operating conditions (heater temperatures, working fluid pressurisations and engine speeds) for both helium and hydrogen working fluids. The experimental data available for validation purposes enable a cyclic energy balance comparison to be performed in terms of the cyclic heat supplied to and removed from the working fluid as well as the net indicated work done. Energy balance closure errors are included in this experimental data, so a means of assessing the magnitude of any experimental/simulation data discrepancies in the light of possible experimental errors is available. Several cyclic mean working fluid temperatures are also reported as are amplitudes and phase angles of the pressure profiles in the expansion and compression spaces, although no quantitative means of assessing the individual reliability of these measurements is provided.

Hence the availability of adequate experimental test data and descriptive documentation as well as the imprimatur of a recognised, independent Stirling machine research center all contribute towards the selection of the GM-GPU3 as a suitable test case for evaluating the simulation model developed in this thesis.

### 7.2 DESCRIPTION OF THE GM-GPU3 ENGINE

The GM-GPU3 as configured for experimental investigation is shown in figure 7.1. The engine has a single cylinder, beta configuration with the piston and displacer motions implemented via a rhombic drive mechanism. Sliding shaft seals are used on all the reciprocating surfaces to separate the expansion, compression and buffer spaces. As the GM-GPU3 is operated as a fully pressurised engine, the seals are subjected only to the differential pressures which arise between the expansion and compression spaces as well as between the compression and buffer spaces. The engine is designed to yield a maximum power output of about 7.5 kW using hydrogen as the working fluid at a mean pressurisation of 69 bars.

A detailed quantitative description of the GM-GPU3, together with an analysis of the rhombic drive kinematics is presented in appendix E. The following brief description of the working fluid flow path is given with reference to figure 7.1. Forty 3.02 mm internal diameter heater tubes rise perpendicularly from the periphery of the expansion space cylinder and are terminated by a header. The header is connected to eight regenerator/cooler assemblies via a second set of 40 tubes so that five tubes are allocated to each assembly.

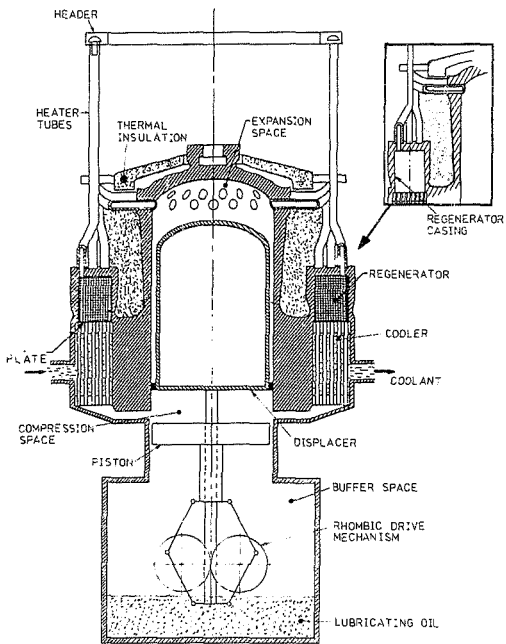


Figure 7.1 Schematic of the GM-GPU3 Stirling engine  
 (adapted from a figure reproduced from reference Th79)

Approximately one third of the lower section of both sets of heater tubes is shrouded with insulation while the remaining portion is heated by a diesel fuel fired burner. The eight regenerator cartridges each consist of 308 layers of 200 mesh stainless steel wire cloth. Thirty nine cooler tubes, with a 1.06 mm internal diameter, are connected to a baffle plate beneath each regenerator matrix. The 312 tubes thus constituting the aggregate cooler connect with an annular plenum which is radially ported to the compression space. Cooling water circulates around the cooler tubes so that, in effect, heat is removed from the entire lower portion of the displacer cylinder assembly.

A tabulation of the salient specifications of the GM-GPU3 used in the simulation programme is given in table 7.1. It may be noted that the heater is represented geometrically as three components (as described above) with the header separating the two sets of tubes connecting to the expansion space and the regenerator. As detailed in section E.4, each set of tubes is further subdivided into insulated and uninsulated portions for the purpose of specifying experimentally determined wall temperature boundary conditions. The volume contained within the expansion space side heater tubes is shown as having active and passive components. This serves to include the gas contained within the instrumentation tubes in the overall heater dead volume while excluding this gas from participating in the convective heat transfer process.

An analysis of the regenerator mesh geometrical properties is detailed in section E.5. The free flow area is computed from the tabulated parameters using a sinusoidal flow area ratio as defined by Finker and

Table 7.1 Salient specifications of the simulated CM-GPU3 Stirling engine

<b>Rhombic drive:</b>	
Crank Radius	13,8 mm
Connecting rod length	46 mm
Eccentricity	20,8 mm
<b>Expansion space:</b>	
Diameter	70,1 mm <sup>3</sup>
Radial clearance volume	3,34 cm <sup>3</sup>
Axial clearance volume	9,15 cm <sup>3</sup>
<b>Compression space:</b>	
Diameter	69,9 mm
Displacer rod diameter	9,53 mm
Radial clearance volume	7,36 cm <sup>3</sup>
Axial clearance volume	13,83 cm <sup>3</sup>
<b>Displacer:</b>	
Shell length	43,59 mm
Shell inside diameter	66,42 mm
Shell outside diameter	69,6 mm
Material	310 stainless steel
<b>Heater - expansion space side:</b>	
No. of tubes	40
Inside diameter	3,02 mm
Active volume	33,36 cm <sup>3</sup>
Passive volume (instrumentation tubes)	2,74 cm <sup>3</sup>
<b>Heater header:</b>	
Hydraulic diameter	5,03 mm
Aggregate flow area	7,94 cm <sup>2</sup>
Aggregate volume	7,67 cm <sup>3</sup>
Aggregate heat transfer area	55,33 cm <sup>2</sup>
<b>Heater - regenerator side:</b>	
No. of tubes	40
Inside diameter	3,02 mm
Volume	37,07 cm <sup>3</sup>
<b>Regenerator:</b>	
No. of casings	8
Casing diameter	23,06 mm
No. of layers in gauze stack	308
Gauze mesh	200 / inch
Gauze wire diameter	0,0406 mm
Volumetric porosity	69,7 %
Volume between heater and matrix	8,75 cm <sup>3</sup>
Volume within matrix	50,6 cm <sup>3</sup>
Volume between matrix and cooler	6,16 cm <sup>3</sup>
Gauze material	304 stainless steel
<b>Cooler:</b>	
No. of tubes	312
Inside diameter	1,08 mm
Volume	13,14 cm <sup>3</sup>

Herbert (PH67). The axial conduction area between gauze layers is defined somewhat arbitrarily by considering the entire matrix to be a homogeneous sponge whose void volume is anisotropically quantified by the volumetric porosity. The radial conduction area between the matrix and regenerator casing is more precisely determined as an aggregation of the mesh wire cross sectional areas in planar contact with the casing.

The tabulated displacer parameters are used to perform a thermal energy balance on the displacer to account for the conduction heat transfer between the expansion and compression spaces via the displacer shell (see section E.2).

### 7.3 EXPERIMENTAL MEASUREMENTS

Two series of experimental tests using helium and hydrogen as working fluids were performed on the GM-GPU3 engine. The first series, termed the 'low-power baseline' tests, is reported in reference Th79. Subsequently, a second series of tests, termed the 'high-power baseline' tests was carried out and is described in reference Th81.

The experimental measurements performed are sufficient to infer hot and cold end energy balances as well as to determine indirectly the indicated power output. As the hot and cold end thermal energy balance measurements are non-controversial and well documented in reference Th79, details of these measurements will not be repeated here. However, some discussion of the indicated work inference procedure is warranted. The shaft power output for all the low-power

tests was determined by measuring the electrical power output delivered by an alternator coupled to the engine. The measured alternator output power was then converted into engine shaft power using a calibrated alternator efficiency correction. In the high-power test series, the shaft power was determined directly from the measured engine speed and a torque measurement supplied by a shaft-mounted transducer.

The total power dissipated by the mechanical linkage and shaft-driven oil pump (located within the crankcase) was assessed by measuring the heat rejected by the crankcase oil which was circulated through an external heat exchanger. The indicated work or pressure-volume hysteresis loss occurring in the buffer space was estimated by measuring the heat rejected to the coolant circulating through a buffer space cooling jacket.

Thus the net indicated power produced is found by adding the shaft power to the crankcase oil heat rejection rate and buffer space coolant heat absorption rate. There is some question as to the overall accuracy of this approach, particularly with regard to the efficacy of inferring the buffer space hysteresis loss from the cooling water heat absorption. However, the experimental energy balance closure errors reported by NASA (Th79, Th81) do provide some quantitative means of assessing the errors which may arise from this source. Some corroboration of the indirect indicated power measurement was provided by direct pressure-volume ( $P-V$ ) diagram measurements made in the expansion and compression spaces. Excellent agreement between the direct and indirect measurements is reported for some of the low-power tests (Th79), although the same level of

agreement was apparently not achieved for all the low-power tests. Apparently more consistent agreement between the indicated works determined from *P-V* diagrams and those inferred from energy balance measurements was achieved in the later series of high-power tests. However, anomalies in the *P-V* diagram results for the helium working fluid high-power tests are still cause for concern. In general terms, then, the indirect energy balance method appears to be an adequate assessment of the indicated power output with universal corroboration being inhibited by deficiencies in the *P-V* diagram measurements.

Other experimental measurements which are relevant to the simulation validation include cyclic mean working fluid temperatures in the compression space and at two locations in the heater tubes. In addition, expansion and compression space dynamic pressure measurements enable pressure swings and phase relationships relative to the displacer top dead center (TDC) or minimum expansion space volume to be reported. As discussed in sections E.3 and E.4 for the compression space and heater respectively, no precise physical locations for the working fluid temperature measurements are supplied (Th79, Th81). Hence, in this regard, comparisons of simulated and experimental cyclic mean working fluid temperatures are subject to an inherent systematic error.

A similar deficiency exists with regard to the pressure measurements. The expansion space pressure transducer was located at the end of a 152 mm long tube which was presumably connected to the expansion space cavity, although no diagrammatic or textual evidence of this is provided. The compression space pressure transducer was approximately flush mounted (Th81), although once again no exact location is

specified. A logical presumption for the mounting location would be on the annular compression space plenum wall (Figure 7.1), although no confirmation of this has been obtained. Several problems with the pressure measurements themselves are reported (Th81). Owing to a lack of water cooling of the pressure transducers during the low power tests, the transducers are postulated as having suffered from a variable, temperature induced sensitivity shift. This deficiency was corrected in the high power tests. A response problem with the expansion space transducer, owing to the length of its attachment tube, is also suggested, but only for the helium working fluid tests.

In view of the experimental uncertainties inherent in the temperature and pressure measurements compared with the relative confidence expressed in the energy balance measurements (Th81), the cyclic energy balance measurements are used here as the primary means of determining the validity of the simulation. The temperature and pressure experimental data are thus used in a more qualitative fashion as a means of clarifying deficiencies in the simulation model as suggested by discrepancies encountered in the experimental/simulation cyclic energy balance comparison.

The remaining experimental measurements of concern are those required to establish the boundary conditions defining a given experimental test. Measurements of the expansion space, heater and regenerator casing wall temperatures provide the hot end thermal boundary conditions (discussed in sections E.2, E.4 and E.5, respectively). Coolant flow rates and temperature drops enable a common cooler and compression space wall temperature to be inferred (section E.6). The cyclic frequency is determined from the output shaft speed measurement

and the working fluid pressurisation is equated to the monitored mean compression space pressure.

#### 7.4 MODELLING ASSUMPTIONS

In applying the one-dimensional simulation model to the GM-GPU3, the assumptions discussed below have been made. These assumptions, by definition, detract from the objectivity of the validation process by introducing artificial dissimilarities between the simulated and actual engines. In order to mitigate these effects, the assumptions made are generally restricted to those predicated by limitations in the description of the engine geometry (Th79) or by the requirements of a purely one-dimensional discretisation. The assumptions are categorised by their area of application.

##### 7.4.1 Fluid Dynamics

1. External and mutual energy transmission to the working fluid is either non-existent or negligible and may be ignored. Specifically, radiation heat transfers between the walls and the gaseous working fluid as well as between different segments of working fluid may be ignored because the thermal radiation of gases such as helium and hydrogen is essentially zero (ED72). Hence  $\dot{E} = 0$  in equations (5.40), (5.42), (5.43) and (5.44).
2. The acceleration of the working fluid caused by the piston and displacer motions is several orders of magnitude larger than the acceleration due to gravity thus permitting gravitational forces

to be ignored. This is a standard practice in vertically oriented Stirling machine simulations (Sc78) which is well-justified empirically since the inclusion of gravitational forces in the momentum equations has a negligible impact on the overall simulation results. Ignoring gravity also permits a considerable simplification in the computer programme because the logistics necessary to determine whether a particular control volume is vertically or horizontally inclined may be eliminated. Hence  $g = 0$  in equations (5.30) and (5.31).

3. The bulk compressibility is identically zero for monatomic gases such as helium and is negligibly small for diatomic gases such as hydrogen (HC54). Hence the bulk compressibility  $\Lambda$  is set to zero in equations (5.30), (5.31), (5.40), (5.42), (5.43) and (5.44).

#### 7.4.2 Boundary Conditions

1. Working fluid leakage across the sliding seals is assumed to be zero. Consequently the mass of the working fluid is taken to be constant over the cycle and no parasitic momentum and enthalpy losses are allowed. This assumption may be justified physically by noting that the seals are subject only to differential pressures which vary in an approximately sinusoidal fashion. Hence, at cyclic steady-state, gas leakage in one direction is compensated by leakage in the opposite direction when the pressure differential changes sign, producing an overall cyclic effect which is small. Pragmatically, neither seal geometry specifications nor pressure differential dependent seal leakage rate data are supplied in references Th79 and Th81. Hence little

- basis for realistically accomodating seal leakage effects exists.
2. The radial temperature gradient in the expansion space cylinder wall is negligibly small. As discussed in section E.2, this enables the cylinder wall boundary condition temperatures to be expressed via a logarithmic profile.
  3. The heater wall temperature boundary co. ditions may be specified by five discrete temperatures as noted in section E.4. This represents a best effort at quantitatively applying qualitative temperature transducer location data given in the form of unscaled schematics (Th79). The experimental cyclic mean gaseous and wall temperatures used are averages of the temperatures measured over several heater tubes at the same axial location.
  4. The radial temperature gradient in the regenerator casings is negligibly small. As described in section E.5, this allows the regenerator casing temperature boundary conditions to be described by a combination of linear and logarithmic profiles. The wall temperatures used to establish these profiles are averages of the temperatures measured on several of the regenerator assemblies at each axial location.
  5. A single experimentally measured aggregate cold-end temperature is used to establish the wall temperature boundary condition for the cooler and compression space as justified by the analysis presented in section E.6.

7.4.3 Conduction Heat Transfers at the System Boundary

1. The cyclic steady-state heat transfer between the expansion and compression spaces via the displacer is primarily dependent upon

the conduction heat transfer through the displacer shell. The contribution of convection loops within the displacer shell cavity is assumed to be negligible and is thus ignored. The displacer shell temperature is determined on a transient basis (see section E.2) by assuming that the upper and lower displacer faces are in instantaneous equilibrium with their adjacent working fluids. This approach enables cyclic integral conduction heat transfers between the expansion and compression spaces to be approximated adequately.

2. Conduction heat transfers between the buffer and compression spaces are ignored as predicated by a lack of adequate geometrical data. This neglect is also justifiable because, apparently, these conduction transfers are not included in the experimental cold-end energy balance which determines the heat removed externally from the working fluid (the experimental result used for validation purposes).

#### 7.4.4 Regenerator Matrix Geometry

1. As alluded to in section 7.2 and detailed in section E.5, a sinusoidal flow area ratio is used to determine the free flow area through the regenerator matrix. This is based upon the assumption that experimental flow data developed for single screen matrices may be generalised to multiple screen matrices. In a compressible flow situation, the use of a sinusoidal area ratio rather than the more conventional orthogonal area ratio is justified on the basis that a sinusoidal area ratio apparently yields a more credible estimate of the choking Mach number

(Or84).

2. The axial matrix conduction area is determined by treating the matrix as a homogeneous sponge whose void to solid area ratio is anisotropically quantified by the volumetric porosity. In the absence of any experimental data quantifying the actual axial conduction area, which is dependent upon random stacking induced effects, the anisotropic assumption is a pragmatic alternative.
3. The radial conduction area between the mesh stack and the regenerator casing is determined by assuming that the individual gauze wires are in planar thermal contact with the casing wall. This appears to be admissible, given the notion of a tightly packed and radially compressed gauze stack.

#### 7.4.5 One-Dimensional Discretization

1. Parallel working fluid flow paths in the heater, regenerator and cooler are aggregated and represented by a single flow path. This assumes that the flow is identical in each parallel path which is given credence by the radial symmetry of the GM-GPU3 engine. Multi-dimensional effects in the expansion and compression space cylinders as well as geometrical differences between individual flow paths can distort the radial symmetry of the flow pattern. The description of such distortions is, however, beyond the capabilities of the one-dimensional simulation model.
2. The actual radially symmetric expansion space topology depicted in figure 7.2 is represented by the one-dimensional topology of figure 7.3.

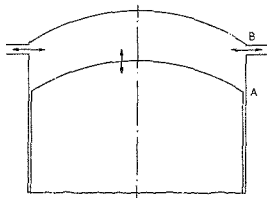


Figure 7.2 Actual two-dimensional expansion space topology

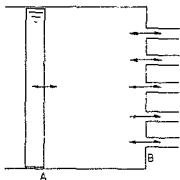


Figure 7.3 Simulated one-dimensional expansion space topology

It is evident in figure 7.2 that the momentum transferred to the working fluid at A is oriented axially while the momentum flux at B is oriented radially. This phenomenon is combined with the influence of the two-dimensional recirculating flow effects discussed in section 6.2. In contrast, the one-dimensional approximation assumes that the momenta at A and B are both axially oriented, so limiting two-dimensional effects to those caused by recirculating flows only. Traditionally (Sc78, UB84, Ur77), the strictly one-dimensional assumption of figure 7.3 has been used in Stirling machine simulation. However, there is recent strong numerical evidence which suggests that ignoring

axial to radial momentum transitions in expansion space dead volumes can be a major source of error (Go87.2). Nevertheless, the strictly one-dimensional interpretation of figure 7.3 is retained here since a more heuristic pseudo-two-dimensional approach might unduly skew the validation process and result in the attribution of undeserved qualities to the one-dimensional simulation model.

3. The radially symmetric, dual piston compression space topology of figure 7.4 may be approximated by the one-dimensional topology of figure 7.5.

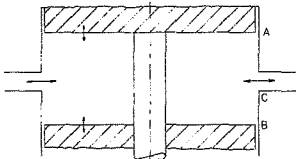


Figure 7.4 Actual two-dimensional compression space topology

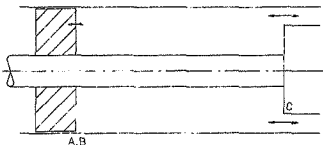


Figure 7.5 Simulated one-dimensional compression space topology

The discrete dual piston motions depicted in figure 7.4 are aggregated into the single piston motion shown in figure 7.5. This aggregate is precise for the volume and rate of change of

volume terms ( $V$  and  $dV/dr$ , respectively). In contrast, the aggregate one-dimensional piston velocity at A in figure 7.5 is defined by:

$$(v_n)_1 = (dV_c/dr) / (A_{cyl} - A_{dr}) \quad (7.1)$$

Hence,  $(v_n)_1$  is unrelated to the momentum boundary conditions actually prevailing in the compression space as depicted in figure 7.4. Under these circumstances, the axial to radial momentum transition phenomenon (noted above for the expansion space) is compounded by the existence of two opposed axial momentum generation sources: (A and B in figure 7.5) producing a coalesced radial momentum flux at C. Thus the one-dimensional discretisation of figure 7.5 is an even more serious assumption than that made for the expansion space. Nevertheless, this assumption has been adopted routinely by previous researchers (Sc78, UB84) since it is a strict application of a one-dimensional spacial discretisation.

Alternate approaches such as that depicted in figure 7.6 have had, of necessity, to be rejected owing to the lack of adequate geometrical data (Th79) for the annular compression space / cooler plenum (section E.3). For example, the approach depicted in figure 7.6 in essence allows for a pseudo-two-dimensional momentum balance to be performed upon the compression space / cooler plenum while still retaining the one-dimensional structure of the momentum equations ((5.30) and (5.31)). A zero radial mass flux on the displacer rod is established as a momentum boundary condition, while the influence of the piston and displacer velocities are manifest only via volume-dependent terms

that do not make an advective contribution to the radial momentum flux at B (in figure 7.6). This approach has been applied successfully to a simulation of the Space Power Demonstrator Engine (Te86, Go87,2). However, as defined, the pseudo-two-dimensional concept does not permit the fluid dynamics of the compression space to be described by the Lagrangian model established in section 5.3.

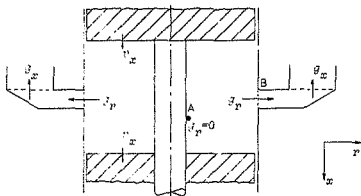


Figure 7.6 Pseudo-two-dimensional compression space discretisation

Therefore, the strict one-dimensional description of the compression space defined by figure 7.5 has been retained, not only owing to the lack of geometrical data, but also in the interests of objectively testing the one-dimensional simulation model as defined in chapter 5. Nevertheless, cognisance of the weaknesses of the one-dimensional compression space topology assumption must be borne in mind when comparing the simulated and experimental data.

Hence, owing to the crucial dissimilarities between the actual and simulated expansion and compression space momentum boundary conditions, in a fundamental sense, the simulated and actual

engines are not identical from a fluid dynamics perspective.

#### 7.5 EMPIRICAL CORRELATIONS

Following the argument presented in section 6.4.3, the friction factor and heat transfer correlations are extracted from Kays and London (KL64). Two classes of correlations are required, one for flows in circular tubes and a second for flows within the regenerator matrix.

The circular tube correlations selected are portrayed in figure 7.7. These correlations represent a summary of the analytic and experimental data available for flow in tubes with abrupt contraction entrances, an appropriate description for each of the individual tubes comprising the heater and cooler of the GM-GPU3. In a one-dimensional system, the heater and cooler heat exchangers are described as an aggregation of their constituent tubes. This predicated the assumption that the working fluid mass flux in each parallel flow path is identical. Hence, evaluation of the friction factor and heat transfer coefficient based on the geometry of a single tube enables the aggregate boundary shear force  $f_o$  and convective heat transfer rate  $\dot{Q}_o$  to be computed.

The correlation curves depicted in figure 7.7 are parametrically dependent upon the length to diameter ratio ( $l/d$ ) of a given circular tube. Thus, applying the correlations to an arbitrarily discretised section of tube is problematic; strictly, the correlations are applicable to entire tubes only. Previous workers (Ba78, Ur77) have chosen to circumvent the problem by arbitrarily selecting correlations

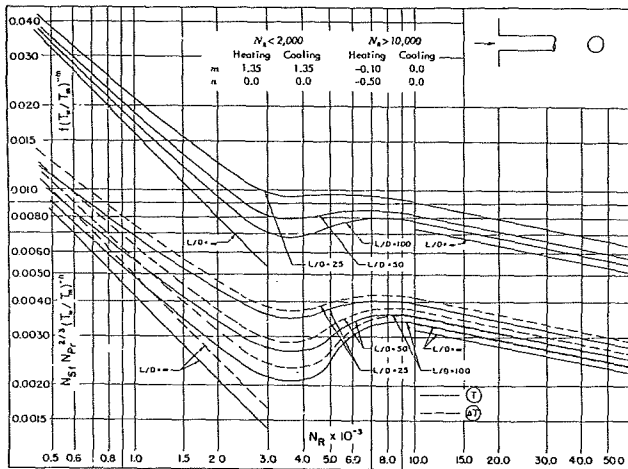


Figure 7.7 Gas flow inside circular tubes with abrupt contraction entrances (extracted from reference KL64)



for infinite  $l/d$  ratios. However, the use of the infinite  $l/d$  profiles in figure 7.7 is unsatisfactory here because the unconditional convergence of iterative numerical schemes (such as that embodied within the implicit algorithms described in section 5.5.2) is dependent upon the absence of any artificial discontinuities which are arbitrarily introduced into the computations. (Conversely, physically real discontinuities, such as shocks, which are explicitly described mathematically do not impose any limitations on an iterative simulation algorithm.)

In particular, the infinite  $l/d$  curves in figure 7.7 include a discontinuity in the laminar to turbulent transition regime for the range  $3000 < N_{Re} < 10000$ . Physically, the laminar to turbulence transition appears to be continuous although a well-defined mathematical description or understanding of the mechanism involved is seemingly as yet unavailable (SS86). Hence, the curves for  $l/d = 100$  in figure 7.7 are selected as the basis of the friction factor and heat transfer correlations used throughout the transfer space of the GM-GPU3. In this context, it should be noted that these correlations are also applied to the heater/regenerator and regenerator/cooler tubular plena as well as to the non-tubular heater header. The potential inaccuracies in using the  $l/d = 100$  correlation profiles in this global fashion on a discretised component basis are incorporated within the parametric validation protocol defined in section 6.5.

One of the attributes of the simulation model is its ability to treat discontinuous changes in cross-sectional flow area explicitly (see section 4.6.2). Hence, the selection of friction factor and heat transfer coefficient correlations for the strictly one-dimensional

expansion and compression spaces defined in section 7.4 appears to be less problematic than suggested by Berchowitz (Be78). The inclusion of momentum modelling in the variable volume spaces (either by a multiple control volume Lagrangian discretisation in the equilibrium algorithm or by a single CEL control volume in the UPD algorithm) simplifies the correlation selection process. In both the UPD and equilibrium algorithms, a continuum mechanics analysis admitting generalised boundary conditions is applied strictly in one-dimension to a space which has a particular non-stationary boundary condition (namely, a moving piston). Hence, to maintain consistency with the continuum mechanics analysis as well as to remain true to the objective simulation model application ethic, the one-dimensional expansion and compression spaces are necessarily no different from circular tubes and are therefore treated as such in the correlation selection process. However, as noted in section 6.2, two-dimensional flows in uni-axial cylinders (that is, cylinders in which the piston motion and boundary fluxes have the same orientation) cannot be represented reliably using a one-dimensional discretisation with its attendant correlations, irrespective of their sophistication. In view of the relatively small convective heat transfers and boundary shear stresses empirically observed for the cylinders of most Stirling machines and for the GM-GPU3 in particular (Th79, Th81), the strict interpretation of the necessity for a one-dimensional circular tube correlation is mainly of pedantic significance, the practical impact being negligible. From the perspective of the validation protocol (section 6.5), the variation of the Lagrangian discretisation parameters  $m_a$  and  $m_c$  has a far greater impact on the engine performance than altering the magnitude of the cylinder friction factors and heat transfer coefficients. Therefore, in terms of

validating the simulation model, the inclusion or exclusion of any friction factor and heat transfer correlations in the expansion and compression spaces is more an issue of consistency than practical importance.

In this context, the geometry of the one-dimensional variable volume space cylinders suggests a selection of the curves with a  $l/d$  ratio of 25 in Figure 7.7 since Kays and London do not present any pipe flow data for tubes with abrupt expansion entrances. These correlations serve purely as a point of reference for parametric variation purposes. In this way, the impact of expansion and compression space heat transfer and multi dimensional dissipation effects on the overall simulation predictions may be demonstrated within the context of the defined validation protocol.

The friction factor and heat transfer coefficient correlations for randomly stacked, woven screen matrices are extracted from Kays and London (1964) and depicted in figures 7.8 and 7.9. Since the GM-GPU3 regenerator has a volumetric porosity of 0.697, interpolation between the curves bounding this value in figures 7.8 and 7.9 is required.

In an effort to adhere as closely as possible to the correlations plotted in figures 7.7, 7.8 and 7.9, they are included in the simulation using a Lagrangian interpolation (Ge70) of the tabulated data produced by a digitisation of the relevant profiles. The digitisation was performed using a flat-bed digitiser with an optically magnified sight and a spatial resolution of 1 in 10000. The details of the digitisation and interpolation procedures are given in section E.7.

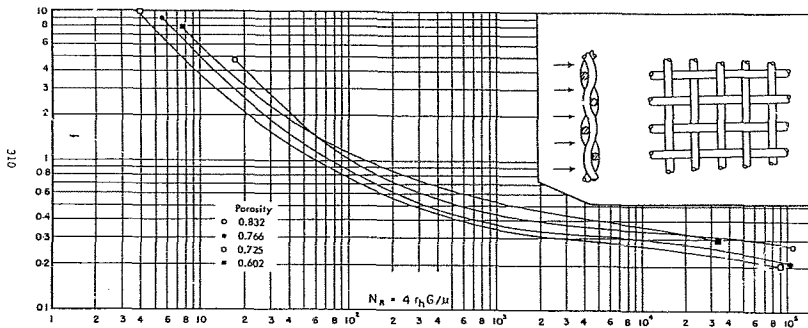


Figure 7.8 Friction characteristics of flow through an infinite randomly stacked woven-screen matrix (extracted from reference KL64)

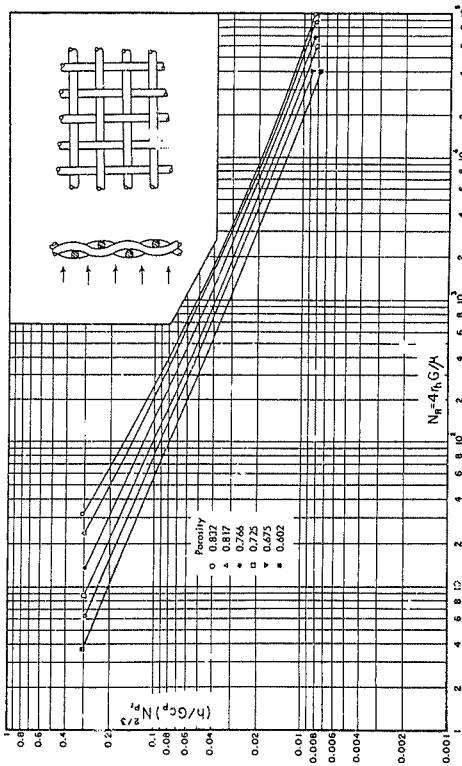


Figure 7.9 linear transfer characteristics of gas flow through an infinite randomly stacked woven-screen matrix (extracted from reference KL64)

As zero Reynolds number conditions may occur during the Stirling cycle (at startup and when the flow reverses), extrapolation to  $N_{Re} = 0$  in figures 7.7, 7.8 and 7.9 is required. A linear regression analysis of the digitised curves in figure 7.7 produces a minimum correlation coefficient of 0,9999 for  $N_{Re} < 800$  (see table E.8). Likewise, a linear regression analysis of the interpolated friction factor correlation curve developed from figure 7.8 yields a correlation coefficient of 0,9999 for  $N_{Re} < 11$ . By a similar procedure, the regression coefficient for the interpolated heat transfer correlation is also 0,9999 for  $N_{Re} < 20$ . Thus the linear regression equations extrapolating the correlations of figures 7.7, 7.8 and 7.9 to a zero Reynolds number (developed in section E.7) appear to be justified on a statistical basis.

For the sake of completeness, it has also been found necessary to extrapolate the correlations of figure 7.7 beyond the Reynolds number of 50000 plotted. Reynolds numbers greater than 50000 at the heater and cooler entrances have been observed to occur when initiating a GIG-GEN engine simulation from rest conditions. However, in all other circumstances, the peak Reynolds numbers have not exceeded 50000 while the maximum Reynolds numbers observed in the regenerator have been within the range plotted in figures 7.8 and 7.9. The extrapolation beyond  $N_{Re} = 50000$  in figure 7.7 is accomplished via a linear regression analysis of the digitised data above Reynolds numbers of 10000. The minimum correlation coefficient of 0,9998 produced (table E.8) warrants the use of the linear regression extrapolation equations developed in section E.7.

In applying the correlations to the simulation in the context of the validation protocol, it has been found convenient to use separate friction factor and heat transfer multipliers ( $K_x$  and  $K_{ht}$  respectively) for the circular tube and regenerator matrix correlations. This enables the influence of the two sets of correlations to be independently assessed by parametric variation.

#### 7.6 NUMERICAL TOPICS

Details of computer programmes embodying the UPD and equilibrium algorithms are presented in appendix F. The programmes, which are written in standard ANSI FORTRAN-77, are accompanied by descriptive tabulations of all the FORTRAN variables used. Also included are algorithmic flow charts and the methodology used to establish the initial cyclic conditions when starting the simulation either from rest (a cold start) or from a condition established by a previous simulation run (a warm start). Hence the issues discussed below are limited to those which are of particular significance to the simulation model developed and its application to the GM-GPU3 engine.

In order to implement the equilibrium and UPD algorithms described in section 5.5.2, several numerical constants *must* be established. These are:

- the integration time increment in the equilibrium algorithm
- the iteration convergence test limit  $\beta$  in equation (5.48)

- the iteration convergence factor  $\beta_{conv}$  in both the equilibrium and UPD algorithms.

It is also necessary to establish whether the simulation has converged to a cyclic steady-state.

These issues, together with a description of the computer hardware and software used to carry out the GM-GPUB simulation are discussed in following subsections.

#### 7.6.1 Numerical Algorithm Constants

The largest physically admissible integration time increment that may be used for a given set of boundary conditions is produced by the UPD algorithm (see section 5.5.2.2). Hence the time increment chosen for the equilibrium algorithm should be sufficiently small in comparison with the UPD algorithm time increment so as to fulfil the equilibrium information propagation hypothesis. Simultaneously, the equilibrium algorithm time increment is bounded below by the desirability of minimising the amount of computation required. On this basis, using an empirical selection process, a time increment defined by a periodic discretisation of 350 increments/cycle has yielded a satisfactory compromise. All the equilibrium simulations performed for the GM-GPUB have thus used a 350 increment/cycle temporal discretisation so as not to add any numerical distortion to the results.

In evaluating the impact of the UPD algorithm, it is useful to introduce a non-dimensional number, termed the characteristic number ( $N_{ch}$ ), as a means of quantifying the information propagation behaviour of Stirling machines. Referring to the discussion in section 5.2, the instantaneous time increment in the UPD algorithm is equal to the machine time characteristic; that is, the interval required for a pressure wave to exactly traverse the unitary pressure domain once. Hence the characteristic number may be defined as the number of pressure wave traverses occurring per cycle or:

$$N_{ch} = (\text{cyclic period}) / (\text{time characteristic})$$

or, using the UPD time increment definition (section 5.5.2.2.):

$$N_{ch} = \Delta t_{per} / \max \left\{ \sum_i l_i / |v_i - (v_a)_i|, \sum_i l_i / |v_i + (v_a)_i| \right\} \quad (7.2)$$

As the maximum characteristic numbers for the entire GM-GPU3 simulation map have not exceeded 240, use of a 35% increment/cycle equilibrium temporal discretisation has proved to be more than adequate for fulfilling the equilibrium algorithm hypothesis while probably being excessive for cases producing characteristic numbers of less than 100.

The iteration convergence test limit,  $\beta$  in equation (5.48), is also subject to bounds. From the standpoint of minimising the amount of computation,  $\beta$  should be as large as possible, while numerical accuracy dictates that the extent to which  $\beta$  may be increased is quite severely constrained. The optimum value of  $\beta = 0.05$  has been determined empirically by applying the implicit algorithms to a variety of physical situations, including natural convection cavity

flows (Go85). This value of  $\beta$  is used for all the simulation runs performed for the GM-GPU3.

In contrast, the iteration convergence factor  $\beta_{conv}$  (section 5.5.2.2, algorithm step 13) may be selected arbitrarily within the range  $0 < \beta_{conv} \leq 1$ . The general criterion for choosing  $\beta_{conv}$  is that it should be as large as possible to enable iterative convergence throughout the cycle with a minimum number of iterations at each time step. Two approaches to choosing  $\beta_{conv}$  have been adopted. In the equilibrium algorithm, an automatic selection procedure dynamically alters  $\beta_{conv}$  at the end of each iteration so as to minimise the number of iterations required for convergence (see section F.4 for a more detailed description). This procedure also has the capability of reducing the integration time increment, when appropriate, to further optimise the convergence process. It may be noted that arbitrary time-step reduction is admissible under the equilibrium algorithm hypothesis. Conversely, no time-step reduction is permissible in the UPD algorithm. This has been found to eliminate any computational advantage accruing from automatically varying  $\beta_{conv}$ . Hence the UPD algorithm utilises a single user-input  $\beta_{conv}$  value over the entire cycle. Generally,  $\beta_{conv}$  values of about 0.5 have yielded adequate performance for all the GM-GPU3 UPD algorithm simulations.

#### 7.6.2 Cyclic Steady-State Convergence

The primary requirement for determining whether cyclic steady state has been achieved is that a cyclic thermal energy balance must be satisfied for the overall working space system as well as for each of

its substituent parts. In the context of the GM-CPU3, energy balances may be performed on the working fluid itself as well as on the regenerator matrix. Treating the working fluid as an isolated system, in terms of the energy conservation formulation of equation (3.31), the first law of thermodynamics (Wa77) may be expressed in cyclic integral terms as:

$$\oint \dot{U} dt = \oint \dot{Q}_s dt - \oint \dot{W} dt \quad (7.3)$$

where the first integral on the right hand side denotes the net heat transfer with the solid boundaries including the regenerator matrix. Hence at cycle steady state,  $\dot{U} = 0$  so that:

$$\langle \dot{Q} \rangle_s = \langle \dot{W} \rangle_{cycle} \quad (7.4)$$

For convenience, the level of cyclic steady-state convergence may be defined in terms of an energy balance error  $\epsilon_{fluid}$  by:

$$\epsilon_{fluid} = \frac{1}{2} \left( \langle \dot{Q} \rangle_{in} - \langle \dot{Q} \rangle_{out} - \langle \dot{W} \rangle_{in} \right)_{cycle} \quad (7.5)$$

where the boundary heat transfer is split into heat addition and heat removal components.

$\epsilon_{fluid}$  is not only a measure of steady-state convergence but is also an overall indicator of the integrity of the simulation model. In practice, it has been observed that the inability to achieve energy balance errors less than 5% is a definitive indication of analytical and/or numerical errors. In this context, a mass balance check is also performed at each time increment as a further test for errors.

From equation (E.31) the cyclic energy balance for each regenerator matrix control volume  $i$  may be described by:

$$(M_m \dot{Q}_m)_i \int (d(T_m)_i / dt) dt = \int ((\dot{Q}_{nm})_i - (\dot{Q}_{nm})_{i+1} + (\dot{Q}_w)_i - (\dot{Q}_s)_i) dt \quad (7.6)$$

where the first two terms within the right hand integral represent the axial heat conducted through the mesh, the third term denotes the radial heat conducted from the casing while the last term signifies the convection heat transfer with the working fluid. At cyclic steady-state convergence the right hand integral must be identically zero which then gives:

$$((T_m)_{i=360}) - (T_m)_{i=1} = (\Delta T_m)_i^{cycle} = 0 \quad (7.7)$$

that is, the final and initial cyclic regenerator matrix temperatures are equal for each regenerator control volume. The temperature difference  $((\Delta T_m)_i)^{cycle}$  is a computationally convenient and sensitive indicator of regenerator thermal convergence and is used as such in the simulation. In particular, the thermal convergence criterion used in the simulation of the GM-CPU3 has been selected somewhat arbitrarily as:

$$\max_i |(\Delta T_m)_i|^{cycle} < 0.1 \text{ K} \quad (7.8)$$

An inordinately large amount of computation is required to achieve this 0.1K criterion for the GM-CPU3. In some cases, this has been demonstrated to amount to the simulation of 100 cycles or more, even though energy balance errors of less than 1% are achieved after five or six cycles. Based upon a suggestion of Urieli (Ur77), the following algorithm has been used successfully to speed up the regenerator thermal convergence process:

From equation (E.31) the cyclic energy balance for each regenerator matrix control volume  $i$  may be described by:

$$\langle N_m \dot{Q}_m \rangle_i \int (\dot{d}(T_m)_i / dt) dt - \int [(\dot{Q}_{nm})_i \cdot (\dot{Q}_{nm})_{i+1} + (\dot{Q}_w)_i \cdot (\dot{Q}_p)_i] dt \quad (7.6)$$

where the first two terms within the right hand integral represent the axial heat conducted through the mesh, the third term denotes the radial heat conducted from the casing while the last term signifies the convection heat transfer with the working fluid. At cyclic steady-state convergence the right hand integral must be identically zero which then requires that:

$$[(T_m)_{e=360} - (T_m)_{e=0}]_i = (\Delta T_m)_i^{1 \text{ cycle}} = 0 \quad (7.7)$$

that is, the final and initial cyclic regenerator matrix temperatures are equal for each regenerator control volume. The temperature difference  $(\Delta T_m)_i^{1 \text{ cycle}}$  is a computationally convenient and sensitive indicator of regenerator thermal convergence and is used as such in the simulation. In particular, the thermal convergence criterion used in the simulation of the GM-GPUJ has been selected somewhat arbitrarily as:

$$\max (\Delta T_m)_i^{1 \text{ cycle}} \leq 0.1 \text{ K} \quad (7.8)$$

An inordinately large amount of computation is required to achieve this 0.1K criterion for the GM-GPUJ. In some cases, this has been demonstrated to amount to the simulation of 100 cycles or more, even though energy balance errors of less than 1% are achieved after five or six cycles. Based upon a suggestion of Urieli (Ur77), the following algorithm has been used successfully to speed up the regenerator thermal convergence process:

$$\{(T_m)_{\theta=0}^*\}_i = \{(T_m)_{\theta=360}\}_i + \beta_{rconv}(\Delta T_m)_{cycle}_i \quad (7.9)$$

where  $\{(T_m)_{\theta=0}^*\}_i$  are the corrected baseline temperatures at the start of the next cycle.

Typically, regenerator convergence factors in the range  $1 \leq \beta_{rconv} \leq 5$  have led to a threefold decrease in the number of cycles required to achieve regenerator thermal convergence. It should however be noted that even under conditions in which equation (7.8) is satisfied, the net regenerator boundary heat transfer will be finite, or from equation (7.6):

$$\left| \sum_i \oint (\dot{Q}_{nm})_i - (\dot{Q}_{nm})_{i+1} + (\dot{Q}_w)_i - (\dot{Q}_w)_i \right| > 0 \quad (7.10)$$

Generally, the residuals at the 0.1K convergence limit do not exceed 5 J; in comparison, achievement of residuals smaller than 1 J requires that the criterion in equation (7.8) be reduced to 0.01K, a prohibitively expensive requirement in terms of the relatively large number of simulations mandated by the validation protocol. The entire issue of regenerator thermal convergence has perplexed other researchers who have developed simulations based on rigorous fluid dynamics considerations (Ge86.). Clearly, a methodology for short-circuiting the simulated physical effects of regenerator matrix thermal inertia would be a useful addition to the art (as opposed to the science) of Stirling machine simulation.

In closing, it may be noted that, as alluded to above, small energy balance errors for the GM-GPUS are obtained with far less computation

than that required to satisfy the regenerator thermal convergence criterion. Hence, in practice, equation (7.8) has proved to be the dominant measure of the achievement of a simulated cyclic steady-state condition.

### 7.6.3 Computer Hardware and Software

Several different processors and compilers have been used in developing, testing and running the UPD and equilibrium algorithm programmes. A chronological summary of the various items of hardware and software used is listed in table 7.2. The initial stages of the simulation programme development were carried out on an IBM mainframe computer. Thereafter, upon the release of an ANSI FORTRAN77 compiler by the Ryan-McFarland Corporation, the code development was shifted to a standard 4.77 MHz IBM Personal Computer equipped with an Intel 8087 arithmetic coprocessor. It soon became apparent that this system was far too slow for code development purposes. At this juncture, an add-in processor board based on an 8 MHz Intel 80286/80287 microprocessor / arithmetic coprocessor set with zero wait-state dynamic random access memory (DRAM) became temporarily available. This accelerated the compilation speed by a factor of about four and the code execution speed by a factor of two. When the 80286 microprocessor board was required elsewhere, the standard IBM PC was modified by the installation of a substitute motherboard supporting a NEC V30 microprocessor, Intel 8087 arithmetic coprocessor, zero wait-state DRAM and a clock speed of 9.54 MHz. This system produced a slightly slower compilation speed than the 80286 based system but the execution speed was increased to almost 2.5 times that of a standard IBM PC.

Table 7.2 Simulation programme development hardware and software chronology

Processor/ Microprocessor	Machine Class	Arithmetic Coprocessor	Clock Speed (MHz)	Memory Mult- states	Operating System	FORTRAN77 Compiler
IBM 4341 <sup>a</sup>	Mainframe	-	-	-	VH/CMS	VS Fortran release 3.0
Intel 8088 (16 bit)	Microcomputer (IBM PC)	Intel 8087	4,77	1	IBM PC DOS version 2.1	Ryan-McFarland version 1.0
Intel 80286 <sup>b</sup> (16 bit)	Microcomputer (IBM PC based)	Intel 80287	8	0	IBM PC DOS version 3.0	Ryan-McFarland version 1.0
NEC V30 <sup>c</sup>	Microcomputer (IBM PC based)	Intel 8087	9,54	0	IBM PC DOS version 3.1	Ryan-McFarland ver. 1.0 and Microsoft ver. 4.0
Motorola 68020 <sup>b</sup> (32 bit)	Workstation (IBM PC based)	Motorola 68801	12,5	1	IBM PC DOS version 3.1	Silicon Valley Software ver. 2.5

Notes:

- a. IBM is the registered trademark of the International Business Machines Corporation.
- b. Installed as a plug-in processor/memory system board on the IBM Personal Computer input/output bus.
- c. An enhanced version of the Intel 8086 microprocessor. NEC is the registered trademark of the Nippon Electric Corporation.

The bulk of the simulation programme development and testing was carried out on this system.

During the final stages of the equilibrium algorithm programme development, the length of the source programme code exceeded the capacity of the Ryan-McFarland compiler which resulted in some spectacular programme failures. Fortunately at this point, use was obtained of an IBM Personal Computer equipped with an add-in 32 bit, 12.5 MHz Motorola 68020/68881 microprocessor / arithmetic coprocessor system which supports the robust Silicon Valley Software FORTRAN77 compiler. The remainder of the equilibrium code development was carried out on the Motorola system, which has a processing capacity roughly equivalent to that of a Digital Equipment Corporation VAX 750 minicomputer. Towards the end of the simulation programme development, Microsoft Corporation released version 4.0 of its FORTRAN77 compiler which, although not error-free, does enable the final versions of both the equilibrium and the UPD algorithm simulations to be run on any computer using one of the Intel 8086 family of microprocessors. All the equilibrium algorithm simulation final runs were performed on the Motorola microprocessor system while the UPD algorithm runs were performed on the modified 9.54 MHz IBM Personal Computer.

The output data produced by the simulation programmes have been processed via the LOTUS 123 spreadsheet programme which has also been used to produce the two-dimensional graphics. The three-dimensional graphics are the output of a specialised programme written by a student under the supervision of the author (see acknowledgements).

## 7.7 VALIDATION RESULTS

The GM-GPU3 experimental performance map is defined in reference Th79 by a total of 67 individual, low-power baseline test data points. Each data point is typically represented by two sets of experimental readings taken sequentially. There is only one high-power baseline performance test data set included in reference Th81, although additional high-power baseline test results are reported as being obtainable from NASA. The experimental test data points used here are selected from the published data only because of their general availability.

The primary criterion for selecting appropriate test data points is an experimental energy balance error less than 10%. This reduces the candidate performance map from 68 to 57 test points; 40 helium and 17 hydrogen working fluid tests respectively. The simulation validation map comprises 9 data points, 4 helium and 4 hydrogen working fluid tests plus an additional test for the simulation calibration phase. The non-calibration experimental test points are chosen to provide a representative range of operating speeds, working space pressurisations, heater temperatures and power outputs. In all cases, the experimental reading set with the lowest energy balance error is selected while a lower energy balance error also governs the choice between two test data points with equivalent experimental parameters. No simulations were performed prior to the non-calibration experimental test point selection. The tests selected are therefore free from any bias incurred from an attempt to choose tests which produce good agreement with the simulation. The calibration experimental test point was chosen arbitrarily because it is included

within the text of reference Th79; the remainder of the test points are reproduced on microfiche and are thus not as convenient to use.

Table 7.3 lists the input parameters required by the simulation model for the nine validation test points. The test description designations used (and adhered to throughout) are the same as those reported in references Th7<sup>6</sup> and Th81. The preface H or HE denotes hydrogen or helium as the working fluid; the digits prior to the hyphen represent the heater wall temperature (1 - 1100°F; 2 - 1200°F; 25 - 1250°F; 3 - 1300°F). The first one or two digits following the hyphen describe the working fluid pressurisation in units of 100 psi (ranging from 2 - 200 psi to 10 - 1000 psi) while the last digit gives the engine speed in decrements of 500 rpm (from 1 - 3500 rpm to 6 - 1000 rpm). In terms of this latter terminology, test HE3-21B should really be defined as HE3-23B in view of its nominal 2500 rpm speed parameter. However, the erroneous designation is maintained to ensure reproducibility. The A or B terminating the designation indicates whether the test parameters correspond to the first or second set of experimental readings taken at each data point. All the hydrogen and helium tests are extracted from the low-power baseline series with the exception of the hydrogen test H25-105A which is the sole high-power baseline test reported in reference Th81.

The hydrogen tests cover a nominal engine speed range of 1500 to 3500 rpm, a pressurisation range of 27 to 69 bars and an average heater wall temperature range of 594 to 726°C. The cold end temperatures vary within 3.8°C of the 20°C mean over the hydrogen test series. A slightly more extensive parameter map is covered by the helium tests which span a speed range of 1000 to 3500 rpm, a pressurisation range

Table 7.3 Input parameter set

Input Parameter	NASA Test Number								
	H1-438	H2-42A	H25-105A	H3-61A	HE1-46A	HE3-21B	HE2-44B	HE3-63B	HE2-101B
Working fluid	Hydrogen	Hydrogen	Hydrogen	Hydrogen	Helium	Helium	Helium	Helium	Helium
Speed (rpm)	2499	2990	1504	3516	998	2496	2003	2503	3495
Charge pressure (bar)	27,4	27,3	29,2	41,3	27,4	13,8	27,4	41,3	69,0
Expansion space wall temperature profile (K)	776,40 588,15 493,15	818,90 636,15 534,15	847,15 680,15 570,15	886,15 722,15 601,15	698,90 521,15 444,15	792,15 600,15 500,15	772,15 579,15 484,15	850,90 656,15 548,15	840,15 707,15 609,15
Heater wall temperature profile (K)	826,15 899,15 906,65 877,15 877,15 877,15 806,15	875,15 952,65 952,15 928,65 929,15 853,15	922,15 1036,65 1014,90 1050,65 1050,65 1016,15 900,15	946,15 1029,15 1034,65 1033,15 1033,15 997,15 913,15	761,15 863,15 903,15 850,65 850,65 858,15 771,15	871,15 984,65 1007,90 968,15 968,15 979,15 879,15	829,15 927,15 957,40 926,15 926,15 905,15 817,15	932,15 1049,65 1052,15 1088,15 1088,15 1007,15 898,15	889,15 1019,65 1022,15 1034,65 1034,65 986,15 836,15
Regenerator casing temperature profile (K)	769,15 626,55 410,15	814,65 640,75 419,65	824,15 651,75 399,15	876,65 666,35 443,65	717,15 634,15 395,15	821,64 681,15 423,65	771,65 647,15 411,15	843,65 696,32 440,15	797,15 647,48 445,15
Cold end temperature (K)	291,10	291,70	296,95	292,90	286,60	287,20	208,70	290,30	297,10

of 14 to 69 bars and a mean heater wall temperature interval of 564 to 756°C. The cold end temperatures are less uniform than those for the hydrogen tests, varying within 7,1°C of a 16,8°C mean.

Table 7.4 Working fluid properties

	Hydrogen	Helium	Reference
Gas constant (J/kg.K)	4125	2085	ED72
Ratio of specific heats	1,40	1,67	ED72
Prandtl number	0,697	0,71	ED72
Fiduciary viscosity (kg/m.s)	$8,35 \times 10^{-6}$	$18,85 \times 10^{-6}$	Br71
Fiduciary viscosity reference temperature (K)	273	273	Br71
Sutherland constant (K)	84,4	80,0	Br71

The helium and hydrogen working fluid properties used in the simulations are given in table 7.4. These data have been extracted from the sources listed and have been corroborated by other references (HC54, Wa77). The gas constant and Prandtl number values tabulated are typical values for the range of temperatures encountered within the GM-GPU3 over the test map specified in table 7.3. The fiduciary temperature and viscosity as well as the Sutherland constant are required for the Sutherland molecular model used to determine the working fluid dynamic viscosity  $\mu$  (see section F.3).

In the following sections, the validation protocol is described in the sequence defined by table 6.1. The specifics of the validation protocol pertaining to the selection of the transfer, expansion and compression space discretisations are described in section 7.7.1. This is followed by a discussion in section 7.7.2 of the characteristics of the simulation model as a function of the baseline

calibration point experimental and simulation data. Thereafter, the baseline and corrected run results are presented in sections 7.7.3 and 7.7.4. To help the reader, all the graphs referred to in sections 7.7.1 and 7.7.2 are collected together at the end of section 7.7.2, beginning on page 360.

#### 7.7.1 Baseline Calibration of the Simulation Model

The baseline calibration experimental data point is defined by helium test HE3-63B (table 7.3). As noted above, no effort was made to deliberately select a test which would indeed enable a baseline calibration to be achieved; the choice of test HE-63B was essentially one of convenience. The baseline calibration phase is carried out in two stages as shown in table 6.1. The first stage leads to a selection of the heater, regenerator and cooler spatial discretisations and the second stage does likewise for the expansion and compression spaces.

7.7.1.1 Spatial discretisation of the heater, cooler and regenerator  
Acceptable minimum levels of spatial discretisation for the heater, regenerator and cooler are determined by holding the coefficients  $K_F$ ,  $K_X$  and  $K_{ht}$  at their baseline values and by representing the expansion and compression spaces by a single control volume each. In the case of the GM-GPU3, as shown in figure E.9 (section E.5), the regenerator is comprised of three sections such that the matrix is bracketed by void plena. These plena are always discretised as single control volumes since they have axial lengths of only 2.6 and 1.8 mm respectively. This is a considerably finer discretisation than that

used in the other unrestricted flow components (as opposed to the restricted flow existing within the matrix).

The baseline calibration simulation run results used to establish the heater discretisation are listed in table 7.5. The runs are performed using intuitively reasonable (Ur77) regenerator and cooler discretisations of 6 control volumes each. As noted in sections 7.1 and E.4, the heater is operationally segmented into the five sections reflected by the sub-discretisation shown in table 7.5. The variation in the tabulated single-run cyclic indicated work outputs and net heat transfers is generally quite small. As the total number of control volumes is increased from 7 to 28, the largest variation amounts to 5% of the initial value for the regenerator heat transfer. On this basis, the 2:4:2:4:2 (or 14 control volume) heater discretisation is chosen as the 1:2:1:2:1 discretisation is too coarse to give an adequate spatial resolution of the flow in the heater for graphical display purposes. The 14 control volume discretisation also approximately defines the 'knee' in the indicated work output and heater heat transfer profiles.

Maintaining heater and regenerator discretisations of 14 and 6 control volumes respectively, the baseline calibration runs to determine the cooler discretisation were performed next. The cyclic indicated work and net heat transfers produced are listed in table 7.6. The 'knee' of the indicated work and cooler heat transfer profiles occurs for a cooler discretisation of about 7 control volumes; hence, a 7 control volume discretisation is selected.

Table 7.5 Heater spatial discretisation calibration with 6 regenerator and cooler control volumes

Sub-component Control Volume Allocation <sup>a</sup>	Total Number of Control Volumes	Indicated Work (J)	Net Heat Transfer in Heater
1:2:1:2:1	7	71,22	306,26
2:4:2:4:2	14	71,44	305,97
3:6:3:6:3	21	71,51	305,78
4:8:4:8:4	28	71,55	305,66

Notes:

- a. listing order given by:  
 (insulated exp. space side : uninsulated exp. space side :  
 header : uninsulated regenerator side : insulated  
 regenerator side)

Table 7.6 Cooler spatial discretisation calibration with 14 heater and 6 regenerator control volumes

No. of Control Volumes	Indicated Work (J)	Net Heat Transfer in Cooler (J)
4	71,00	-85,28
5	71,26	-86,08
6	71,44	-86,62
7	71,57	-87,01
8	71,67	-87,31

Finally, using the 14 and 7 control volume discretisation for the heater and cooler respectively, the regenerator discretisation baseline calibration was performed and produced the results given in table 7.7.

Table 7.7 Regenerator spatial discretisation calibration with 14 heater and 7 cooler control volumes

No. of Control Volumes	Indicated Work (J)	Net Heat Transfer in Regenerator (J)	Net Heat Transfer in Heater (J)	Net Heat Transfer in Cooler (J)
6	71,57	27,44	306,07	-87,01
8	73,22	17,12	304,73	-80,06
10	74,29	10,62	303,94	-75,63
12	75,00	6,03	303,38	-72,49
14	75,54	2,57	303,02	-70,13

In this case, the variations in the tabulated parameters are substantial as predicated by the discussion of porous advection effects in section 6.3. Since  $K_p = 0$  for the baseline runs, the net heat transfers demonstrate the impact of regenerator discretisation on the enthalpy fluxes entering the heater and cooler. The variation in net regenerator heat transfer is somewhat spurious. This arises because after the simulation of a single cycle from rest conditions, the regenerator matrix is very far from convergence at a steady-state condition. Hence, from equation (7.10), the matrix cyclic heat residuals, which generally change sign through the regenerator, may or may not sum to zero, depending on the discretisation. Based on the indicated work and heater and cooler heat transfer profiles, a 12 control volume spatial discretisation of the regenerator approximates the optimum and is thus selected.

The net GM-GPU3 transfer space spatial discretisation amounts to a total of 35 control volumes over a length of 328 mm, yielding an average spatial resolution of 4 mm per control volume. This is finer than the discretisation allocated by Urieli as being

optimum (Ur77) for a generic Stirling machine working space. Use of this level of discretisation to perform all the GM-CPU3 simulations mandated by the validation protocol (more than 830 simulated engine cycles for the 9 test points considered) demonstrates the relative computational efficiency of the simulation model.

#### 7.7.1.2 Spatial discretisation of the expansion and compression spaces

A summary of the cyclic energy balance results for the baseline calibration of the simulation model in terms of the expansion and compression space Lagrangian discretisation parameters  $m_e$  and  $m_c$  is presented in table 7.8. As discussed in section 7.3, the primary means of calibration is a comparison of the cyclic energy parameters, namely, the indicated work done and the net heat externally supplied to and removed from the working fluid.

The data presented in table 7.8 includes the test HE3-63B experimental energy balance results together with their simulated counterparts produced by the equilibrium algorithm. Five levels of Lagrangian discretisation were tested for the expansion and compression spaces with both spaces having the identical discretisation as stipulated in table 6.1. As  $m_e$  and  $m_c$  are increased, the minimum and maximum number of control volumes produced by the simulation over a cycle also increase, although in a different qualitative fashion in the expansion and compression spaces. The influence of the Lagrangian discretisation is discussed first for the expansion space and then for the compression space.

Table 7.8 Test HE3-63B baseline calibration simulation runs: cyclic energy balance comparison

Calibration Parameters and Results	Data Source					
	Experi- mental	Equilibrium Algorithm				
Lagrangian discretisation parameter	-	1	2	3	4	6
Minimum:maximum no. of mass/energy CV's produced over cycle in expansion space	-	1:1	1:2	1:2	1:3	1:4
Minimum:maximum no. of mass/energy CV's produced over cycle in compression space	-	1:1	2:2	2:4	3:5	5:7
External heat supplied (J)	271.52	280.48	261.01	263.35	255.66	248.73
External heat rejected (J)	176.64	167.11	175.68	177.54	173.08	168.83
Indicated work (J)	91.		88.29	89.80	86.55	83.87
Matrix heat balance residual (J)	-	-2.60	-3.05	-3.36	-3.42	-3.77
Energy balance error <sup>a</sup> (%)	1.60	0.02	-0.17	-0.21	-0.19	-0.07
External heat supply discrepancy <sup>b</sup> (%)	-	3.3	-3.9	-3.0	-3.8	-8.4
External heat rejection discrepancy <sup>b</sup> (%)	-	5.5	-0.5	0.5	-2.0	-4.4
Indicated work discrepancy <sup>b</sup> (%)	-	6.	-2.4	-1.4	-5.0	-7.9

Notes:

- a. Simulation energy balance error determined using equation (7.5).  
 b. Discrepancy = 100 (simulation value - experimental value) / (experimental value)

The expansion space minimum discretisation remains constant at unity. This means that, irrespective of the value of  $m_p$ , a condition for which no Lagrangian control volumes are present always exists within the cycle. In these circumstances, the entire space is represented by the CEL (combined Eulerian/Lagrangian) control volume. As  $m_p$  increases, the portion of the cycle during which only the CEL control volume exists is reduced.

This effect is illustrated by the three-dimensional temperature field plots given in figures 7.10 to 7.14. These plots (in common with all the three-dimensional plots presented) are arranged so that position along the one-dimensional axis of the engine is represented by the Y axis, crank angle (which corresponds to the temporal dimension) is plotted along the X axis while the field properties (temperature, pressure or velocity) are denoted by the Z axis. In accordance with the system model of figure 5.4, the expansion space is located spatially at the origin of the Y axis followed by the heater, regenerator, cooler and compression space in the direction of increasing Y.

The case for which  $m_p = 1$  (no Lagrangian control volumes exist throughout the cycle) is shown in figure 7.10. Note that the piston face temperature profiles in the expansion and compression spaces are included only as a spatial bound, since, by definition, the piston face and CEL mass/energy control volume centroid temperatures are identical. The creation and elimination of a single Lagrangian control volume which occurs when  $m_p = 2$  is depicted in figure 7.11. Increasing  $m_p$  to three does not produce an additional Lagrangian control volume but increases the period for which the single

Lagrangian control volume exists, as shown in Figure 7.12. A further increase of  $m_g$  to four produces two Lagrangian control volumes (Figure 7.13), while three Lagrangian control volumes are created and eliminated over the cycle (Figure 7.14) when  $m_g = 6$  (the largest value simulated). Viewing the discretisation sequence (Figures 7.10 to 7.14) as a whole, the portion of the cycle during which only the CEL control volume exists is reduced as  $m_g$  is increased.

The principal physical effect of altering the Lagrangian discretisation in the expansion space can be seen in the temperature gradient. Under fully mixed conditions when  $m_g = 1$  (Figure 7.10), the temperature gradient between the expansion space CEL and first transfer space or heater control volume is relatively small, steepening as  $m_g$  is increased. Referring to Figures 7.15, 7.16 and 7.17 (which depict the velocity fields for the 1, 3 and 6 Lagrangian control volume discretisations), when the working fluid flows in a negative direction from the compression to the expansion spaces (shown by the dashed lines), expansion space control volumes are created. Conversely, control volumes are eliminated during periods of positive flow. Hence the expansion space functions as a 'first-in, last-out' buffer in which the working fluid (or gas) entering first is cooler (owing to its shorter residency in the heater) while the gas entering last is hotter since it has been convectively heated during passage through the regenerator and heater. The one-dimensional Lagrangian model does not permit advective fluid interchange via recirculation within the expansion space; hence the observed temperature stratification.

The physical effect of this stratification is evident in the external heat supply results listed in table 7 d. As  $m_c$  is increased, the gas advected into the heater from the expansion space during periods of positive flow becomes hotter on average, so reducing the convective temperature gradient between the gas and heater wall. This is reflected by the increase in cycle maximum temperatures (which occur in the heater) reported in figures 7.10 to 7.14. Furthermore, as the maximum heater temperature increases, the convective temperature gradient may reverse in sign at certain points in the cycle, causing heat to be removed from the gas in the heater. These convective heat transfer effects in the heater become more significant as  $m_c$  is increased, causing a concomitant net decrease in the cyclic external heat supplied. Over the discretisation range considered, the external heat supply decrease amounts to 31,8 J (or 11% of the simulated external heat supply when  $m_c = 1$ ). This trend is not entirely consistent as a small increase (2 J) in external heat supply occurs when  $m_c$  is increased from 2 to 3. This is probably a particular consequence of the phase angle between the creation and elimination processes and the flow field reversal points.

A similar stratification effect occurs in the compression space although with an altered mechanism. As  $m_c$  is increased, not only does the maximum number of control volumes in the compression space increase but so too does the minimum number of control volumes. Hence for  $m_c = 2$  and  $m_c = 3$  there is at least one Lagrangian control volume present over the entire cycle (figures 7.11 and 7.12) while when  $m_c = 4$  and  $m_c = 6$ , two and four control volumes respectively are always present (figures 7.13 and 7.14). In addition, it may be noted that irrespective of the value of  $m_c$ , at most two Lagrangian control

volumes are created and eliminated over a cycle as shown in figures 7.12, 7.13 and 7.14. The only effect of changing the value of  $m_c$  is that the period of existence of the Lagrangian control volume created second increases while that of the control volume created first decreases.

Viewed as a whole, figures 7.10 to 7.14 demonstrate that there is a pocket of gas adjacent to the piston which never leaves the compression space of the simulated GM-GPU3 engine. The impact of this is revealed by comparing figures 7.10 and 7.14 which contrast the compression space temperature gradients occurring under fully mixed ( $m_c = 1$ ) and virtually unmixed ( $m_c = 6$ ) compression space flow field conditions. The consequences of this phenomena are elaborated further in discussions of the baseline and corrected simulation results.

Figures 7.10 and 7.11 show that the cyclic minimum temperature (which occurs in the compression space) decreases sharply by 58K when  $m_c$  is incremented from 1 to 2, so introducing a single omnipresent Lagrangian control volume in the compression space. Thereafter, further increments of  $m_c$  produce a more gradual decline in cyclic minimum temperature which reaches 15K when  $m_c = 6$  (figures 7.12 to 7.14). These phenomena are a direct result of the isolation of the pocket of gas adjacent to the compression space piston. The isolated gas pocket more or less undergoes a separate adiabatic cycle which is advectively decoupled from the events occurring elsewhere in the working space. A further consequence of this decoupling is that the temperature gradients tend to be small in the purely Lagrangian section of the cylinder and increase rapidly towards the CEL control volume end. As the Lagrangian control volume creation process occurs

primarily during the positive flow portion of the cycle (see figures 7.15 to 7.17) while the control volume eliminations occur during the negative flow portion, by the inverse mechanism described for the expansion space, the gas entering the compression space first is warmer than the gas entering last and vice versa. This accounts for the relatively steep temperature gradients observed for the portion of the cylinder gas dynamically involved in the advection process.

The mechanism by which the heat rejected externally decreases with increasing  $m_c$  (reflected in table 7.8) is a direct consequence of the concomitant decrease in the mass of compression space gas actively involved in the advection process. Hence from figures 7.10 to 7.14, the average temperature of the gas advected into the cooler during the negative flow portion of the cycle decreases as  $m_c$  increases. This reduces the convective temperature gradient in the cooler which causes the amount of heat removed in the cooler to be decreased. As  $m_c$  increases, the reduction in heat removal becomes more acute on a cyclic integral basis. The impact on the external heat rejected amounts to 17.6 J (or 9.4% of the  $m_c = 1$  value) over the  $m_c$  range tested. The same anomaly noted for the expansion space also occurs when  $m_c$  is increased from 2 to 3, producing a 2 J increase in external heat rejection.

In concert with the behaviour of the external heat transfers, the indicated work outputs also decrease as  $m_e$  and  $m_c$  are increased. This mimicry includes an indicated work increase to accompany the anomalous rise in external heat transfers when  $m_e$  and  $m_c$  are increased from two to three. The correspondence between the indicated work and external heat transfer behaviour is a consequence of the changes in the

expansion and compression space one-dimensional temperature fields caused by variations in the Lagrangian discretisation.

Comparing the experimental cyclic energy balance data with those produced by the equilibrium algorithm simulation, it is apparent that in all three comparison categories included in table 7.8, a three control volume discretisation of the expansion and compression spaces ( $m_e = m_c = 3$ ) produces the minimum discrepancies. A maximum error of 3% in the external heat supplied is produced by this level of discretisation. The largest energy balance error occurring over the simulated baseline calibration map amounts to 0.21% which is an order of magnitude smaller than the HE3-63B experimental energy balance error. The largest matrix heat balance residual produced is 3.77 J (for the 0.01K criterion of equation (7.6)) or 1.5% of corresponding external heat supplied. The smallness of numbers testifies to the integrity of the baseline calibration simulations owing to the absence of any systematic errors.

In summary, based upon the validation protocol, the baseline calibration phase leads to the selection of  $m_e = m_c = 3$  as the desired expansion and compression space discretisation. The physical implications of this selection as well as an assessment of the simulation model in the light of the HE3-63B experimental test data is the subject of the following section.

7.7.2 Baseline Calibration Phase Evaluation of the Simulation Model

The evaluation of the simulation model in terms of the baseline calibration phase results is performed in two segments. The first segment covers a discussion of the physical implications of a one-dimensional discretisation of the expansion and compression spaces in the light of the HE3-63B experimental test data. The second segment addresses the effects of information propagation and looks at certain salient characteristics of the simulation model which are not directly related to the validation exercise.

7.7.2.1 Physical implications of the one-dimensional, variable volume space discretisation

In section 6.2, it is argued that the primary purpose of parametrically varying the one-dimensional Lagrangian discretisation of the expansion and compression spaces is to establish empirically a level of discretisation which emulates the actual state of mixing within the cylinders. As noted in section 7.4.2, the validity of this approach is strongly qualified by its lack of compliance with the actual two-dimensional boundary topology of the GM-CPU3 cylinders. Hence, the question at issue is whether the choice of  $m_e = m_c = 3$  produced by the baseline calibration phase is physically relevant or whether it is a purely fortuitous consequence of the numerically well-behaved nature of the HE3-63B test parameters. Insight to this question may be obtained from a comparison of the simulated mean cyclic parameters with their experimental counterparts given in table 7.9.

Table 7.9 Test RES-658 baseline calibration simulation runs: cyclic parameter comparison

Data Source	Lagrangian Discretisation Parameter	Mean Heater Entr. Temp. (°C)	Mean Heater Midpoint Temp. (°C)	Mean Comp. Space Dead Volume Temp. <sup>a</sup> (°C)	Pressure Swing (bar)		Pressure Profile Phase Angle <sup>b</sup> (deg)			
					Exp. Space	Comp. Space	Exp. Space		Comp. Space	
							Min.	Max.	Min.	Max.
Experimental	-	682,	697,	98,	28,9	29,4	295,	70,	285,	70,
Equilibrium algorithm	1	688,1	687,9	83,0	22,3	23,5	302,4	81,3	292,1	80,2
	2	688,7	688,4	85,8	20,8	22,0	301,4	81,3	292,1	80,2
	3	693,4	690,8	80,6	21,0	22,3	301,4	81,3	292,1	80,2
	4	696,1	691,9	79,2	20,3	21,7	303,4	81,8	294,2	80,7
	6	698,9	692,7	78,2	19,8	21,1	298,3	82,8	293,1	80,7

Notes:

- a. Taken to be the CEL control volume temperature in the simulation.
- b. With reference to the displacer TDC (minimum expansion space volume).

In all cases, the mean heater entrance temperatures simulated are greater than those measured; a maximum discrepancy of  $6.1^{\circ}\text{C}$  occurs when  $m_e = 1$ . Conversely, the experimental mean heater midpoint temperatures are greater than their simulated counterparts with the smallest discrepancy of  $4.3^{\circ}\text{C}$  occurring for  $m_e = 6$ . Noting the systematic errors inherent in the experimental temperatures discussed in section 7.3, these discrepancies may just as likely be due to heat transfer correlation errors as to a physically inadmissible one-dimensional discretisation of the expansion space. Furthermore, the relative smallness of these temperature discrepancies shows that, on balance, a one-dimensional discretisation of the expansion space may be appropriate, notwithstanding its two-dimensional boundary topology. Undoubtedly this arises partly because all the working fluid in the expansion space is coupled to the heater via advection as portrayed by figures 7.10 to 7.14. The increase in mean heater entrance and midpoint temperatures with increasing  $m_e$  shown in table 7.9 also validates the mechanism discussed in section 7.7.1.2 for explaining how the cyclic external heat supplied decreases as  $m_e$  increases.

However, the same degree of confidence in the one-dimensional discretisation cannot be expressed for the compression space. Noting the error arising from the uncertainty in the location of the mean compression space dead volume temperature measurement (section 7.3), a minimum discrepancy of  $14.2^{\circ}\text{C}$  ( $14.5\%$  in Celsius terms) is somewhat unpalatable. Qualitatively, the simulated mean compression space dead volume temperature behaviour (temperatures decreasing as  $m_c$  increases) does support the mechanism for describing decreased external cyclic heat rejections with increasing  $m_c$  (see section 7.7.1.2). The rise in

mean temperature when  $m_c$  is incremented to two is a consequence of the introduction of an isolated, cyclically omnipresent Lagrangian control volume in the compression space.

Additional insight into the adequacy of the one-dimensional discretisations of the expansion and compression spaces may be obtained by considering the simulated pressure-volume diagrams given in figures 7.18 to 7.22. Both the compression and expansion space diagrams for all values of  $m_e$  and  $m_c$  are identical in shape. Taking cognisance of the pressure amplitude scaling effect, they also appear to be similar in all respects to the only examples of experimental helium pressure-volume diagrams given in reference Th79 (see figure 7.23 for a reproduction). Hence, at least from this qualitative perspective, the one-dimensional Lagrangian discretisation of the expansion and compression spaces appears to be justified.

An examination of the expansion and compression space pressure profile parameter tabulation reveals what appear to be significant quantitative discrepancies between the experimental and simulated data (table 7.9). On a qualitative basis, however, both the experimental and simulated pressure profiles have the same behaviour, as is depicted by the simulated profiles in figures 7.24 to 7.28. In all these cases, the compression space pressure profile leads that of the expansion space by  $5.2$  to  $10.3^\circ$  at the profile minima while the profiles are almost in phase (a  $1.1$  to  $2.1^\circ$  compression space phase lead) at their maxima. As these figures (together with figures 7.18 to 7.22) are plotted to the same pressure scale, the trend of decreasing pressure swing with increasing  $m_e$  and  $m_c$  can be observed. At the calibration point ( $m_e = m_c = 3$ ), the simulation predicts that

the compression space pressure profile leads that of the expansion space by 9,3 and 1.7° at the profile minima and maxima respectively while the corresponding measured phase advances are 10 and 0°. In view of the uncertainties in the pressure measurements noted in section 7.3, this is judged to be an acceptable level of geometrical similarity. Hence, the qualitative agreement between the phase angle behaviour of the experimental and simulated pressure profiles does contribute to resolving the issue of the adequacy of the simulation model in portraying information propagation effects. It also lends credence to the experimental observations of Berchowitz (Be78) who noted similar behaviour for very different experimental boundary conditions, behaviour not replicated by the Urieli/Berchowitz simulation model (Be78, Ur77).

Nevertheless, on a quantitative basis, the pressure profile parameter discrepancies are indicative of a deficiency in the simulation model, notwithstanding the agreement (absolute errors globally less than 8,5%) obtained between the simulated experimental cyclic energy balance results (table 7.8). The significance of these discrepancies is enhanced by the measured/simulated compression space dead volume mean temperature differences (ranging from 12,2 to 19,8°C) observed. This is also true, although to a much lesser extent, for the heater mean temperature differences. The following analysis is developed as a means of shedding some light on the significance of the mean cyclic parameter discrepancies.

From equations (E.1) and (E.2) (in section E.1), the motions of the displacer and piston produced by a rhombic drive mechanism may be approximated reasonably well by sine curves. The pressure profiles in

the expansion and compression spaces are also approximately sinusoidal (figures 7.24 to 7.28). Hence the indicated work done on each piston and displacer face may be approximated by:

$$dW_{ideal} = P_{amp} \sin(\theta + \phi) d(V_{amp} \sin \theta) \quad (7.11)$$

The subscript 'ideal' is used to distinguish the rate of work done as an ideal approximation of the actual work rate.  $P_{amp}$  and  $V_{amp}$  are the sinusoidal profile amplitudes and  $\phi$  is the phase angle between the pressure and volume profiles.

Integrating equation (7.11) over a cycle:

$$W_{ideal} = P_{amp} V_{amp} \int_0^{2\pi} \sin(\theta + \phi) \cos \theta d\theta \quad (7.12)$$

Using trigonometric substitution and noting that sine curves are periodic over  $2\pi$  produces the result:

$$W_{ideal} = P_{amp} V_{amp} \pi \sin \phi \quad (7.13)$$

From the GN-GPU3 kinematics described in section E.1 and the tabulated pressure profiles parameters (table 7.9), the phasor diagram of figure 7.29 may be constructed

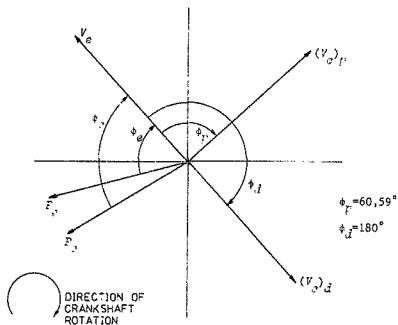


Figure 7.29 GM-GPU3 pressure and volume variation phasor diagram

Using the displacer top dead center (minimum  $V_d$ ) as a fiduciary point, the compression and expansion space pressure profiles lead  $V_e$  by  $\phi_c$  and  $\phi_e$  respectively. The compression space volume variation due to the piston motion  $(V_c)_p$  lags  $V_e$  by  $\phi_p$  while that due to the displacer  $((V_c)_d)$  lags by  $180^\circ$  ( $\phi_d$ ). Hence substituting these relationships into equation (7.13) and summing the contributions of the displacer and piston faces produces the net ideal cyclic indicated work:

$$W_{ideal} = \pi \{ (P_{amp} V_{amp})_e \sin \phi_e + (P_{amp} V_{amp})_c \{ \sin(\phi_c + \phi_p) + \sin(\phi_c + \phi_d) \} \} \quad (7.14)$$

since, from equations (E.1) to (E.9), the motions of the displacer and piston are symmetrical, or:

$$(V_{amp})_c = \{ (V_{amp})_c \}_d = \{ (V_{amp})_c \}_p = L_{cr} (A_{cyl} - A_{dr}) \quad (7.15.1)$$

Also:

$$\langle V_{amp} \rangle_e = I_{cr} A_{cyl} \quad (7.15.2)$$

Substituting equations (7.15) into equation (7.14):

$$W_{ideal} = \pi I_{cr} \{ (P_{amp})_e A_{cyl} \sin \phi_e + (P_{amp})_c (A_{cyl} - A_{dr}) \times \{ \sin(\phi_c + \phi_p) + \sin(\phi_c + \phi_d) \} \} \quad (7.16)$$

In order to use this analysis to gain physical insight from the pressure profile parameters, it is useful to define a correction factor  $\beta_{ideal}$  which accommodates the inaccuracy introduced by the sinusoidal profile assumptions.  $\beta_{ideal}$  is defined by:

$$\beta_{ideal} = (W / W_{ideal})_{simulation} \quad (7.17)$$

Since the experimental and simulated pressure-volume diagrams are similar in shape and differ in area only as a function of their pressure amplitudes, it may be assumed that:

$$\langle \beta_{ideal} \rangle_{simulated} \approx \langle \beta_{ideal} \rangle_{experimental} \quad (7.18)$$

Hence the corrected experimental indicated work determined from the pressure profile parameters is given by:

$$W_{p/p} = \beta_{ideal} (W_{ideal})_{experimental} \quad (7.19)$$

Finally, an experimental pressure swing compensation factor  $\beta_{comp}$  is defined by:

$$\beta_{comp} = W_{experimental} / W_{p/p} \quad (7.20)$$

$\beta_{comp}$  is intended to account for:

- the response error of the expansion space transducer
- the uncertainty in the compression space measurement transducer location
- the systematic errors in producing the experimental pressure profile data from apparently manual analogue oscilloscope and oscillograph readings.

Substituting equation (7.19) into equation (7.20):

$$\beta_{comp} = (W/W_{ideal})_{experimental} / \beta_{ideal} \quad (7.21)$$

Assuming, for the sake of comparative convenience, that the effect of  $\beta_{comp}$  may be exercised on the experimental pressure amplitudes only (in reality, there are experimental errors in both the amplitudes and phase angles), then the compensated experimental pressure swing is given by:

$$(P_{swing})_{P/P} = \beta_{comp} (P_{swing})_{experimental} \quad (7.22)$$

Note that, from equation (7.16), equation (7.22) is applicable to both the expansion and compression space pressure swings.

Using data from tables 7.8, 7.9 and E.1, the above analysis is applied to the baseline calibration phase pressure profile parameters. The phase angles  $\phi_e$  and  $\phi_c$  are taken to be the mean of the angles measured at the expansion and compression space pressure profile maxima and minima. The value of  $\beta_{ideal}$  chosen for substitution into equation (7.21) is that produced by the baseline calibration run for which  $m_e = m_c = 3$ . The results are compiled in table 7.10 which lists the uncorrected ideal indicated work  $W_{ideal}$  from equation (7.16),  $\beta_{ideal}$  produced by each simulation run from equation (7.17),  $\beta_{comp}$  from

Table 7.10 Test ME3-63B baseline calibration simulation runs: Ideal indicated work results generated using pressure profile parameters

Data Source	Lagrangian Discretisation Parameter ( $n_e = n_c$ )	Uncorrected Ideal Indicated Work (J)	Ideal Work Correction Factor ( $\beta_{ideal}$ )	Experimental Pressure Swing Compensation Factor <sup>a</sup> ( $\beta_{comp}$ )	Compensated Pressure Swing Comparison <sup>b</sup> (bar)		Average Pressure Profile Phase Advance (degrees)	
					Expansion Space	Compression Space	Expansion Space ( $\phi_e$ )	Compression Space ( $\phi_c$ )
Experimental	-	109,01	-	0,894	25,8	26,3	87,5	92,5
Equilibrium Algorithm	1	102,37	0,944	-	22,3	23,5	78,15	83,85
	2	95,51	0,931	-	20,8	22,0	78,65	83,85
	3	96,13	0,934	-	21,0	22,3	78,65	83,85
	4	95,40	0,907	-	20,3	21,7	77,40	82,55
	6	92,91	0,903	-	19,8	21,1	79,45	83,10

Notes:

- a. Based on an ideal work correction factor of 0,934.  
 b. Only the experimental swings are compensated; the simulated swings are replicated from table 7.9.

equation (7.21) and the compensated experimental pressure swing from equation (7.22). Also tabulated are the simulated pressure swings which are replicated from table 7.9 and the mean pressure profile phase advances used in equation (7.15) to produce  $W_{ideal}$ .

The uncorrected ideal indicated works follow the same trend as the indicated works listed in table 7.8. This trend is also evident in the behaviour of  $\beta_{ideal}$  which experiences a relatively sharp decrease in value when  $m_a$  and  $m_c$  are incremented from 3 to 4. Hence, from the change in compression space temperature field characteristics evident in figures 7.12 and 7.13, the omnipresent existence of two Lagrangian control volumes in the compression space apparently does produce a discontinuous degradation in the quality of the one-dimensional discretisation model. The experimental pressure-swing compensation factor  $\beta_{comp}$  shows an estimated experimental error of 10,6% in the pressure measurements which appears to be reasonable in the light of the experimental problems discussed in section 7.3. Using the compensated experimental swings to conduct the experimental/simulation pressure swing comparison yields discrepancies in the range of 1,36 to 23,3% for the expansion space and 10,6 to 19,8% for the compression space. At the calibration point, the expansion and compression space pressure swing discrepancies are 18,6 and 15,2% respectively. Comparing the average phase angle advances, the discrepancy ranges are 9,2 to 11,5% and 9,4 to 10,8% for the expansion and compression spaces respectively, while the corresponding calibration point discrepancies are 10,1 and 10,3%.

The pressure swing discrepancies in particular, together with the 17,4°C difference at the calibration point in the mean compression space dead volume temperatures, are in sharp contrast to the small calibration point energy balance discrepancies in the range of 0,5 to 3,0% given in table 7.8. Therefore, based on these data, it may be concluded that while the simulation model of the GM-GPU3 is thermodynamically equivalent to the actual engine it is not fluid dynamically equivalent. Thermodynamic equivalency implies that the simulated and actual boundary conditions are identical for the mass and energy conservation balances. Fluid dynamic equivalency requires thermodynamic equivalency in addition to identical boundary conditions for the momentum conservation balance. Referring to figures 7.2 to 7.5, it is evident that the simulated and actual engines are not fluid dynamically equivalent in the variable volume spaces (as noted in section 7.4.5). Specifically, this is a result of the two-dimensional boundary condition topology of the actual expansion and compression spaces which is neglected in the strictly one-dimensional simulation model. Judging from the better agreement obtained between the experimental and simulated mean heater temperatures (notwithstanding the transducer placement uncertainties alluded to in section 7.3), the degree of fluid dynamic non-equivalency occurring in the expansion space appears to be less than that occurring in the compression space.

Therefore, in closure, the baseline calibration phase leads to the conclusion that the thermodynamic equivalency of the simulation model as applied in a strictly one-dimensional context is validated by the experimental data. The lack of fluid dynamic equivalency is a result of the inability of a one-dimensional discretisation of the variable volume spaces to describe two-dimensional effects adequately. It is

important to note that this is strictly a boundary condition related problem; the data do not support the existence of any inherent deficiencies in the simulation model *per se*, other than its prescribed limitation (see section 1.4) to a one-dimensional system.

This is substantiated not only by the good agreement in energy balance results obtained over the entire baseline calibration map (the largest single comparison discrepancy being less than 8.5%), but also by the geometrical identity of the experimental and simulated pressure-volume diagrams and the similarity of the expansion and compression space pressure profile characteristics. Any inherent errors in the simulation model would not permit this level of agreement. Moreover, the thermodynamic equivalency of the simulation model is achieved precisely because the simulated mass flux field adjusts to its imposed one-dimensional boundary conditions. This produces the simulation/experimental energy balance agreement mandated by the equivalency of the actual and simulated mass and energy conservation balance boundary conditions. As the fluid dynamic non-equivalency occurs only in the variable volume spaces, the mass flux field adjustment is manifested in a physically consistent way: the temperatures advected from the expansion and compression spaces have different values from those measured (table 7.9) and there are discrepancies between the measured and simulated pressure profile parameters (see table 7.10). The assertion that there are no inherent errors in the simulation model is also supported by additional validation work performed on the NASA Space Power Demonstrator Engine (Go87.2) which is briefly summarized in chapter 8. The issue of whether the thermodynamic equivalency of the simulation model demonstrated by the test HE3-63B baseline calibration comparison may

be confirmed over a representative engine test map is addressed in the baseline and corrected phases of the simulation protocol.

#### 7.7.2.2 Simulation model characteristics

The cyclic parameter and energy balance results produced by the UPD and equilibrium algorithms are compared against their experimental counterparts for test HE3-638 in table 7.11. Both the single ( $m_e = m_c = 1$ ) and the calibrated ( $m_e = m_c = 3$ ) expansion and compression space Lagrangian discretisation results are tabulated for the equilibrium algorithm in order to facilitate the discussion of information propagation effects.

Table 7.11 Test HE3-638 baseline simulation runs: simulation model characteristics

Parameter	Experimental	UPD Algorithm	Equilibrium Algorithm	
			$m_e = m_c = 1$	$m_e = m_c = 3$
External heat supplied (J)	271,52	279,76	280,48	263,35
External heat rejected (J)	176,64	186,97	186,43	177,54
Indicated work (J)	91,07	94,06	96,6	89,8
Matrix heat balance residual (J)	-	-1,72	-2,60	-3,36
Energy balance error <sup>a</sup> (%)	1,40	0,15	0,02	-0,21
Mean heater entrance temp. (°C)	682,	690,1	688,1	693,4
Mean heater midpoint temp. (°C)	697,	690,3	687,9	690,8
Mean comp. space dead volume temp. <sup>b</sup> (°C)	98,	83,4	83,8	80,6
Exp. space pressure swing (bar)	28,9	22,2	22,3	21,0
Comp. space pressure swing (bar)	29,4	23,5	23,5	22,3
Exp. space min: max pressure phase angle <sup>c</sup> (deg)	295, :70,	303, 8:82,5	302, 4:81,3	301, 4:81,3
Comp. space min: max pressure phase angle <sup>c</sup> (deg)	285, :70,	292, 5:82,5	292, 1:80,2	292, 1:80,2
Transfer space maximum Mach no.	-	0,051	0,051	0,052
Transfer space maximum Reynolds no.	-	15775,1	15874,4	14980,0
Characteristic number	-	95,8	-	-

**Notes:**

- a. Simulation energy balance error determined using equation (7.5).
- b. Taken to be the CEL control volume temperature in the simulation.
- c. With reference to the displacer TDC (minimum expansion space volume).

Of primary interest in assessing the intrinsic characteristics of the simulation model is the extent to which information propagation

effects appear to influence the simulation results. This assessment may be made most directly by comparing the results produced by the UPD algorithm with those of the singly discretised equilibrium algorithm ( $m_e = m_c = 1$ ). The cyclic energy balance results agree within 0,3% for the external heat transfers and within 3% for the indicated work. In similar vein, the mean heater entrance and midpoint temperatures differ by 2,4°C at most, while the pressure swing and compression space dead volume temperatures agree within 0,5% and 0,5°C respectively. The differences in the pressure profile phase angles (amounting to 3% at most) are primarily a result of the much lower temporal resolution produced by the UPD algorithm (96 increments/cycle, since test HE3-638 yields  $N_{ch} = 95,8$ ) compared with that used for the equilibrium algorithm (350 increments/cycle). The maximum Mach numbers in the transfer space are identical for the UPD and singly discretised equilibrium algorithms while their maximum transfer space Reynolds numbers agree within 0,65%. As the Mach numbers are small, both the UPD and equilibrium algorithms function well within their region of applicability, which is bounded by the sonic limit (section 5.2). Thus, on balance, there are no significant differences between the UPD and equilibrium algorithms with  $m_e = m_c = 1$  on a cyclic parameter basis. The small differences that do exist fall within the ambit of numerical temporal resolution effects.

The similarity of the two algorithms extends to their transient behaviour as well. Figures 7.30 to 7.32 portray the temperature, velocity and pressure fields for the UPD algorithm. A comparison of the temperature field plots of figures 7.10 and 7.30 reveals no geometrical differences while the maximum and minimum temperatures are within 0,8% of each other. Similar geometrical identity is apparent

for the velocity fields of figures 7.15 and 7.30 while in this case the maxima and minima agree within 0.2%. Lastly, the pressure fields of figures 7.32 and 7.33 replicate each other; their maxima and minima differ by 0.2 and 0.04% respectively. This is corroborated at a finer level of detail by the similitude of the pressure-volume diagrams (figures 7.18 and 7.34) and the expansion and compression space piston face pressure profiles (figures 7.24 and 7.35). Since information propagation effects in the context of the UPD and equilibrium algorithm postulates are most likely to manifest themselves in pressure field dissimilarities, the level of agreement achieved between the algorithms in this regard is significant.

Therefore it may be concluded that information propagation effects do not have a significant impact on either the cyclic or the transient predictions of the simulation model when applied to the GM-CPU3 engine for characteristic numbers of 95.8 (produced by the HE3-63B test parameters) or greater. Under these conditions, the equilibrium information propagation hypothesis appears to be well-founded. It must nevertheless be noted that for other engine topologies, particularly under extreme pressurisation and operating frequency conditions (which yield characteristic numbers of 35 or less), notable differences between the UPD and equilibrium algorithm predictions have been observed (Go87.1).

Referring once more to table 7.11, differences between predictions of the UPD and calibrated equilibrium algorithms ( $m_c = m_e = 3$ ) appear to be caused principally by the influence of the expansion and compression space Lagrangian discretisation and not by the influence of information propagation effects. This endows the baseline and

corrected phases of the validation protocol with additional value because the dual algorithm implementation of these phases enables an assessment of the influence of Lagrangian discretisation effects over a broader experimental test parameter map. However, caution in this regard is mandatory in cases yielding characteristic numbers of 95 or less. In these cases, information propagation and discretisation effects may exist simultaneously, preventing either effect from being definitively isolated as the cause of any observed discrepancies.

A few of the more salient characteristics of the simulation model *per se* which are not of immediate relevance to the validation protocol are worth a brief note.

The temperature fields in the heater, regenerator and cooler are geometrically identical irrespective of the expansion and compression space discretisation (figures 7.10 to 7.14 and figure 7.30). A feature of interest in the transfer space portion of these plots is the cyclic hysteresis evident at the regenerator boundaries. Over the cycle, the working fluid (or helium gas) temperatures within the regenerator itself have an invariant linear gradient and seem to be constant, irrespective of the gas flow direction. In the case of the GM-GPU3 regenerator, this offers ample justification for the use of constant linear temperature gradients within the regenerator, as is usually assumed in Schmidt (Sc1871) (or isothermal) and ideal pseudo-Stirling (or adiabatic) (Be78, Go79) analyses.

The velocity field profiles of figures 7.15 to 7.17 and figure 7.31 are also geometrically identical over the transfer space (heater, regenerator and cooler). The velocity profiles in the tubular heat

exchanger comprising the heater and cooler are not perfectly sinusoidal but may be more appropriately represented by a multi-harmonic Fourier series. The impact of the abrupt area changes is also apparent at the heater header, regenerator and variable volume space boundaries. Of particular interest is the time delay taken for the velocity reversal to propagate from the compression space piston face to that of the expansion space. This is shown by the locus of the interface between the solid and dashed plot lines, the latter denoting negative velocities. In the case of the positive/negative transition visible on the velocity field plots, the flow reversal propagation delay amounts to approximately 50° of crankshaft rotation.

The change in velocity at abrupt flow area contractions does not produce any observable discontinuities in the cyclic pressure fields shown in figures 7.32, 7.33, 7.36 and 7.37. The pressure drops associated with these flow area contractions are too small to be visible within the resolution afforded by the pressure scale plotted. However, they may be observed in the sample simulation programme output listings given in appendix G. In compliance with the temperature and velocity fields, the pressure fields are geometrically similar over the transfer space irrespective of the variable volume space Lagrangian discretisation. Comparing the velocity and pressure fields, a positive pressure gradient across the regenerator occurs (as expected) during periods of negative flow, and vice versa. The heater and cooler pressure drops are relatively minor in comparison with the regenerator pressure drop, even in the presence of the losses encountered at flow area discontinuities. Hence, from a validation perspective, dissipation effects are liable to be of major impact in the regenerator only, suggesting that the accuracy of the empirical

Friction factor correlations is of greater significance in the regenerator than elsewhere. Referring to figures 7.36 and 7.37, the overall smoothness of the pressure surfaces surrounding the points at which Lagrangian control volumes are created or eliminated in the variable volume spaces is apparent. This attests to the adequacy of the numerical algorithms used to interface the Eulerian and Lagrangian spaces.

Examples of the cumulative heat transfers in the heater, regenerator and cooler are shown for the UPD and calibrated equilibrium algorithms in figures 7.38 and 7.39. These geometrically identical figures are typical of those produced for all the simulation runs throughout the validation protocol. Both the heater and cooler cumulative heat transfers generally increase monotonically in absolute value with crank angle (an exception occurring over the first  $40^\circ$  during which heat is rejected in the heater), while the regenerator cumulative heat transfer is sinusoidal, terminating with a small positive value. This small cumulative cyclic heat transfer (ranging between 2 and 4 J over the baseline calibration simulation map) is a measure of the overall regenerator inefficiency. The residual gaseous cyclic heat transfer in the regenerator is supplied via heat conduction from the regenerator casing wall.

The mean cyclic regenerator matrix temperatures for the UPD and calibrated equilibrium algorithms are depicted in figures 7.40 and 7.41. These geometrically identical profiles are not as linear as they appear, but are slightly hyperbolic in a concave downwards orientation. Nevertheless, their near-linearity coupled with the linearity of the gaseous temperature gradient in the regenerator

(figures 7.10 to 7.14 and figure 7.30) gives credence to the porous flow advection model postulated in section 6.3. This is further reinforced by noting that all the baseline calibration simulation runs were performed with a porous advection coefficient ( $K_p$ ) of zero.

Finally, the overall energy balance results for the baseline calibration phase of the validation protocol are summarized in table 7.12.

Table 7.12 Baseline calibration phase energy balance discrepancies

	UPD Algorithm	Equilibrium Algorithm with $m_e = m_c = 3$
External heat supply discrepancy (%)	3.0	-3.0
External heat rejection discrepancy (%)	5.8	0.5
Indicated work discrepancy (%)	3.3	-1.4

The largest discrepancy of 5.8% for the external heat rejection (produced by the UPD algorithm) is not a definitive measure of the apparent energy balance parameter prediction accuracy or thermodynamic equivalency of the simulation model. However, in view of the extensive evaluation of all the baseline calibration phase simulated data performed, this level of agreement does not seem to be fortuitous and helps to substantiate the second thesis statement (see section 1.3). In other words, when applied over a one-dimensional spatial integration path, a volume-averaged continuum mechanics analysis permits the working fluid behaviour of a Stirling machine to be determined. Such a one-dimensional analysis also enables an assessment of the fluid dynamic non-equivalency arising from dissimilar actual and simulated boundary conditions to be made.

This latter feature is a unique characteristic of the simulation model and results from its rigorous analytic foundation. This has an important practical application in denoting which regions of a Stirling machine can benefit from a two-dimensional discretisation in order to meaningfully impact prediction accuracy.

The baseline calibration simulations demonstrate the thermodynamic equivalence of the simulation model and GM-GPU3 engine for the test HE3-63B experimental conditions. Hence an inquiry most pertinent to the baseline and corrected phases of the simulation protocol is whether the thermodynamic equivalency is sustained over a broader range of engine operating conditions.

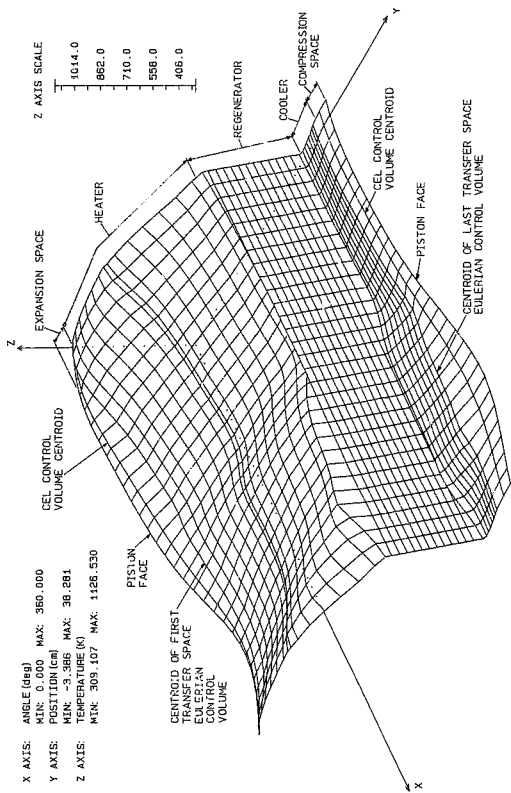
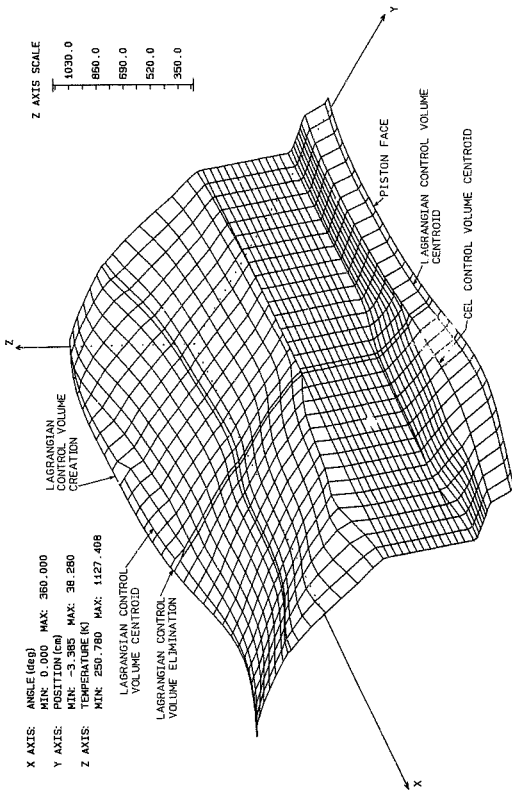


Figure 7.10 HE3-63B/1 baseline, equilibrium run temperature field



X AXIS: ANGLE (deg) MIN: 0.000 MAX: 360.000  
 Y AXIS: POSITION (cm) MIN: -3.385 MAX: 38.280  
 Z AXIS: TEMPERATURE (K) MIN: 250.780 MAX: 1127.408

Z AXIS SCALE  
 1030.0  
 860.0  
 690.0  
 520.0  
 350.0

Figure 7.11 HE3-63B/2 baseline, equilibrium run temperature field

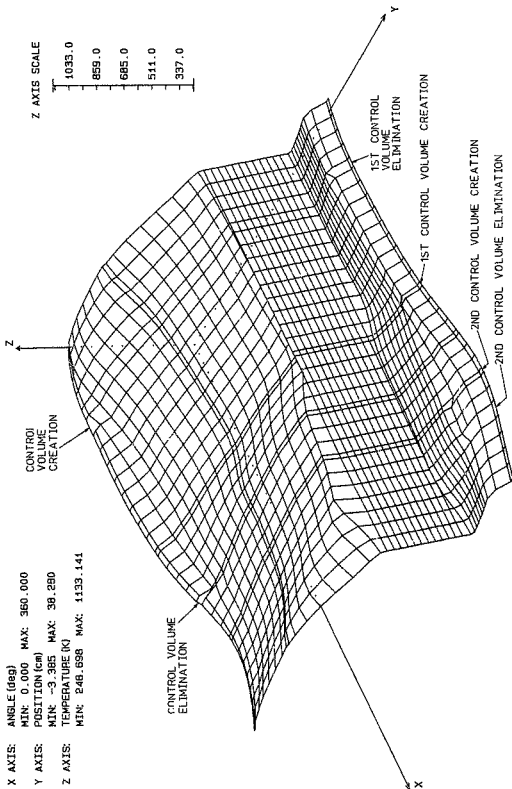


Figure 7.12 HE3-63B/3 baseline, equilibrium run temperature field

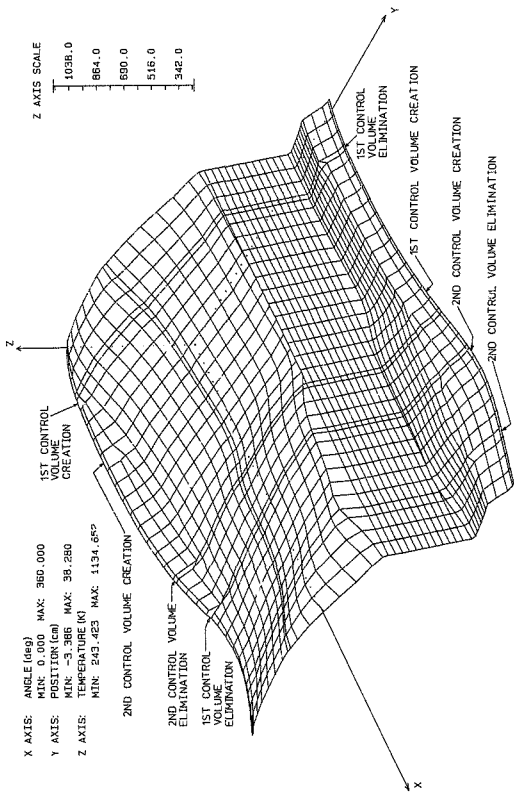
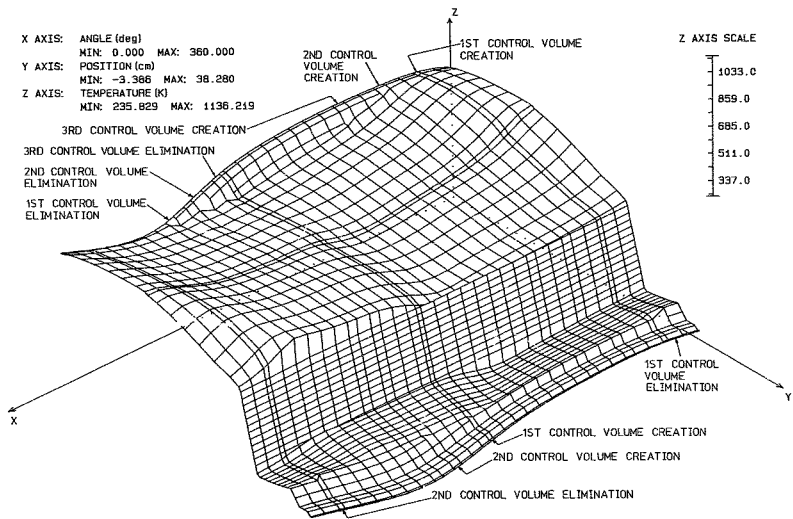


Figure 7.13 HE3-63B/4 baseline, equilibrium run temperature field



364

Figure 7.14 HE3-63B/6 baseline, equilibrium run temperature field

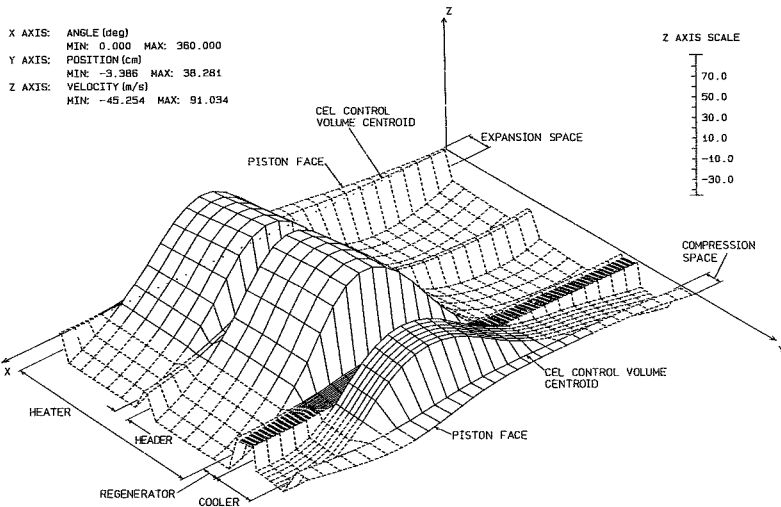
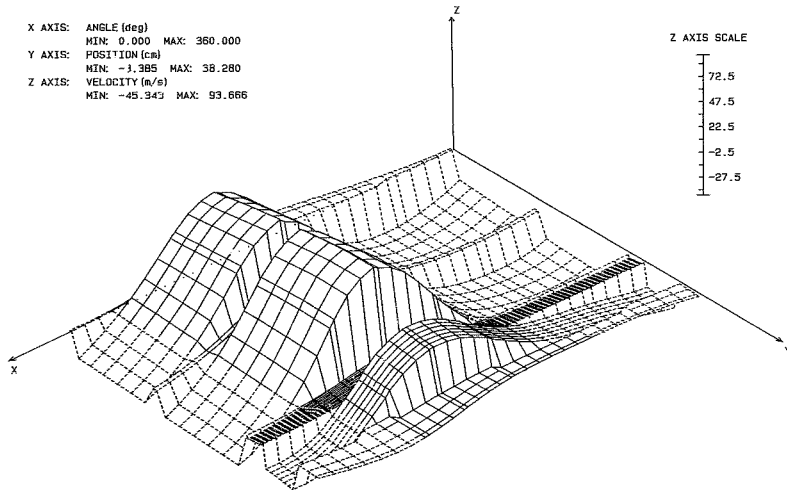
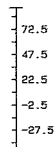


Figure 7.15 HE3-63B/1 baseline, equilibrium run velocity field

X AXIS: ANGLE (deg)  
MIN: 0.000 MAX: 360.000  
Y AXIS: POSITION (cm)  
MIN: -3.385 MAX: 38.280  
Z AXIS: VELOCITY (m/s)  
MIN: -45.343 MAX: 93.666

Z AXIS SCALE



366

Figure 7.16 HE3-63B/3 baseline, equilibrium run velocity field

X AXIS: ANGLE (deg)  
MIN: 0.000 MAX: 360.000  
Y AXIS: POSITION (cm)  
MIN: -3.386 MAX: 36.280  
Z AXIS: VELOCITY (m/s)  
MIN: -45.394 MAX: 91.437

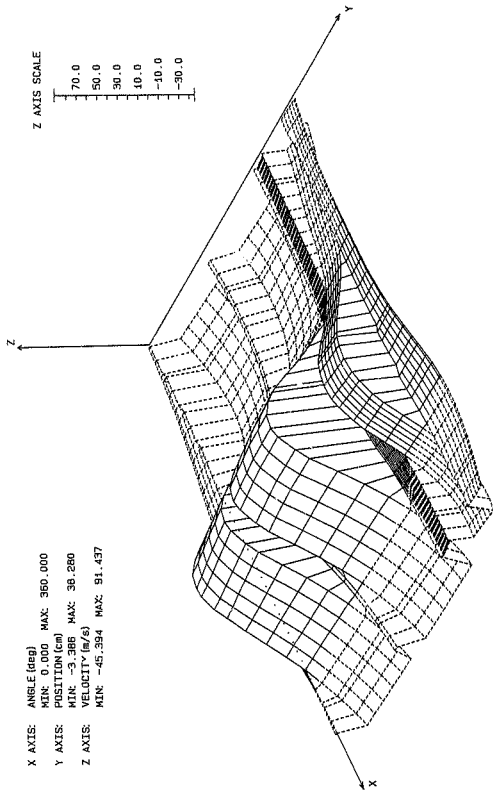
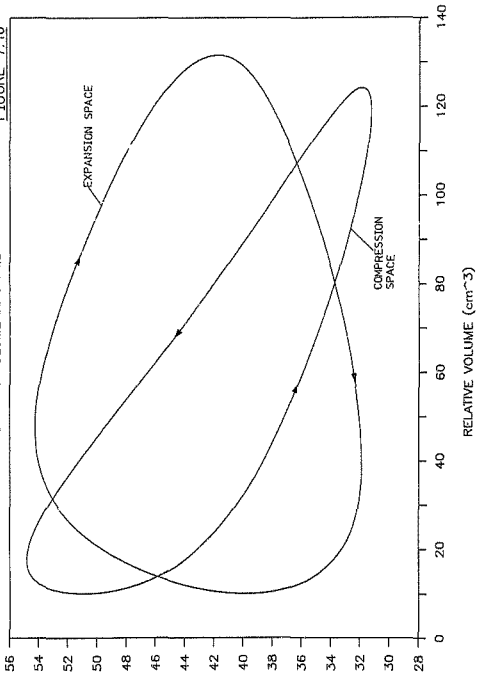


Figure 7.17 HE3-63B/E baseline, equilibrium run velocity field

# HE-3-63B/1 BASELINE EQUILIBRIUM RUN

PRESSURE-VOLUME DIAGRAMS

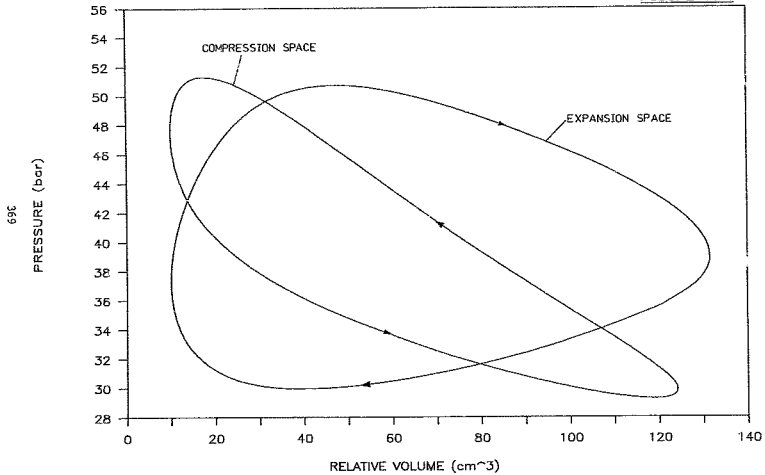
FIGURE 7.18



# HE3-63B/2 BASELINE EQUILIBRIUM RUN

PRESSURE-VOLUME DIAGRAMS

FIGURE 7.19



**Author** Goldberg Louis Franklin

**Name of thesis** A Computer Simulation And Experimental Development Of Liquid Piston Stirling Cycle Engines. 1979

***PUBLISHER:***

University of the Witwatersrand, Johannesburg

©2013

***LEGAL NOTICES:***

**Copyright Notice:** All materials on the University of the Witwatersrand, Johannesburg Library website are protected by South African copyright law and may not be distributed, transmitted, displayed, or otherwise published in any format, without the prior written permission of the copyright owner.

**Disclaimer and Terms of Use:** Provided that you maintain all copyright and other notices contained therein, you may download material (one machine readable copy and one print copy per page) for your personal and/or educational non-commercial use only.

The University of the Witwatersrand, Johannesburg, is not responsible for any errors or omissions and excludes any and all liability for any errors in or omissions from the information on the Library website.